Vibronic luminescence properties of tetragonal transition metal complexes

John K. Grey

Department of Chemistry
McGill University, Montreal
(Quebec) Canada

March 2004

A thesis submitted to the Graduate and Postdoctoral Studies Office
in partial fulfillment of the requirements of the degree of

Doctor of Philosophy

Your file Votre référence
ISBN: 0-494-06304-1
Our file Notre référence
ISBN: 0-494-06304-1

Abstract

The luminescence properties of *trans*-dioxo rhenium(V) and osmium(VI) [d^2] and square-planar platinum(II) and palladium(II) [d^8] transition metal complexes have been studied as a function of temperature and pressure. Both types of complexes studied have idealized D_{4h} point group symmetry with the d^2 systems representing the tetragonally compressed limit of a six-coordinate complex in the D_{4h} point group and the d^8 systems representing the tetragonally elongated limit. The observed luminescence in both classes of complexes has been assigned as a metal-centered (d→d) $^3E_g \rightarrow {}^1A_{1g}$ transition. The application of external pressure provides a means to induce minor changes in the molecular geometries of these model systems that reveal the delicate interplay between structural and electronic properties. Pressure-dependent spectroscopic data are analyzed quantitatively using theoretical models adapted from high-resolution low-temperature spectra where emitting state displacements along vibrational coordinates are determined from resolved vibronic structure. These combined experimental and theoretical techniques allow for a full characterization of the ground and emitting state potential energy surfaces and their explicit dependence on structural parameters.

trans-Dioxo rhenium(V) and osmium(VI) complexes have formal metal-oxo double bonds and the electronic structures of these tetragonal systems are also influenced by the ancillary ligands bonded to the *trans*-$[MO_2]^{n+}$ moiety. A series of *trans*-$[ReO_2]^+$ complexes with substituted *N,N,N',N'*-ethylenediamine ligands were studied that show markedly varying luminescence energies and bandshape characteristics. Pressure-dependent luminescence spectra at room temperature show resolved structure in the high-frequency (~900 cm^{-1}) O=Re=O symmetric (a_{1g}) stretching mode. Variable pressure causes the vibronic patterns to change and a detailed analysis is performed using potential energy surfaces from a coupled states model with the time-dependent theory of spectroscopy. Additional work was carried out on *trans*-dioxo osmium(VI) complexes with monodentate isothiocyanate ligands that show highly resolved vibronic structure at low temperature in both metal-ligand and ligand-centered a_{1g} vibrational modes, allowing for a detailed analysis of the emitting state geometries.

Temperature- and pressure-dependent spectroscopic studies of thiocyanate and selenocyanate complexes of platinum(II) and palladium(II) revealed significant variations of luminescence intensities and lifetimes. Luminescence intensities at room temperature and ambient pressure are weak and almost undetectable. By lowering temperature, the intensities and lifetimes increase by several orders of magnitude and low temperature (ca. 5 K) luminescence spectra show broad, highly resolved bands indicating large displacements along multiple vibrational modes, including Jahn-Teller active non-totally symmetric stretching (b_{1g}) and bending (b_{2g}) modes. By increasing pressure on single crystal samples at room temperature (ca. 300 K), large increases for both luminescence intensities and lifetimes by up to three orders of magnitude are observed. The largest effect occurs for the lower energy emitting palladium complexes. Quantitative analyses of emitting state displacements are then used to rationalize the large pressure effects.

Résumé

Les propriétés de luminescence de complexes *trans*-dioxo du rhénium(V) et de l'osmium(VI) [d^2] et de composés de structure plan-carrée du platine(II) et du palladium(II) [d^8] sont étudiées en fonction de la température et de la pression. Les deux familles de complexes ont la symétrie idéalisée du groupe ponctuel D_{4h} avec les systèmes d^2 représentant la limite tétragonalement comprimée et les systèmes d^8 représentant la limite tétragonalement allongée. La luminescence observée dans les deux classes de complexes a été attribuée à une transition d—d $^3E_g \rightarrow {}^1A_{1g}$. L'application de la pression externe fournit des moyens d'induire des changements mineurs sur les géometries moléculaires de ces systèmes modèles, indiquant l'effet d'un changement des propriétés structurales sur les états électroniques. Des données spectroscopiques dépendantes de la pression sont analysées quantitativement en utilisant les modèles théoriques adaptés aux spectres à haute résolution mesurés à basse température. Les déplacements des puits d'énergie potentielle des états le long de coordonnées normales de vibration sont déterminés à partir de la structure vibronique résolue. Ces techniques expérimentales et théoriques combinées mènent à une caractérisation détaillée des surfaces d'énergie potentielle et de leur dépendance quantitative par rapport aux paramètres structuraux.

Les complexes *trans*-dioxo du rhénium(V) et de l'osmium(VI) ont des liaisons doubles métal-oxo. De plus, les structures électroniques de ces systèmes sont influencées par les ligands auxiliaires. On a étudié une série de complexes comportant le motif *trans*-$[ReO_2]^+$ avec des ligands éthylènediamine substitués. Ces complexes possèdent des énergies de luminescence nettement différentes. Les spectres de luminescence dépendant de la pression à température ambiante montrent une structure résolue dans la vibration d'étirement symétrique O=Re=O avec une fréquence de ~900 cm^{-1}. Les changements de la structure vibronique observés lors de la variation de pression permettent une analyse détaillée utilisent les surfaces d'énergie potentielle d'un modèle d'états couplés. Les spectres résultants sont alors calculés eu utilisant la théorie de la spectroscopie dépendante du temps. Des travaux additionnels ont été menés à bien sur des complexes

trans-dioxo de l'osmium(VI) avec des ligands isothiocyanato qui montrent une structure vibronique résolue à basse température indiquant la présence des vibrations métal-ligand ainsi que des vibrations centrées sur le ligand. Cette analyse détaillée a permis de déterminer la géométrie de l'état initial de la transition d'émission.

Les études spectroscopiques à pression et température variables des complexes thiocyanato et sélenocyanato du platine(II) et du palladium(II) ont indiqué des variations significatives des intensités et des durées de vie de luminescence. Les intensités de luminescence à température et pression ambiantes sont faibles et presque indétectables. À basse température (ca. 5 K), les intensités et les durées de vie augmentent de plusieurs ordres de grandeur. Aussi, les spectres de luminescence montrent des bandes résolues indiquant de grands déplacements le long des coordonnées normales, incluant des coordonnées Jahn-Teller non-totalement symétriques. En augmentant la pression à température ambiante sur des monocristaux, on observe des grandes augmentations pour les intensités et les durées de vie de luminescence jusqu'à trois ordres de grandeur. Le plus grand effet se produit pour les complexes de palladium(II) ayant les plus basses énergies d'émission parmi les complexes étudiés. Des analyses quantitatives des changements structuraux des états excités sont présentées et mènent à une compréhension détaillée des effets de pression.

Foreword

In accordance with guideline C of the "Guidelines for Thesis Preparation" (Faculty of Graduate Studies and Research), the following text is cited:

"As an alternative to the traditional thesis format, the dissertation can consist of a collection of papers that have a cohesive, unitary character making them a report of a single program of research. The structure for the manuscript-based thesis must conform to the following:

Candidates have the option of including, as part of the thesis, the text of one or more papers submitted, or to be submitted for publication, or the clearly duplicated text (not the reprints) of one or more published papers. These texts must conform to the "Guidelines of Thesis Preparation" with respect to font size, line spacing and margin sizes and must be bound together as an integral part of the thesis. (Reprints of published papers can be included in the appendices at the end of the thesis).

The thesis must be more than just a collection of manuscripts. All components must be integrated into a cohesive unit with a logical progression from one chapter to the next. In order to ensure that the thesis has continuity, **connecting texts that provide logical bridges between the different papers are mandatory**.

As manuscripts for publication are frequently very concise documents, where appropriate, **additional material must be provided** (*e.g.* in appendices) in sufficient detail to allow a clear and precise judgment to be made of the importance and originality of the research reported in the thesis.

In general, when co-authored papers are included in a thesis the candidate must have made a substantial contribution to all papers included in the thesis. In addition, the candidate is required to make an explicit statement in the thesis as to who contributed to such work and to what extent. This statement should appear in a single section entitled "Contributions of Authors" as a preface to the thesis. The supervisor must attest to the accuracy of this statement at the doctoral defense. Since the task of the examiners is made more difficult in these cases, it is in the candidate's interest to clearly specify the responsibilities of all the authors of the co-authored papers.

> When previously published copyright material is presented in a thesis, the candidate must include signed waivers from the publishers and submit these to the Graduate and Postdoctoral Studies Office with the final deposition, if not submitted previously. The candidate must include signed waivers from any co-authors of unpublished manuscripts."

This dissertation is written in a form of seven papers. The papers each comprise one chapter in the main body of the thesis (Chapters 3 to 9), with a general introduction to this work in the first chapter followed by a detailed description of experimental setups in the second chapter and conclusions in the tenth chapter. Following the procedure outlined above, the papers have been published or submitted to scientific journals. A list of the papers is given below:

Chapter 3: *Chem. Phys. Lett.* **2002**, *366*, 361-367.

Chapter 4: *Can. J. Chem.* (G. Herzberg memorial issue), accepted for publication.

Chapter 5: *J. Phys. Chem. A* **2001**, *105*, 6269-6272.

Chapter 6: *J. Am. Chem. Soc.* **2002**, *124*, 11699-11708.

Chapter 7: *Inorg. Chem.*, submitted for publication.

Chapter 8: *J. Am. Chem. Soc.* **2002**, *124*, 9384-9385.

Chapter 9: *Inorg. Chem.* **2003**, *42*, 6503-6518.

All of these publications include my research supervisors, Professors Ian S. Butler and Christian Reber, as co-authors since the work was performed under their direction. Chapter 3 includes Mélanie Marguerit as a co-author who participated in this work as part of her summer research project, which involved performing some of the Raman measurements. Chapter 5 includes Dr. Myriam Triest as a co-author for assisting in the implementation of numerical methods for calculating luminescence spectra. Other than the contributions stated above, all of the work presented in this dissertation was initiated and undertaken by the author.

Acknowledgements

I would first like to thank my research directors, Professors Christian Reber and Ian S. Butler for their support and encouragement for this work. Your insight and enthusiasm was steadfast throughout the duration of my project and I have truly benefited from my experience in your laboratories.

Dr. Myriam Triest also played a large role in helping me get my project "off-the-ground" and she has always shown strong support for which I am truly grateful.

I am especially grateful to the Natural Sciences and Engineering Research Council of Canada and to the Fonds de Recherche sur la Nature et les Technologies (Québec) for financial support in the form of postgraduate scholarships.

Past and present members of both the Butler group (McGill University) and Reber group (Université de Montréal) are also recognized for their assistance in learning much of the techniques used in my project. These persons include Guillaume Bussière, Bruno Larue, Rémi Beaulac, François Baril-Robert, Étienne Lanthier and Marie-Christine Nolet at the Université de Montréal and Stephanie Warner of McGill who instructed me in the operation of diamond-anvil cells.

Mélanie Marguerit and Kari Frantzen, summer undergraduate students, also deserve recognition for their assistance.

Lastly, I would like to thank my family for their support and encouragement and Caroline for your patience and understanding.

Table of Contents

List of Frequently Used Symbols

AOM	angular overlap model program
Å	Angstrom
abs	absorbance
B, C	Racah parameters: interelectronic repulsion terms
c	speed of light (2.998×10^{10} cm s^{-1})
°C	degrees Celsius
DAC	diamond-anvil cell
DFT	density functional theory
D	dissociation energy (cm^{-1}) for a Morse potential energy surface
δr	change in bond length (Å)
Δ	normal coordinate offset in dimensionless units
Δ_π	$2e_\pi(E) + 2e_\pi^{\parallel}(L) - 4e_\pi^{\perp}(L)$: vertical energy separation between d_{xy} and d_{xz},d_{yz} orbitals for *trans*-ME_2L_4 (D_{4h}) complexes
Δt	time interval
ε	molar absorptivity ($M^{-1}cm^{-1}$)
e_σ	angular overlap parameter: sigma-type orbital overlap
$e_\pi^{\parallel}$, $e_\pi^{\perp}$	angular overlap parameters: anisotropic π-type orbital overlap, parallel and perpendicular relative to the equatorial plane of the molecule
en	*N,N,N',N'*-ethylenediamine
E_{00}	energy of the electronic origin transition
E_m	half of Stokes shift
E_{max}	energy of the band maximum
fs	femtosecond (10^{-15} s)
ϕ	wavepacket
$\langle\phi \mid \phi(t)\rangle$	auto-correlation function giving the overlap of a time-dependent wavepacket, ϕ (t), onto the intial wavepacket , ϕ

Φ	luminescence quantum yield, = $k_R + k_{NR} / k_R$ or τ / k_R
Γ	phenomenological damping factor (cm^{-1})
$\hbar\omega$	vibrational frequency (cm^{-1})
$\Delta\hbar\omega$	change in vibrational frequency (cm^{-1})
hν	quantum of photon energy (nm or cm^{-1})
HOMO	highest occupied molecular orbital
$I_{lum}(\omega)$	luminescence intensity as a function of frequency
Im	imidazole
1,2-Me_2Im	1,2-dimethylimidazole
k	= $k_R + k_{NR}$: overall luminescence decay rate constant given as the sum of the radiative and nonradiative rate constants (s^{-1})
k_B	Boltzmann constant (0.692 cm^{-1}/K)
kbar	kilobar (10^3 bar)
K	Kelvin
K_{xy}	= $3B + C$: two-electron interelectronic repulsion term
LMCT	ligand-to-metal charge transfer
LUMO	lowest unoccupied molecular orbital
λ	wavelength (nm)
MIME	missing mode effect
m, M	mass
mL	milliliter
MLCT	metal-to-ligand charge transfer
mJ	millijoule
μJ	microjoule
μm	micrometer
μs	microsecond (10^{-6}s)
n-Bu_4N	*n*-tetrabutylammonium cation
NIR	near-infrared region of the electromagnetic spectrum
nm	nanometer (10^{-9} m)
ns	nanosecond (10^{-9} s)

NCS^-	isothiocyante
$[O=Re=O]^+$	*trans*-rhenium(V) dioxo moeity
py	pyridine
π, π^*	pi bonding and anti-bonding overlap symmetry
PPh_4^+	tetraphenylphosphonium cation
PPN^+	*bis*-triphenylphosphoranylideneammonium cation
Q	normal coordinate, Å or dimensionless
ΔQ	normal coordinate offset in Å
R_1	694.2 nm peak of the ruby $^2E \rightarrow {}^4A_2$ emission used to calibrate pressure
Ref	reference
SCN^-	thiocyanate
S	Huang-Rhys factor, dimensionless ($S = \frac{1}{2}\Delta^2$)
σ, σ^*	sigma bonding and anti-bonding overlap symmetry
t, t_0	time
teen	*N,N,N',N'*-tetraethylethylenediamine
tmen	*N,N,N',N'*-tetramethylethylenediamine
τ	$= k^{-1}$: luminescence lifetime (s)
UV	ultraviolet region of the electromagnetic spectrum
Vis	visible region of the electromagnetic spectrum
V_{ij}, C_{ij}	coupling matrix elements between the electronic states i and j (cm^{-1})
ζ	spin-orbit coupling constant (cm^{-1})

List of Tables

List of Figures

List of Schemes

Chapter 1

Introduction

1.1 Effect of structural variations on electronic and optical properties in molecular chromophores.

In molecular chromophores, minor perturbations in the surrounding medium often lead to significant changes in the optical properties through small changes in the structure or geometry of the molecule. This effect can be probed by spectroscopic techniques where changes in band shapes and energies can be quantitatively correlated to structural properties of the molecule. The application of external pressures on molecular chromophore systems is perhaps the most effective means of characterizing this interplay between structure and electronic properties.[1-6] This technique has seen much use in chemistry,[6-12] biology[13,14] and physics,[15-18] which has led to the discovery of new photophysical and photochemical properties that would not be possible to study otherwise. As pressure is applied to a molecular system, structural changes take place that give rise to significantly changed or fundamentally different optical properties. An analogous, but often more subtle, effect can be induced in some chromophores (molecules or atoms) doped into host matrices where the lattice causes small structural changes through lattice strain effects that often lead to significant changes in the optical properties of the chromophore. This effect has been described as a "chemical pressure"[19] whereby the surroundings perturb the electronic structure *via* small changes in its geometry.

In the research described herein, the fundamental question posed is; "How do the electronic and optical spectroscopic properties of luminescent molecules vary with small, *specific* changes in the molecular geometry." To address this question, variable external pressure and temperature spectroscopic techniques are applied to luminescent transition metal complexes. The changes in the luminescence properties, i.e., band shapes, energies, and emitting state relaxation dynamics, are determined using resolved features in experimental data and theoretical methods to extract important structural and

spectroscopic parameters. Luminescent solid systems are excellent models for studying the effects of either a chemical or externally applied pressure since the amount of static disorder is much less than in the solution phase. Furthermore, luminescence techniques provide a means to probe the nature of the ground state in much more detail than afforded from vibrational spectroscopic methods.[20] The experimental techniques and methods of analysis used in this research may also be extended to many other interesting systems possessing optical properties that vary significantly with the geometry or certain structural parameters and surrounding medium.

When an external pressure is applied to molecular crystals, the volume of the crystal decreases which creates an imbalance between intermolecular (i.e., crystal packing forces) and intramolecular forces resulting in decreases in bond lengths and other variations in the molecular geometry. Transition metal complexes are ideal model systems for such experiments due to their rich electronic structures and sensitivity of metal d-orbitals to their local environment. These features enable a wide range of tunability of optical properties with only relatively minor structural perturbations, similar to the effect of ligand substitution on the metal. Traditionally, simple complexes, such as highly symmetric homoleptic molecules or dopant ions in a host lattice, have been studied spectroscopically with variable external pressure.[1,5,8] In these cases, ligand-field theory can be used to the fullest extent to rationalize pressure-induced shifts of band energies and changes in band shapes for electronic transitions localized on the metal atom(s). Some examples of optical phenomena arising from applied external perturbations on transition metal systems will be outlined in the next section.

For the work described in the body of this thesis, the main strategy involves the 'quantitative transferability' of physical models from variable temperature (5—300 K), high-resolution spectroscopic data to room temperature (ca. 300 K), pressure-dependent results. This first requires a detailed characterization of the ground and emitting state potential energy surfaces from resolved vibrational (vibronic) fine structure[21] often observed in low-temperature, ambient-pressure spectra. These models are adapted to describe room-temperature, pressure-dependent luminescence spectra where the change in fundamental spectroscopic parameters can be related to changes in molecular structure and bonding properties. The ability to interchange models between data sets arising from

the independent variation of two physical variables is unprecedented and opens up new possibilities for understanding and controlling the optical properties of a diverse number of chromophore systems.

1.2 Transition metal complexes as model systems

The utility of metal complexes as spectroscopic probes in understanding the effect of minor structural perturbations is reflected in the large number of research reports showing a broad range of effects with variable pressure.[22-33, 35-106] In general, the typical response of a molecular transition metal coordination compound to pressure can range from a continuous shift of electronic bands, due to changes in the energies of orbitals implicated in the transition, to drastic effects such as a change of the ground electronic spin state (spin–crossover)[22-34] or pressure-induced isomerization (piezochromism)[35-44] leading to completely different optical properties. In much of the previous studies involving coordination compounds, simple complexes are used that possess relatively high point group symmetries (i.e., octahedral, tetrahedral, or square-planar) which enable the full use of group theoretical constraints and ligand-field theory (LFT) or molecular orbital (MO) theory to rationalize trends in pressure-dependent spectroscopic data. In many spectroscopic studies, it is often convenient to describe electronic transitions as population changes between one-electron orbital configurations instead of multielectron states. In terms of LFT, the electronic states are constructed from the metal d-orbitals, which means that it is only capable of rationalizing metal-centered (d—d) transitions, whereas MO theory includes contributions from the ligands in the total MO. MO theoretical treatments are required to rationalize charge transfer spectra where electronic transitions are no longer strictly localized on the metal center. In the MO terms, the ground state is often described as the highest occupied molecular orbital (HOMO) and the first one electron transition populates the lowest unoccupied molecular orbital (LUMO). The energy of this transition is approximately the ground- and excited state energy difference. The spectroscopic results presented in this thesis are primarily concerned with these frontier MO transitions where simple orbital schemes are effective in explaining electronic transitions and provide a basis for understanding how varying

molecular geometry affects the energies and normal coordinate offsets between electronic states.

Because pressure decreases the sample volume, this in turn gives rise to decreasing metal-ligand bond lengths and, depending on crystal packing forces, changes in bond angles. These variations in molecular geometry and structure cause changes in the distribution of electron density and can lead to significant variations in the energy differences between electronic states. In theoretical terms, this effect is often interpreted as changes in overlap between localized orbitals on the constituent atoms. Spectroscopically, this is observed as band maxima that shift to higher or lower energy, increasing or decreasing band-widths (FWHM) and changes in band shapes and intensities or, sometimes, completely different spectroscopic characteristics when electronic states are close in energy. For transition metal complexes, the simplest physical picture for understanding these effects is given by classical ligand-field energy level diagrams, such as that shown in Figure 1.1 for a six-coordinate, octahedral (O_h) metal complex that will serve as a benchmark in the following considerations.

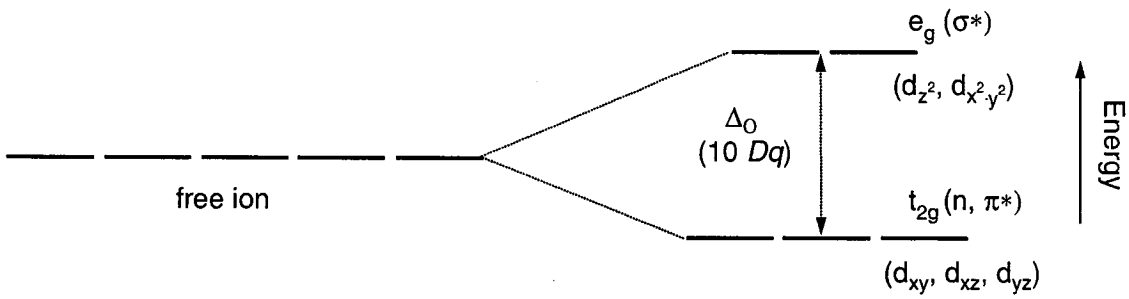

Figure 1.1. Energy splittings of the five d-orbitals of a transition metal ion for an octahedral (O_h) complex.

In this scheme, the number of electrons belonging to the metal center and the strength of the ligand-field dictate the type of electronic transitions observed between the d-orbitals, often called metal-centered (d—d or ligand-field) transitions. The t_{2g} levels consist of the d_{xy}, d_{xz} and d_{yz} orbitals and are σ non-bonding, but have π symmetry and may interact with ligand π-bonding or antibonding (π*) orbitals, whereas the e_g levels (d_{z2} and d_{x2-y2})

are of σ-antibonding (σ*) in character. The energy separation between the t_{2g} and e_g levels is given by 10 *Dq* in Figure 1.1. The magnitude of 10 *Dq* is related to the inverse fifth (spherical, point-charge ligands) and the inverse sixth power (dipolar ligands) of the distance between the ligands and metal center, which implies that an applied pressure resulting in a decrease of metal-ligand bond lengths will always lead to an increase of 10 *Dq* due to a greater destabilization of the e_g orbitals relative to the t_{2g} orbitals. However, interelectronic repulsion energies (described by the Racah parameters *B* and *C*) have a large influence on the energy difference between the electronic states probed by spectroscopy. These parameters tend to decrease with increasing pressure because the reduction in sample volume leads to an increase of covalency. The observed changes in spectroscopic properties as a function of pressure therefore includes both ligand-field and interelectronic repulsion considerations.

In transition metal complexes there are two types of electronic transitions that arise upon absorption or emission of a photon between d-orbitals, inter- and intraconfigurational transitions. Interconfigurational d—d transitions involve populating orbitals that are of different bonding character than the original orbital, which leads to large distortions along metal-ligand normal coordinates and broad optical bands. For example, promoting an electron to the σ* e_g orbitals from the non-bonding t_{2g} orbitals in an octahedral (O_h) complex causes a large displacement along metal-ligand symmetric stretching modes, due to the significant weakening of the metal-ligand bonds. This type of transition often results in weak or unobservable luminescence intensities for many transition metal complexes because of efficient nonradiative deactivation of the emitting state, which is especially prominent for complexes where the energy difference between the ground and emitting states is small (i.e., first-row complexes). The other situation is when optical excitation causes an intraconfigurational transition, such as a spin-flip, that can only occur in transition metal systems with more than one unpaired electron, but does not involve a change in the orbital occupancy. In this scenario, a spin-flip transition does not lead to appreciable structural distortions since the orbital parentage of the excited state remains the same, thus yielding narrower bands and the luminescence quantum efficiency effectively depends on the energy gap between the ground and emitting states. Most pressure-dependent studies of complexes with interconfigurational transitions are

typically performed at room temperature and spectra are virtually devoid of any resolved vibronic structure. In this situation, optical bands tend to shift in energy and the intensity (or absorbance) can vary appreciably. Figure 1.2 shows an example of this case where the band maximum shifts to lower energy (red shift) with increasing pressure that is rationalized by a simple two-state diagram.

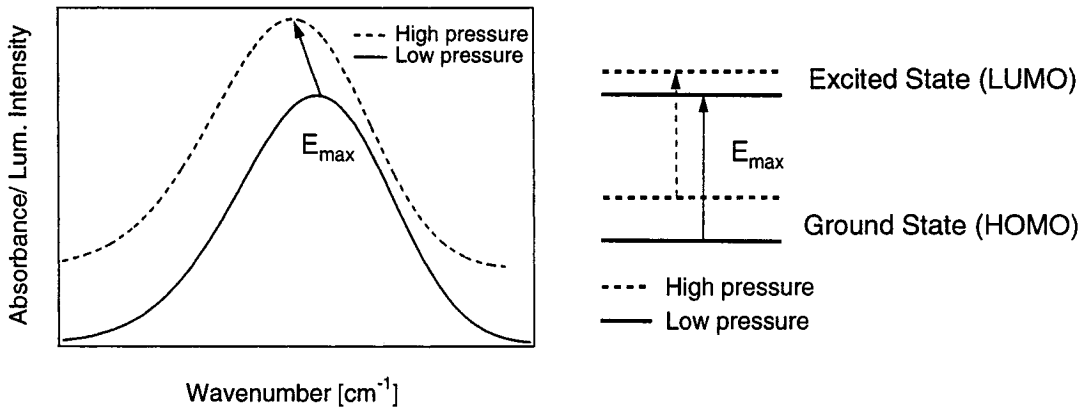

Figure 1.2. Qualitative physical picture for the "classical" effect of pressure with energy level diagrams for the ground (e.g. $HOMO^1$ configuration) and excited ($HOMO^0$ $LUMO^1$ configuration) states at low (solid) and high (dashed) pressures.

In this framework, the change in optical properties depends mainly on the bonding character of the orbitals implicated in the electronic transition and the shift of the band maximum energy, E_{max}, is a measure for the effect of pressure on the energy difference between orbitals (i.e., 10 Dq). Generally, there are simple empirical trends that can be invoked for understanding the behavior of particular optical bands with pressure. For example, σ^* orbitals (e_g) are more destabilized in energy than π^* orbitals (t_{2g}) and orbitals of δ-symmetry or non-bonding orbitals, therefore it is expected that transitions to σ^* orbitals will show stronger shifts in energy than those to π^* and so on. In terms of ligand-field states as depicted in standard Tanabe-Sugano diagrams, this is similar to states that change rapidly in energy with increasing Dq, or pressure. The ability of pressure-dependent spectroscopy to characterize bonding properties through changes in optical spectra using these simple considerations underscores its utility as a modern method for characterization of molecular optical properties. However, when vibronic structure is resolved, it is necessary to use more sophisticated models (i.e., potential

energy surfaces) to account for other important spectroscopic parameters, such as the vertical energy separation between lowest vibrational levels of states, E_{00}, and the horizontal offset of the potential minima along all displaced normal coordinates. These models will be discussed in more detail in section 1.3.

To date, most pressure-dependent spectroscopic studies performed on molecular transition metal complexes have kept within the confines of the simple physical picture afforded by the energy level diagrams in Figures 1.1 and 1.2 that only shift in energy. Nevertheless, these models have been successful in rationalizing changes in pressure-dependent optical spectra with metal-ligand bonding properties if the electronic structures have been characterized. Based on the pioneering work of Drickamer and co-workers, variable pressure studies have revealed a variety of interesting phenomena in transition metal complexes, including spin-crossover transitions and pressure-induced isomerizations leading to new optical properties (piezochromism), as well as the effect of variable pressure on excited state relaxation properties and the parameterization of ligand-field terms. These effects are summarized briefly below.

Spin-crossover transitions have been studied in many d^6 Fe(II) complexes where an application of an external perturbation, such as light fields, temperature or pressure, can lead to a change in the ground electronic spin state of the system.[22-25] For an octahedral complex with a weak ligand field, the six d-electrons will be oriented in the t_{2g} and e_g levels with spins aligned to minimize interelectronic repulsion energies (i.e., $10Dq < \Delta_S$, where Δ_S is the spin-pairing energy) leading to a ground state of high-spin (HS) multiplicity, thus obeying Hund's rule. In terms of the simple ligand-field diagram in Figure 1.1, a pressure-induced decrease of metal-ligand bond lengths will cause an increase in energy of the σ^* e_g orbitals that induces a spin-crossover transition when $10Dq > \Delta_S$ leading to a low spin (LS) state where all six d-electrons are paired in the t_{2g} orbitals, violating Hund's rule. LS→HS relaxation has also been studied by Hauser and co-workers through determination of activation volumes as a function of pressure in mixed crystals.[26-30] At low temperatures, application of external pressures accelerate tunneling rates between the two spin states in a thermally induced spin-crossover transition.[26,27] In solid spin-crossover systems, external pressures can also be used to probe long range solid-state interactions and cooperative effects on the nature of the spin-

crossover transition and subsequent relaxation processes.[31-33] Interestingly, chemical pressures have been utilized in Fe(II) systems to induce spin-crossover transitions. For example, the ground electronic spin-state properties of an Fe(II)-organic nanoporous framework can be tuned by incorporation of exchangeable "guest" molecules of varying sizes, which introduce a strain on the lattice causing small changes in the geometry around the metal center that lead to spin-crossover transitions.[34] In a similar application, chemical pressures were used to turn $[Co(2,2'\text{-bipyridine})_3]^{3+}$ into a spin-crossover system by doping it into a host lattice.[19]

Piezochromism is a pressure-induced change in the geometry of a metal complex that gives rise to entirely different optical transitions.[35,36] These isomerization transitions, like spin-crossover phenomena, can either occur abruptly (phase transition) or continuously depending on the extent of cooperativity throughout the lattice. Useful prototypical systems for these studies are salts of four- and five-coordinate Cu(II) complexes, which have originally shown interesting thermochromic properties.[37-39] The two geometrical limits for the four-coordinate systems range from square-planar (D_{4h}) to tetrahedral (T_d) and a pressure-induced isomerization between these two limits causes a dramatic change in the optical properties. In Cu(II) complexes with substituted ethylenediamine ligands, an axial compression is favored with increasing pressure that causes changes in the d-orbital splitting patterns that may be followed between the two geometries.[40] Ferraro and co-workers have also used external pressures to induce changes in the molecular geometries of some five-coordinate Ni(II) and Co(II) complexes from trigonal-bipyramidal to square-pyramidal,[41,42] where the trigonal-bipyramidal structure could be converted to a square-pyramidal geometry more easily than the opposite structural interconversion. Another example of piezochromism has been reported in racemic lanthanide-based systems where pressure-induced changes in the f—f luminescence excitation properties of Eu(III) complexes with poly-carboxylate ligands provide quantitative information on the free energy differences between different isomeric forms.[43,44] Linkage isomerism is an important topic within this area that occurs with ambidentate ligands that have more than one mode of coordination to a metal center. Metal complexes of the thiocyanate and nitro ligands are among the most studied systems and the mode of coordination depends on the 'hardness' or 'softness' of the metal

center.[45-48] The application of external pressure favors particular linkage isomers and could be used in conjunction with a variation of ligands or ligand substituent groups to further tune the properties of the metal center.[49-51] Thiocyanate and selenocyanate complexes of platinum(II) and palladium(II) (Chapters 8 and 9) and an osmium(VI) *trans*-dioxo thiocyanate complex (Chapter 7) studied here show no spectroscopic evidence for either a temperature- or pressure-induced linkage isomerization.

The application of pressure on emissive molecules provides a wealth of information on how excited state relaxation properties depend on small changes in molecular geometries. Luminescent transition metal complexes are ideally suited for such work considering their wide range of tunable optical properties and *tris*-(2,2'-bipyridine) complexes of Ru(II) are among the most well-studied systems. The metal-to-ligand charge transfer (MLCT) luminescence spectra of these complexes have been reported as a function of external pressure and the luminescence quantum yields (Φ), lifetimes (τ), as well as the radiative and nonradiative rate constants (k_R and k_{NR}) decrease with increasing pressure by up to a factor of two. The decreases in these parameters were also strongly dependent on the nature of the solvent or counterion and in both cases can be attributed to more efficient energy transfer or ion-pairing effects due to the decrease in sample volume.[52-55] Riehl and co-workers have used variable temperature and pressure to study excitation energy transfer and luminescence quenching from lanthanide complexes to *tris*-(phenanthroline) Ru(II) complexes.[56] One of the most examined systems in pressure-dependent spectroscopy is the Cr(III) ion doped into various ionic host lattices. The emitting state can vary between an interconfigurational $^4T_{2g} \rightarrow {}^4A_{2g}$ transition and an intraconfigurational $^2E_g \rightarrow {}^4A_{2g}$ spin-flip transition with a change in host lattice or an external pressure. The effect of pressure on the luminescence properties of doped Cr(III) systems has been reviewed recently by Bray[57] and the data demonstrate that a pressure-induced increase in ligand-field strength can be used to switch the emitting state in many of these systems. Güdel and co-workers have also reported detailed spectroscopic studies on doped transition metal ions as a function of pressure, such as Jahn-Teller excited state distortions in doped Cr(III) systems,[58] V(III) luminescence properties,[59,60] Mn(II) doped perovskites, and luminescence upconversion in Ti(II) and Ni(II) doped lattices.[61,62] It has further been shown that the change in emitting state can also be induced by pressure in

molecular Cr(III) complexes with careful choice of ligands.[63] Yersin and co-workers have also performed variable pressure measurements at low temperature on organoplatinum(II) complexes in various media to study relaxation dynamics and to characterize the nature of the emitting states as well as zero-field splittings.[64,65] In almost all of these cases, the emitting state normal coordinate offsets were small. In contrast, chapters 8 and 9 report pressure-induced increases of luminescence intensities and lifetimes up to three orders of magnitude at ca. 30 kbar for complexes that undergo large, multiple emitting state displacements.

Pressure-dependent spectroscopic methods have aided synthetic chemists in understanding the catalytic process of bond activation, ligand exchange/insertion and electron transfer. Much of the pioneering work in this area has been performed by van Eldik and co-workers and has led to a better understanding of the mechanistic steps in many inorganic, bioinorganic and organic reactions through the pressure dependence of thermodynamic activation parameters.[7,66-78] In addition to pressure-dependent studies on simple complexes with only one metal center, there has been much interest in other transition metal-based systems having more than one metal center, such as binuclear complexes with metal-metal quadruple bonds (δ-bonds) and quasi one-dimensional arrays consisting of square-planar platinum(II) and gold(I) complexes that possess semiconductor-like properties.

Since the discovery of the metal-metal quadruple bond by Cotton and co-workers, these systems have proven to be excellent models for understanding properties of metal-metal multiple bonds.[79-82] Based on the twisted ethylene model, it was expected that pressure can destroy δ-symmetry by inducing a displacement along a torsional coordinate,[83] which can be controlled to an extent by the structural properties of the ligands. Considering the current interest in these systems as multielectron photocatalysts,[84,85] the application of pressure provides a simple means to determine how specific structural changes can influence the electronic properties of metal-metal multiply bonded systems. An analogous problem has been addressed by Drickamer and co-workers who have investigated the effect of pressure on twisted intramolecular charge transfer (TICT) transitions in organic chromophores doped into polymer matrices. At high pressures, the formation of the TICT state was shown to be retarded through the

torsional coordinate displaced in the charge transfer transition.[86-89] Exchange interactions are purely electronic effects that have been probed in Cr(III) dimer complexes by monitoring the shifts of absorption and luminescence spectra which enabled the extraction of exchange parameters as a function of pressure.[90,91] The electronic and optical properties of simple metal complexes also become quite complex when metal-centers are capable of interacting with one another, as is observed in many Au(I) and Pt(II) square-planar complexes with cyanide ligands and other planar aromatic ligands. These square-planar complexes are usually stacked directly on top of one another, thus favoring axial interactions between metal centers and the distance between complexes (~3—4 Å) is governed by the choice of counterion.[92] The close proximity of metal centers implies that the ground electronic state wavefunction is no longer localized on the metal center of one complex, but delocalized over many complexes. By applying an external pressure to the system, the overlap between metal orbitals increases and the luminescence spectra, decay kinetics, as well as energy transfer processes often show large variations from their ambient values.[93-104] A recent example is found in the $Pt(bpy)Cl_2$ complex that can crystallize into two forms in the solid state; red (linear chain) and yellow (non-linear chain). This system undergoes a phase transition from the red to yellow form at 17.5 kbar that causes a strong discontinuity in the emission spectra.[105]

The luminescence photophysics of more complex inorganic-based systems, such as nanocrystalline semiconductors, have also been studied through the use of external pressure. The size-dependent optical properties intrinsic to these materials are very sensitive to changes in their local environment and external pressures have have provided another means to characterize these novel systems.[106-108] Other recent work has been directed towards understanding charge and electron transfer processes, both experimentally and theoretically, through variable molecular structure on magnetic properties in quasi one-dimensional charge transfer complexes[109] and general studies on the use of pressure to characterize electron transfer.[110]

From the first studies involving only simple complexes, these examples demonstrate the potential for these techniques in characterizing the interdependence of structural and optical properties of a wide variety of inorganic, organic and polymer

systems, which provides valuable information into the ability to tune these properties. Finally, as detection and optics become more sophisticated, it will be advantageous to implement pressure-dependent techniques with other physical methods and further extend the scope of these methods in materials characterization, which may lead to the discovery of many new and interesting properties.

1.2.1 Electronic structures of d^2 and d^8 metal complexes

In this work, the luminescence spectra of d^2 and d^8 second- and third-row transition metal complexes were studied as a function of temperature and pressure and specific complexes were chosen according to their molecular geometry and electronic structure. *trans*-$[MO_2(L)_4]^{n+}$ (where M = Re(V) or Os(VI) and L = ancillary nitrogen-donating ligand) [d^2] and square-planar $[M(XCN)_4]^{2-}$ (where M = Pt(II), Pd(II) and X=S,Se) [d^8] complexes were used as model systems, both of which have idealized D_{4h} symmetry. The d^2 *trans*-dioxo complexes represent the tetragonally compressed limit of the D_{4h} point group where the metal-oxo bond lengths are shorter than are the metal-ligand bond lengths by up to 0.1 Å,[111] whereas the square-planar Pt(II) and Pd(II) complexes represent the tetragonally elongated limit of this point group. Figure 1.3 shows the structural diagrams for both types of complexes studied with some of the relevant parameters determined from crystallographic data of these and similar complexes.

The high symmetry of these model complexes also simplifies the assignment of resolved vibronic structure where the number of ground state vibrational bands is much less than in lower symmetry systems, where degenerate vibrations split into several bands. Furthermore, the lowering of molecular point group symmetry with increasing pressure is simpler to follow where the new geometry can be deduced from the data with the aid of correlation diagrams found in standard texts.[112-114] Although the orbital parentage of the d—d electronic states are different for both systems, the ground and emitting states have the same symmetry that allows for the interchange of symmetry labels between both types of complexes.

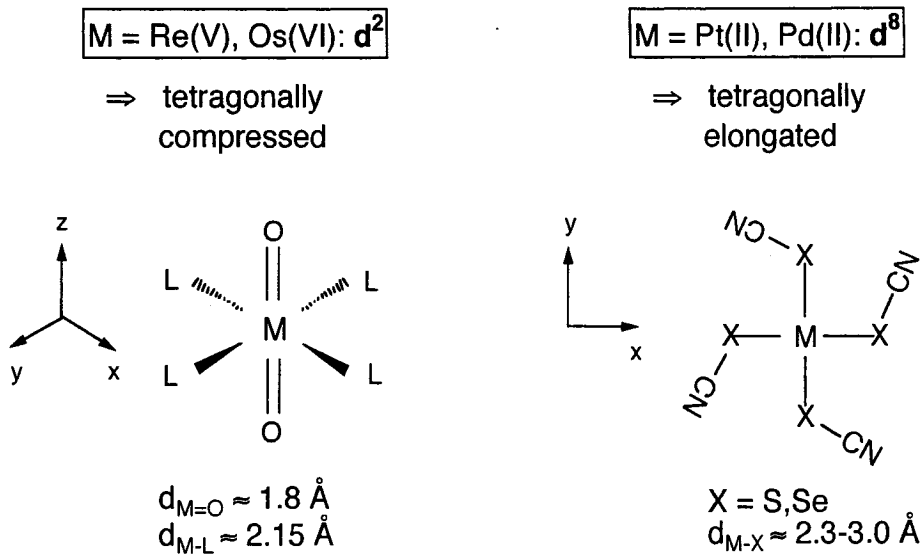

Figure 1.3. Structural diagrams of *trans*-dioxo (d^2) and square-planar (d^8) D_{4h} transition metal complexes.

In D_{4h} symmetry, the ground states are both spin and orbitally nondegenerate ($^1A_{1g}$) for both d^2 and d^8 electronic configurations, due to the pairing of electrons in the HOMO. The first excited state (emitting state) is of triplet character and orbitally degenerate (^3E_g) that arises from a one-electron interconfigurational transition to the LUMO of each system. Figure 1.4 shows energetic ordering of the d-orbitals for both configurations corresponding to the two tetragonal limits of D_{4h} point group symmetry. Because spin-orbit coupling is significant in second- and third-row transition metal complexes, this first excited state is split into several components (A_{1g}, A_{2g}, E_g, B_{1g}, B_{2g}), which typically leads to congested absorption spectra for the $^1A_{1g} \rightarrow {}^3E_g$ transition and luminescence occurs from the lowest energy spin-orbit component of the ^3E_g state. Both classes of complexes described above have spectroscopic properties that have been the subject of many experimental and theoretical studies.

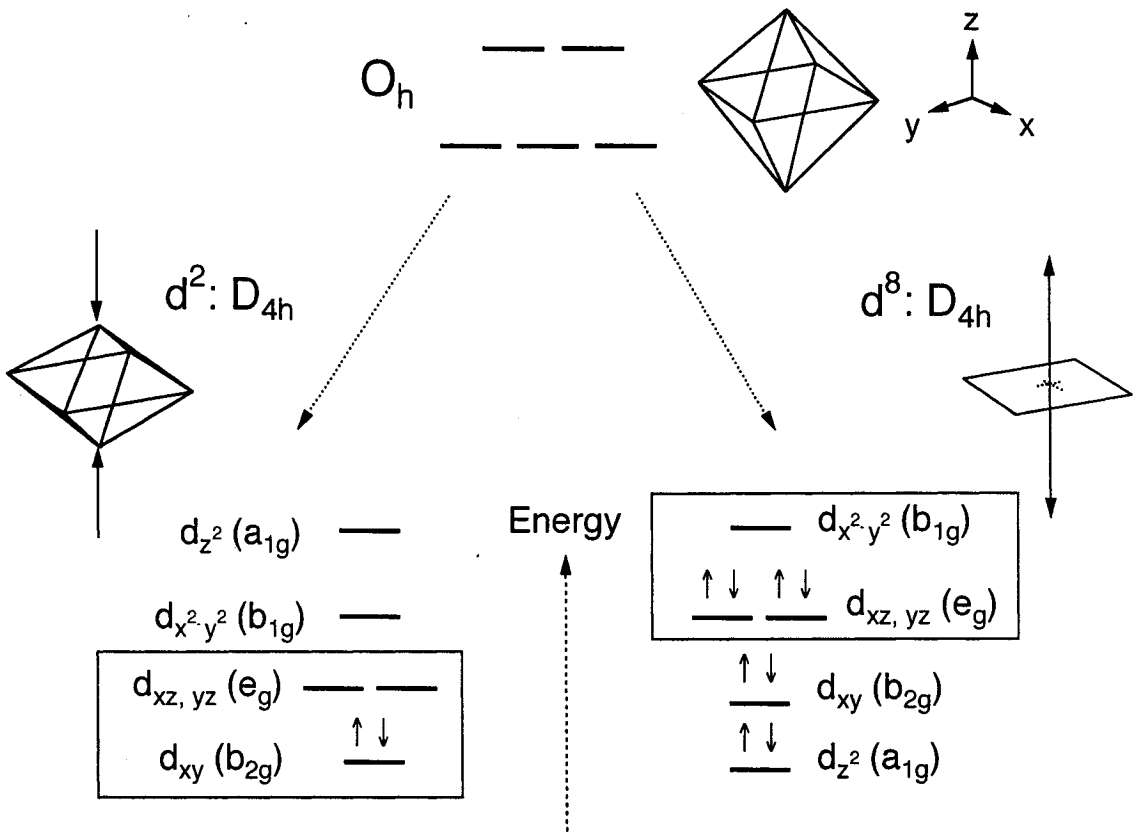

Figure 1.4. d-orbital splittings for d^2 and d^8 electronic configurations within the geometrical limits of the D_{4h} point group.

trans-Dioxo d^2 metal complexes with metal-ligand multiple bonds display unique optical properties and have well-characterized electronic structures.[115,116] From the pioneering work of Jørgensen, Ballhausen and Gray on complexes of the vanadyl and molybdenyl ions, most of the optical spectra of five- and six-coordinate tetragonal systems can still be understood in terms of the same energetic orderings of the metal d-orbitals.[117,118] These complexes are often described in idealized D_{4h} point group symmetry and the labels from this point group are used for the metal d-orbitals and vibrational modes. The d_{xy} (b_{2g}) → d_{xz}, d_{yz} (e_g) transition can be tuned over a wide range of energies and is formally a non-bonding→π^* transition due to the change in orbital occupancy from the largely nonbonding b_{2g} orbital to π^* metal-oxo character orbitals. Most of the third-row complexes luminesce in the visible-NIR region and show vibronic progressions in the high-frequency, totally symmetric (a_{1g}) O=M=O stretching modes. The energies of

the b_{2g} (HOMO) and e_g (LUMO) orbitals can be described by purely electronic parameters, which are K_{xy} for the former and Δ_π for the latter. K_{xy} is a two-electron interelectronic repulsion term defined as $3B+C$ (B and C are the Racah parameters) and Δ_π is a ligand-field defined as $2e_\pi(O)-2e_\pi(L)$[115] where e_π are the angular overlap parameters describing the degree of π overlap from the oxo and ancillary ligands, respectively. The first one-electron transition (HOMO-LUMO) leads to ^3E_g and ^1E_g excited states with the triplet lower in energy by $2K_{xy}$. Temperature-dependent spectroscopic studies on *trans*-dioxo Re(V) complexes by Gray and Winkler were the first to reveal the interesting features belonging to this class of complexes.[119,120] Low-temperature absorption and luminescence spectra of the prototypical *trans*-$[ReO_2(pyridine)_4]^+$ and *trans*-$[ReO_2(CN)_4]^+$ complexes exhibit well-resolved vibronic structure in the O=Re=O and Re-ligand totally symmetric stretching modes of approximately 900 cm^{-1} and 200—400 cm^{-1}, respectively. The luminescence bands in these systems are broad, over 3000 cm^{-1} at the FWHM, indicating large structural rearrangements in the emitting state. The strongly emissive *trans*-$[ReO_2(pyridine)_4]^+$ complex was also studied here as a function of pressure (Chapter 4), which takes advantage of the well-resolved structure observed in room-temperature luminescence spectra to apply theoretical models developed from low-temperature spectra. The detailed characterization of the electronic structures of *trans*-dioxo and other metal-ligand multiply bonded complexes has attracted the interest of synthetic chemists for use in atom-transfer catalysis.[116,121] For example, Yam and co-workers studied the spectroscopy and photochemistry of osmium(VI) complexes with macrocyclic, porphyrin-like ligands that has led to the elucidation of the multielectron transformations of oxygen-atom transfer.[122-124] Through careful and detailed low-temperature luminescence measurements, Reber and co-workers have developed theoretical models for the ground electronic states that incorporate interactions between excited electronic states of the same symmetry that explains the appearance of anharmonic bandshapes.[125-127] In a similar vein, Chapters 5 and 6 explore the effect of pressure on a series of *trans*-dioxo rhenium(V) complexes with anharmonic band shapes that are susceptible to changes in molecular geometries. This anharmonicity results from avoided crossings with excited states of the same symmetry and it was determined that the position of the avoided

crossings could be changed by applying external pressures. Because the luminescence transitions in *trans*-dioxo complexes are formally d—d transitions, vibronic progressions are only expected in metal-ligand vibrational modes (i.e., O=M=O and M-L modes). Chapter 7 reports a temperature-dependent luminescence spectroscopic study of the *trans*-$[OsO_2(NCS)_4]^{2-}$ complex that shows evidence for an emitting state displacement in the CS symmetric stretching mode, which represents the first observation of ligand-centered distortion in the *trans*-dioxo class of complexes.

At the other geometrical limit of the D_{4h} point group, square-planar Pt(II) and Pd(II) complexes exhibit unique optical properties and many have found other uses such as catalysts in synthetic applications. The electronic structures of these systems have been well-studied, but the literature reports often differ on the energetic ordering of the d-orbitals in these systems.[128-130] For all possible splitting patterns, the d^8 electronic configuration is best stabilized in the square-planar geometry which avoids populating the strongly σ^* $d_{x^2-y^2}$ (b_{1g}) orbital. All one-electron d—d transitions are to this orbital, leading to large displacements along metal-ligand bonding coordinates and broad optical spectra. Previous spectroscopic measurements on this class of complexes has revealed emitting state displacements in a Jahn-Teller-active vibration.[131-133] In this work, the luminescence properties of Pt(II) and Pd(II) thiocyanate and selenocyanate complexes displayed large variations in intensities and lifetimes with variable temperature and pressure. Low-temperature luminescence spectroscopic measurements have also revealed a large displacement in a Jahn-Teller active metal-ligand *bending* distortion, which has not been observed before in this class of complexes.[133] The application of external pressures on these systems, at room temperature, leads to large increases in luminescence intensity and lifetimes by several orders of magnitude (Chapters 8 and 9). In transition metal complexes, there have been no reported enhancements similar in magnitude for systems that maintain the same emitting state throughout the pressure range studied.[57,134]

The work presented in the following represents the first time where quantitative information relating the interdependence of molecular geometry and electronic properties has been extracted from the optical spectra of molecular transition metal complexes. This has been facilitated primarily by resolved vibronic structure in the luminescence spectra

and allows for the use of modern theoretical tools such as the time-dependent theory of spectroscopy. The lack of vibronic structure in many conventional pressure-dependent studies has severely limited further insight into the nature of both ground and excited states and thus can only be rationalized in qualitative terms as in Figures 1.1 and 1.2. One of the major shortcomings of the energy level schemes is that the molecular vibrations are neglected, making it difficult to quantitatively study systems that undergo large structural changes upon absorption or emission of a photon. In order to account for nuclear distortions that accompany electronic transitions, the pressure-dependent changes observed in vibronic patterns must be explained using potential energy surface (PES) models. The application of more sophisticated theoretical models provides a means to quantitatively determine the relevant parameters that influence the observed optical properties, which is very important since the electronic structures of transition metal complexes depend strongly on geometrical configurations.

1.3 Potential energy surface models

Although the insight that has come from the simple physical pictures illustrated in Figures 1.1 and 1.2 is significant and applicable to a diverse number of systems, this description of electronic states and optical transitions is quite limited. Most pressure-dependent spectroscopic studies on transition metal complexes are devoid of any resolved features, which necessitates the use of energy level diagrams in interpreting trends in the energies of optical transitions as a function of pressure. However, no explicit information regarding changes in structure can be inferred from them aside from highly symmetric complexes that – in the absence of Jahn-Teller distortions – have equivalent metal-ligand bond lengths, which can be determined by changes in 10 Dq, due to this parameter's relationship to the metal-ligand bond distance. This simple model cannot be extended to lower symmetry systems where the metal center does not 'feel' an isotropic ligand-field. To extract out information relating the changes in energy between electronic states, band widths, and other important characteristics, the electronic states must be described as potential energy surfaces that are offset along each of the displaced normal coordinates (vibrational modes) of the molecule. PES models are most applicable in cases where

optical spectra show resolved vibronic structure in one or more vibrational modes of the molecule ($3N$-6, where N is the number of atoms in a nonlinear polyatomic molecule).

Figure 1.5 illustrates ground and emitting states as harmonic potential energy surfaces with a nonzero offset along the normal coordinate, Q. The ability to describe electronic states as potential energy surfaces arises from the Born-Oppenheimer approximation that separates nuclear motions from electronic motions based on their respective timescales, the latter being approximately three orders of magnitude faster. This approximation allows the total wavefunction of an electronic state to be separated into electronic and nuclear parts where the former depends on the nuclear coordinates, but only in a parametric fashion. In addition, the Condon approximation states that an electronic transition occurs instantaneously with the nuclei fixed in their equilibrium ground state configuration (e.g., vertical absorption transition in Figure 1.5). Following an electronic transition, the slow-moving nuclei respond to the new potential energy arising from the different electronic configuration (excited state PES) by relaxing to a new equilibrium configuration geometry – corresponding to the potential minimum of the excited state – along each displaced normal coordinate, Q. In d—d transitions of metal complexes, this is almost always the totally symmetric metal-ligand stretching modes and the degree of structural rearrangement in the excited state is reflected in the horizontal offset (ΔQ) between the ground and excited state potential minima along each displaced normal coordinate. At this point, the molecule can emit a photon (typically in the Vis-NIR range) or decay nonradiatively back to the ground state. Conditions that invalidate the Born-Oppenheimer approximation are in cases of degeneracy of electronic states, when vibrational frequencies are comparable to the energy separation between electronic states, and the crossing of electronic states (PESs) of the same symmetry. One particularly interesting situation is when the PESs of electronic states cross close to the Franck-Condon region of an electronic transition. This effect has been explored in great detail in Chapters 6 and 9 and is most pronounced for lower energy emitting systems in which the crossing point between the ground- and emitting state PESs is in close proximity to the Franck-Condon region of the luminescence transition. The PES model provides a solid basis for explaining both radiative and nonradiative transitions and is also applicable to other fundamental photophysical and photochemical processes.

Based on the PES model, the amount by which the molecule distorts along a particular bonding coordinate through individual normal coordinate offsets, ΔQ, can be determined for each displaced mode. When conditions are suitable (i.e., low temperature), vibronic intervals appear in the spectra that correspond to vibrational frequencies in the respective mode(s), such as those shown in the spectra in Figure 1.5. When there is no resolved vibronic structure, the Stokes shift ($2S\hbar\omega_i$) provides another means to obtain a reasonable estimate of the amount of structural rearrangement incurring in the molecule assuming that only the totally symmetric modes are displaced (i.e., $\hbar\omega_i = \hbar\omega_{a1g}$ in Figure 1.5). The Huang-Rhys parameter, S, which is defined as $\frac{1}{2}\Delta^2$ (Δ is the offset in dimensionless units). E_{00} in this model is the energy of the electronic origin transition, which is defined as the vertical energy difference between the lowest vibrational levels of the two states.

Despite the more realistic description of optical transitions in molecular chromophores, the PES model has seen only limited use, mostly for qualitative considerations, in pressure-tuning spectroscopy of coordination complexes. The chief reason is that most electronic spectra are measured at room temperature where higher energy vibrational levels of initial state ($\nu_i = 1,2,..$) are thermally populated according to Boltzmann statistics ($\hbar\omega_i < k_BT$) and transitions can originate from these higher levels and lead to a superposition of different spectra. The other reason is that interconfigurational ligand-field transitions (d—d) often give rise to many displaced vibrational modes that lead to congested spectra. In this work, room-temperature pressure-dependent spectroscopic data are analyzed quantitatively using PES models developed from the analysis of low-temperature spectra.

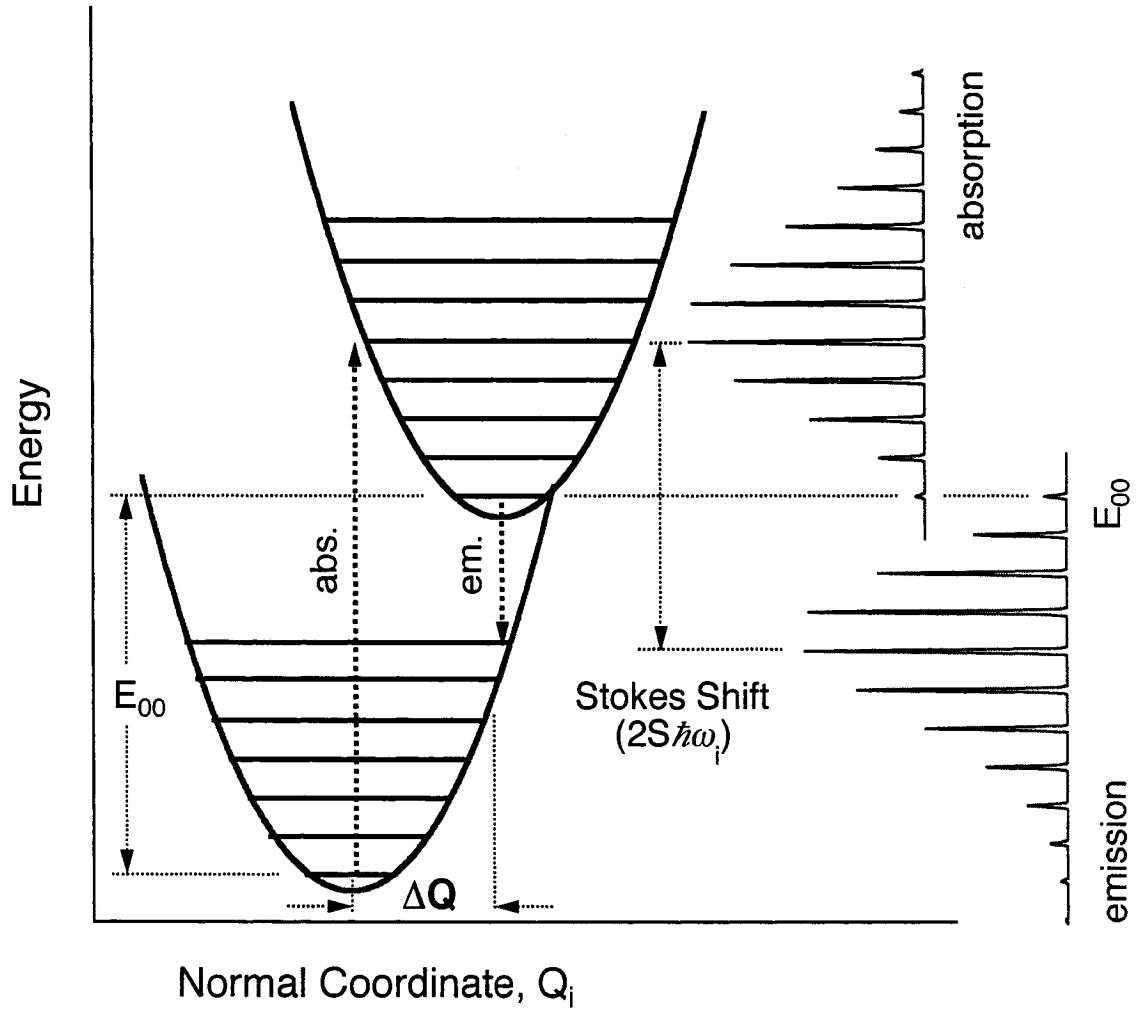

Figure 1.5. PES model with important spectroscopic parameters defined for both an absorption and emission transition.

1.3.1 Quantitative transferability of parameters

The previously established criterion for using PES models to describe electronic states was resolution of vibronic structure in experimental spectra, which provides the key for understanding specific structural distortions between the ground and emitting states. In pressure-dependent spectroscopy, the size restrictions on the amount of sample that can be used in a DAC makes low temperature experiments difficult due to extensive optimization procedures to excite an optical transition and collect the signal. Most pressure-dependent spectroscopic measurements are therefore performed at room temperature (ca. 300 K), allowing for a reduction in the number of variables in the experiment. However, vibronic structure is almost never resolved in room-temperature electronic spectra of transition metal compounds and most complexes are non-emissive, which further limits variable pressure experiments. When vibronic structure is resolved it is possible to determine many important spectroscopic parameters describing the PESs of the electronic states involved in the transition. PES models are developed to explain the intensity distributions of each progression-forming mode and can be adapted to pressure-dependent spectra measured at room temperature. This approach is only applicable when there are at least partially resolved vibronic progressions. The normal coordinate offset, ΔQ, is the essential link between temperature-dependent and pressure-dependent models that is very difficult to determine for spectra with no resolved vibronic structure. In virtually all cases, pressure decreases ΔQ which causes the intensity distributions of resolved progressions to change. The pressure dependence of this parameter can then be used to establish a correlation between the molecular structure and electronic/optical properties. Figure 1.6 shows a depiction of the effect of pressure on PESs corresponding to the ground and emitting states with the previously defined parameters from Figure 1.5.

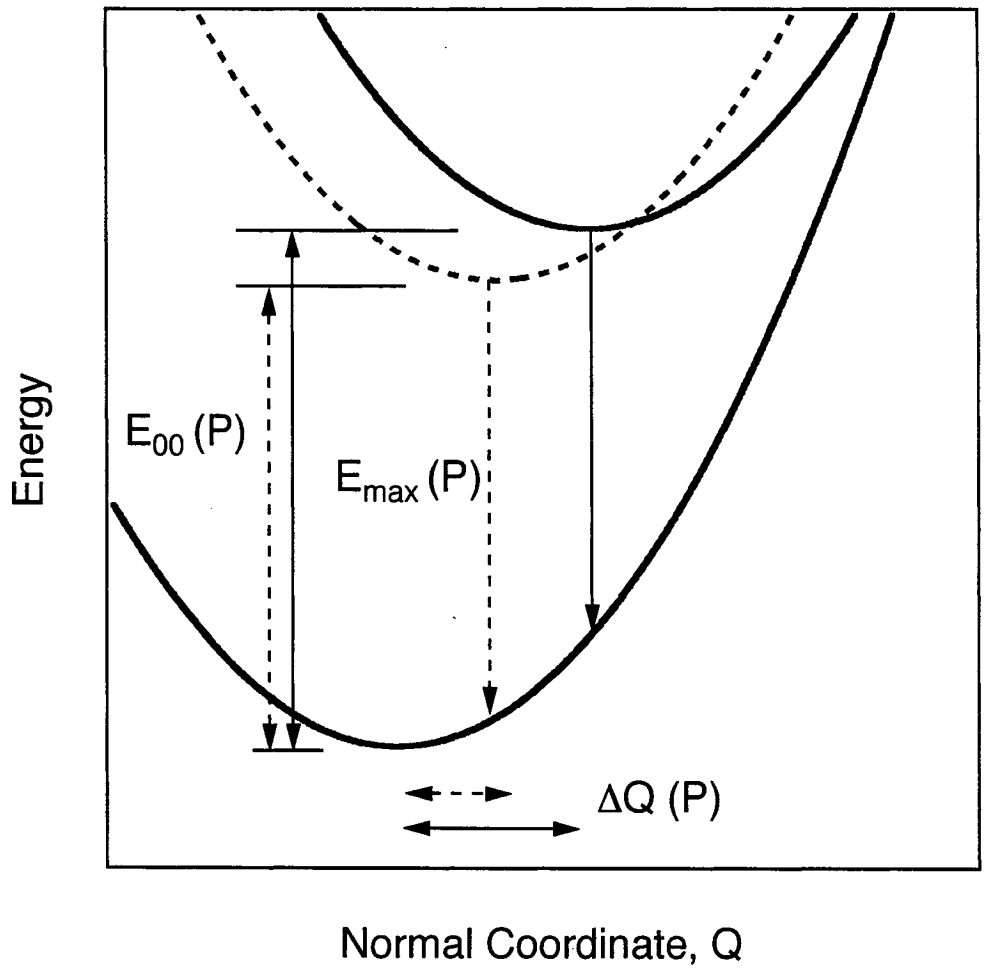

Figure 1.6. PES model showing the effect of an external pressure on important spectroscopic parameters. Solid lines: ambient (~low) pressure, dashed lines: high pressure.

The PES model yields a more detailed insight into the influence of pressure on important structural and electronic properties of molecular chromophores far beyond the qualitative, shifting orbital energy level diagrams shown in Figure 1.2. This approach is applied in Chapters 4—6 and 9, where PES models were developed based on well-resolved low temperature luminescence spectra and then transferred to variable pressure, constant temperature (ca. 300 K) luminescence spectra. The application of PES models to pressure-dependent spectra is valid when there are no structural phase transitions that occur within the pressure range studied. To extract quantitative information from the modeling process, theoretical methods are used that are based on the time-dependent theory of spectroscopy that will be covered in the next section.

There are two physical scenarios that arise from the spectroscopic measurements of the d^2 and d^8 complexes studied here that can be explained using PES models. First, the dominant effect found in the d^2 *trans*-dioxo complexes is that the luminescence properties are largely influenced by the energetic proximity of the ground and excited states as well as the magnitude of the normal coordinate displacements. In some of the *trans*-dioxo rhenium(V) complexes, luminescence band shapes were found to be anharmonic which changed as a function of pressure. This anharmoncity is due to avoided crossings between the ground electronic state and excited states of the same symmetry. Its spectroscopic consequences are strongly dependent on the luminescence energy and normal coordinate displacements in both the O=Re=O and Re-ligand stretching modes.[126,127] The crossing of electronic states represents a breakdown of the Born-Oppenheimer approximation where eigenvalues of the two states are degenerate at the same position along the normal coordinate, Q,[135,136] and electronic states of the same symmetry cannot cross when there is a perturbation connecting them, producing avoided crossings. When these avoided crossings are close to the Franck-Condon region (i.e., complexes with low luminescence energies) they exert a greater influence on the luminescence band shape. Coupled ground and excited states in close proximity causes a flattening of the ground state PES at positive values along Q thereby increasing anharmonicity. Upon applying pressure, the decrease of metal-ligand bond lengths causes ΔQ to decrease, which moves the avoided crossings to higher energy leading to a ground state PES that is more harmonic in character. This effect is observed in the *trans*-

dioxo rhenium(V) complexes with substituted ethylenediamine ligands (Chapters 5 and 6) where substitution of this ligand leads to tunable luminescence energies with a range of about 5000 cm^{-1} between the least- and most-substituted complexes. However, some *trans*-dioxo complexes do not exhibit spectroscopic evidence for anharmonicity and the ground state PES can be described by a harmonic PES, which is suitable for the *trans*-$[ReO_2(pyridine)_4]^+$ complex discussed in Chapter 4. The pressure dependences of important spectroscopic parameters, such as ΔQ, E_{00}, and E_{max}, show different trends for coupled states systems than those where there is no evidence for significant interactions between states. Figure 1.7 depicts the net effect of pressure on the shape of the ground state where the pressure-induced decrease of $\Delta Q_{Re=O}$ pushes up the ground state surface at positive values of $Q_{O=Re=O}$, reducing the anharmonicity of the ground state. The adiabatic (non-crossing) states are represented by the solid (low pressure) and dotted (high pressure) traces and the diabatic (crossing) states are given by the dashed traces.

The square-planar systems, reported in Chapters 8 and 9, show a large enhancement of luminescence intensities and lifetimes as a function of pressure. From preliminary studies, it was determined that this enhancement was due to a large decrease of the nonradiative rate constant, k_{NR}. An analytical model was adapted to explain these trends in a semi-quantitative manner. This model is based on the strong-coupling limit of classical radiationless decay theory originally derived to calculate temperature-dependent luminescence decay rate constants whereby the probability for nonradiative transitions depends exponentially on the activation energy barrier (E_A). This quantity is defined as the energy difference between the potential minimum of the emitting state and the energy at which the emitting state and ground state PESs cross and can be expressed in terms of an effective emitting state displacements along each normal coordinate (ΔQ_{eff}). Based on quantitative calculations performed on the low-temperature luminescence spectra, it is possible to rationalize the large pressure effect using the low temperature parameters in an effective coordinate model for the nonradiative rate constant. Figure 1.8 shows a PES depiction of the effect of pressure on the rate activation energy for a nonradiative transition.

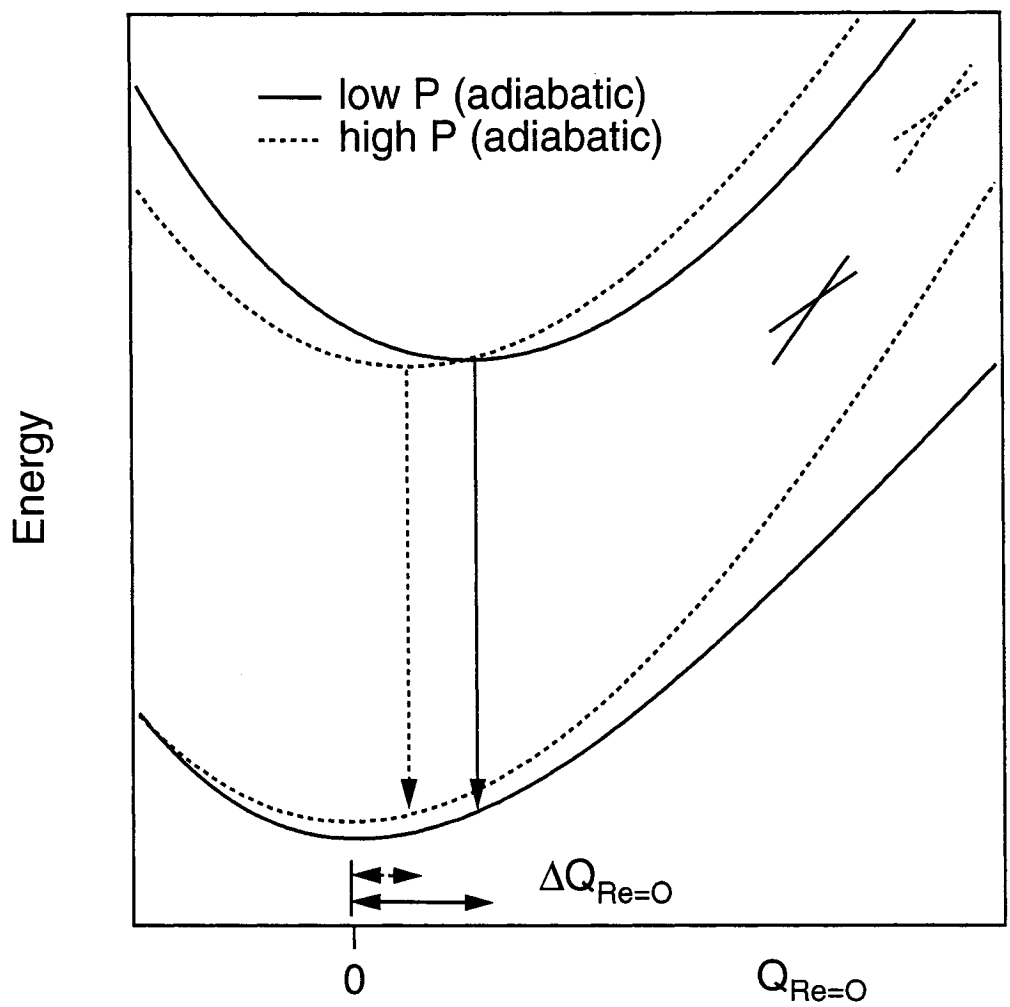

Figure 1.7. PES model with the ground and emitting states diplaced along the O=Re=O coordinate showing the effect of pressure on anharmonic ground states. The dashed traces represent the adiabatic states at high pressure and the solid traces represent the adiabatic states at low pressure. As pressure increases, ΔQ decreases which causes the avoided crossings (small lines) to increase in energy leading to a more harmonic ground state adiabatic PES at higher pressure (dotted trace).

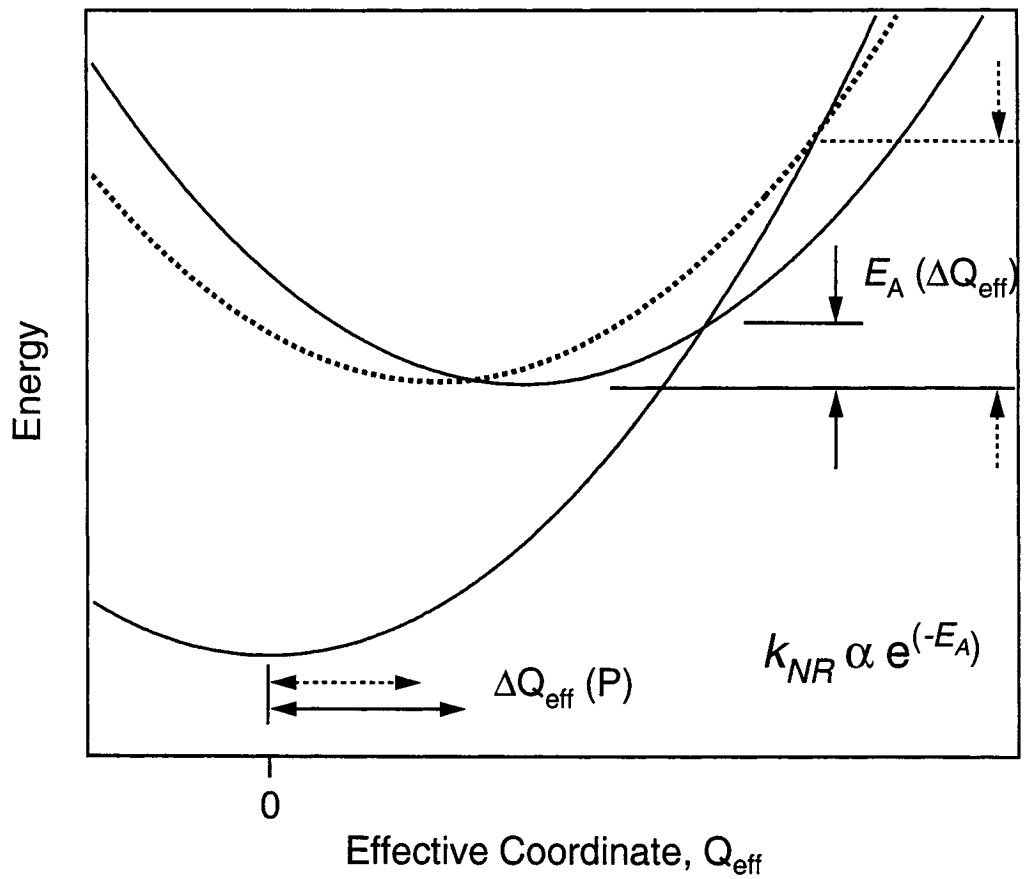

Figure 1.8. PES model representing square-planar systems where an increased pressure decreases the normal coordinate offset and, ultimately, the activation energy (E_A) for nonradiative transitions. This leads to an exponential decrease in the nonradiative rate constant (k_{NR}) which causes large increases in both luminescence intensities and lifetimes. Solid lines: ambient pressure, dotted lines: high pressure.

1.4 Theoretical methods: The time-dependent theory of spectroscopy

When a molecule absorbs or emits a photon, a wavepacket (i.e., a non-stationary wavefunction) is created on the final state of the transition and evolves according to the time-dependent Schrödinger equation.[139-141] This situation is most relevant in time-resolved spectroscopy where a short laser pulse induces an electronic transition and creates a discrete wavepacket on the final PES. The application of this theoretical approach to static, or continuous wave, spectroscopy is permitted by the superposition principle that states that these wavepackets simply arrive at the final PES at different times. This method has been used extensively to calculate fits to experimental spectra and allows for a detailed analysis of features both in the frequency and time domains.

The time-dependent approach is equivalent to the 'classic' Franck-Condon picture where the intensity of an electronic transition depends on the square of the electronic part of the transition dipole moment which is then modulated by the vibrational part. The overlap integral between vibrational eigenfunctions of the initial and final states dictates the intensity distributions of resolved vibronic progressions that is primarily determined by the degree of displacement between potential minima, ΔQ in Figure 1.5, and energy difference between states, E_{00}. The parameter ΔQ can only be obtained by first guessing its value by iteratively fitting experimental spectra. Because the work described in the following chapters is primarily concerned with the characterization of luminescence properties, only the calculation of luminescence spectra will be covered. Eq. 1.1 defines the intensity of luminescence spectra.

$$I_{lum.} = C\omega^3 \int_{-\infty}^{+\infty} \exp(i\omega t)\left[\langle \phi | \phi(t) \rangle \exp(-\Gamma^2 t^2 + \frac{iE_{00}}{\hbar} t)\right] dt \qquad \text{eq. 1.1}$$

In the time-dependent formalism, the most important quantity in the time-dependent theory is the autocorrelation function that is the overlap of the time-dependent wavepacket with the initial (t=0) wavepacket along all displaced coordinates. This quantity is represented by $\langle \phi | \phi(t) \rangle$ and takes on values from 0 to 1 (i.e., 0% to 100%

overlap of the time-dependent wavepacket with the initial wavepacket at t = 0. C is a constant and the dependence on the cube of the frequency is a consequence of the Einstein coefficient for spontaneous emission. Γ represents the phenomenological Gaussian damping factor that is adjusted to achieve resolution of vibronic lines as observed in experimental data and E_{00} is the energy of the origin transition from the experiment. The physical meaning for the damping factor is that it represents the 'thermal bath' into which excitation energy can be transferred irreversibly. The expression in brackets is then Fourier-transformed into frequency space, gives the calculated spectrum in the frequency domain. This formalism is not limited to any particular type of PES and multiple dimensions are easily accommodated.

Figure 1.9 illustrates the time-dependent approach for calculating luminescence spectra. A wavepacket is created on the final state PES (ground state for luminescence transitions) by the vertical projection (Condon approximation) of the lowest energy vibrational eigenfunction of the emitting state. Because this wavefunction is not an eigenfunction of the final PES, it evolves in time according to the time-dependent Schrödinger equation (i.e., a wavepacket). The top graph shows a Franck-Condon transition to the ground state PES with the time evolution of the wavepacket and the bottom graph is a plot of the absolute autocorrelation function with time and recurrences at t > 0 are shown. As the wavepacket moves away from the Franck-Condon region (t = 0), the overlap decreases and reaches a minimum when it is at the opposite region of the PES (t = 19 fs). Upon returning to its initial position, the overlap increases albeit lesser than the original value due to the effect of the damping factor, Γ (shown by the shaded area close to t ~ 38 fs) leading to a recurrence. The shaded region between the time-dependent wavepacket and the initial wavepacket in the top panel of Figure 1.9 corresponds to point (3) in the bottom panel where the overlap has almost reached its maximum. When more than one mode is displaced, the wavepacket will follow the path of steepest descent, which corresponds to the highest frequency mode.

In the harmonic approximation (e.g., Figure 1.5), there is no mixing of vibrational motions, no change in vibrational frequencies between the initial and final states and the transition dipole moment is constant which means that the wavepacket will follow a Lissajous trajectory.[137,138] In this idealized case, the time-dependent Schrödinger

equation can be solved analytically and this approach is employed in Chapters 4, 7 and 9 to model experimental spectra. However, when there is coupling between vibrational modes, this model fails in reproducing the intensity distributions of vibronic progressions and the time-dependent Schrödinger equation must be solved by numerical means (i.e., split-operator method).[139] In Chapters 5 and 6, anharmonic ground state PESs are used to reproduce experimental spectra that show significant deviations from the harmonic PES models. Because vibronic structure is well-resolved in most cases, experimental parameters are used, such as the energy of electronic origin (E_{00}) and vibrational frequencies ($\hbar\omega_I$) of all displaced modes to calculate experimental spectra.

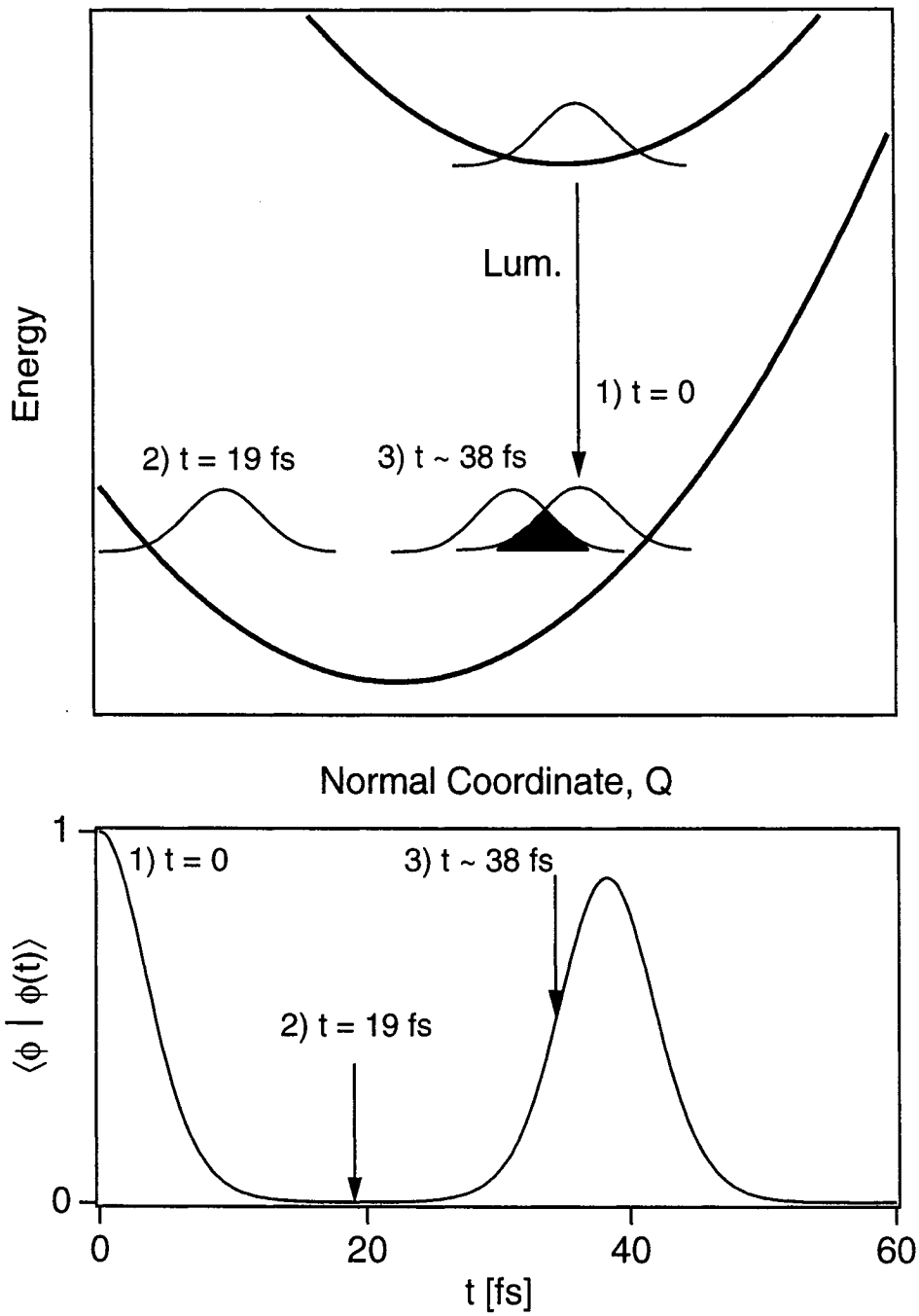

Figure 1.9. Depiction of a luminescence transition (such as in Figure 1.5) according to the time-dependent theory of spectroscopy. Wavepacket motion is shown in 'snapshots' with the initial wavepacket at t = 0 (1) and two other times. The bottom panel shows the autocorrelation overlap between the time-dependent wavepacket and the initial wavepacket. The first recurrence occurs at 38 fs corresponding to a frequency of 870 cm^{-1} ($\omega = 2\pi/\tau$).

1.5 Organization of content

This thesis consists of ten chapters including this introduction followed by an outline of instrumentation and final conclusions at the end of the main body. The main focus is to understand the interplay between molecular structure and electronic properties through optical spectra. The electronic structures of the ground and excited states are first characterized with temperature-dependent spectroscopic techniques using PES models described in this introduction. These models are then adapted to room-temperature, variable pressure luminescence spectra that provide a quantitative means to determine the effect of varying molecular structure on the optical properties of the system.

Chapter 3 investigates the effect of an external pressure on the Raman spectra of d^2 rhenium(V) and osmium(VI) complexes with metal-ligand multiple bonds. Because luminescence properties in these systems depend strongly on metal-ligand bond distances, this work has enabled a correlation to be drawn between the pressure-dependent trends for both vibrational and luminescence spectra.

Chapter 4 presents temperature- and pressure-dependent luminescence spectra of the prototypical *trans*-$[ReO_2(pyridine)_4]^+$ complex. Low-temperature vibronic bandshapes show well-resolved progressions in the O=Re=O and Re-N(py) symmetric stretching modes and the ground electronic state is modeled with two-dimensional harmonic PESs. Room-temperature, pressure-dependent spectra show resolution in a mode closely matching the high frequency O=Re=O mode and an effective coordinate model is used to extract the pressure dependence of all spectroscopic parameters.

Chapter 5 explores the effect of external pressure on the luminescence spectrum of a *trans*-dioxo rhenium(V) complex that exhibits anharmonicity. The pressure-dependent spectra were modeled using a Morse PES to represent the ground state where the dissociation energy could be adjusted to reproduce the anharmonicity in a phenomenological fashion.

Chapter 6 is an in-depth systematic investigation of the effect of pressure in a series of structurally related *trans*-dioxo rhenium(V) complexes. Based on previous low temperature spectra of these complexes, anharmonicity arises from interactions between

the ground and excited states of the same symmetry. These interactions vary depending on the luminescence energies and, through a coupled states model, it is shown that these interactions between states can be tuned by external pressures.

Chapter 7 investigates temperature-dependent luminescence spectra of three salts of the *trans*-$[OsO_2(NCS)_4]^{2-}$ complex that shows highly resolved vibronic structure in the NIR region. Investigation of the vibronic structure reveals a significant displacement in the ligand-centered CS symmetric stretching mode only 30 cm^{-1} less than the O=Os=O stretching mode. The appearance of a ligand-centered mode is highly unusual for what is formally a d—d transition that should only contain progressions in metal-ligand modes.

Chapter 8 reports the unusual and large enhancement of the luminescence properties of the $[Pd(SCN)_4]^{2-}$ complex with increasing pressure. Luminescence intensities and lifetimes increase up to three orders of magnitude at ca. 30 kbar from their values measured at ambient conditions.

Chapter 9 presents a full investigation into the origin of this large pressure-induced enhancement in luminescence properties using platinum(II) and palladium(II) thiocyanate and selenocyanate complexes. Temperature-dependent luminescence intensities and lifetimes vary significantly between 5—300 K and low temperature spectra exhibit well-resolved long vibronic progressions in multiple vibrational modes, including Jahn-Teller active non-totally symmetric stretching and bending modes. Spectra are calculated using a multi-dimensional harmonic PES for the ground state allowing for the extraction of emitting state displacements in each vibrational mode. Temperature- and pressure-dependent luminescence decay data are rationalized using a model based on the strong-coupling limit of radiationless decay theory, which allows the use of spectroscopic parameters determined from the calculations of low temperature spectra to rationalize the large differences in lifetime enhancement between platinum(II) and palladium(II) complexes.

References

(1) Drickamer, H. G. In *Solids under pressure*; Warhauser, P. D., Ed.; McGraw-Hill: New York, 1963, p 357.

(2) Drickamer, H. G.; Frank, C. W. *Ann. Rev. Phys. Chem.* **1972**, *23*, 39.

(3) Drickamer, H. G.; Frank, C. W. *Electronic Transitions and the High Pressure Chemistry and Physics of Solids*; Chapman and Hall: New York, 1973.

(4) Drickamer, H. G. *Ann. Rev. Phys. Chem.* **1982**, *33*, 25.

(5) Drickamer, H. G. *Acc. Chem. Res.* **1986**, *19*, 329.

(6) Hazen, R. M. *The New Alchemists*; Times Books: New York, 1993.

(7) van Eldik, R.; Klarner, F.-G. *High pressure chemistry: Synthetic, mechanistic and supercritical applications*; Wiley-VCH: Weinheim, Germany, 2003.

(8) Ford, P. C.; Crane, D. R. *Coord. Chem. Rev.* **1991**, *111*, 153.

(9) Hazen, R. M.; Finger, L. W. *Comparative Crystal Chemistry: Temperature, Pressure, Composition, and Variation of Crystal Structure*; Wiley: New York, 1982.

(10) Ferraro, J. R. *Vibrational Spectroscopy at High External Pressures: the Diamond Anvil Cell*; Wiley: New York, 1984.

(11) Edwards, C. M.; Butler, I. S. *Coord. Chem. Rev.* **2000**, *199*, 1.

(12) Grey, J. K.; Butler, I. S. *Coord. Chem. Rev.* **2001**, *219-221*, 713.

(13) Sharma, A.; Scott, J. H.; Cody, G. D.; Fogel, M. L.; Hazen, R. M.; Hemley, R. J.; Huntress, W. T. *Science* **2002**, *295*, 1514.

(14) Ihalainen, J. A.; Ratsep, M.; Jensen, P. E.; Scheller, H. V.; Croce, R.; Bassi, R.; Korppi-Tommola, J. E. I.; Freiburg, A. *J. Phys. Chem. B* **2003**, *107*, 9086.

(15) Drickamer, H. G. *Comm. Solid State Physics* **1980**, *9*, 197.

(16) Drickamer, H. G. *Physica A* **1989**, *156*, 179.

(17) Drickamer, H. G.; Lang, J. M.; Dreger, Z. A. In *AIP Conf. Proc.*, 1994; Vol. 309, p 1491.

(18) Curie, D.; Berry, D. E.; Williams, F. *Phys. Rev. B* **1979**, *20*, 2323.

(19) Hauser, A.; Amstutz, N.; Delahaye, S.; Sadki, A.; Schenker, S.; Sieber, R.; Zerara, M. *Structure and Bonding* **2003**, *106*, 81.

(20) Brunold, T.; Güdel, H. U. In *Inorganic Electronic Structure and Spectroscopy*; Solomon, E. I., Lever, A. B. P., Eds.; John Wiley: New York, 1999, p 259.

(21) Flint, C. D. *Coord. Chem. Rev.* **1974**, *14*, 47.

(22) Gütlich, P.; Garcia, Y.; Spiering, H. In *Magnetism: Molecules to Materials IV*; Miller, J. S., Drillon, M., Eds.; Wiley-VCH, 2003, pp 271-344.

(23) Gütlich, P.; Garcia, Y.; Goodwin, H. A. *Chem. Soc. Rev.* **2000**, *29*, 419.

(24) Gütlich, P.; Hauser, A.; Spiering, H. *Angew. Chem. Intl. Ed. Engl.* **1994**, *33*, 2024.

(25) Ferraro, J. R.; Basile, L. J.; Garcia-Ineguez, P.; Paoletti, P.; Fabbrizzi, L. *Inorg. Chem.* **1976**, *15*, 2342.

(26) Schenker, S.; Hauser, A.; Wang, W.; Chan, I. Y. *J. Chem. Phys.* **1998**, *109*, 9870.

(27) Jeftic, J.; Hauser, A. *J. Phys. Chem. B* **1997**, *101*, 10262.

(28) Wang, W.; Chan, I. Y.; Schenker, S.; Hauser, A. *J. Chem. Phys.* **1997**, *106*, 3817.

(29) Hinek, R.; Spiering, H.; Schollmeyer, D.; Gütlich, P.; Hauser, A. *Chem. Eur. J.* **1996**, *2*, 1427.

(30) Jeftic, J.; Hauser, A. *Chem. Phys. Lett.* **1996**, *248*, 458.

(31) Jeftic, J.; Hinek, R.; Capelli, S. C.; Hauser, A. *Inorg. Chem.* **1997**, *36*, 3080.

(32) Jeftic, J.; Romstedt, H.; Hauser, A. *J. Phys. Chem. Solids* **1996**, *57*, 1743.

(33) Hinek, R.; Gütlich, P.; Hauser, A. *Inorg. Chem.* **1994**, *33*, 567.

(34) Halder, G. J.; Kepert, C. J.; Moubaraki, B.; Murray, K. S.; Cashion, J. D. *Science* **2002**, *298*, 1762.

(35) Bray, K. L., Drickamer, H.G. *J. Phys. Chem.* **1990**, *94*, 2154.

(36) Bray, K. L.; Drickamer, H. G. *J. Phys. Chem.* **1991**, *95*, 559.

(37) Fabbrizzi, L.; Micheloni, M.; Paoletti, P. *Inorg. Chem.* **1974**, *13*, 3019.

(38) Lever, A. B. P.; Mantovani, E.; Donini, J. C. *Inorg. Chem.* **1971**, *10*, 2424.

(39) Kennedy, B. P.; Lever, A. B. P. *J. Am. Chem. Soc.* **1973**, *95*, 6907.

(40) Bray, K. L.; Drickamer, H. G.; Schmitt, E. A.; Hendrickson, D. N. *J. Am. Chem. Soc.* **1989**, *111*, 2849.

(41) Ferraro, J. R.; Meek, D. W.; Siwiec, E. C.; Quattrochi, A. *J. Am. Chem. Soc.* **1971**, *93*, 3862.

(42) Ferraro, J. R.; Nakamoto, K. *Inorg. Chem.* **1972**, *11*, 2290.

(43) Muller, G.; Riehl, J. P.; Schenk, K. J.; Hopfgartner, G.; Piguet, C.; Bünzli, J.-C. G. *J. Phys. Chem. A* **2002**, *106*, 12349.

(44) Maupin, C. L.; Mondry, A.; Liefer, L.; Riehl, J. P. *J. Phys. Chem. A* **2001**, *105*, 3071.

(45) Pearson, R. G. *J. Am. Chem. Soc.* **1963**, *85*, 3533.

(46) Pearson, R. G. *Science* **1966**, *151*, 172.

(47) Burmeister, J. L. *Coord. Chem. Rev.* **1990**, *105*, 77.

(48) Kishi, S.; Kato, M. *Inorg. Chem.* **2003**, *42*, 8728.

(49) Boldyreva, E.; Ahsahs, H.; Uchtmann, H. *Ber. Buns. Ges.* **1994**, *98*, 738.

(50) Mares, M.; Palmer, D. A.; Kelm, H. *Inorg. Chim. Acta* **19892**, *60*, 123.

(51) Ferraro, J. R.; Fabbrizzi, L. *Inorg. Chim. Acta* **1978**, *26*, L15.

(52) Yersin, H.; Gallhuber, E. *Inorg. Chem.* **1984**, *23*, 3745.

(53) Fetterolf, M. L.; Offen, J. *J. Phys. Chem.* **1985**, *89*, 3320.

(54) Fetterolf, M. L.; Offen, J. *J. Phys. Chem.* **1986**, *90*, 1828.

(55) Fetterolf, M. L.; Offen, J. *Inorg. Chem.* **1987**, *26*, 1070.

(56) Maupin, C. L.; Meskers, S. C. J.; Dekkers, H. P. J. M.; Riehl, J. P. *J. Phys. Chem. A* **1998**, *102*, 4450.

(57) Bray, K. L. *Top. Curr. Chem.* **2001**, *213*, 1.

(58) Wenger, O. S.; Valiente, R.; Güdel, H. U. *J. Chem. Phys.* **2001**, *115*, 3819.

(59) Reber, C.; Güdel, H. U. *J. Lumin.* **1988**, *42*, 1.

(60) Wenger, O. S. Güdel, H. U. *Chem. Phys. Lett.* **2002**, *354*, 75.

(61) Wenger, O. S.; Salley, G. M.; Güdel, H. U. *J. Phys. Chem. B* **2002**, *106*, 10082.

(62) Wenger, O. S.; Salley, G. M.; Valiente, R.; Güdel, H. U. *Phys. Rev. B* **2002**, *65*, 212108.

(63) Yersin, H.; Huber, P.; Gietl, G.; Trümbach, D. *Chem. Phys. Lett.* **1992**, *199*, 1.

(64) Yersin, H.; Trümbach, D.; Wiedenhofer, H. *Inorg. Chem.* **1999**, *38*, 1411.

(65) Yersin, H.; Strasser, J. *Coord. Chem. Rev.* **2000**, *208*, 331.

(66) van Eldik, R.; Hubbard, C. D. In *High Pressure Chemistry*; van Eldik, R., Klaerner, F.-G., Eds.; Wiley-VCH, 2002, pp 3-40.

(67) Macyk, J.; van Eldik, R. *Biochim. Biophys. acta* **2002**, *1595*, 283.

(68) Procelewska, J.; Zahl, A.; van Eldik, R.; Zhong, H. A.; Labinger, J. A.; Bercaw, J. E. *Inorg. Chem.* **2002**, *41*, 2808.

(69) Khoshtariya, D. E.; Dolidze, T. D.; Neubrand, A.; van Eldik, R. *J. Mol. Liquids* **2000**, *89*, 127.

(70) Khoshtariya, D. E.; Bajaj, H. C.; Tregloan, P. A.; van Eldik, R. *J. Phys. Chem. A* **2000**, *104*, 5535.

(71) van Eldik, R.; Meyerstein, D. *Acc. Chem. Res.* **2000**, *33*, 207.

(72) van Eldik, R.; Ducker-Benfer, C.; Thaler, F. *Adv. Inorg. Chem.* **2000**, *49*, 1.

(73) van Eldik, R. *Coord. Chem. Rev.* **1999**, *182*, 373.

(74) van Eldik, R. *NATO Science Series E: Applied Sciences* **1999**, *358*, 267.

(75) Stochel, G.; van Eldik, R. *Coord. Chem. Rev.* **1999**, *187*, 329.

(76) van Eldik, R. *Coord. Chem. Rev.* **1999**, *182*, 373.

(77) Schindler, S.; Hubbard, C. D.; van Eldik, R. *Chem. Soc. Rev.* **1998**, *27*, 387.

(78) van Eldik, R.; Ford, P. C. *Adv. Photochem.* **1998**, *24*, 61.

(79) Shapely, J. R.; Drickamer, H. G. *J. Clust. Sci* **1994**, *5*, 145.

(80) Roginski, R. T.; Carroll, T. L.; Moroz, A.; Whittlesey, B. R.; Shapley, J. R.; Drickamer, H. G. *Inorg. Chem.* **1988**, *27*, 3701-3706.

(81) Carroll, T. L.; Shapely, J. R.; Drickamer, H. G. *J. Chem. Phys.* **1986**, *85*, 6787.

(82) Morris, D. E.; Sattelberger, A. P.; Woodruff, W. H. *J. Am. Chem. Soc.* **1986**, *108*, 8270.

(83) Morris, D. E.; Tait, C. D.; Dyer, B. R.; Schoonover, J. R.; Hopkins, M. D.; Sattelberger, A. P.; Woodruff, W. H. *Inorg. Chem.* **1990**, *29*, 3447.

(84) Heyduk, A. F.; Nocera, D. G. *Science* **2001**, *293*, 1639.

(85) Cotton, F. A.; Nocera, D. G. *Acc. Chem. Res.* **2000**, *33*, 483.

(86) Dreger, Z. A.; Lang, J. M.; Drickamer, H. G. *Chem. Phys.* **1992**, *166*, 193.

(87) Dreger, Z. A.; White, J. O.; Drickamer, H. G. *Chem. Phys. Lett.* **1998**, *290*, 399.

(88) Zhu, A.; Wang, B.; White, J. O.; Drickamer, H. G. *Chem. Phys. Lett.* **2000**, *321*, 394.

(89) Zhu, A.; Wang, B.; White, J. O.; Drickamer, H. G. *J. Phys. Chem. A* **2003**, *107*, 6932.

(90) Riesen, H.; Güdel, H. U. *J. Chem. Phys.* **1987**, *87*, 3166.

(91) Riesen, H.; Güdel, H. U. *Inorg. Chem.* **1987**, *26*, 2347.

(92) Gliemann, G.; Yersin, H. In *Structure and Bonding*; 1985; Vol. 62. p. 87.

(93) Strasser, J.; Yersin, H.; Patterson, H. H. *Chem. Phys. Lett.* **1998**, *295*, 95.

(94) Patterson, H. H.; Yersin, H.; Trümbach, D.; Strasser, J.; Assefa, Z. Book of Abstracts (INOR-588), *216th ACS National Meeting*; ACS: Boston, MA, 1998.

(95) Yersin, H.; Trümbach, D.; Patterson, H. H.; Assefa, Z. *Inorg. Chem.* **1998**, *37*, 3209.

(96) Yersin, H.; Riedl, U. *Inorg. Chem.* **1995**, *34*, 1642.

(97) Trümbach, D.; Kritzenberger, J.; Yersin, H. *Inorg. Chim. Acta* **1994**, *216*, 245.

(98) Shirotani, I.; Konno, M.; Taniguchi, Y. *Synth. Met.* **1989**, *29*, F123.

(99) Stroud, M.; Drickamer, H. G.; Zietlow, M. H.; Gray, H. B.; Swanson, B. I. *J. Am. Chem. Soc.* **1989**, *111*, 66.

(100) Coffer, J. L.; Shapley, J. R.; Drickamer, H. G. *Chem. Phys. Lett.* **1988**, *149*, 487.

(101) Roessler, U.; Yersin, H. *Phys. Rev. B* **1982**, *26*, 3187.

(102) Yersin, H.; Stock, M. *J. Chem. Phys.* **1982**, *76*, 2136.

(103) Yersin, H.; von Ammon, W.; Stock, M.; Gliemann, G. *J. Lumin.* **1979**, *18-19*, 774.

(104) Stock, M.; Yersin, H. *Chem. Phys. Lett.* **1976**, *40*, 423.

(105) Wenger, O. S.; Garcia-Revilla, S.; Güdel, H. U.; Gray, H. B.; Valiente, R. *Chem. Phys. Lett.* **2004**, *384*, 190.

(106) Meulenberg, R. W.; Strouse, G. F. *Phys. Rev. B* **2002**, *66*, 035317.

(107) Crichton, W. A.; Mezouar, M.; Grande, T.; Stølen, S.; Grzechnik, A. *Nature* **2001**, *414*, 622.

(108) Tolbert, S. H.; Herbold, A. B.; Brus, L. E.; Alivisatos, A. B. *Phys. Rev. Lett.* **1996**, *76*, 4384.

(109) Hamlin, J. J.; Beckett, B. R.; Tomita, T.; Schilling, J. S.; Tyree, W. S.; Yee, G. T. *Polyhedron* **2003**, *22*, 2249.

(110) He, L.; Li, H.; Fan, J.; Li, S.; Gan, Q.; Zhang, G.; Zhang, B.; Li, Y.; Yang, G. *Chem. Phys. Lett.* **2003**, *378*, 263.

(111) Mayer, J. M. *Inorg. Chem.* **1988**, *27*, 3899.

(112) Drago, R. S. *Physical Methods for Chemists, 2nd Ed.*; Saunders College Pub.: Fort Worth, Toronto, 1992.

(113) Salthouse, J. A.; Ware, M. J. *Point group character tables and related data*; Cambridge University Press: New York, 1972.

(114) Harris, D. C.; Bertolucci, M. D. *Symmetry and Spectroscopy*; Oxford University Press, 1978.

(115) Miskowski, V. M.; Gray, H. B.; Hopkins, M. D. In *Adv. in Trans. Met. Coord. Chem.*; Che, C.-M., Yam, V. W.-W., Eds.; JAI Press: Greenwich, CT, 1996; Vol. 1, p 159.

(116) Nugent, W. A.; Mayer, J. M. *Metal-Ligand Multiple Bonds*; John Wiley: New York, 1988.

(117) Jørgensen, C. K. *Acta. Chem. Scand.* **1957**, *11*, 73.

(118) Ballhausen, C. J.; Gray, H. B. *Inorg. Chem.* **1962**, *1*, 111.

(119) Winkler, J. R.; Gray, H. B. *J. Am. Chem. Soc.* **1983**, *105*, 1373.

(120) Winkler, J. R.; Gray, H. B. *Inorg. Chem.* **1985**, *24*, 346.

(121) Espenson, J. H. *Adv. Inorg. Chem.* **2003**, *54*, 157-202.

(122) Yam, V. W.-W.; Che, C.-M. *Coord. Chem. Rev.* **1990**, *97*, 93.

(123) Yam, V. W.-W.; Tam, K.-K.; Cheng, M.-C.; Peng, S.-M.; Wang, Y. *J. Chem. Soc. Dalton Trans.* **1992**, 1717.

(124) Yam, V. W. W.; Che, C.-M. *J. Chem. Soc., Chem. Comm* **1988**, 100.

(125) Savoie, C.; Reber, C.; Bélanger, S.; Beauchamp, A. L. *Inorg. Chem.* **1995**, *34*, 3851.

(126) Savoie, C.; Reber, C. *J. Am. Chem. Soc.* **2000**, *122*, 844.

(127) Landry-Hum, J.; Tessier, V.; Ernzerhof, M.; Reber, C. *Coord. Chem. Rev.* **2002**, *233-234*, 63.

(128) Martin, D. S. *Inorg. Chim. Acta Rev.* **1971**, *5*, 107.

(129) Tuszynski, W.; Gliemann, G. *Z. Naturforsch.* **1979**, *34a*, 211.

(130) Bridgeman, A. J.; Gerloch, M. *J. Chem. Soc. Dalton Trans.* **1995**, 197.

(131) Preston, D. M.; Güntner, W.; Lechner, A.; Gliemann, G.; Zink, J. I. *J. Am. Chem. Soc.* **1988**, *110*, 5628.

(132) Reber, C.; Zink, J. I. *J. Phys. Chem.* **1991**, *95*, 9151.

(133) a) Pelletier, Y.; Reber, C. *Inorg. Chem.* **1997**, *36*, 721. b) Pelletier, Y.; Reber, C. *Inorg. Chem.* **2000**, *39*, 4535.

(134) Moreno, M.; Aramburu, J. A.; Barriuso, M. T. *Structure and Bonding* **2003**, *106*, 127.

(135) Longuet-Higgins, H. C. *Adv. Spectroscopy* **1961**, 429.

(136) Teller, E. *J. Phys. Chem.* **1937**, *41*, 109.

(137) Herzberg, G. *Infrared and Raman Spectra of Polyatomic Molecules: Molecular Spectra and Molecular Structure Vol II*; D. Van Nostrand: New York, 1945. p. 63.

(138) Triest, M.; Masson, S.; Grey, J. K.; Reber, C. *PhysChemComm* **2000**, article 12.

(139) Heller, E. J. *J. Chem. Phys.* **1975**, *62*, 1544.

(140) Heller, E. J. *Acc. Chem. Res.* **1981**, *14*, 368.

(141) Zink, J. I.; Kim Shin, K.-S. In *Adv. Photochem.*; Volman, D. H., Hammond, G. S., Neckers, D. C., Eds.; John Wiley: New York, 1991; Vol. 16, p 119.

(142) Feit, M. D.; Fleck Jr., J. A.; Steiger, A. *J. Comp. Phys.* **1982**, *47*, 412.

Chapter 2

Instrumentation

This chapter describes in general detail the various experimental setups and capabilities required to obtain the high quality spectroscopic data needed for quantitative analysis. The setups and procedures outlined here will be relevant for subsequent chapters that briefly highlight specific conditions and parameters associated with each experiment.

2.1 Control of physical variables: Pressure and temperature

The fundamental goal of this work is to characterize and control the interplay between the physical structure-geometry and the electronic-optical properties of specific molecular complexes. This approach first requires a detailed knowledge of the electronic structure that can be obtained through detailed features in temperature-dependent spectra. In the measurements involving variable temperature, a continuous flow (Oxford CF 1204) and microscope-based (Janis ST 500) liquid helium cryostats are used to achieve temperature control between 5—300 K. The temperature in the interior of the cryostat is controlled by of a Rh-Fe thermocouple that regulates the temperature within ±1 K with the aid of an external temperature controller. Helium gas flow is regulated by valves on the transfer lines from the dewars to the siphon arms of the cryostats. Samples are typically mounted on metal rods, or cold finger for the microscope system, and fixed into place using silicone grease. The microscope cryostat requires that the sample area be evacuated to pressures of ca. 10^{-5} mbar to avoid thermal loads that would cause condensation on the windows and make temperature control difficult.

The application of high pressures on crystalline solids is achieved through the use of diamond-anvil cells (DAC). The DAC works by mechanically compressing two opposing diamonds (pistons) with a sample positioned in between and can reach pressures of up to 70 kbar (~70,000 atm).[1] Other types of DACs have been made for specific experiments such as for achieving pressures in the Mbar range,[2] low-

temperature/ high pressure DACs[3-5] and DACs for use in solution-phase studies.[6] Figure 2.1 shows a schematic of a DAC with the individual components labeled.

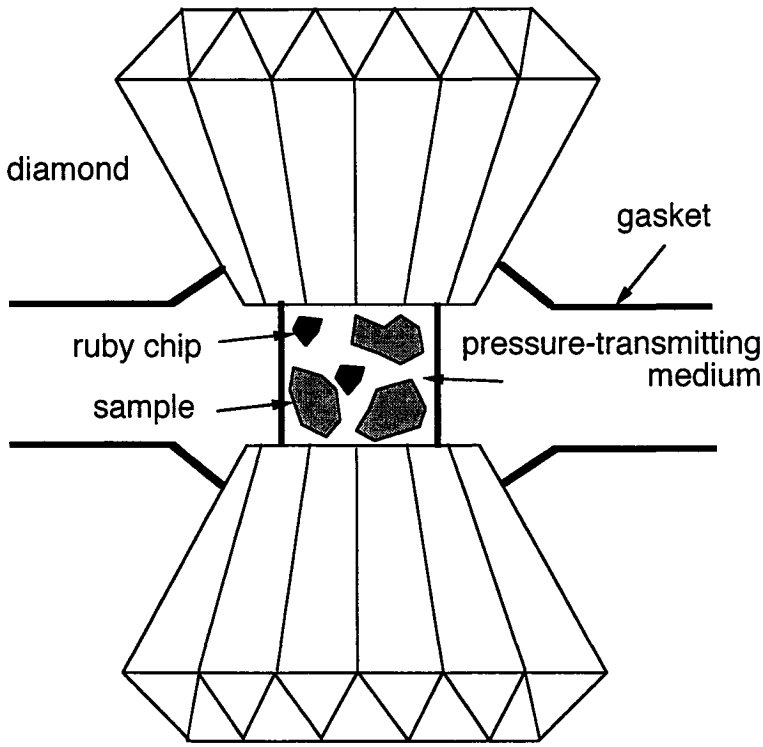

Figure 2.1. Schematic of the working space in the diamond-anvil cell.

In this diagram, a sample is positioned into a gasket (inconel steel) within a chamber of approximately 200 μm in diameter along with a pressure calibrant material and a pressure-transmitting medium. The most popular and reliable pressure calibrant is ruby where the intense $^2E \rightarrow {}^4A_2$ emission has a well-known pressure dependence[7] and can be efficiently pumped with excitation wavelengths of 630 nm and lower. Pressure is calibrated by following the more intense peak of the doublet emission (R_1: 694.2 nm) using the following equation:

$$P(kbar) = 3808\left[\left(\frac{\Delta\lambda_{R_1}}{\lambda^0_{R_1}} + 1\right)^5 - 1\right] \qquad \text{eq. 2.1}$$

$\lambda^0_{R_1}$ is the ambient pressure position of the R_1 peak and $\Delta\lambda_{R_1}$ is the pressure-induced shift relative to the ambient position. The use of a pressure-transmitting medium guarantees a quasi-hydrostatic environment for the sample thus minimizing pressure gradients. Some commonly used pressure-transmitting media are Nujol oil, 1:4 methanol-water, and glycerol.

2.2 Luminescence spectroscopy

Luminescence spectroscopy is widely used as a means to probe the nature of the ground state potential energy surface and provides detailed information into emitting state distortions as well as an understanding of competing nonradiative processes. Spontaneous emission from the transition metal complexes described previously in section 1.2 can be observed using both coherent (laser) and incoherent (lamp) sources. The observed luminescence decay rate constant, k, is the sum of both radiative (k_R) and nonradiative (k_{NR}) rate constants and the lifetime of the emitting state is simply the inverse of the observed rate. In systems where there are large structural distortions, such as interconfigurational d–d transitions, k_{NR} usually dominates and the observed luminescence is weak.

Two spectrometers are used for the collection of luminescence data that have different spectral sensitivities and detection ranges. A microscope spectrometer (Renishaw 3000) is used in both temperature- and pressure-dependent measurements with argon ion (488 and 514.5nm), helium-neon (633 nm), and diode (782 nm) excitation sources. This system is equipped with a multi-channel charge-coupled device (CCD) camera that is capable of detecting signals between 400—1000 nm. Because high power (20-100×) objectives are used to focus and collect the excitation and signal, very small amounts of sample may be used. The second system is a step-scan instrument that uses an argon ion laser as excitation and a monochromator to disperse the emitted light. The broad range of detection afforded by this instrument (400—1500 nm) make it ideal for studies the UV to near-infrared (NIR).

Scheme 2.1 shows a diagram for the microscope-based spectrometer and the operation is discussed in the following. For pressure-dependent measurements, the DAC is placed on a mechanical stage that can be translated in the x-y plane and excitation is

focused onto the sample area by adjusting the z focus. Temperature-dependent measurements call for the use of the micro-cryostat described previously, which is mounted on the base of the microscope. An interference filter is placed either before or after the beam expander and excitation is then directed to the microscope and centered in the optical field. The appropriate holographic notch filter is then placed into position to reject all excitation light and the sample signal then passes through the entrance slit and dispersed by a grating (1800 lines/mm). Incident radiant power on the samples is typically on the order of 1 mW and can be adjusted (attenuated) by neutral density filters built into the microscope.

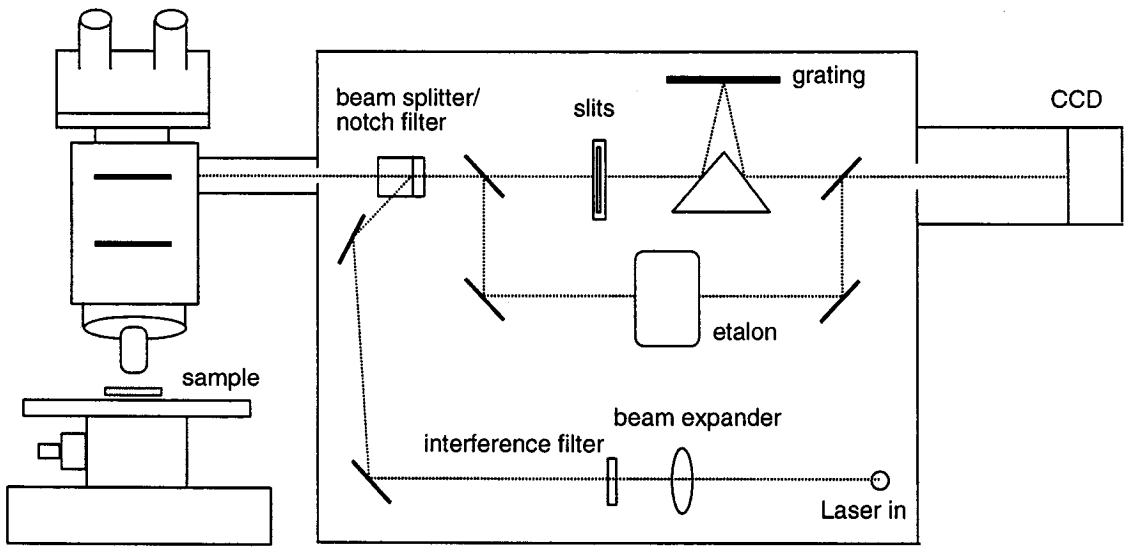

Scheme 2.1. Layout of the microscope spectrometer used for Raman and luminescence measurements.

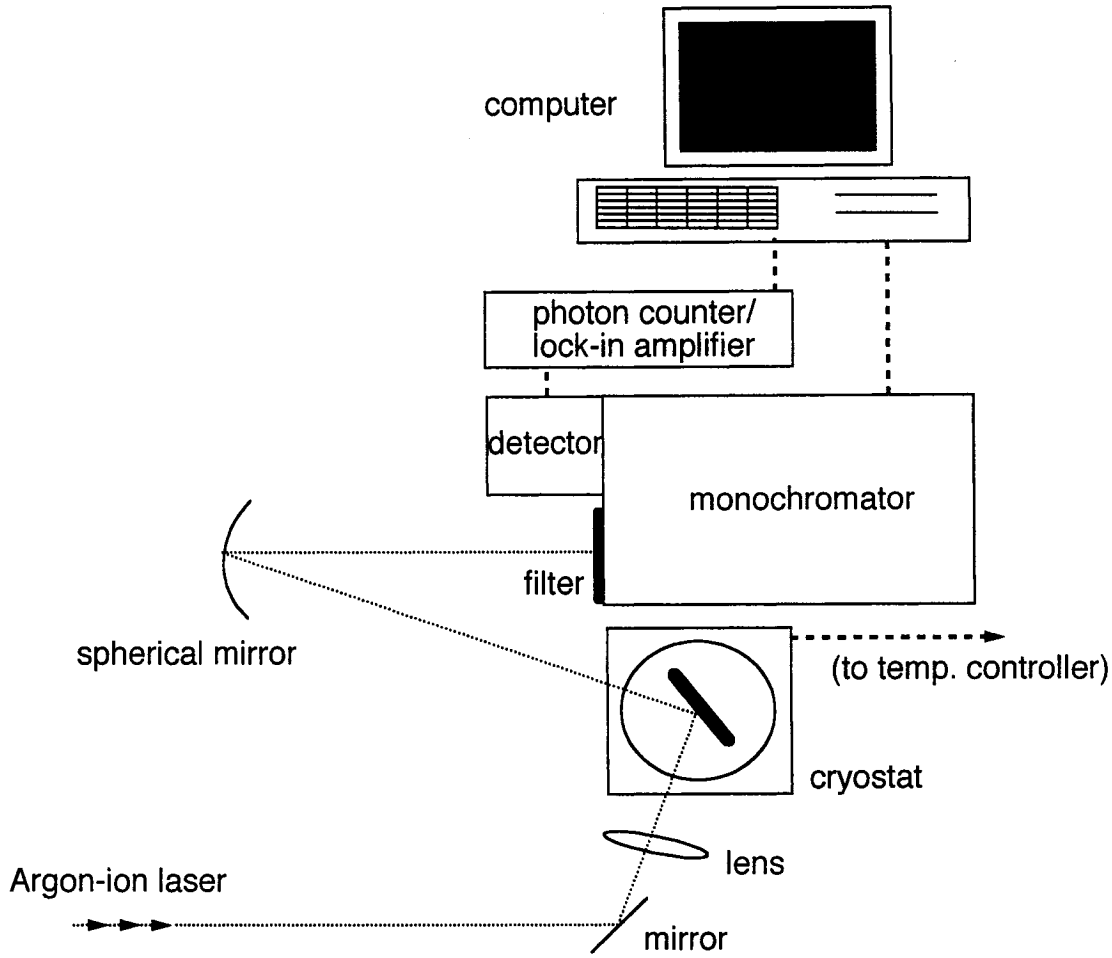

Scheme 2.2. Experimental setup for measuring temperature-dependent luminescence spectra.

Scheme 2.2 illustrates the step-scan instrument for use in temperature-dependent studies only. Samples are cooled in the continuous flow cryostat using either liquid helium (boiling point 4 K) or liquid nitrogen (boiling point 77 K) as cryogens. The excitation source is an argon-ion laser (Spectra Physics Stabilite 2017) that can operate in broad band UV (350—370 nm: 0.1 W) or single mode visible (458—514.5 nm: 0.1—1 W). The excitation is first passed through a dove prism and then an interference filter upon exiting the laser head to remove plasma lines then directed and focused onto the sample using a quartz lens. The signal is collected at 90° using a spherical mirror and focused onto the entrance slit of a 0.5m monochromator (SPEX 500M, 600 lines/mm

grating). A long pass filter (Schott RG 610, 645; OG 570, 590) is placed in the entrance path to reject excitation. After dispersion of the signal, the emitted light is detected with either photomultiplier tubes (Hammamatsu R928, R406) or photodiodes (Applied Detector Corporation 403 UL) connected to either a photon counter (Stanford Research Systems SR 400) or lock-in amplifier (Stanford Research Systems SR 510 or SR 830). When using the lock-in amplifier, an optical chopper (Stanford Research Systems SR 540) is placed before the entrance slit to modulate the signal at a particular frequency (e.g., 400 Hz). Because the photodiode is sensitive to the surroundings (i.e., cosmic events), an in-house program is used to reject anomalous 'spikes' in data by sampling a selected number of values and removing outlying points outside of the tolerance.[8]

All spectra obtained on both systems are corrected for system response to obtain the true signal from the sample. This is accomplished by generating a correction factor by measuring a spectrum of a blackbody emitter (tungsten lamp at 3000 K) under the exact same experimental conditions and scaled to a theoretical blackbody spectrum at 3000 K. The factor, f, is then obtained by dividing the theoretical spectrum, $I_{\text{theoretical}}$, by the spectrum of the lamp, I_{lamp}.

$$f = I_{\text{theoretical}} / I_{\text{lamp}} \qquad \text{eq. 2.2}$$

and

$$I_{theoretical} = \frac{2\pi}{hc\lambda^4}\left[\exp\left(\frac{hc}{k_B T\lambda}\right) - 1\right]^{-1} \qquad \text{eq. 2.3}$$

where λ is the wavelength in Å. The experimental luminescence spectrum is then multiplied by f to obtain the true response from the sample. Because many of the compounds studied have appreciable intensity in regions where spectral sensitivity varies greatly as a function of wavelength, it is critical that experimental spectra be corrected before any relevant information can be extracted. Spectra are corrected in wavelength units prior to conversion to wavenumber according to the procedure described by Ejder[9] and reported in arbitrary units.

2.3 Raman spectroscopy

Raman spectroscopy is a powerful tool for understanding the physical structure of a particular system and, depending on excitation wavelengths, may also provide information into emitting state displacements along specific vibrational modes. The Raman phenomenon originates from the inelastic scattering of monochromatic electromagnetic radiation and scattering intensity is proportional to the change in polarizability of the electron density. The complexes studied here have idealized D_{4h} point group symmetry and possess inversion symmetry thus giving rise to two types of vibrational modes, *u*- (ungerade-odd) and *g*- (gerade-even) parity. The law of mutual exclusion states that the *g*-parity modes are Raman active and the *u*-parity modes are only IR active. Because resolved vibronic progressions in electronic transitions can only be in totally symmetric (a_{1g}) vibrational modes, Raman spectroscopy is a valuable tool for characterizing the ground state vibrational modes that are displaced in the course of the luminescence transition. Figure 2.2 shows a potential energy level diagram of a Raman transition with excitation both off and on resonance with excited electronic states.

Raman spectra were obtained using the microscope spectrometer described above and a double monochromator system (SPEX 14018) using the argon-ion laser as an excitation source. The scattered light is focused onto the entrance slit of the monochromator and is dispersed over a 0.85m pathlength with two 1800 lines/mm gratings. The detection system consists of a R928 PMT in a thermoelectric cooler (Products for Research) that reduced thermal noise allowing for higher signal-to-noise ratios. It is important to point out that the Raman effect, except for cases when the excitation wavelength is on resonance with an electronic transition, only probes a small region of the ground state PES (as shown in Figure 2.2). In systems where large structural distortions occur during an electronic transition, such as with the d^2 and d^8 transition metal complexes studied here, Raman techniques usually do not provide sufficient details into the nature of the ground state PES compared to luminescence techniques.

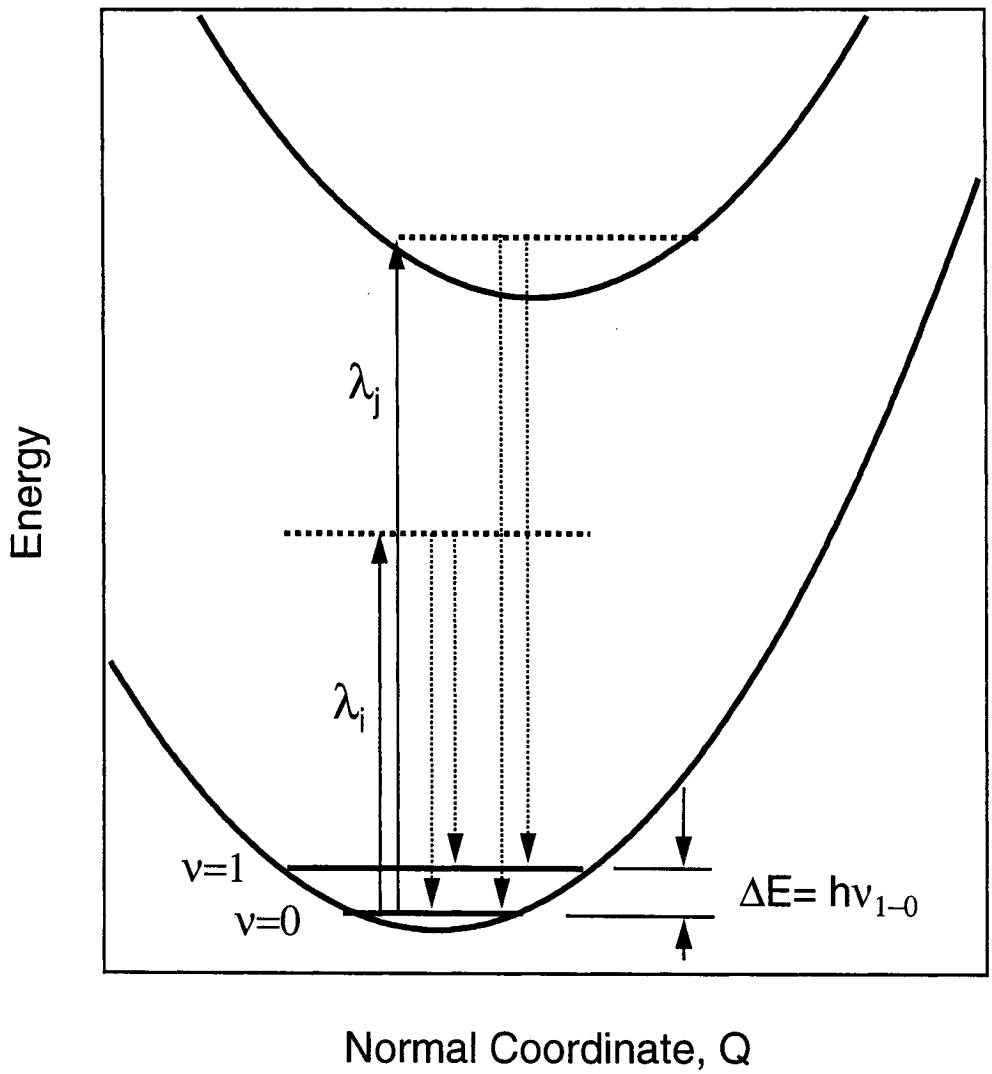

Figure 2.2. Theoretical picture of Raman transitions both off resonance (λ_i) and on resonance (λ_j) with an electronic transition.

2.4 Luminescence lifetime measurements

Scheme 2.3 shows the experimental setup for the measurement of luminescence decay. Samples are cooled in the continuous flow cryostat and excitation is achieved using a Nd:YAG pulsed laser (Continuum Mini-lite) with 5—10 ns pulse width. The time-dependent luminescence is dispersed through the 0.5m monochromator using the appropriate long-pass filter to reject excitation. Detection consists of a PMT and decay traces are displayed, averaged and saved on a digital oscilloscope (Tektronix TDS 380) triggered by a photodiode (Thorlabs FDS 100). Decay is assigned by fitting traces with either single- and double-exponential functions using least-squares methods.

Pressure-dependent luminescence lifetime measurements can be performed using the DAC described earlier with the Nd:YAG pulsed laser. Due to the small sample volume of the DAC, it is not possible to disperse the time-dependent luminescence signal in a monochromator and the PMT detector is placed directly in the optical path to collect the maximum amount of signal. A long-pass filter is placed at the front of the PMT to reject excitation and the laser is used in low energy mode to reduce potential damage to the DAC.

2.5 Excitation and absorption spectroscopy

In order to understand the excited state electronic structures, namely the properties of the emitting state, it is necessary to characterize the absorption features of the molecules under study. Absorption spectroscopy is the most straightforward and direct technique of ascertaining information on the excited states of the system where light is absorbed only when it is on resonance with a particular excited state. Excitation spectroscopy involves exciting the sample with variable wavelength excitation and, by monitoring the luminescence at a fixed wavelength, reveals the same information as an absorption spectrum. Both of these methods are useful in that they may be used in a complementary fashion. For single crystal samples, it is possible to perform polarized absorption measurements whereby, after the unique axis of the crystal is identified using cross-polarizers, the polarization of the incident beam can be rotated thus revealing absorption anisotropies for lower symmetry complexes. In excitation spectroscopy, the excitation intensity can be monitored at different wavelengths across the luminescence

band, making it possible to determine the presence of multiple emitters, i.e., luminescent impurities.

Absorption spectra are obtained from a Varian CARY 5E spectrometer operating in double-beam mode. Single crystal samples are mounted and masked on a sample plate and cooled in the continuous flow cryostat described previously. For polarized measurements, extinction directions are determined using a polarizing microscope and Glan-Taylor calcite polarizers are placed in the sample and reference beams. Neutral density filters are placed in the reference beam path to attenuate signals in order to keep absorbance values at a reasonable level.

Scheme 2.4 shows the experimental setup for excitation spectroscopic measurements. The excitation source is a Xenon arc lamp (150 W, ICL LX-150UV) and the light is first passed through a 10 cm cell filled with water to remove IR radiation. The beam is then focused onto the entrance slit of the 0.5m monochromator, which provides variable wavelength excitation over a range of 450-700 nm. A UV cutoff filter (KV 420) is placed at the exit slit to remove residual UV radiation and the beam is collimated and focused onto the sample (cooled in the continuous flow cryostat) with quartz lenses. Luminescence from the sample is collected at 90° using a spherical mirror and focused onto the entrance slit of the luminescence monochromator (0.75m, SPEX 1800 II) with a long-pass filter to reject excitation light. The detection system consists of a PMT tube (Hammatsu R928 or R406) along with a photon counter or lock-in amplifier and the excitation monochromator is controlled by a computer.

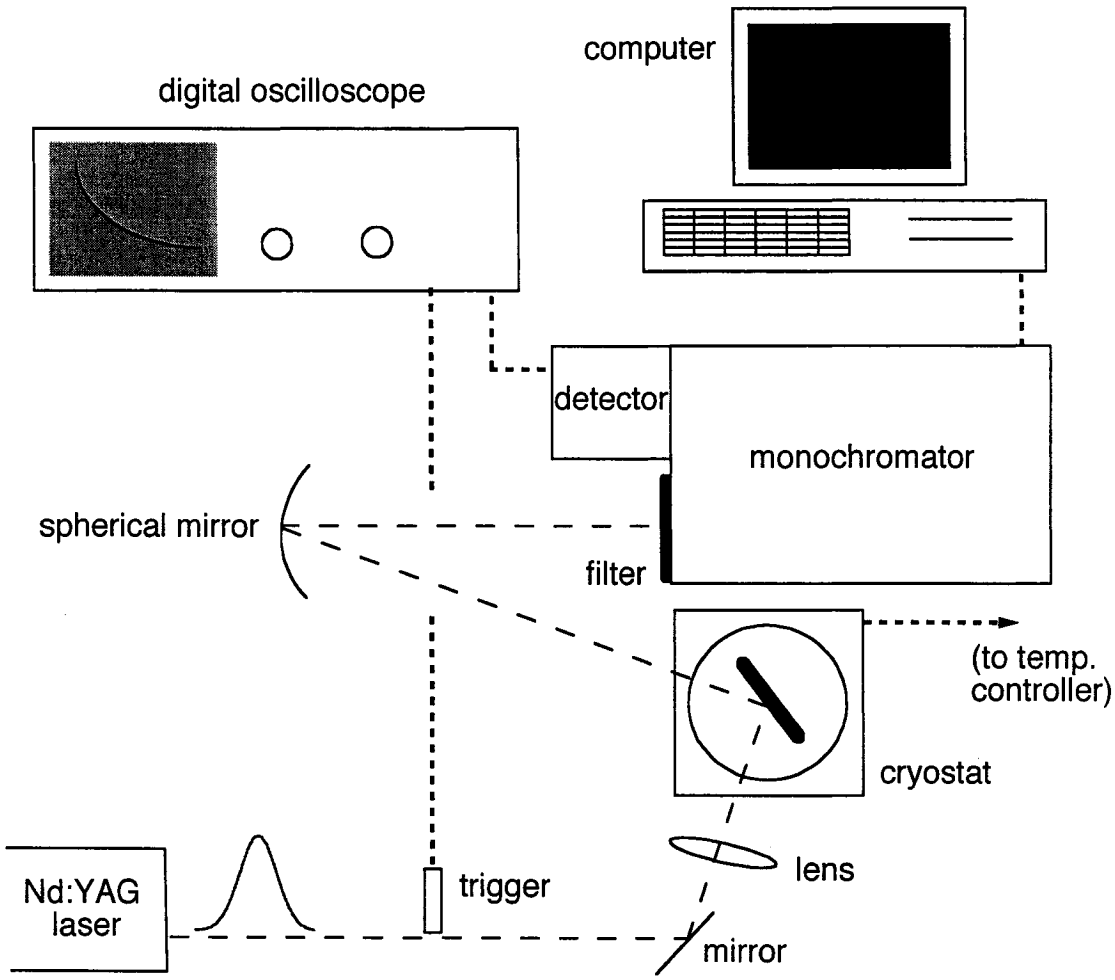

Scheme 2.3. Experimental setup for measuring luminescence decay kinetics.

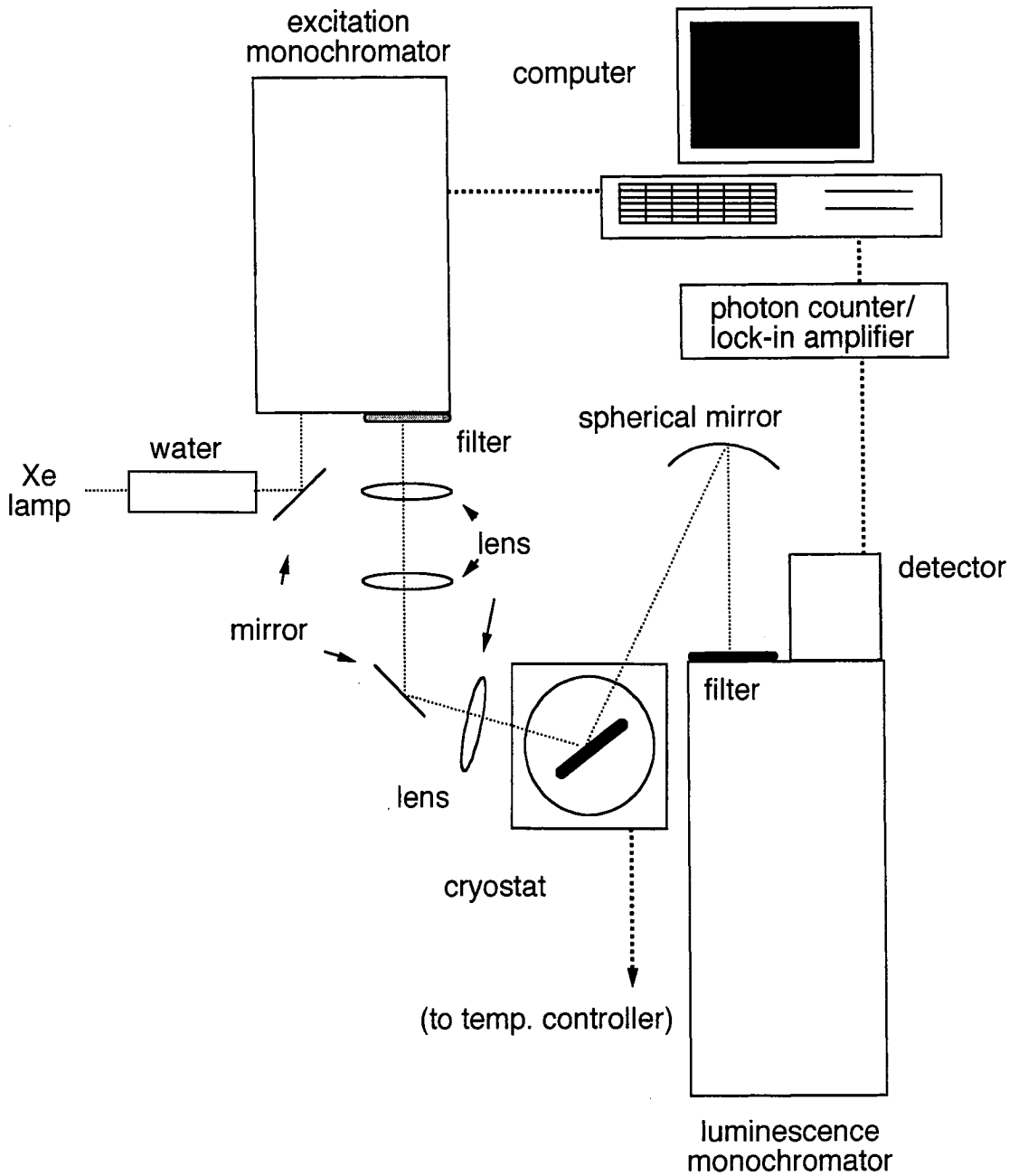

Scheme 2.4. Experimental setup for the measurement of excitation spectroscopy.

References

(1) Weir, C. E.; Lippincott, E. R.; Van Valkenburg, A.; Bunting, E. N. *J. Natl. Bur. Stand. A* **1959**, *63*.

(2) Mao, H. K.; Bell, P. M. *Science* **1979**, *200*, 1145.

(3) Bassett, W. A.; Shen, A. H.; Buckman, M.; Chou, I.-M. *Rev. Sci. Instr.* **1993**, *64*, 2340.

(4) Riesen, H.; Kindler, U.; Güdel, H. U. *Rev. Sci. Instr.* **1987**, *58*, 1122.

(5) Webb, A. W.; Gruber, D. U.; Towle, L. C. *Rev. Sci. Instr.* **1976**, *47*, 59.

(6) Zahl, A.; Igel, P.; Weller, M.; Khoshtariya, D. E.; Hamza, M. S. A.; van Eldik, R. *Rev. Sci. Instr.* **2003**, *74*, 3758.

(7) Piermarini, G. J., Block, S., Barnett, J.D., Forman, R.A. *J. Appl. Phys.* **1975**, *46*, 2774.

(8) Oetliker, U.; Reber, C. *J. Near Infrared Spectrosc.* **1995**, *3*, 63.

(9) Ejder, E. *J. Opt. Soc. Am.* **1969**, *59*, 223.

Chapter 3

Pressure-Dependent Raman Spectroscopy of Metal-Oxo Multiple Bonds in Rhenium(V) and Osmium(VI) Complexes

Reprinted from *Chem. Phys. Lett.* **2002**, *366*, 361-367.

This chapter presents a survey of the effect of external pressure on the stretching vibrations involving metal-oxo multiple bonds of *trans*-dioxo and mono-oxo rhenium(V) and osmium(VI) complexes. Metal-ligand vibrational frequencies involving double and triple bonds increase (blue-shift) with pressure according to the nature of the metal center and ancillary ligands. Because the ligand-field optical spectra of these complexes depend on the metal—oxo and metal—ancillary ligand bond lengths, the trends in the blue-shifts can be compared to the respective shifts in optical spectra. Pressure-dependent luminescence spectra, recorded at room temperature, of a *trans*-dioxo rhenium(V) complex exhibit resolved vibronic structure with a progression in a high frequency metal-oxo stretching mode that shows a change of the intensity distribution with pressure.

3.1 Introduction

Transition metal complexes with metal-ligand multiple bonds possess many well-characterized spectroscopic properties.[1-5] The ambient-pressure vibrational frequencies of stretching modes involving the metal-ligand multiple bonds often vary noticeably between compounds with different ancillary ligands or metal centers. These frequencies can also be modified by applying external pressure on solid samples of metal complexes containing metal-ligand multiple bonds. Raman spectroscopy reveals these detailed pressure effects and provides insight into the nature of the metal-ligand multiple bonds, which are often described as double and triple bonds for dioxo and mono-oxo complexes, respectively. We study the Raman spectra of a series of six-coordinate, d^2 rhenium(V) and osmium(VI) *trans*-dioxo and mono-oxo species, and one nitrido complex, as a

function of external pressure. Ancillary ligands on the *trans*-$[O=M=O]^{n+}$ and $[M\equiv O]^{n+}$ moieties are chosen depending on the mode of ligation and other structural properties. Upon ligand substitution, the ambient pressure metal-oxo multiple bond lengths vary by as much as 0.1 Å [6] and vibrational frequencies for dioxo and mono-oxo stretching modes typically range from 870 cm^{-1} to 920 cm^{-1} and from 950 cm^{-1} to 1000 cm^{-1}, respectively.

External pressure is an effective method for probing the variation of bond lengths on the electronic structures of materials and it is especially attractive to investigate combined electronic and vibrational effects spectroscopically. Excited states significantly influence the ground state of the title complexes [4,7] and we use pressure-dependent Raman spectroscopy to gain complementary experimental information on this interaction. Pressure-dependent luminescence measurements on rhenium(V) *trans*-dioxo complexes exhibit resolved vibronic structure at room temperature and a substantial red-shift with pressure. These measurements provide extensive insight into the nature of the ground state potential energy surface and allow us to rationalize changes of the vibrational frequencies caused by a decrease of the energy difference between the ground and emitting states.[8,9]

3.2 Experimental

Single crystal samples of rhenium(V) and osmium(VI) *trans*-dioxo and mono-oxo complexes were synthesized and characterized using methods in the literature.[4,7] Abbreviations used for ancillary ligands are given in Table 3.1. External pressures were applied on the crystalline samples by diamond-anvil cell (DAC; High Pressure Diamond Optics) techniques. Paraffin oil was used as pressure transmitting medium and pressure was calibrated using the R_1 line of the ruby $^2E \rightarrow {}^4A_2$ emission.[10] We estimate an error of ± 2 kbar in the reported pressures from several independent data sets of the $[ReO_2(en)_2]^+$ complex. This value is representative for all complexes in the pressure range reported. Raman spectra were measured with a Renishaw 3000 microscope system with argon ion excitation sources (488 nm and 514.5 nm lines, Spectra-Physics). When sample luminescence was close to the excitation source, a near-infrared diode laser (Renishaw NIR 782) was used to avoid luminescence backgrounds. The vibrational frequencies at all pressures were determined by fitting a Gaussian function to a wavenumber range

containing the band maximum using least squares methods. The choice of this region is not critical; peak positions do not vary by more than 1.5 cm^{-1} when this region is chosen either to include all points with intensities higher than 30% of the peak height or to include only points at more than 80% of the height. Pressure-dependent luminescence spectra were measured using the same setup and were corrected for instrument response.[8,9]

3.3 Spectroscopic Results

Room temperature, pressure-dependent Raman spectra of selected Re(V) *trans*-dioxo and mono-oxo and Os(VI) *trans*-dioxo complexes are shown in Figures 3.1 and 3.2, illustrating the effects of pressure on the stretching frequencies of the metal-ligand multiple bonds. Molar absorptivities of all complexes studied are on the order of 10 $M^{-1}cm^{-1}$ or less at the excitation wavelengths used, therefore, resonance Raman enhancements can be neglected. The characteristic trend for most of the complexes studied is a monotonic increase of the vibrational frequencies with pressure, an effect that is clearly seen in Figure 3.1a-d and is similar for all complexes. In addition, there is a broadening of the bands with increasing pressure. However, the integrated intensity of the Raman band remains approximately constant with increasing pressure. Table 3.1 summarizes the pressure dependence of all metal-ligand multiple bond vibrational frequencies studied here. These trends are shown graphically in Figures 3.3 and 3.4. Even seemingly subtle structural deviations to ancillary ligand substituent groups lead to a markedly different pressure-dependent behavior for the vibrational frequencies associated with metal-oxo bonds. This is illustrated by the pressure-induced increase of the O=Re=O stretching mode frequency by 0.55 cm^{-1}/kbar for the *trans*-$[ReO_2(1\text{-MeIm})_4]^+$ complex whereas the *trans*-$[ReO_2(1,2\text{-}Me_2Im)_4]^+$ complex shows a 0.69 cm^{-1}/kbar increase, larger by almost 25%. These pressure-induced shifts are much larger than the typical behavior of other *trans*-dioxo complexes of rhenium(V) for which the average shift in Table 3.1 is about 0.4 cm^{-1}/kbar.

Compound[a]	Vibrational Frequency [cm^{-1}]	Assignment	Pressure dependence [cm^{-1}/ kbar]
$[ReO_2(en)_2]^+$	898	$\nu_{O=Re=O}$	0.37 ±0.01
$[OsO_2(en)_2]^{2+}$	918	$\nu_{O=Os=O}$	0.29 ±0.02
$[ReO_2(tmen)_2]^+$	868	$\nu_{O=Re=O}$	0.42 ±0.02
$[ReO_2(1\text{-}MeIm)_4]^+$	896	$\nu_{O=Re=O}$	0.55 ±0.01
$[ReO_2(1,2\text{-}Me_2Im)_4]^+$	900	$\nu_{O=Re=O}$	0.69 ±0.04
$[OsO_2(NCS)_4]^{2-}$	888	$\nu_{O=Os=O}$	0.35 ±0.04
$[OsO_2(mal)_2]^{2-}$	892	$\nu_{O=Os=O}$	0.37 ±0.04
$[ReOCl_3(dppe)]$	981	$\nu_{Re=O}$	0.27 ±0.04
$[ReOBr_3(dppe)]$	981	$\nu_{Re=O}$	0.27 ±0.02
$[ReOCl_2(OEt)(dppe)]$	997	$\nu_{Re=O}$	0.27 ±0.02
$[ReO(NCS)_5]^{2-}$	950	$\nu_{Re=O}$	0.11 ±0.02
$[ReN(PPh_3)(O\text{^}P)_2]$	999	$\nu_{Re=N}$	0.28 ±0.02

[a] Ligand abbreviations: en = *N,N,N',N'*-ethylenediamine; tmen = *N,N,N',N'*-tetramethylethylenediamine; 1-MeIm = 1-methylimidazole; $1,2\text{-}Me_2Im$ = 1,2-dimethylimidazole; NCS = isothiocyanate; mal = malonate; dppe = 1,2-diphenylphosphinoethane; O^P = 1-phenyl-2-(diphenylphosphino)ethanolate.

Table 3.1. Summary of pressure-induced shifts of Raman frequencies of Re(V) and Os(VI) *trans*-dioxo and Re(V) mono-oxo and nitrido complexes.

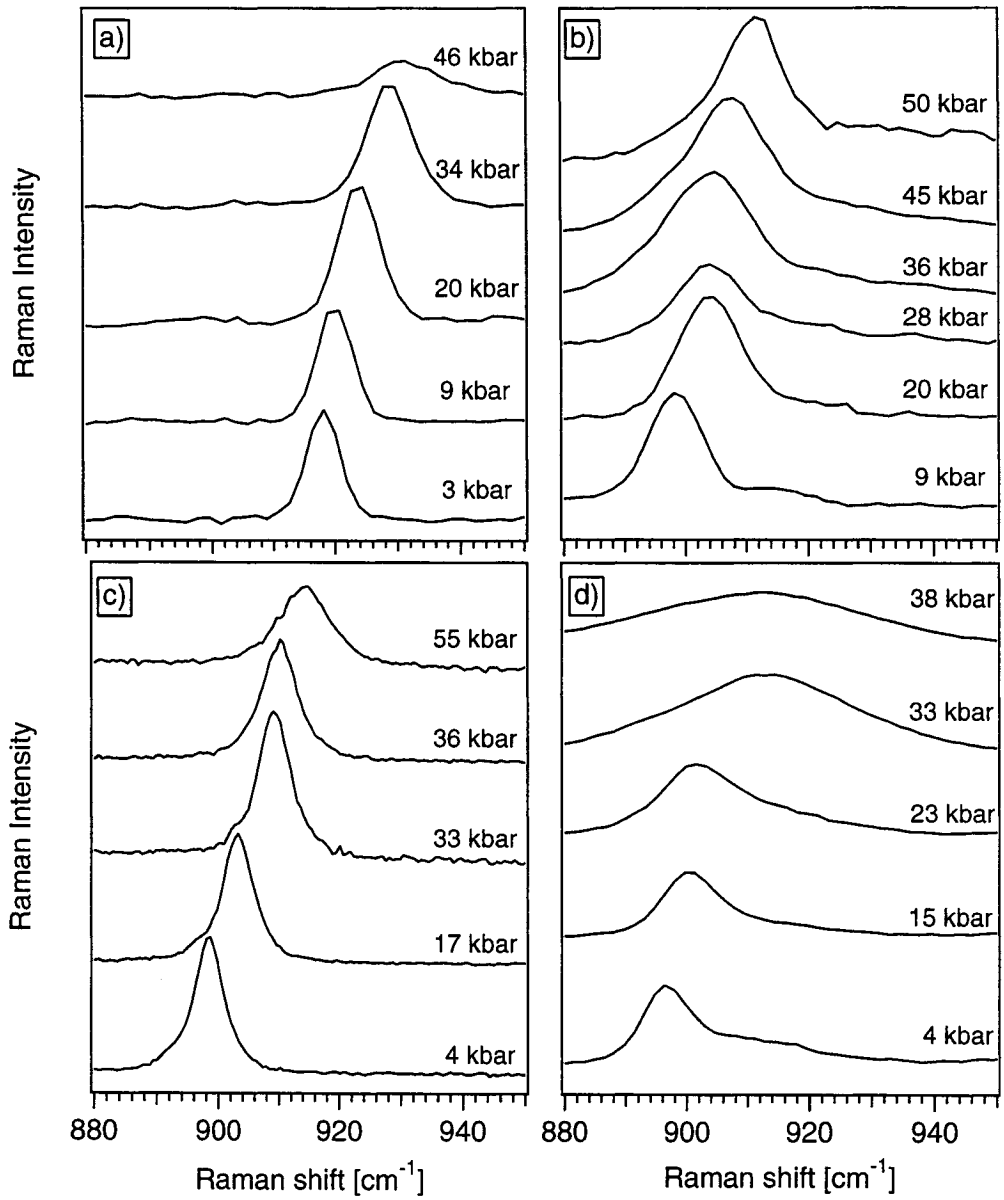

Figure 3.1. Pressure-dependent Raman spectra showing the shift of the O=M=O symmetric stretching frequency as a function of pressure for, a) $[OsO_2(en)_2]^{2+}$; b) $[OsO_2(mal)_2]^{2+}$; c) $[ReO_2(en)_2]^{+}$; d) $[ReO_2(1\text{-MeIm})_4]^{+}$.

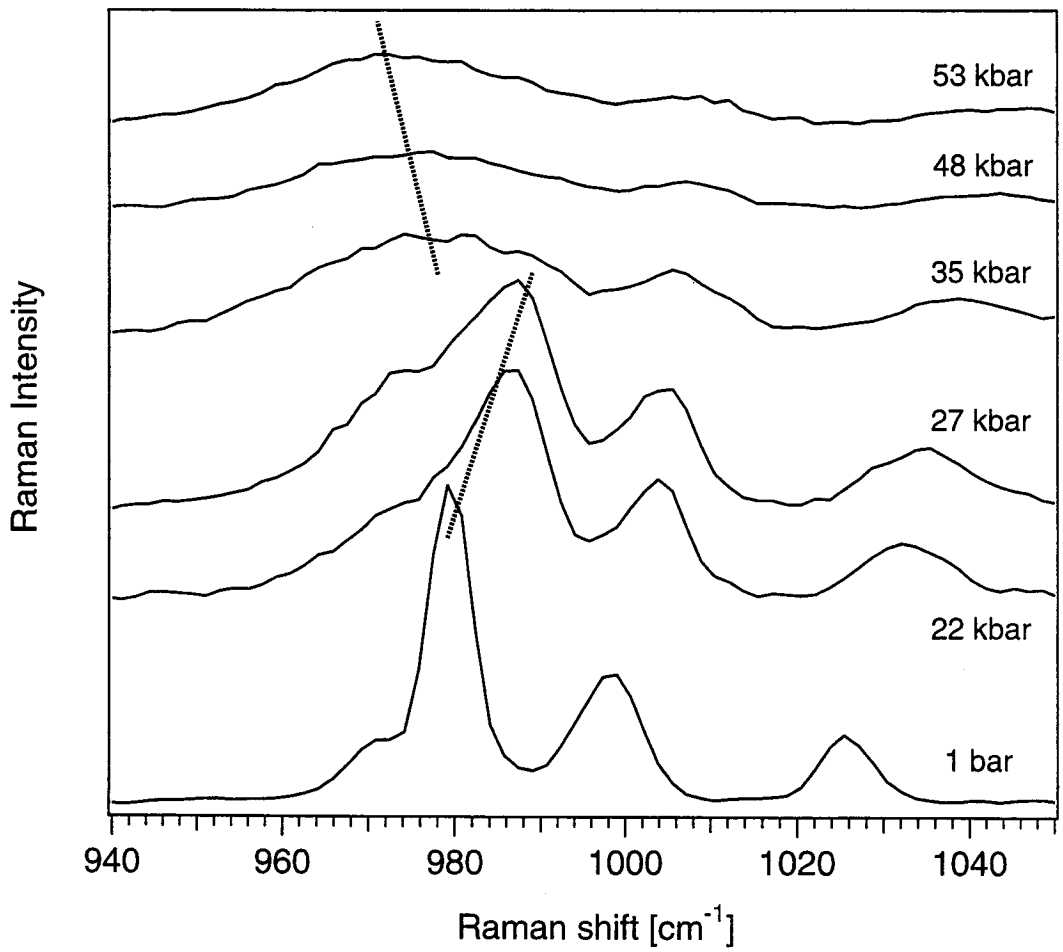

Figure 3.2. Pressure-dependent Raman spectra of $[ReO(Br)_3(dppe)]$. The Re≡O stretching frequency (981 cm^{-1}) shows a characteristic increase up to 30 kbar and then a decrease of this frequency. Hashed lines are included as guides for the eye.

For molecules with only one oxo or nitrido ligand coordinated to the metal center, the formal metal-ligand bond order changes from two to three.[5] Higher frequencies than for *trans*-dioxo complexes are observed at ambient pressure, as expected for the higher formal bond order and shorter metal-ligand bonds. Figure 3.2 illustrates the effect of pressure on the [ReO(Br_3)(dppe)] complex. Its Re≡O stretching frequency increases smoothly by 0.27 cm^{-1}/kbar up to approximately 30 kbar, a trend similar to the *trans*-dioxo complexes. At higher pressures, the Re≡O symmetric stretching frequency of [ReO(Br_3)(dppe)] (981 cm^{-1} at ambient pressure) decreases. The peaks at 998 cm^{-1} and 1025 cm^{-1} are modes centered on the dppe ligand, which shift smoothly to higher frequency with pressure throughout the pressure range reported here. To the best of our knowledge, this unusual decrease of the Re≡O stretching frequency has not been reported for transition metal complexes with metal-ligand multiple bonds. Figure 3.4 shows the pressure-dependent Raman frequencies for four oxo and one nitrido complex. The three related mono-oxo complexes with one dppe ligand show a monotonic increase of the Re≡O multiple bond stretching frequency of 0.27 cm^{-1}/kbar, as listed in Table 3.1. Two of these complexes show a distinct *decrease* of this frequency at pressures higher than 30 kbar, with an average shift of –0.24 cm^{-1}/kbar. Unlike the other mono-oxo complexes, the Re≡O stretching frequency of the $[ReO(NCS)_5]^{2-}$ complex shows a much smaller increase with pressure of 0.11 cm^{-1}/kbar. This is likely an effect related to the nature of the ancillary ligands and their ability to interact with the metal π-symmetry orbitals.

Pressure-dependent luminescence spectra showing resolved vibronic structure provide unique insight into excited state properties, such as the emitting state displacement along the Franck-Condon active normal coordinates of the molecule.[8,9,11,12] This method also probes a larger region of the ground state potential energy surface than Raman spectroscopy. We observe resolved vibronic structure, at room temperature, from the pressure-dependent luminescence of *trans*-$[ReO_2(1,2\text{-}Me_2Im)_4]^+$ in Figure 3.5. The luminescence of this *trans*-dioxo complex is assigned as a $^3E_g \rightarrow {}^1A_{1g}$ transition (D_{4h}) [5] with a transfer of Re-oxo π-antibonding electron density from the d_{xz},d_{yz} orbitals to the Re-oxo nonbonding d_{xy} orbital. The luminescence spectra in Figure 3.5 show a partially resolved vibronic progression in the O=Re=O symmetric stretching mode with up to three quanta easily distinguished. Low-temperature luminescence spectra of *trans*-dioxo

complexes reveal that the O=Re=O and Re-Ligand symmetric stretching modes are the Franck-Condon active vibrational modes for these complexes. The low frequency Re-N(imidazole) symmetric stretching modes are not resolved in the room temperature luminescence of the *trans*-$[ReO_2(1,2\text{-}Me_2Im)_4]^+$ complex. As pressure increases, we see a change in the intensity distribution of the vibronic components, indicating a decrease of the normal coordinate offset between the ground and emitting state potential minima, and a shift of the overall luminescence profile to lower energy by 2 cm^{-1}/kbar. Previously reported pressure-dependent luminescence spectra of a series of ethylenediamine *trans*-dioxo rhenium(V) complexes show red-shifts up to 8 cm^{-1}/kbar.[8,9]

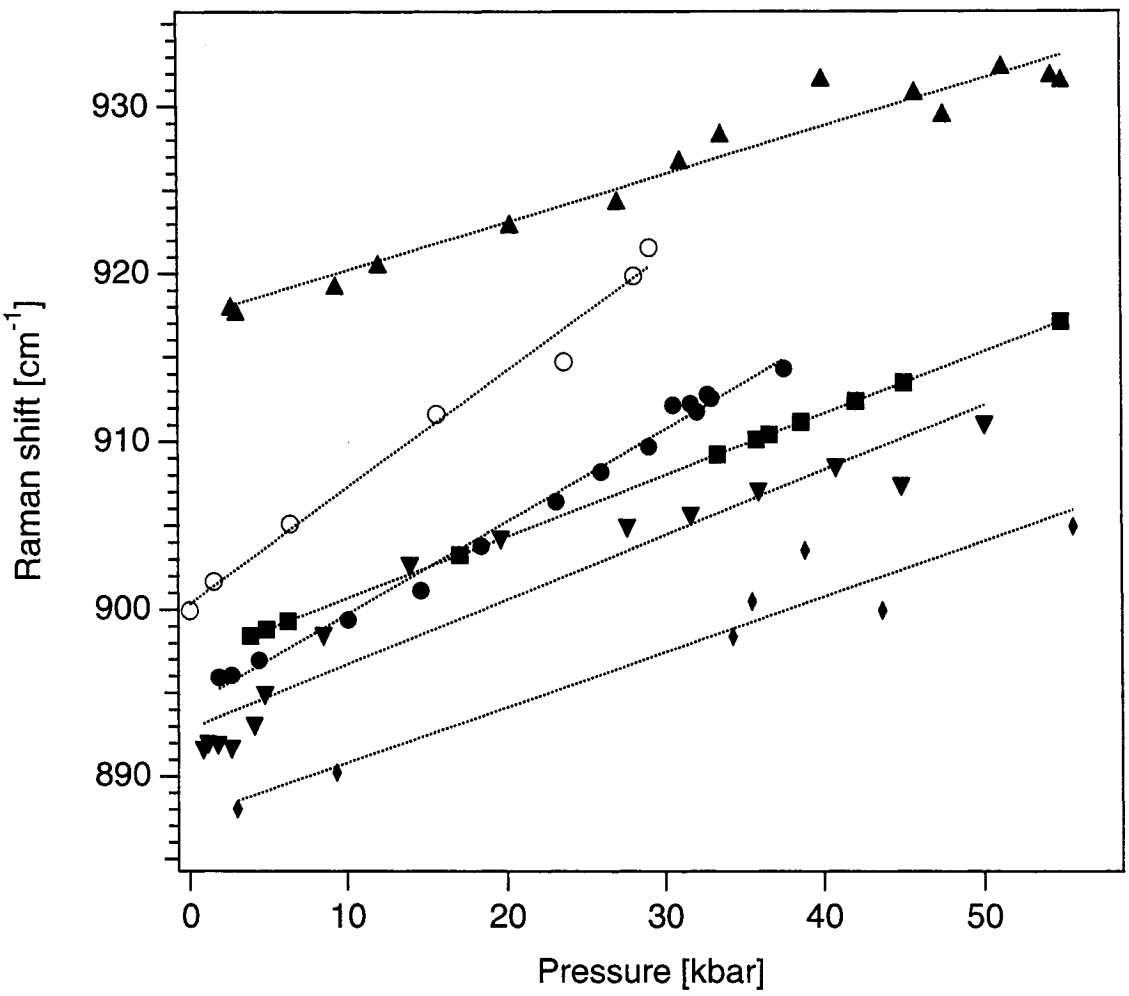

Figure 3.3. Pressure-induced shifts of the O=M=O symmetric stretching frequency of all *trans*-dioxo complexes studied. Symbols for each complex are given as follows: $[OsO_2(en)_2]^{2+}$ (▲), $[ReO_2(en)_2]^+$ (■), $[ReO_2(1\text{-MeIm})_4]^+$ (●), $[ReO_2(1,2\text{-}Me_2Im)_4]^+$ (O),$[OsO_2(mal)_2]^{2+}$ (▼), $[OsO_2(NCS)_4]^+$ (♦).

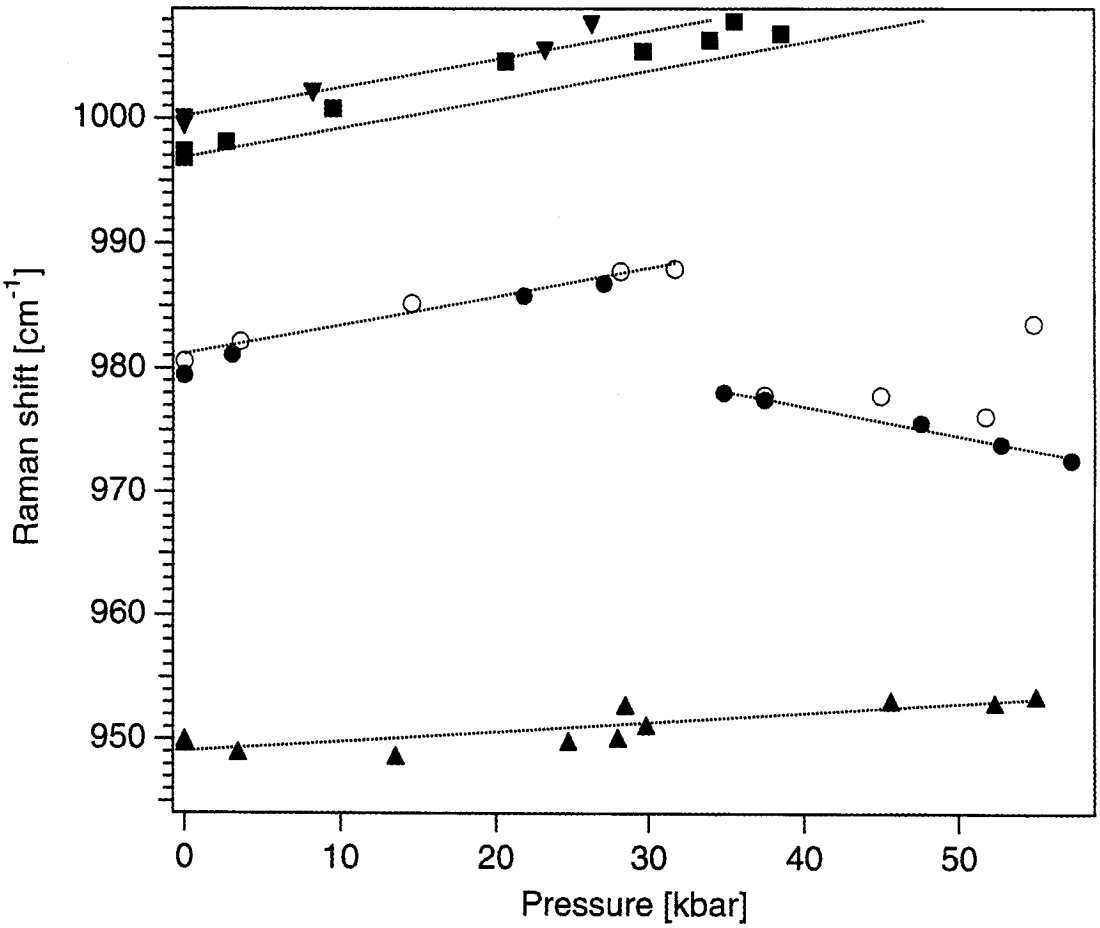

Figure 3.4. Pressure-induced shifts of M≡X; X = O, N, stretching modes. Symbols for each complex are given as follows: [ReN(PPh_3)(O^P)] (▼), [ReO$(Cl)_2$(OEt)(dppe)] (■), [ReO$(Br)_3$(dppe)] (●),[ReO$(Cl)_3$(dppe)] (O), [ReO$(NCS)_5]^+$ (▲).

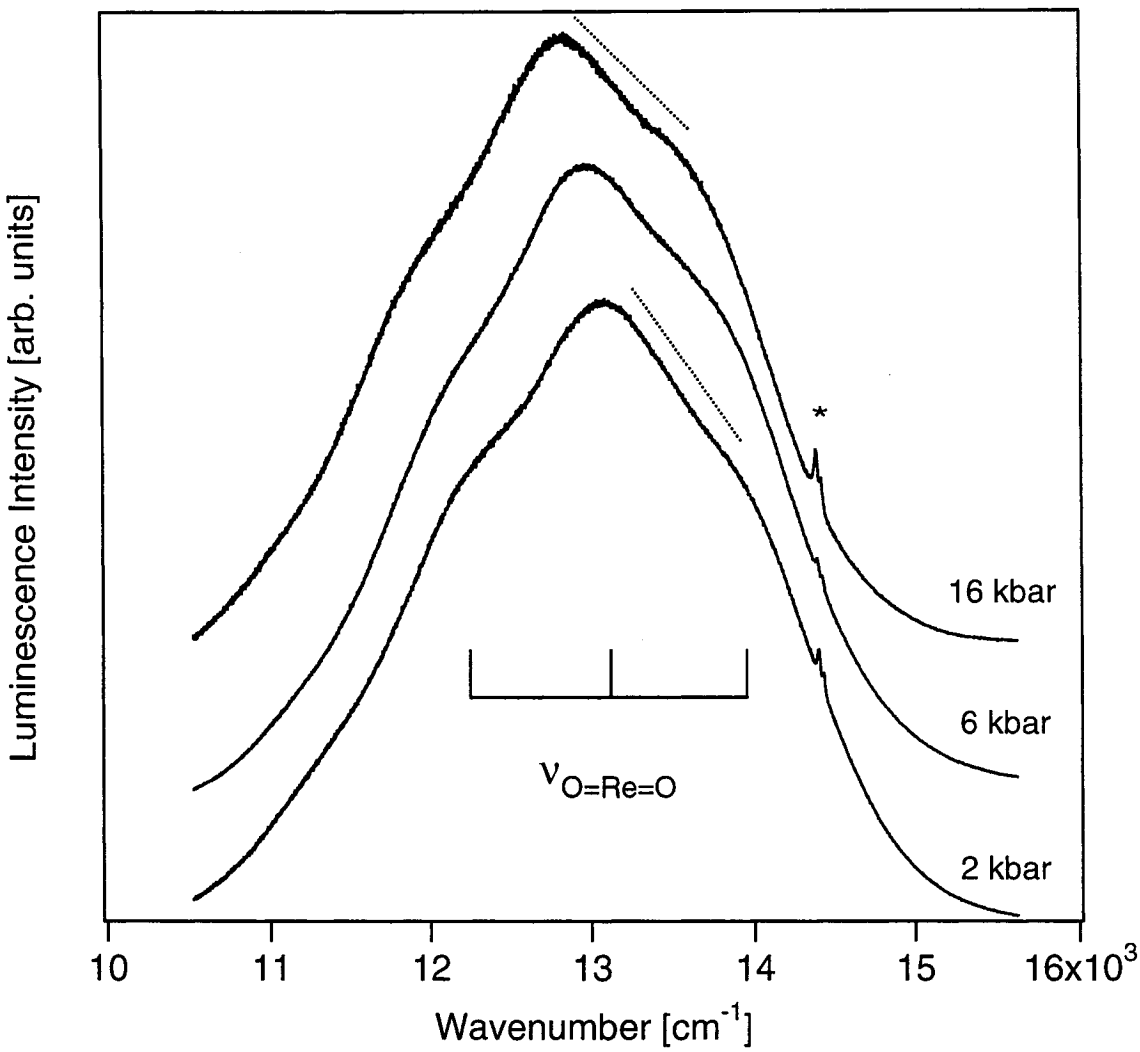

Figure 3.5. Pressure-dependent luminescence of *trans*-$[ReO_2(1,2\text{-}Me_2Im)_4]^+$ showing resolved vibronic structure in the O=Re=O symmetric stretching mode. The hashed lines on the 2 kbar and 16 kbar spectra illustrate the change in relative intensity distribution between first and second members of the progression. * denotes the ruby emission.

3.4 Discussion

The data presented in Figures 3.1-3.5 and Table 3.1 show the effect of pressure on metal-ligand multiple bonds. Within a series of complexes, the pressure dependence of the metal-ligand vibrational frequencies involving multiple bonds can be categorized according to the overall bond order. In general, the metal-oxo frequencies of metal-ligand double bonds show a larger increase of approximately 0.4 cm^{-1}/kbar with pressure than metal-ligand triple bonds, where an average shift of 0.2 cm^{-1}/kbar is observed. Figure 3.3 shows the O=M=O vibrational frequencies as a function of pressure for all rhenium(V) and osmium(VI) *trans*-dioxo complexes studied. Despite the variation of ancillary ligands and metal centers for these complexes, virtually all of the vibrational frequencies show identical increases with pressure. The notable exception to this behavior are the two *trans*-$[ReO_2]^+$ complexes with substituted imidazole ligands where the O=Re=O frequency increases more strongly with pressure for the ligand with two methyl groups on the imidazole ring. This effect is surprising since the ambient pressure frequencies for the two complexes are identical. One possible explanation for this discrepancy is the fact that an extra methyl group causes steric crowding around the nitrogen donor atom and may influence the stretching motions of the O=Re=O mode. Another reason is that the methyl group is an electron-donating substituent group and a larger number of methyl groups on this conjugated ligand will likely result in substantial π-donation to the metal d_{xz},d_{yz} orbitals, an effect that is very small for saturated nitrogen donor ligands such as ethylenediamine. Decreasing the Re-N(Im) bond lengths results in an increase in π-bonding to the metal center that influences the Re-oxo bonds *via* the d_{xz},d_{yz} orbitals.

Luminescence spectra with resolved vibronic structure provide further information on the ground and emitting state potential energy surfaces and their relative displacements along a particular normal coordinate.[8,9] The spectra of $[ReO_2(1,2Me_2\text{-}Im)_4]^+$ in Figure 3.5 show pressure-dependent vibronic structure in the O=Re=O symmetric stretching mode. This pressure dependence has been quantitatively analyzed for *trans*-dioxo complexes with ethylenediamine ligands using models based only on the O=Re=O coordinate,[8,9] showing the influence of the metal-oxo bond on the

luminescence properties of the title complexes. The intensity distribution within the progression shows that the metal-oxo bond length difference between the triplet and singlet states decreases somewhat with pressure, but the triplet state has longer metal-oxo bonds than the singlet ground state at all pressures. The luminescence band maximum of the $[ReO_2(1,2Me_2\text{-}Im)_4]^+$ complex in Figure 3.5 shows a pressure-induced red-shift of 2 cm^{-1}/kbar. In contrast, $[ReO_2(tmen)_2]^+$, which emits in a similar energy range,[8] shows a red-shift larger by a factor of 3. Ref. 9 presents a correlation between the pressure-induced red-shift and the luminescence energy for three *trans*-dioxo complexes with different ethylenediamine ligands. Figure 3.5 shows that the nature of the ancillary ligands also has a significant influence on the red-shift. The π-conjugated imidazole ancillary ligands allow for significant π interaction leading to similar destabilizations for the d_{xy} and d_{xz} , d_{yz} orbitals, and to a smaller red-shift with pressure. Ancillary ligands can therefore be optimized to lead to either very large or very small pressure effects on the singlet-triplet energy difference.

The effect of excited electronic states on ground-state vibrational frequencies is illustrated by the rhenium-oxo complexes in Figures 3.2 and 3.4. These compounds have a lower triplet-singlet energy difference than the *trans*-dioxo complexes.[13] It can be expected that the pressure-induced red-shift of the electronic transition described in the preceding section will bring the ground and emitting states close enough in energy to observe significant changes in the ground state Re≡O vibrational frequency. The ground and several excited states of these systems are coupled and, as pressure brings states closer in energy, avoided crossings lead to a flattened ground state potential surface and therefore a decrease in the Re≡O frequency, in contrast to the usual frequency increase with increasing pressure. This is the most likely reason for the pressure-induced decrease of the Re≡O frequency for two rhenium(V) mono-oxo complexes by almost 10 cm^{-1} starting at 30 kbar and for the continuing monotonic decrease of this frequency at higher pressures. Other metal-ligand and ligand-centered vibrational modes all show smooth, monotonic increases over the same pressure range, which suggests that this behavior is not due to a structural phase transition. The experimental results in Figures 3.2 and 3.4 provide evidence for the onset of a new type of spin-crossover transition involving the

singlet ground state and a spin-orbit level of the lowest energy triplet excited state of a six-coordinate d^2 complex.

References

(1) Winkler, J. R.; Gray, H. B. *J. Am. Chem. Soc.* **1983**, *105*, 1373.

(2) Winkler, J. R.; Gray, H. B. *Inorg. Chem.* **1985**, *24*, 346.

(3) Savoie, C.; Reber, C. *Coord. Chem. Rev.* **1998**, *171*, 387.

(4) Savoie, C.; Reber, C. *J. Am. Chem. Soc.* **2000**, *122*, 844.

(5) Miskowski, V. M.; Gray, H. B.; Hopkins, M. D. In *Adv. in Trans. Met. Coord. Chem.*; Che, C.-M., Yam, V. W.-W., Eds.; JAI Press: Greenwich, CT, 1996; Vol. 1, p 159.

(6) Mayer, J. M. *Inorg. Chem.* **1988**, *27*, 3899.

(7) Savoie, C.; Reber, C.; Bélanger, S.; Beauchamp, A. L. *Inorg. Chem.* **1995**, *34*, 3851.

(8) Grey, J. K.; Triest, M.; Butler, I. S.; Reber, C. *J. Phys. Chem. A* **2001**, *105*, 6269.

(9) Grey, J. K.; Butler, I. S.; Reber, C. *J. Am. Chem. Soc.* **2002**, *124*, 11699.

(10) Piermarini, G. J., Block, S., Barnett, J.D., Forman, R.A. *J. Appl. Phys.* **1975**, *46*, 2774.

(11) Wenger, O. S.; Güdel, H. U. *Chem. Phys. Lett.* **2002**, *354*, 75.

(12) Wenger, O. S.; Valiente, R.; Güdel, H. U. *J. Chem. Phys.* **2001**, *115*, 3819.

(13) Oetliker, U.; Savoie, C.; Stanislas, S.; Reber, C.; Connac, F.; Beauchamp, A. L.; Loiseau, F.; Dartiguenave, M. *Chem. Comm.* **1998**, 657.

Chapter 4

Temperature- and Pressure-Dependent Luminescence Spectroscopy on the *trans*-$[ReO_2(pyridine)_4]^+$ Complex: Analysis of Vibronic Structure, Luminescence Energies, and Bonding Characteristics

This chapter reports temperature and pressure-dependent luminescence spectra of *trans*-$[ReO_2(pyridine)_4]I$ crystals that exhibit resolved vibronic structure providing a detailed view into how molecular structure changes after absorption or emission of a photon. Low temperature spectra reveal long vibronic progressions in the totally symmetric O=Re=O (907 cm^{-1}) and Re-N(pyridine) (212 cm^{-1}) stretching modes, indicating large structural displacements along these normal coordinates. Room temperature spectra are somewhat less-resolved, however, intervals closely matching the O=Re=O frequency (~870 cm^{-1}) persist. The variable pressure spectra exhibit distinct changes in the vibronic patterns and luminescence energies decrease by 16±2 cm^{-1}/kbar. The pressure-dependent spectroscopic changes are modeled using one-dimensional, effective coordinate potential energy surfaces to represent the initial and final electronic states, from which the quantitative normal coordinate offsets can be determined. The pressure dependence of other important spectroscopic parameters are compared with those obtained from other *trans*-dioxo rhenium(V) complexes (Chapters 5 and 6).

4.1 Introduction

Transition metal complexes with metal-oxygen multiple bonds have received much attention for uses in oxygen atom transfer catalysis and as photochemical sensitizers.[1-5] The electronic structures of many second- and third-row metal-oxo complexes have been

* Slight modifications have been made to the original manuscript for clarity and continuity.

well studied both spectroscopically and theoretically since the seminal work of Gray and Winkler.[6,7] We present and analyze temperature- and pressure-dependent luminescence spectra of the *trans*-[ReO_2(pyridine)$_4$]I compound that show well-resolved vibronic structure, even at room temperature, and provide an in-depth view into how the molecular geometry changes in the emitting state. Perhaps the most relevant application of *trans*-dioxo complexes to the results presented in the following is their use as luminescent probes to determine the influence of host-guest interactions in layered materials,[8] where a *trans*-[ReO_2(pyridine)$_4$]$^+$ complex was intercalated into hectorite lattices and changes in the resolved vibronic structure and luminescence energies determined from low temperature luminescence spectra were used to understand the nature of interaction between the host lattice and the guest luminophore. These host-guest interactions represent what has become known as a "chemical pressure" and here we use a *trans*-dioxo rhenium(V) complex to study the effect of external pressure on the resolved luminescence spectrum. Pressure-dependent emitting state normal coordinate offsets, luminescence band maxima energies and energies of the electronic origin transition are determined quantitatively based on a model developed from the low- temperature luminescence spectrum.

The six-coordinate [Xe $5d^2$] *trans*-dioxo class of complexes usually are described in idealized D_{4h} point group symmetry and show well-resolved vibronic structure in their low temperature electronic spectra.[7] Long progressions in high frequency (900-1000 cm^{-1}) metal-oxo stretching modes are often observed, indicating a large structural change along metal-oxo coordinates in the emitting state, and the offset of the ground and emitting state potential energy minima can be determined from the intensity distribution of the resolved vibronic progressions. The high vibrational frequencies of the metal-oxo modes are due to the strength of the formal M=O double bonds. This feature makes such complexes amenable to room temperature spectroscopic studies due to the low thermal population of higher vibrational levels allowing vibronic structure to persist even at relatively high temperatures. By applying high external pressures to single crystals of these systems, it is possible to determine the change in the metal-oxo normal coordinate offset as a function of pressure through the changes in vibronic patterns. We have previously used the resolved structure in a O=Re=O totally symmetric stretching mode to

study the influence of pressure on coupling interactions between the ground- and excited electronic state potential energy surfaces in a series of *trans*-[ReO_2(*N,N,N',N'*-ethylenediamine)$_2$]$^+$ complexes.[9,10] The ethylenediamine ligands effectively "clamp" to the metal center, thus resisting changes in molecular geometry due to changes in intermolecular packing forces with increasing pressure, whereas the pyridine ligands of the title compound are expected to be more susceptible to pressure-induced changes in molecular geometry. Furthermore, the luminescence properties of the title complex show a strong dependence on the environment whereby the luminescence energy and intensity distribution of vibronic progressions change noticeably upon changing counterions. The pressure dependence on the luminescence spectra of both I^- and BF_4^- salts is presented and compared.

The ground and excited state electronic structures of d^2 *trans*-dioxo complexes are well-known and have been parameterized in terms of ligand-field strength and interelectronic repulsion.[11] For these and other six-coordinate tetragonal complexes, the five d-orbitals are split in the following fashion in increasing energy: $d_{xy}(b_{2g})$, d_{xz}, $d_{yz}(e_g)$, $d_{x^2-y^2}$ (b_{1g}), $d_z^2(a_{1g})$. The ground electronic state in the title complex is both spin and orbitally non-degenerate ($^1A_{1g}$) in D_{4h} symmetry due to the pairing of the two d electrons in the d_{xy} orbital (HOMO). The energy of this state depends on the two-electron parameter, K_{xy}, which is defined as $3B$+C where B and C are the Racah parameters describing interelectronic repulsion. Promotion of one electron to the e_g orbitals (LUMO) leads to both ^1E_g and ^3E_g excited states separated by $2K_{xy}$ with the triplet state at lower energy. Due to strong spin-orbit coupling effects intrinsic to third-row transition metal atoms, the ^3E_g state is split into several components and luminescence occurs from the lowest energy spin-orbit components. The energy of the LUMO depends on the difference in π overlap between the oxo and ancillary ligands to the metal d orbitals, which is defined by the ligand-field parameter, Δ_π. In *trans*-dioxo complexes with anisotropic π-donating ligands, such as the pyridine ligands in the title compound, Δ_π is represented as $2e_\pi(O)+2e_{\pi||}(\text{ligand})-4e_{\pi\perp}(\text{ligand})$ where e_π is the angular-overlap parameter describing π overlap between the metal e_g and b_{2g} orbitals with ligand orbitals of π-symmetry that accounts for contributions both parallel and perpendicular to the ML_4 equatorial plane.[11] The pyridine ligands are oriented perpendicular to the equatorial plane

where the lone, unhybridized p-orbital on the nitrogen atom has the maximum π interaction with the metal center, causing $e_{\pi||} \approx 0$ and Δ_π then becomes $2e_\pi(O)$-$4e_{\pi\perp}$(ligand).[11] Because the energy difference between the ground and emitting states depends on both ligand-field effects arising from metal-ligand bond lengths and interelectronic repulsion parameters, one of the goals of this work is to rationalize the pressure-dependent change in luminescence energies in terms of K_{xy} and Δ_π and compare to previous studies of *trans*-dioxo complexes.

We calculate the well-resolved 5 K luminescence spectrum of the title complex using harmonic potential energy surfaces with the ground- and emitting states displaced along the O=Re=O and Re-N(pyridine) symmetric stretching modes. The two-dimensional model can then be adapted to calculate room temperature pressure-dependent luminescence spectra using potential energy surfaces displaced along a single effective coordinate with predominant O=Re=O stretching character. The pressure-induced changes of the most important parameters are compared to those reported for complexes with less π-bonding characteristics.[9,10,12] The title complex demonstrates the quantitative transferability of parameters obtained from low-temperature spectra to less resolved room temperature spectra.

4.2 Experimental

trans-$[ReO_2(py)_4]I$ and *trans*-$[ReO_2(py)_4]BF_4$ were synthesized following literature methods[13] and all starting materials were used as received. Luminescence and Raman spectra were recorded as a function of temperature and pressure on a microscope spectrometer described previously.[9,10] Crystalline samples were placed in a liquid helium cryostat (Janis ST 500) and temperature was controlled between 300 and 5 K. Variable pressure experiments were carried out by placing samples in a gasketed diamond-anvil cell (DAC). All spectra were unpolarized and corrected for spectrometer response. Absorption measurements were performed on a Varian CARY 5E spectrometer. For the absorption spectra, the *trans*-$[ReO_2(py)_4]I$ compound was dissolved in water and the solution was allowed to evaporate slowly on quartz plates, which produced a thin layer of microcrystals on the surface.

4.3 Spectroscopic Results

4.3.1 Variable temperature luminescence spectroscopy

Fig. 4.1 shows the luminescence spectra of *trans*-$[ReO_2(py)_4]I$ at 5 K (bottom panel), 100 K (middle panel), and 300 K (top panel). All spectra measured over the indicated temperature range show resolved vibronic structure in the high-frequency O=Re=O totally symmetric stretching mode, with an average progression interval of 905 cm^{-1}. This mode is observed in the 300 K Raman spectrum at 907 cm^{-1}. At temperatures lower than 150 K, progressions in the lower frequency (211 cm^{-1}) Re-N(pyridine) totally symmetric stretching mode are visible on the lower energy side of the main (O=Re=O) progression. In the 5 K spectrum shown in Fig. 4.1, up to seven quanta of the O=Re=O mode can be observed, indicating a large change in emitting-state rhenium-oxo bond length compared to the ground state equilibrium configuration. At 300 K the vibronic structure in the luminescence spectrum becomes less resolved and the observed high frequency progression interval decreases to an average 870 cm^{-1}.

The highest energy discernible maximum of the 5 K spectrum appears at approximately 17200 cm^{-1} and overlaps with the lowest energy absorption onset, shown in Fig. 4.2. The luminescence spectrum consists of two bands, the first, labeled **A** in Fig. 4.1, originates from the highest energy peak and the more intense band, labeled **B** in Fig. 4.1, begins at 314 cm^{-1} lower in energy. The beginning of each cluster of lower frequency Re-N(py) progressions are indicated by tick marks for both bands **A** and **B** for the 5 K spectrum in Fig. 4.1 and the clusters of vibronic transitions are exact replicas, i.e., they have the same relative intensity distributions across the entire luminescence spectrum. All energy positions of individual vibronic peaks and frequency intervals are listed in Table 4.1 for the dominant vibronic band, **B**. It is also interesting to note the decrease in the O=Re=O frequency toward the lower energy side of the spectrum by approximately 4 cm^{-1} for each subsequent quantum of the O=Re=O mode, which becomes 25 cm^{-1} lower at the highest quantum of this mode. Comparison with the 5 K luminescence spectrum of the tetraphenylborate $(BPh_4)^-$ salt of this complex reveals a similar trend where this interval decreased by 10 cm^{-1} between the second and third quanta followed by an anomalous large increase between the third and fourth quanta by 30 cm^{-1}.[7] This apparent anharmonicity was also observed in theoretical calculations on

the *trans*-$[ReO_2(ethylenediamine)_2]^+$ complex where it was revealed that the ground electronic state potential energy surface was anharmonic along the O=Re=O coordinate.[14]

Fig. 4.2 shows the effect of temperature on the intensity distribution between the two bands, **A** and **B**. As temperature increases, the intensity of band system **A** increases whereas band system **B** shows a slight decrease. The higher energy bands (**A**) of the BPh_4^- salt also demonstrate similar temperature-dependent characteristics as those observed in Fig. 2 and were assigned as transitions from a second luminescent state slightly higher in energy.[7] This assignment was consistent with temperature-dependent luminescence lifetimes where the higher energy state becomes thermally populated at higher temperatures and leads to a decrease in the lifetime from 68 μs (5 to 70 K) to 32 μs at room temperature.[7] The temperature-dependent features in Fig. 4.2 are in agreement with this assignment, further supported by the different band widths for transitions labeled as **A** and **B**, indicating transitions originating from different components of the ^3E_g excited state.

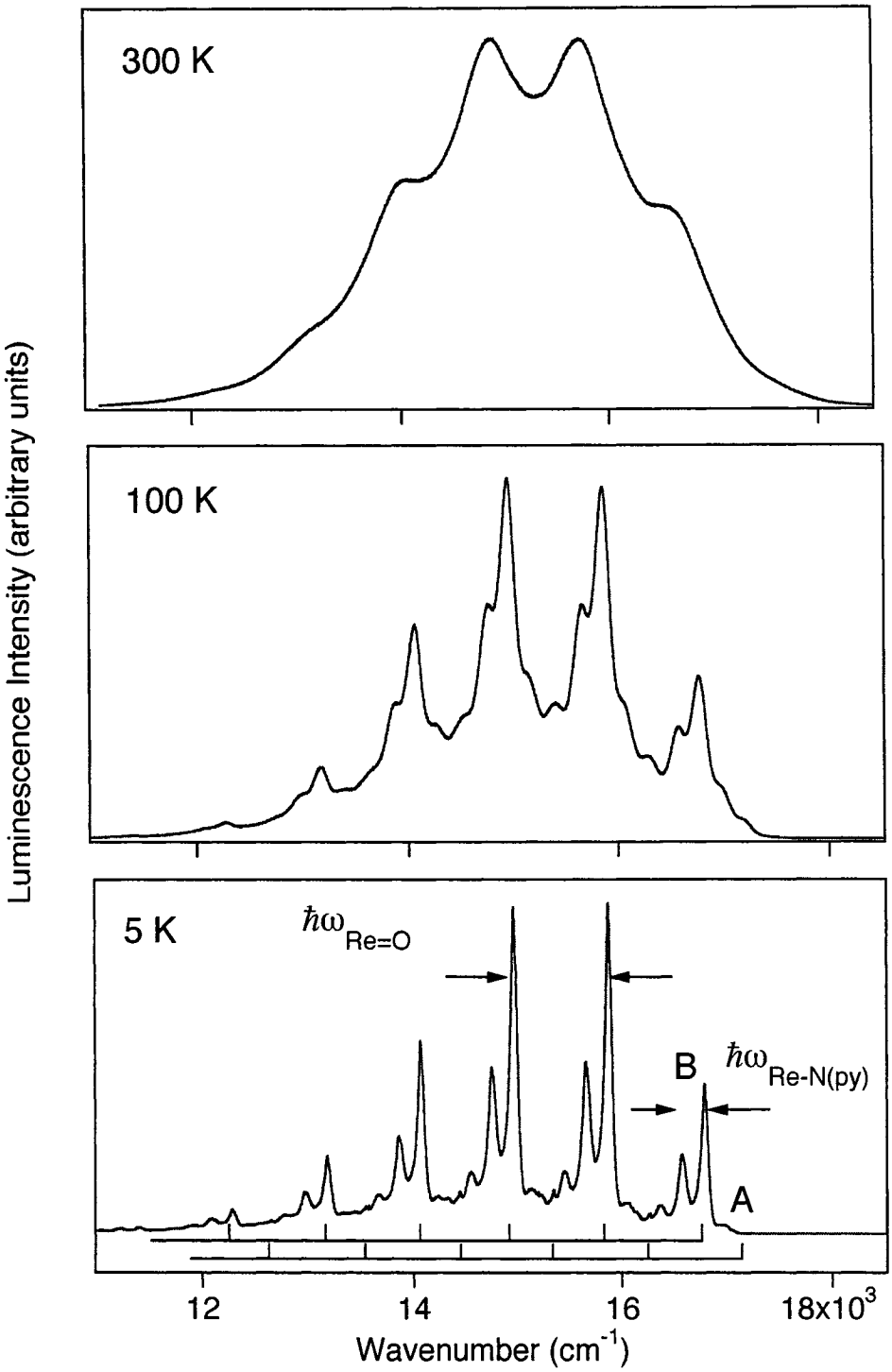

Figure 4.1. Luminescence spectra of single-crystals of *trans*-[ReO_2(pyridine)$_4$]I at three temperatures: 300 K (top panel), 100 K (middle panel) and 5 K (bottom panel). Frequency intervals of the two resolved progressions are indicated by arrows. The tick marks below the 5 K spectrum mark the beginning of clusters for the two bands, labeled **A** and **B**, that comprise the total spectrum.

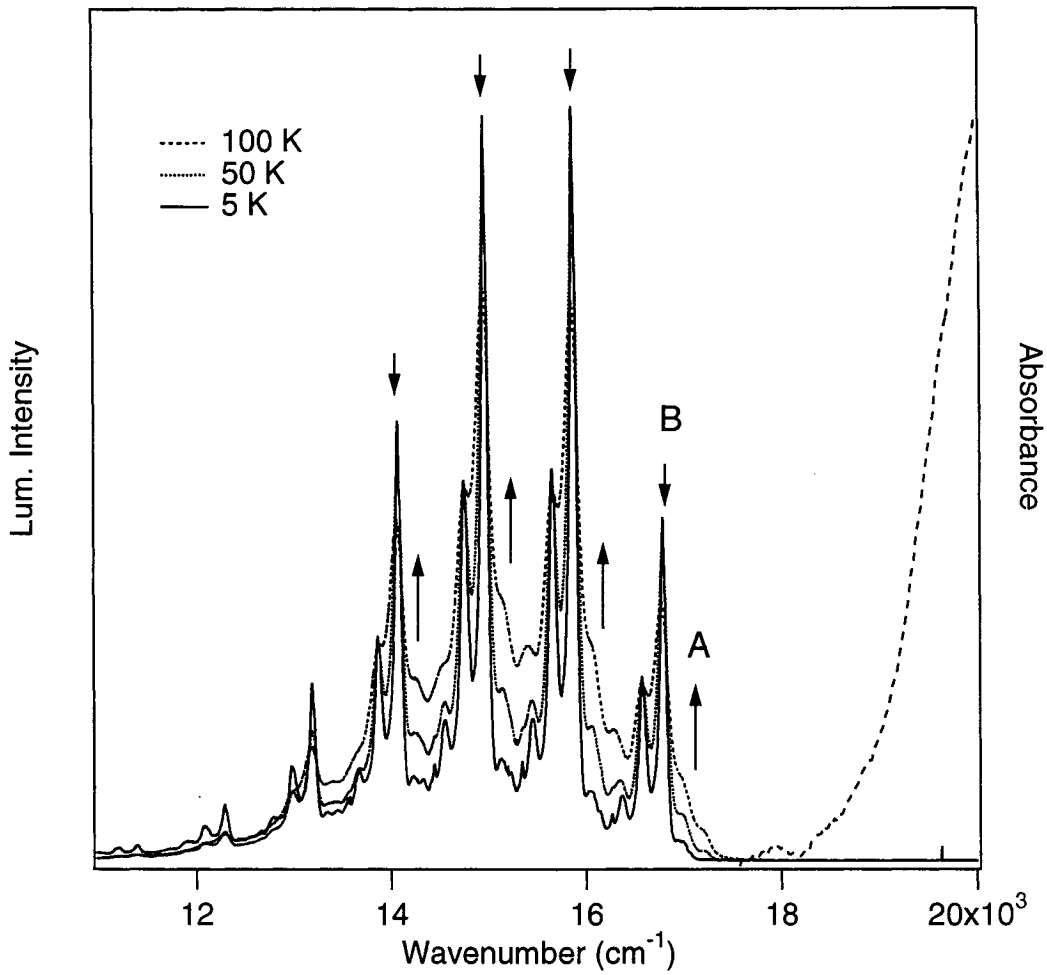

Figure 4.2. Temperature-dependent luminescence spectra of *trans*-[ReO_2(pyridine)$_4$]I. Upward arows show the increase of intensity for band system **A** and downward arrows show the decrease of intensity of intensity for band system **B** with increasing temperature. The 300 K absorption spectrum from microcrystals of the title compound is indicated as a hatched line on the right hand side.

Peak energy (cm^{-1})[a]	Energy intervals (cm^{-1})	
	Re-N[b]	
16784		**O=Re=O**[c]
16573	211	
16364	209	
15877		907
15666	211	
15460	206	
14972		905
14764	208	
14561	203	
14073		899
13866	207	
13668	198	
13178		895
12974	204	
12783	191	
12286		892
12091	195	
11911	180	
11400		886
11211	189	
11028	183	

[a] ±3 cm^{-1}. [b] Raman: 211 cm^{-1} (300 K). [c] Raman: 905 cm^{-1} (300 K)

Table 4.1. Vibronic energy spacings in the 5 K luminescence spectrum of *trans*-$[ReO_2(py)_4]I$.

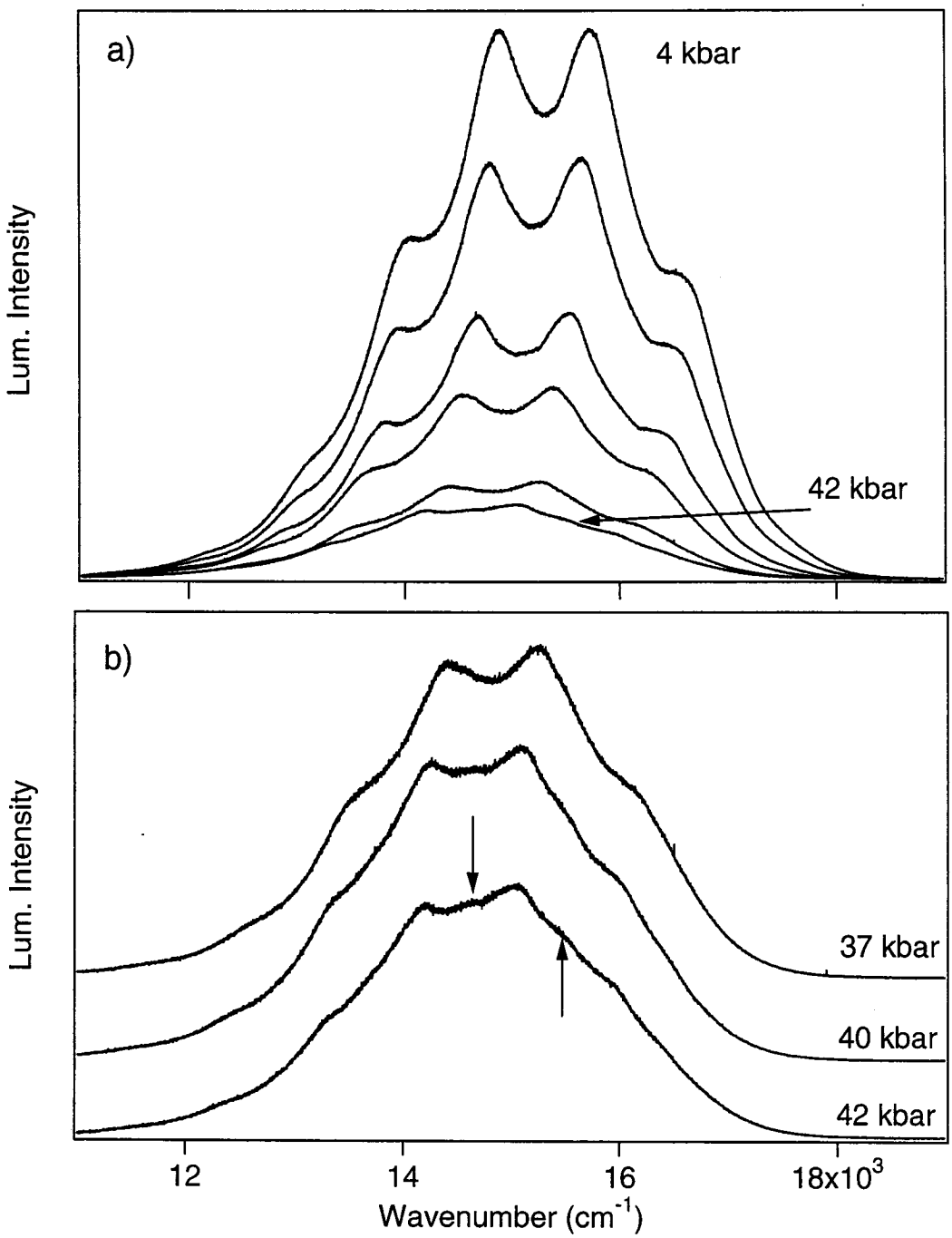

Figure 4.3. Selected pressure-dependent single-crystal luminescence spectra of *trans*-$[ReO_2(pyridine)_4]I$ recorded at room temperature (ca. 300 K). Individual pressures are in descending order: 4 kbar (top trace), 13 kbar, 21 kbar, 29 kbar, 37 kbar and 42 kbar (bottom trace). b) High pressure luminescence spectra with additional features indicated by arrows.

4.3.2 Variable pressure luminescence spectroscopy

Fig. 4.3 shows the effect of pressure on the luminescence spectrum of the title complex. The dominant progression interval in the room temperature spectra is 870 cm^{-1}, almost 40 cm^{-1} less than the observed O=Re=O vibrational frequency in the Raman spectrum. As pressure increases, the luminescence intensities show steady decreases, an effect that is often observed and most likely due to efficient energy transfer to deep traps at high pressure. In addition, the intensity distribution within the resolved progression change with increasing pressure, which can be observed by comparing the second and third members of the 4 kbar spectrum in Fig. 4.3a and the 42 kbar spectrum in Fig. 4.3b. The energy of the luminescence band maximum (E_{max}) shows a visible decrease with increasing pressure that can be seen qualitatively by following a particular vibronic peak. Luminescence spectra at the highest working pressures (37 to 42 kbar) also reveal additional features not observed in the lower pressure spectra and indicated in Fig. 4.3b by arrows. Pressure-dependent Raman spectra of the title compound show smooth shifts of the O=Re=O stretching mode to higher frequencies by 0.53 cm^{-1}/kbar. This value is similar to the pressure-induced shifts determined for various *trans*-dioxo rhenium(V) complexes with substituted imidazole ligands, which range from 0.55 to 0.69 cm^{-1}/kbar, and larger than those found in complexes with ethylenediamine ligands (0.37 to 0.42 cm^{-1}/kbar).[12]

4.4 Discussion

The title complex has exact D_{4h} point group symmetry for the *trans*-ReO_2N_4 fragment and we use the labels from this symmetry group to describe the electronic states and relevant vibrational modes. The removal of electron density in the x,y plane to the π^* LUMO orbital results in large changes in metal-ligand bond lengths along the Re-N(py) and O=Re=O coordinates, therefore these modes are expected to have the largest displacements between ground- and emitting state potential minima. Only one emitting state is considered in the model for both temperature- and pressure-dependent luminescence spectra where the most intense luminescence band (**B**) is analyzed.

4.4.1 Analysis of the temperature-dependent vibronic structure

The detailed spectroscopic features shown in Figs. 4.1 and 4.2 provide a means to analyze the rich vibronic structure and characterize the ground and emitting state potential energy surfaces. We use two-dimensional harmonic potential surfaces with the ground and emitting states displaced along the totally symmetric O=Re=O and Re-N(pyridine) stretching modes. The luminescence spectrum is calculated using the time-dependent theory of luminescence spectroscopy, an approach which has been described in detail before.[15-17] Briefly, a wavepacket is created on the final potential energy surface (ground state) upon emission of a photon from a molecule in the emitting state at t = 0. The shape of the luminescence spectrum is given by eq. 4.1,

$$I_{lum}(\omega) = C\omega^3 \int_{-\infty}^{+\infty} e^{i\omega t} \langle \phi | \phi(t) \rangle dt \qquad \text{eq. 4.1}$$

where $I_{lum}(\omega)$ is the luminescence intensity at the frequency ω, C is a constant scaling factor, and $\langle \phi | \phi(t) \rangle$ is the autocorrelation function. Its absolute value can be visualized as the overlap of the initial wavepacket, $\phi = \phi(t = 0)$, with the time-dependent wavepacket , $\phi(t)$. The autocorrelation is calculated from a closed-form analytical equation obtained by making several assumptions: (a) the vibrational frequencies, ω, in the ground and excited states are identical and both states are represented by harmonic potential energy surfaces, (b) there is no mixing of normal coordinates, and (c) the transition dipole moment is constant. The autocorrelation for the *k*th mode is then given by eq. 4.2,

$$\langle \phi_k | \phi_k(t) \rangle = \exp\left[-\frac{\Delta_k^2}{2}\left(1 - \exp(-i\omega_k t)\right) - \frac{i\omega_k t}{2} \right] \qquad \text{eq. 4.2}$$

for harmonic ground and emitting state potential energy surfaces with minima displaced by Δ_k in dimensionless units.[18] For multiple displaced modes, the total autocorrelation is the product of autocorrelations for each individual mode,

$$\langle \phi | \phi(t) \rangle = \prod_k \langle \phi_k | \phi_k(t) \rangle \exp\left(\frac{-iE_{00}t}{\hbar} - \Gamma^2 t^2 \right) \qquad \text{eq. 4.3}$$

where E_{00} is the energy of the electronic origin and Γ is a Gaussian damping factor that determines the width of individual vibronic transitions, both in cm^{-1} units. After calculating the total overlap, the result is Fourier transformed (eq. 4.1) to give the spectrum. The uncoupled coordinates for the ground state are a good assumption because clusters of vibronic transitions observed across the entire luminescence band are "replicas" of each other. This feature arises from Lissajous motion of the wave packet along the two displaced normal coordinates, as was superbly illustrated by Herzberg for two orthogonal harmonic oscillators with different force constants, k_x and k_y, leading to a complicated pattern resulting from the superposition of the individual motions.[19,20] The appearance of replicas in the vibronic structure of electronic spectra is due to these uncoupled individual motions, justifying the use harmonic potential energy surfaces and eq. 4.3 to describe the wave packet motion on the final (ground) state potential energy surface. Two other salts of the *trans*-$[ReO_2(py)_4]^+$ complex also show such replicas[7], however, the I^- salt studied here shows the best resolution of vibronic structure where there are two distinct progression-forming modes and details of the vibronic patterns can be carefully scrutinized.

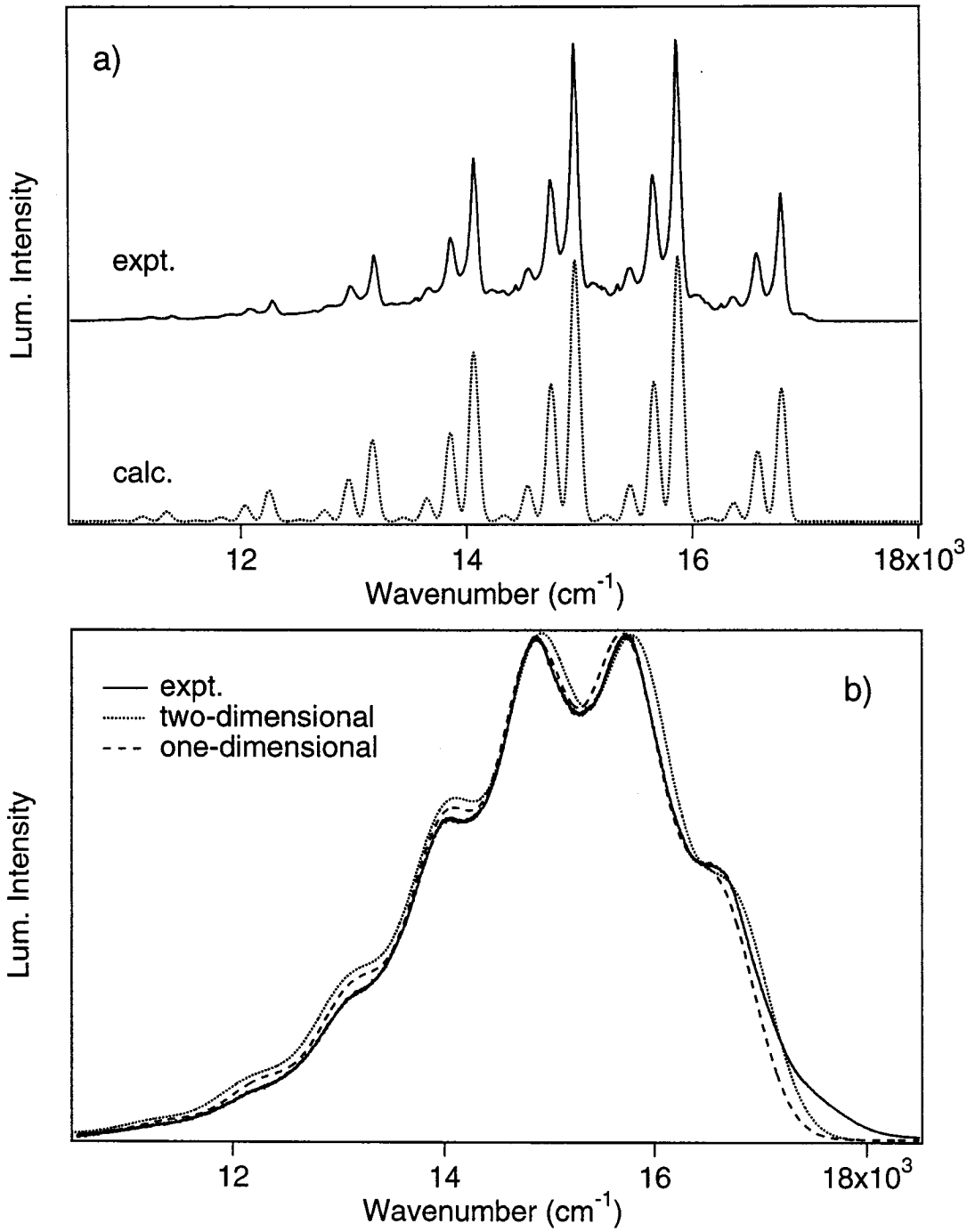

Figure 4.4. a) Experimental (solid trace) and calculated (dotted trace) of the 5 K luminescence spectrum shown in the bottom panel of Fig. 4.1 using two-dimensional harmonic potential energy surfaces and parameters from Table 4.2. b) Comparison of the 300 K luminescence spectrum with the broadened two-dimensional calculated spectrum (dotted trace) and best-fit one-dimensional effective mode model (dashed trace).

Fig. 4.4a compares the experimental luminescence spectrum at 5 K to the spectrum calculated with eq. 4.1. The energy, E_{00}, of the origin transition for the calculation was set to the first resolved peak in progression **B** at 16786 cm^{-1}. All parameters used in this calculation are collected in Table 4.2. Literature values for the emitting-state bond length changes for individual Re=O and Re-N(py) bonds were found to be 0.07 and 0.03 Å, respectively, for the BPh_4^- salt.[7] The offset along the Re-N coordinate is negative due to the removal of electron density from the x,y plane thus decreasing these bonds and resulting in a negative emitting state offset along this coordinate.(21) In this model, only the absolute values can be determined since harmonic potential energy surfaces are used. From the calculated 5 K luminescence spectra, we determine values of 0.074 and 0.022 Å for the Re=O and Re-N(pyridine) bond length changes based on the normal coordinate offsets in Table 4.2,[21] values similar to those calculated for the BPh_4^- salt indicating that different counterions do not lead to large changes in emitting state distortions along the same normal coordinates. For other *trans*-$[ReO_2]^+$ complexes with aromatic nitrogen-donor ligands, such as substituted imidazoles, the emitting state distortions along the Re=O bond lengths are in a similar range to those given above, between 0.07 and 0.09 Å whereas some Re-N(ligand) distortions are much larger.[22,23]

parameter	5 K	300 K
E_{00}	16786	16570
$\hbar\omega_{O=Re=O}$ (cm^{-1})	907	870
$\hbar\omega_{Re=N}$ (cm^{-1})	212	
$\Delta Q_{O=Re=O}$ (Å)	0.105	0.106
ΔQ_{Re-N} (Å)	0.045	
Γ (cm^{-1})	30	250

Table 4.2. Parameter values used to calculate the spectra in Figure 4.4.

Previous luminescence measurements and analyses of near-infrared emitting *trans*-$[ReO_2]^+$ complexes revealed coupling between normal coordinates in the ground electronic state based on the non-replica clusters of vibronic bands.[23,24] The coupling is induced by avoided crossings between the ground and excited states of the same symmetry.[14] This effect is also mediated by the magnitude of the normal coordinate offset for each displaced vibrational mode. In lower energy emitting systems with large emitting state normal coordinate displacements the coupling effect is much stronger and leads to noticeably anharmonic luminescence bandshapes. However, the title complex luminesces at higher energy and the emitting state distortion along the Re-N(py) stretching mode is much less than in other *trans*–dioxo rhenium(V) complexes, thus making the coupling effect comparatively smaller since the avoided crossings between same-symmetry states occur farther away from the Franck-Condon region of the luminescence transition. These trends explain why there is no spectroscopic manifestation of coupling interactions between the ground and excited states in the title complex, which further justifies the use of harmonic potential energy surfaces with uncoupled coordinates to describe the ground electronic state.

Luminescence spectra of *trans*-dioxo complexes of rhenium(V) with substituted ethylenediamine ligands measured at room temperature display partially resolved vibronic structure in the O=Re=O totally symmetric stretching mode.[10] Analyses of these bandshapes were achieved with one-dimensional potential surfaces due to the lack of resolution in the lower frequency Re-ligand modes at higher temperatures. Fig. 4.4b shows the 300 K spectrum with a calculated spectrum using the same parameter values in Table 4.2 for the 5 K spectrum (Figure 4.4a, bottom trace), but with the damping factor, Γ, increased to 250 cm^{-1}. The agreement is very good between the experimental spectrum at 300 K and the broadened two-dimensional calculated spectrum, however, for the pressure-dependent spectra measured at 300 K, the lack of resolved structure in the Re-N(py) lower frequency mode forbids the use of a two-dimensional model to determine changes in emitting state offsets.

The room temperature spectra can also be calculated with a model based on effective one-dimensional potential energy surfaces, which is necessary to extract the

normal coordinate offsets as a function of pressure. In order to fit the 300 K spectrum with the one-dimensional model, a lower vibrational frequency of 870 cm^{-1}, a value close to the O=Re=O frequency of 907 cm^{-1}, but not observed in the ground state Raman spectrum of the title compound is used. Fig. 4.4b shows the best-fit two-dimensional calculated spectrum (5 K) broadened to achieve the same resolution as the spectrum measured at 300 K compared to the best-fit calculated spectrum obtained from the one-dimensional effective coordinate model. The agreement between calculated spectra from these two models is very good and the values for the $\Delta Q_{O=Re=O}$ parameter do not vary significantly, indicating that the O=Re=O mode is the dominant contribution to the effective coordinate and confirming that the offsets ΔQ obtained from the one-dimensional model can be reliably interpreted as Re=O bond length changes. We use the effective coordinate model to determine pressure-induced changes in 300 K luminescence spectra.

4.4.2 Effect of pressure on the luminescence spectrum at room temperature

The majority of previous pressure-dependent spectroscopic studies involving transition metal complexes have focused largely on octahedral systems where the pressure-induced decrease in metal-ligand bond lengths leads to increases in $10Dq$.[25-28] Because changes in both π- (t_{2g}) and σ-bonding (e_g) contribute to this ligand-field parameter and spectra are usually devoid of resolved vibronic structure, analyses are usually restricted to qualitative energy level diagrams whereby states (orbitals) shift in energy relative to one another. In the idealized D_{4h} point group symmetry of the title complex, the t_{2g} level splits into the b_{2g} (HOMO) and e_g (LUMO) levels and we only consider this orbital energy difference that depends on Δ_π. The energy difference between the $^1A_{1g}$ ground state and the ^3E_g emitting state is then $\Delta_\pi - 3K_{xy}$. As an external pressure is applied to the title compound, the energy of the luminescence transition will change according to the variation of both parameters. It has been found in pressure-dependent spectroscopic studies involving doped transition metal ions (i.e. Cr^{3+} in ruby) and molecular coordination compounds that the Racah parameters decrease with increasing pressure resulting in an increase of covalency.[25-29] In the title compound, this expected decrease of K_{xy} leads to a blue-shift of the spectrum if the value of Δ_π does not

change appreciably. However, the experimental pressure-dependent spectra shown in Fig. 4.3 reveal a substantial red-shift with increasing pressure, which implies a strong decrease of Δ_π with pressure. The dominance of this parameter is apparent in its definition where the π contribution from the pyridine ligand, $e_{\pi\perp}$, has a large influence on Δ_π. Because it is easier to compress metal-ligand single bonds (Re-N) than double bonds (Re=O), an increasing pressure corresponds to a large increase of $e_{\pi\perp}$ but only a small increase of e_π(O), leading to a large decrease of Δ_π if no changes in the orientation of the pyridine ligands occur. This significant decrease of Δ_π as a function of pressure is a manifestation of strong π bonding between the metal center and ancillary ligands. This is confirmed by a comparison with systems having similar luminescence energies as the title compound, but smaller π interactions from the ancillary ligands, such as *trans*-[ReO_2(*N,N,N′,N′*-tetramethylethylenediamine)$_2$]Cl.[10] In this compound, the luminescence band maximum shows a much smaller pressure-dependent red-shift that indicates a smaller variation of Δ_π in complexes with ancillary ligands that do not form strong metal-ligand π bonds.

In the pressure-dependent luminescence spectra reported in Fig. 4.3, the partially resolved vibronic structure provides an opportunity to study the effect of pressure on the Re=O bond length differences from the changes in vibronic patterns and energies of the luminescence origin and band maximum. These important spectroscopic parameters are extracted by fitting a calculated spectrum to the experimental spectrum at each measured pressure using the effective coordinate one-dimensional harmonic potential energy surface model described in the previous section. The energy of the electronic origin transition at each pressure was assumed to be the first resolved shoulder observed in the luminescence bands. This assumption is necessary due to thermal broadening of the vibronic bands and, at ambient pressure, leads to an energy that is lower than the 5 K value by approximately 200 cm^{-1}. Fig. 4.5 shows the comparison between calculated and experimental spectra at selected pressures.

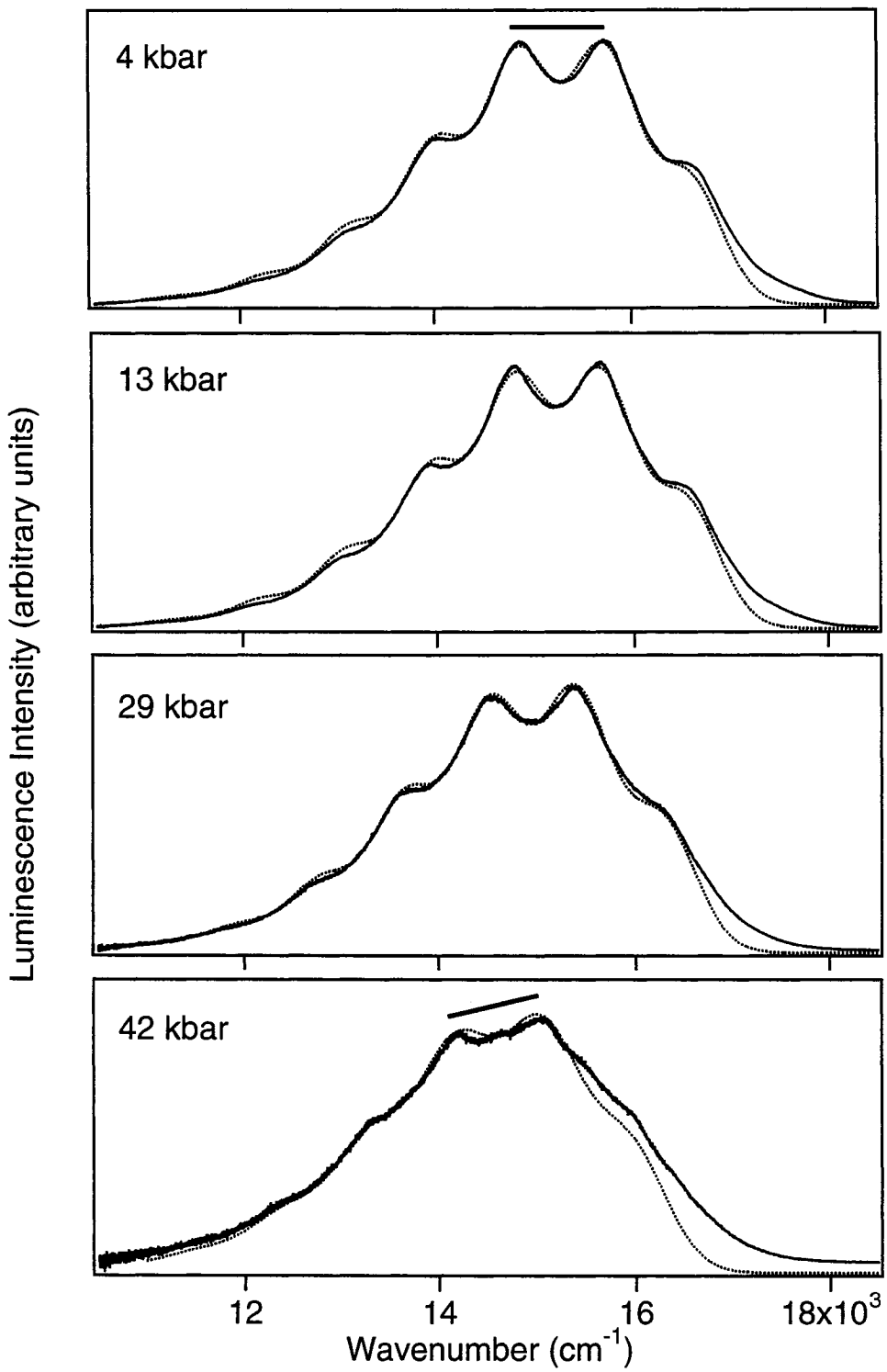

Figure 4.5. Selected pressure-dependent luminescence spectra with the calculated spectra shown as dotted traces calculated using parameter values from Table 4.3. The slanted lines shown in the top and bottom panels are included as a guide for the eye to illustrate the change in intensity distribution for the resolved vibronic progression.

The agreement between the calculated spectra and the pressure-dependent luminescence bands is excellent and the parameters used to calculate the spectra are summarized in Table 4.3. At the highest pressures, starting from 37 kbar (Fig. 4.3b) there is additional intensity to the blue side of the first vibronic transition. This feature closely corresponds to the position of the less intense band system, **A**, observed in the temperature-dependent luminescence spectra. This band could gain intensity if the two emitting states have different pressure dependence, thus leading to an increased population of **A** at the expense of **B**. Another possibility for the appearance of this feature arises from a pressure-induced increase of inhomogeneity throughout the lattice, creating a luminophore slightly different in structure than that found in ambient pressure spectra. Because the pyridine ligands are oriented perpendicular to the ML_4 plane, a pressure-induced change in crystal packing forces could favor a structure where the pyridine ligand twists around the Re-N single bond axes. This change in orientation of the pyridine ligand would then alter its contribution to Δ_π and the magnitude of red-shift would be expected to decrease at higher pressures. We cannot rule out any of these possibilities in rationalizing the pressure-dependent luminescence properties of the title compound based on the spectra in Fig. 4.3.

P (kbar)	E_{00} (cm^{-1})	$\hbar\omega_{O=Re=O}$ (cm^{-1})	$\Delta Q_{O=Re=O}$ (Å)	Γ (cm^{-1})	E_{max} (cm^{-1})
4	16570	865	0.1063	245	15299
13	16505	865	0.1062	245	15243
21	16380	870	0.1061	245	15121
29	16245	870	0.1053	250	15008
37	16145	870	0.1050	260	14911
40	15955	870	0.1049	260	14736
42	15885	870	0.1035	275	14706

Table 4.3. Parameter values used to calculate the pressure-dependent luminescence spectra in Figure 4.5.

In typical pressure-dependent studies, the energy of the band maximum is the only spectroscopic parameter reported quantitatively. Because most pressure-dependent electronic spectra of transition metal complexes are devoid of any resolved vibronic structure, the unresolved bands (absorption or luminescence) are fitted with Gaussian functions from which the energy of the band maxima can be determined and qualitative energy level diagrams can be used to rationalize pressure-induced shifts in energy. In contrast, our spectra with resolved vibronic structure allow us to determine not only the shift of the band maximum, but also the pressure-induced shift of the normal coordinate offset, $\Delta Q_{O=Re=O}$, and the energy of the electronic origin, E_{00}, quantities obtained from the fit of calculated spectra to the experimental results. The quantitative calculated spectra in Fig. 4.5 can be phenomenologically broadened (by increasing Γ) to give an unresolved band whose overall maximum, E_{max}, is easily determined. This procedure is necessary due to the fact that individual vibronic maxima are not suitable to describe how the overall band maximum changes with pressure. Fig. 4.6 shows the effect of pressure on the parameters used in the calculation of the room-temperature, pressure-dependent luminescence spectra.

Fig. 4.6a demonstrates that the energies of the electronic origin, E_{00}, and the energies of the luminescence band maxima, E_{max}, have very similar pressure-dependent behavior, which justifies the choice of harmonic potential energy surfaces to describe the ground electronic state and our rationalization in the changes in luminescence energies in terms of purely electronic parameters, Δ_π and K_{xy}. This is in contrast to the trends observed in the substituted ethylenediamine complexes, where E_{00} and E_{max} have a markedly different response to increasing pressure due to avoided crossings between the ground state and excited states of the same symmetry.[10]

Fig. 4.6b illustrates the effect of pressure on the normal coordinate offset, $\Delta Q_{O=Re=O}$, determined from the one-dimensional calculated spectra. All normal coordinate offsets decrease as a function of pressure due to the reduced sample volume, however the extent to which they vary depends on the influence of intermolecular packing forces on the intramolecular properties, such as metal-ligand bond lengths and angles. The pressure-induced decrease of $\Delta Q_{O=Re=O}$ was found to be -6×10^{-5} Å/kbar, much smaller than

determined for substituted ethylenediamine complexes of rhenium(V) where this decrease is on the order of -1×10^{-4} Å/kbar.[10] This previous study showed that as luminescence energies increase, bandshapes become more harmonic and the decrease of $\Delta Q_{O=Re=O}$ became smaller, and the title complex confirms this trend.

In contrast, the pressure-induced red-shift of the luminescence band maximum is much larger, 16±2 cm^{-1}/kbar, than determined for *trans*-dioxo rhenium(V) complexes with substituted ethylenediamine ligands, with red-shifts of less than 10 cm^{-1}/kbar.[10] We attribute this large red-shift to the ancillary pyridine ligands that form strong π bonds with the metal center, illustrating that both interactions between electronic states and the detailed nature of the metal-ligand bonds can be probed via the observed pressure effects on the luminescence spectra of *trans*-dioxo complexes.

Figure 4.7 illustrates the effect of the counterion on the luminescence properties of the *trans*-$[ReO_2(py)_4]^+$ luminophore. Despite that both I^- and BF_4^- have similar ionic radii,[30] both salts exhibit markedly different vibronic patterns and luminescence energies. The effect of counterion substitution shows that the luminescence properties of the title complex can be tuned by an alternative means, viz., a chemical pressure, which further demonstrates its utility as a probe for the influence of intermolecular forces on intramolecular properties.

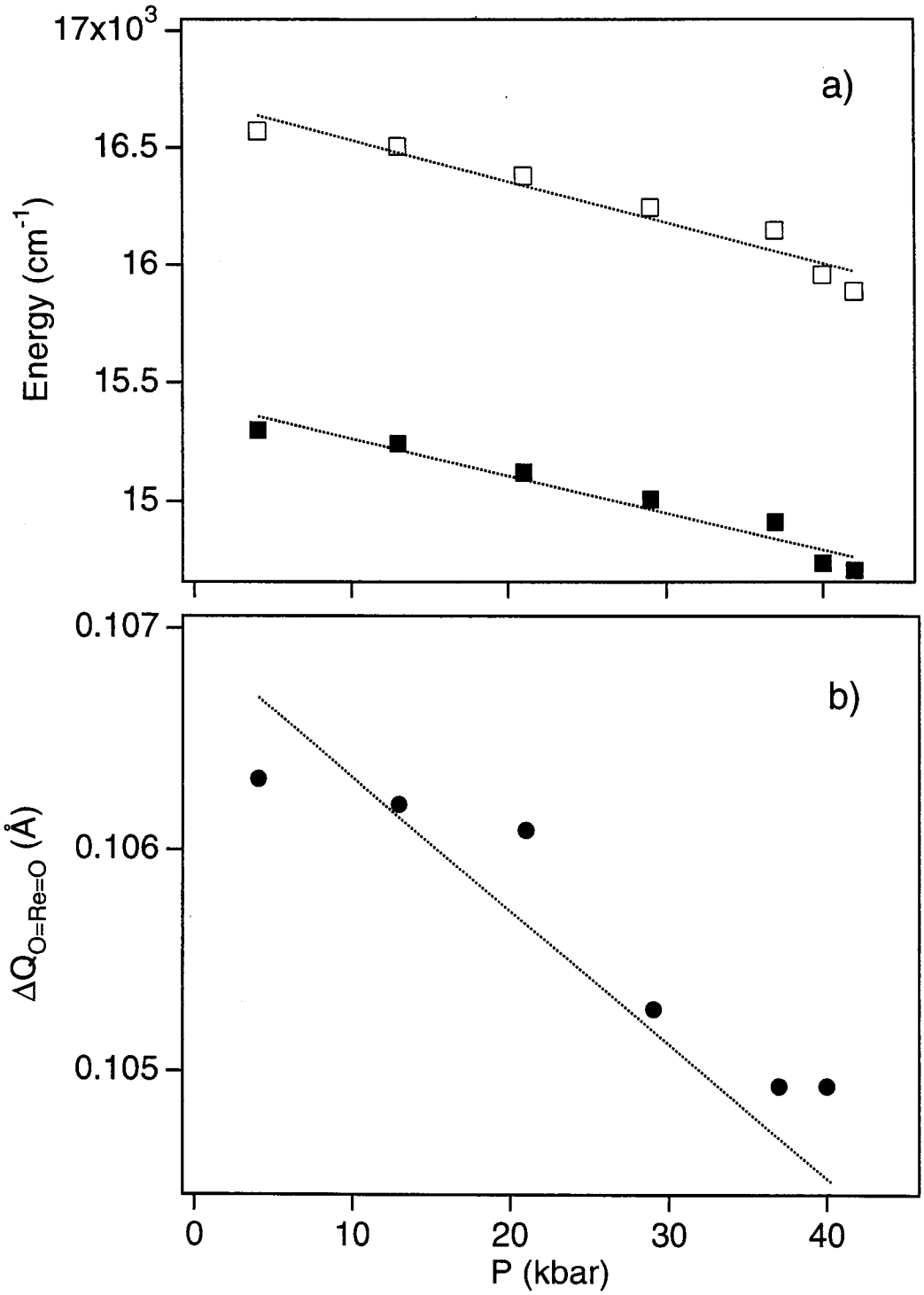

Figure 4.6. a) Pressure dependence of the origin transition, E_{00}, (open squares) and the energy of the luminescence band maximum, E_{max}, (solid squares). b) Pressure dependence of the normal coordinate offset, $\Delta Q_{O=Re=O}$, from the one-dimensional model.

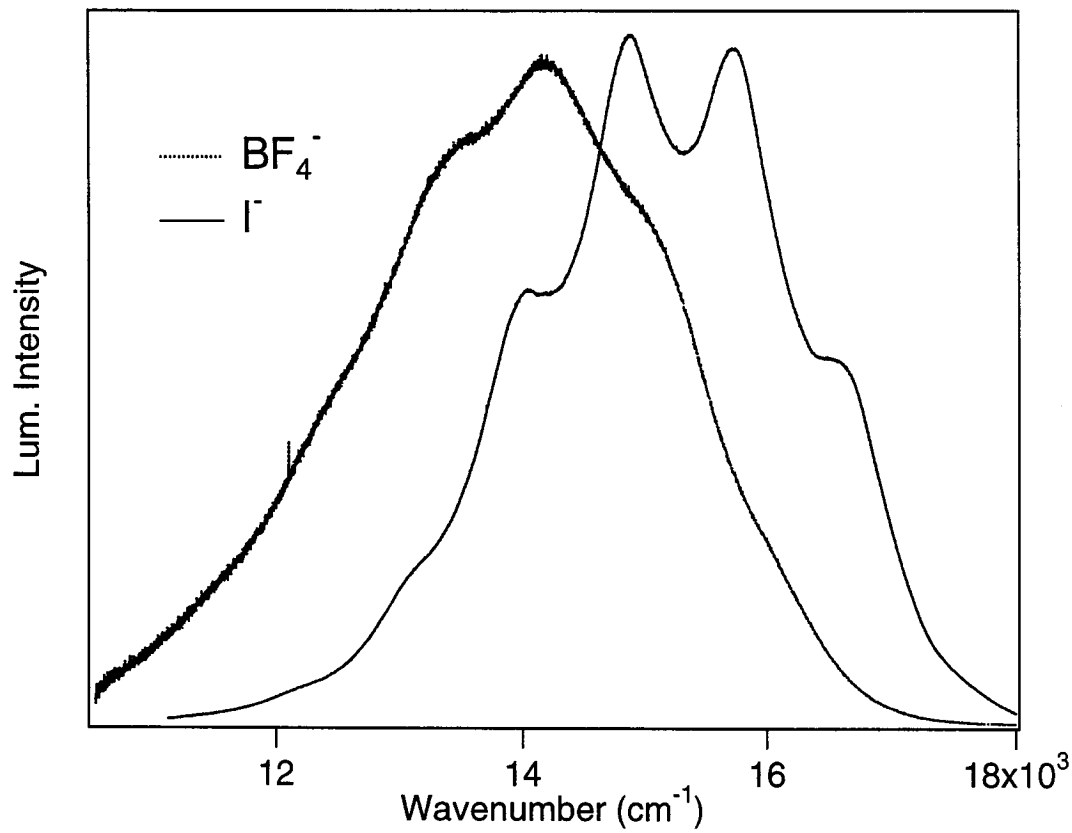

Figure 4.7. 300 K luminescence spectra of *trans*-$[ReO_2(py)_4]I$ (solid) and *trans*-$[ReO_2(py)_4]BF_4$ (dotted).

4.5 Conclusion

The *trans*-[ReO_2(pyridine)$_4$]I luminophore is an excellent system to study the effect of an external perturbation on the resolved vibronic luminescence spectrum at room temperature due to the sensitivity of its luminescence properties to the crystalline environment. We find that the luminescence energies of complexes with monodentate ligands that have strong π-bonding interactions with the metal center, such as pyridine, are more susceptible to changes in the crystalline environment whereas *trans*-$[ReO_2]^+$ complexes with chelating and weakly π-interacting ligands tend to show smaller variations. The analysis of less resolved room temperature spectra with one-dimensional potential energy surfaces reveals the effects of pressure on the spectroscopic parameters defining the ground and emitting states. These subtle aspects of metal-ligand bonding can be quantitatively derived from the temperature- and pressure-dependent luminescence spectra of related *trans*-dioxo complexes.

References

(1) Che, C.-M.; Yam, V. W.-W.; Cho, K.-C.; Gray, H. B. *Chem. Comm.* **1987**, 948.

(2) Thorp, H. H.; Kumer, C. V.; Turro, N. J.; Gray, H. B. *J. Am. Chem. Soc.* **1989**, *111*, 4364.

(3) Thorp, H. H.; Van Houten, J.; Gray, H. B. *Inorg. Chem.* **1989**, *28*, 889.

(4) Che, C.-M.; Cheng, W.-K.; Yam, V. W.-W. *J. Chem. Soc. Dalton Trans.* **1990**, 3095.

(5) Nugent, W. A.; Mayer, J. M. *Metal-Ligand Multiple Bonds*; John Wiley: New York, 1988.

(6) Winkler, J. R.; Gray, H. B. *J. Am. Chem. Soc.* **1983**, *105*, 1373.

(7) Winkler, J. R.; Gray, H. B. *Inorg. Chem.* **1985**, *24*, 346.

(8) Newsham, M. D.; Giannelis, E. P.; Pinnavaia, T. J.; Nocera, D. G. *J. Am. Chem. Soc.* **1988**, *110*, 3885.

(9) Grey, J. K.; Triest, M.; Butler, I. S.; Reber, C. *J. Phys. Chem. A* **2001**, *105*, 6269.

(10) Grey, J. K.; Butler, I. S.; Reber, C. *J. Am. Chem. Soc.* **2002**, *124*, 11699.

(11) Miskowski, V. M.; Gray, H. B.; Hopkins, M. D. In *Adv. in Trans. Met. Coord. Chem.*; Che, C.-M., Yam, V. W.-W., Eds.; JAI Press: Greenwich, CT, 1996; Vol. 1, p 159.

(12) Grey, J. K.; Marguerit, M.; Butler, I. S.; Reber, C. *Chem. Phys. Lett.* **2002**, *366*, 361.

(13) Beard, J. H.; Casey, J.; Murmann, R. K. *Inorg. Chem.* **1965**, *4*, 797.

(14) Landry-Hum, J.; Tessier, V.; Ernzerhof, M.; Reber, C. *Coord. Chem. Rev.* **2002**, *233-234*, 63.

(15) Heller, E. J. *J. Chem. Phys.* **1975**, *62*, 1544.

(16) Heller, E. J. *Acc. Chem. Res.* **1981**, *14*, 368.

(17) Zink, J. I.; Kim Shin, K.-S. In *Adv. Photochem.*; Volman, D. H., Hammond, G. S., Neckers, D. C., Eds.; John Wiley: New York, 1991; Vol. 16, p 119.

(18) The conversion of the emitting state offset for a particular mode from dimensionless units to Å is given by,

$$\Delta Q_k = \sqrt{\frac{N_A \hbar}{4\pi^2 c \hbar \omega_k M}} 10^8 \Delta_k$$

where N_A is Avogodro's number, $\hbar$ is Planck's constant in erg s, c is the speed of light in cm s^{-1}, $\hbar\omega_k$ is the frequency of the vibration in cm^{-1}, and M is the mass of the mode in g mol^{-1}

(19) G. Herzberg. *Molecular Structure and Molecular Spectra. Infrared and Raman Spectra of Polyatomic Molecules: Molecular Spectra and Molecular Structure Vol II*; van Nostrand: New York, 1945; Vol. II, p 63.

(20) S. Masson, M. Triest, J. K. Grey and C. Reber. Phys. Chem. Comm. article 12, 64 (2000). Available at http://www.rsc.org/CFmuscat/intermediate_abstract.cfm?FURL=/ej/qu/2000/b008386k/index.htm&TYP=EON [cited 26 January 2004].

(21) The conversion of the emitting state distortion, ΔQ (Å), to individual bond-length distortions is: for O=Re=O, $\frac{1}{\sqrt{2}}\Delta Q_{O\text{-}Re\text{-}O} = \Delta r_{Re\text{-}O}$ and, for Re- N(pyridine), $\frac{1}{2}\Delta Q_{Re\text{-}N} = \Delta r_{Re\text{-}N}$, assuming that these coordinates are the sole contributors to the normal modes.

(22) Savoie, C.; Reber, C. *Coord. Chem. Rev.* **1998**, *171*, 387.

(23) Savoie, C.; Reber, C. *J. Am. Chem. Soc.* **2000**, *122*, 844.

(24) Savoie, C.; Reber, C.; Bélanger, S.; Beauchamp, A. L. *Inorg. Chem.* **1995**, *34*, 3851.

(25) Parsons, R. W., Drickamer, H.G. *J. Chem. Phys.* **1958**, *29*, 930.

(26) Stephens, D. R., Drickamer, H.G. *J. Chem. Phys.* **1961**, *34*, 937.

(27) Stephens, D. R., Drickamer, H.G. *J. Chem. Phys.* **1961**, *35*, 429.

(28) Balchan, A. S., Drickamer, H.G. *J. Chem. Phys.* **1961**, *35*, 356.

(29) Bray, K. L. *Top. Curr. Chem.* **2001**, *213*, 1.

(30) Butler, I. S.; Harrod, J. F. *Inorganic Chemistry - Principles and Applications*; Benjamin/Cummings: Redwood City, California, 1989, p. 50.

Chapter 5

Effect of Pressure on the Vibronic Luminescence Spectrum of a *trans*-Dioxo Rhenium(V) Complex

This chapter reports the effect of an external pressure on the luminescence spectra of the *trans*-$ReO_2(tmen)_2Cl$ (tmen = tetramethylethylenediamine, $(H_3C)_2N(CH_2)_2N(CH_3)_2$) luminophore. Unlike the *trans*-$[ReO_2(pyridine)_4]^+$ complex, the bandshapes of the tmen complex are anharmonic and become more harmonic with increasing pressure. The room temperature luminescence spectra show pressure-dependent vibronic structure involving the high-frequency O=Re=O stretching mode in the $^3E_g \rightarrow {}^1A_{1g}$ transition (D_{4h} point group). The anharmonicity is taken into account, phenomenologically, by using a Morse potential energy surface to represent the ground electronic state and the dissociation energy, D, and the normal coordinate offset, ΔQ, is varied to reproduce the experimental bandshape.

5.1 Introduction

Luminescence spectra recorded at different pressures reveal important information on the electronic structure of a wide variety of solid materials.[1-5] Transition metal complexes are particularly attractive for such studies because their electronic states involve different equilibrium geometries and bonding characteristics, an ideal situation to explore pressure effects on electronic transitions in the visible spectral region. Typically, experimental observations based on pressure-tuned electronic spectra are reported as shifts in the band maxima to either lower or higher energy and changes in band envelopes. These pressure-induced spectroscopic changes are usually analyzed with purely electronic energy level diagrams,[1-5] most often with ligand-field states, an

* Slight modifications have been made to the original manuscript for clarity and continuity.

approach that is not sufficient to analyze effects such as bond length differences between the ground and excited states. Resolved vibronic structure is essential for a more detailed analysis, and many low-temperature, ambient pressure electronic spectra have been analyzed in detail.[6-11] The majority of the high-pressure studies have been carried out at room temperature or at moderate low temperatures where the vibronic progressions underlying absorption or luminescence bands are broadened, and unresolved band envelopes are observed. Resolved vibronic structure has been reported in a few pressure studies on doped impurities, frozen solutions, and molecules in solid matrices which usually show only short progressions of a vibrational mode or pure electronic (0-0) transitions, not leading to significant bond length changes between the initial and final states of the transition.[12,13] Purely electronic effects, such as ground-state exchange splittings, have been determined as a function of external hydrostatic pressure in neat crystalline coordination compounds, again using transitions with weak or absent vibronic structure.[14]

We present a series of pressure-tuned luminescence spectra from *trans*-dioxo bis-(*N,N,N',N'*-tetramethylethylenediamine)-rhenium(V) with a resolved long progression at room temperature involving the Raman-active O=Re=O stretching mode. *trans*-Dioxo complexes of rhenium(V) show low-temperature absorption and luminescence spectra with well resolved vibronic structure at ambient pressure.[6-11] The O=Re=O vibrational frequencies are on the order of 900 cm^{-1}, higher by more than a factor of two than the majority of metal-ligand stretching modes in coordination compounds. This high frequency leads to spectra that show resolved vibronic structure even at room temperature. The experimental energies and intensity distributions allow us to define the ground and emitting state potential energy surfaces along the normal coordinate of this vibrational mode. We calculate the luminescence spectra arising from these potentials and are able to characterize quantitatively the ground and emitting states as a function of pressure.

5.2 Experimental

trans-$ReO_2(tmen)_2Cl$ was synthesized and characterized using literature techniques.[11,15] In order to apply pressure to a crystalline sample, diamond-anvil cell

(DAC) techniques were used. A small crystal of the title compound, a ruby chip, and Nujol were loaded into a gasketed DAC (300μm diameter, High-Pressure Diamond Optics) and pressure was raised, in increments, up to 51 kbar. The R_1 peak of the ruby emission was used to calibrate pressures within ± 10% of the actual pressure,[16] and Nujol was used as the pressure-transmitting medium. Luminescence spectra were collected with a Renishaw 3000 Raman microscope (20× objective), using the 514.5 nm line of an Ar^+ laser for excitation. The ruby chip was strategically placed so that the excitation laser could be focused to different regions of the sample area of the DAC. This allows us to obtain spectra from the sample with little or no interference from the intense ruby emission.

5.3 Results and Discussion

Figure 5.1 shows pressure-tuned luminescence spectra from the title compound exhibiting resolved vibronic structure at room temperature. The emitting state for this and similar *trans*-dioxo complexes has been assigned, in idealized D_{4h} point group symmetry, as a transition from a spin-orbit component of the ^3E_g excited state to the $^1A_{1g}$ ground state.[6-11] The electronic configuration for these two states are $(d_{xz,yz})^1(d_{xy})^1$ and $(d_{xy})^2$, respectively, with the z axis parallel to the O=Re=O double bonds. The energy range and maxima are also in good agreement with previously published low-temperature spectra at ambient pressure. The dominant progression in the totally symmetric O=Re=O stretching mode is indicated in Figure 5.1 for the spectra recorded at ambient pressure and 35 kbar. The progression interval, in the room temperature spectra of Figure 5.1, is approximately 870 cm^{-1} at ambient pressure, corresponding to the totally symmetric O=Re=O stretching mode of the molecule observed in the ambient pressure Raman spectrum. As pressure increases to about 51 kbar, the frequency of this mode increases to 887 cm^{-1}, indicating a higher Re=O force constant at high pressure. Table 5.1 summarizes the experimental Raman frequencies, showing the effect of pressure on the order a few tens of kilobars on the force constant of metal-ligand multiple bonds. To our knowledge, this is the first report on pressure induced frequency changes for a metal-oxo double bond.

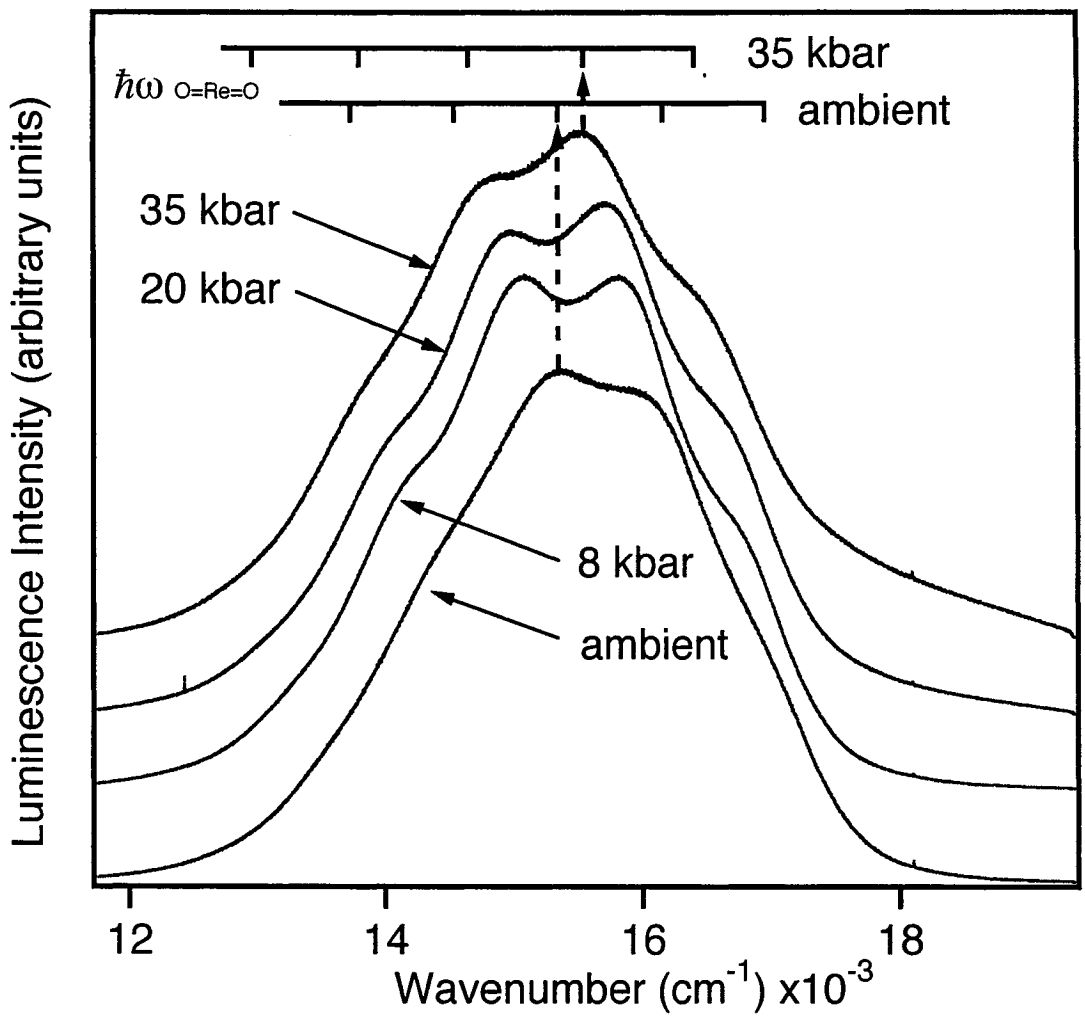

Figure 5.1. Luminescence spectra of *trans*-$ReO_2(tmen)_2Cl$ as a function of pressure at room temperature. Spectra are offset along the ordinate for clarity.

One of the most important features in this series of pressure-tuned luminescence spectra is the change of the intensity distribution within the vibronic pattern. The most intense component of the progression in Figure 5.1 shifts from the third to the second member at higher pressures, as indicated by the vertical dotted lines in Figure 5.1. In addition, the overall luminescence spectra show a noticeable red-shift as pressure increases, illustrated by the two lines with ticks at each vibronic transition throughout the progression.

Pressure (kbar)	$\hbar\omega_{O=Re=O}$ (cm^{-1})
ambient	868
6	869
11	870
25	877
31	880
37	883
46	886
51	887

Table 3.1. Frequency of the totally symmetric O=Re=O stretching mode determined from Raman spectra as a function of pressure.

We can understand these pressure-induced changes quantitatively by using time-dependent theory of spectroscopy[17-19] with one-dimensional potential surfaces to calculate the luminescence spectrum at each pressure. As a first approximation, the harmonic potentials in eqs. 5.1 and 5.2 are used for the ground and emitting states in the calculations.

$$E_{GS} = 1/2\ \hbar\omega\ Q^2 \qquad \text{eq. 5.1}$$

$$E_{ES} = 1/2\ \hbar\omega(Q - \Delta Q)^2 + E_{00} \qquad \text{eq. 5.2}$$

Q is the normal coordinate and ΔQ is the offset between the ground and excited potential minima, in dimensionless units, as illustrated in Figure 5.4. E_{00} is the energy of the origin of the emission and $\hbar\omega$ is the frequency of vibration of the mode described by the normal coordinate Q, both quantities are in wavenumber units. We choose identical vibrational frequencies for both the initial and final states in our calculations. A lower value of 795 cm^{-1}, determined from low-temperature absorption spectra,[7,10] does not lead to a significant improvement between observed and calculated spectra. Calculated spectra using both harmonic and Morse potential energy surfaces with emitting state frequencies of 795 cm^{-1} and 870 cm^{-1} (ground state value) are also compared for the ambient pressure spectrum.

Figure 5.2 shows a comparison of experimental and calculated spectra, using eqs. 5.1 and 5.2. The experimental luminescence band shape is not well described by a harmonic ground-state potential. The most significant deviations occur on the low energy side of the band. The agreement between the calculated spectrum and the experiment is improved significantly by using a Morse potential to represent the ground state. It is given by:

$$E_{GS} = D\left(1 - e^{-\left(0.1218\frac{\hbar\omega}{\sqrt{\frac{D}{m}}}\right)Q}\right)^2 \qquad \text{eq. 5.3}$$

where D is the dissociation energy, in cm^{-1}, m is the mass of the mode in the ReO_2 fragment in g/mole, $\hbar\omega$ is the same vibrational frequency, in cm^{-1}, as for the harmonic potential energy surfaces in eqs. 5.1 and 5.2, and Q is the normal coordinate in units of Å. The dissociation energy, D, was adjusted while holding ΔQ, E_{00}, and $\hbar\omega$ close to the values used to define the simplest model based on harmonic potentials in eqs. 5.1 and 5.2. This procedure leads to a significantly improved agreement between experimental and calculated spectra. Table 5.2 summarizes the parameters obtained from calculating the pressure-tuned luminescence spectra. The emission originates only from the lowest vibrational level of the excited state. Its eigenfunction is defined by the harmonic region and the potential minimum along Q and is not significantly affected by anharmonicity. We therefore use the harmonic excited state potential described by eq. 5.2. Figure 5.2 shows that the calculated spectra obtained with a Morse potential for the ground state are in excellent agreement with the experimental data throughout the pressure range reported here.

Figure 5.3 shows the effect of the choice of frequency in the emitting using both harmonic and Morse potential energy surfaces for the ground electronic state at ambient pressure. The dashed traces represent the spectra calculated with a value of 795 cm^{-1} for the emitting state frequency of the O=Re=O mode. There is a clear discrepancy between the spectra with identical frequencies in the ground and emitting states and those calculated with a lower emitting state frequency. Based on these differences, it is possible to conclude that the reduction of the O=Re=O frequency does not have an appreciable effect on the luminescence bandshapes.

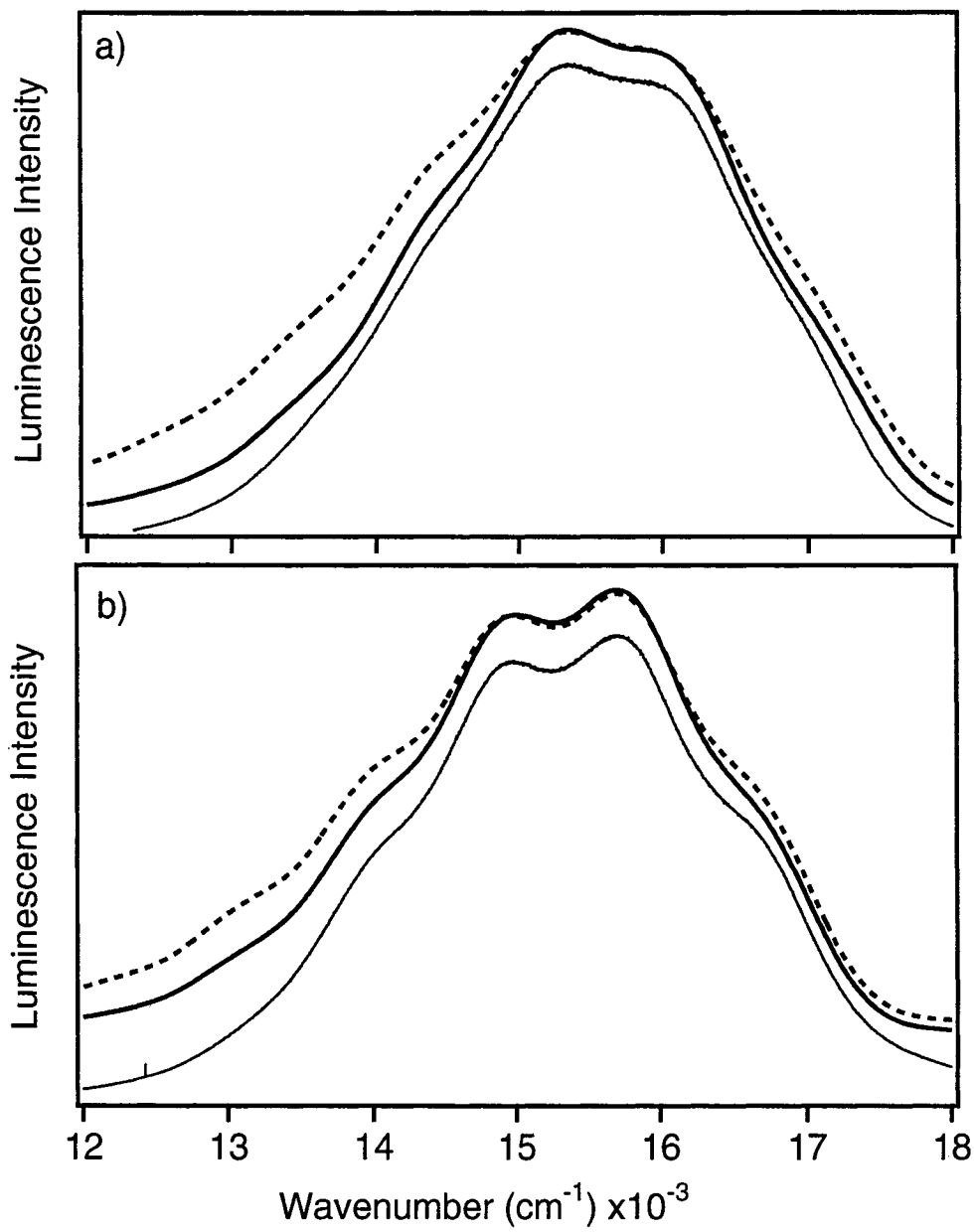

Figure 5.2. Comparison of experimental and calculated luminescence spectra at ambient pressure (a), and 35 kbar (b). The lowest trace in each panel denotes the experimental spectra. The calculated spectra obtained for harmonic and Morse ground state potentials are shown as dashed and solid lines, respectively. The calculated spectra are offset from the experimental trace along the ordinate for clarity.

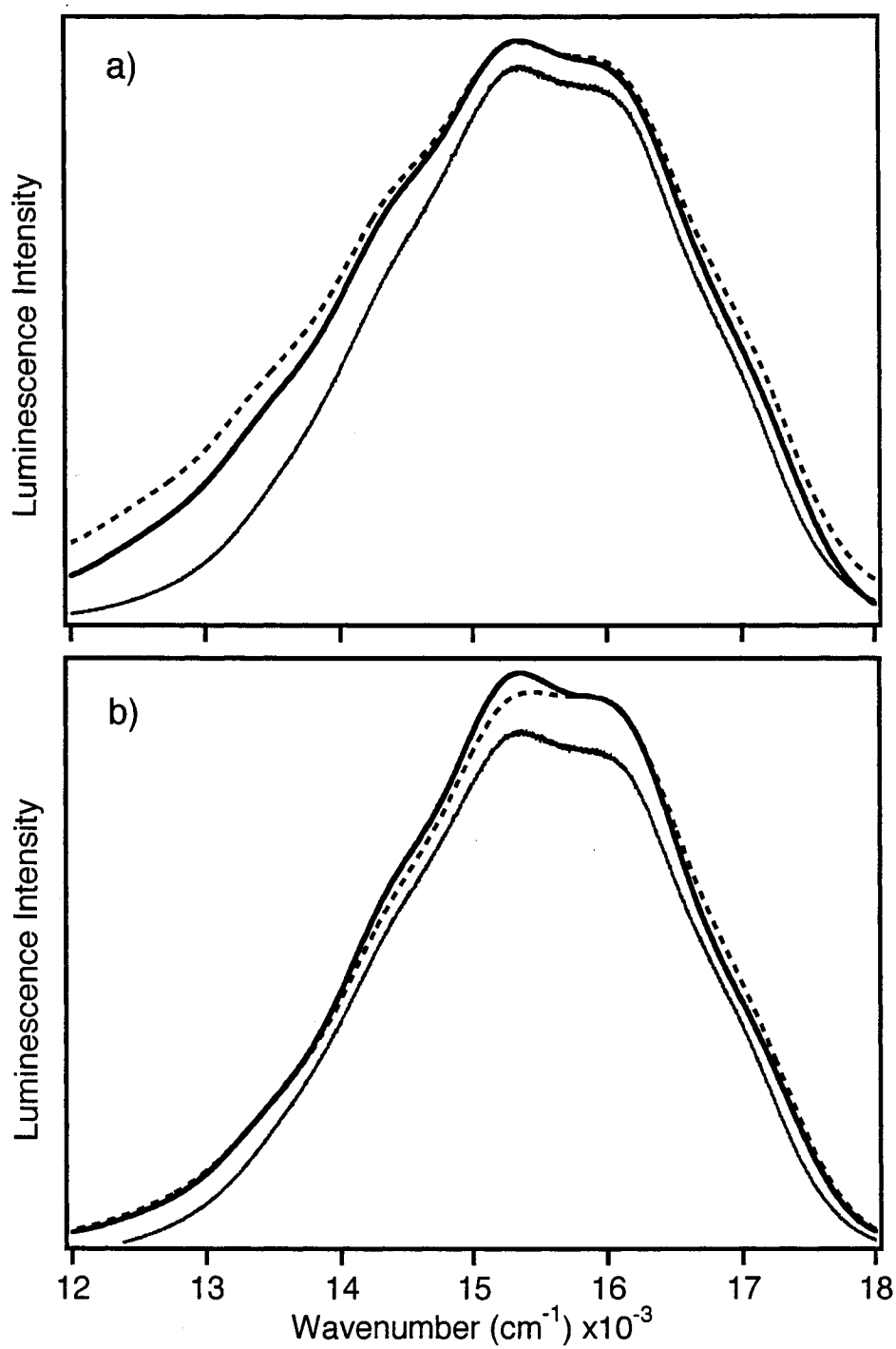

Figure 5.3. Effect of the change in frequency of the O=Re=O stretching mode in the emitting state using harmonic potentials (a) and Morse potentials (b) for the ground state at ambient pressure. a) solid trace: $\hbar\omega_{Re=O}{}^{GS} = \hbar\omega_{Re=O}{}^{ES}$ =870 cm^{-1}; dashed trace: $\hbar\omega_{Re=O}{}^{GS}$ = 870 cm^{-1}, $\hbar\omega_{Re=O}{}^{ES}$ =795 cm^{-1}, b) solid trace: $\hbar\omega_{Re=O}{}^{GS} = \hbar\omega_{Re=O}{}^{ES}$ =870 cm^{-1}; dashed trace: $\hbar\omega_{Re=O}{}^{GS}$ = 870 cm^{-1}, $\hbar\omega_{Re=O}{}^{ES}$ =795 cm^{-1} (D = 80 000 cm^{-1}, Table 5.2).

The anharmonicity in the experimental spectra is due to avoided crossings between the potential surface of the $^1A_{1g}$ ground-state and excited states with the same symmetry.[10,11] The coupling between states flattens the ground-state potential surface at positive values of Q. The Morse potential is therefore a phenomenological description of the ground-state potential surface. The full account of this effect, established from low-temperature, ambient pressure spectra, involves two vibrational modes and three coupled electronic states. These spectra show deviations from the Poisson bandshape, which results from a harmonic ground state potential, on the low energy side of the band, in qualitative agreement with the deviations illustrated in Figure 5.2. The cross-section through the ground state potential surface in Ref. 11 deviates from a harmonic curve in close analogy to the difference between the harmonic and Morse curves for the ground state in Figure 5.4. Our ambient temperature spectra are less resolved than the low-temperature luminescence spectra, showing only the high-frequency, totally symmetric O=Re=O stretching mode, and therefore we cannot fit all of the parameters required for the full coupled states model.[11] The Morse potential in equation 5.3, however, provides a good description with few adjustable parameters. This model explains the shape of the luminescence band envelope as a function of pressure. At pressures above 45 kbar, the vibronic structure washes out and the intensity of the emission drops significantly, indicating that non-radiative pathways dominate at higher pressures as a result of a strongly distorted excited state.

pressure (kbar)	$\hbar\omega_{O=Re=O}$ (cm^{-1})	E_{00} (cm^{-1})	ΔQ (dimensionless)	D (cm^{-1})
Ambient	870	16,950	2.28	80,000
2	875	16933	2.26	85,000
8	875	16,725	2.22	90,000
20	880	16,627	2.15	100,000
30	885	16,430	2.13	140,000
35	885	16,447	2.11	160,000

Table 5.2. Parameters determined from the calculated luminescence spectra, as illustrated in Figure 5.2. All quantities are defined in eqs. 5.1-5.3.

The use of Morse potentials to model the ground-state energy surface of the title compound yields the best fit to the experimental ambient pressure spectrum, significantly better than does the calculation using the harmonic ground-state potential in eq. 5.1. This comparison is illustrated in Figure 5.2a. As pressure increases, the overall luminescence band shape is closer to the Poisson bandshape expected for harmonic potential surfaces, as shown in Figure 5.2b, where the differences between the spectra calculated with harmonic and Morse potential surfaces are smaller than those in Figure 5.2a. By increasing the dissociation energy, D, of the Morse potential with increasing pressure, we can reproduce this behavior quite effectively. The red shift of the experimental spectra in Figure 5.1 leads to a decrease in E_{00}, as given in Table 5.2. The frequency, $\hbar\omega$, determined from the calculated luminescence spectra increases with pressure by the same amount as do the Raman frequencies given in Table 5.1. The precision of the frequencies in Table 5.2 is lower than for the Raman frequencies in Table 5.1, a difference due to the lower resolution of the luminescence spectra. The offset, ΔQ, decreases with pressure, contributing to the change in the intensity distribution of the vibronic progression observed experimentally, allowing us to estimate the pressure-induced bond-length change of the Re=O double bonds. The decrease over the pressure range reported in Table 5.2 corresponds to a bond length change of 0.01 Å, on the same order as the variation of ambient pressure Re=O bond lengths for different ancillary ligands.[20]

The potential surfaces for the ground and excited states at low and high pressures are shown in Figure 5.4, illustrating the effect of pressure on the shapes of these surfaces. The red shift of the emission with increasing pressure is a consequence of both the decrease of the energy difference, E_{00}, between the lowest vibrational levels within the ground and emitting state potential surfaces and the smaller anharmonicity, corresponding to a higher dissociation energy, D, of the ground state potential surface in eq. 5.3. High-pressure pushes the ground state surface in Figure 5.4 to higher energy in the normal-coordinate range of the luminescence maximum, indicated by the vertical arrow, an effect that causes the band envelope to become more harmonic at high pressure. The time-dependent theory of spectroscopy affords an alternative view of this effect on the ground state potential surfaces by considering the recurrence times for the O=Re=O stretching mode in the time-domain. Figure 5.5a shows the absolute autocorrelation

overlap[21] for the lowest pressure (ambient) and highest pressure (35 kbar) and Figure 5.5b is the difference of these overlaps. As pressure increases, the ground state becomes more harmonic (i.e., increasing value of D) and is reflected in the change in autocorrelation overlap between the limits of the pressure range studied. The change of the intensity distribution within the vibronic progression depends on two pressure-induced effects: first, the decrease of the offset, ΔQ, between the minima of the potential curves with increasing pressure and, second, the increase of the dissociation energy, D, with pressure. This latter effect is expected to dominate when the ground-state potential surface at ambient pressure is strongly anharmonic, and becomes less important for complexes with a nearly harmonic ground-state potential surface at ambient pressure.

The deviation from a harmonic ground-state potential in the title complex is caused by coupling between the ground-state and emitting-state surfaces, and we therefore expect distinctly different pressure effects on the emission spectra of *trans*-dioxo complexes with higher or lower energy luminescence than shown in Figure 5.1. Our results show that the spectroscopic effects of coupling between electronic states, even if they are separated by more than 10^4 cm^{-1}, can be better understood by pressure-tuning methods applied to spectra with resolved vibronic structure.

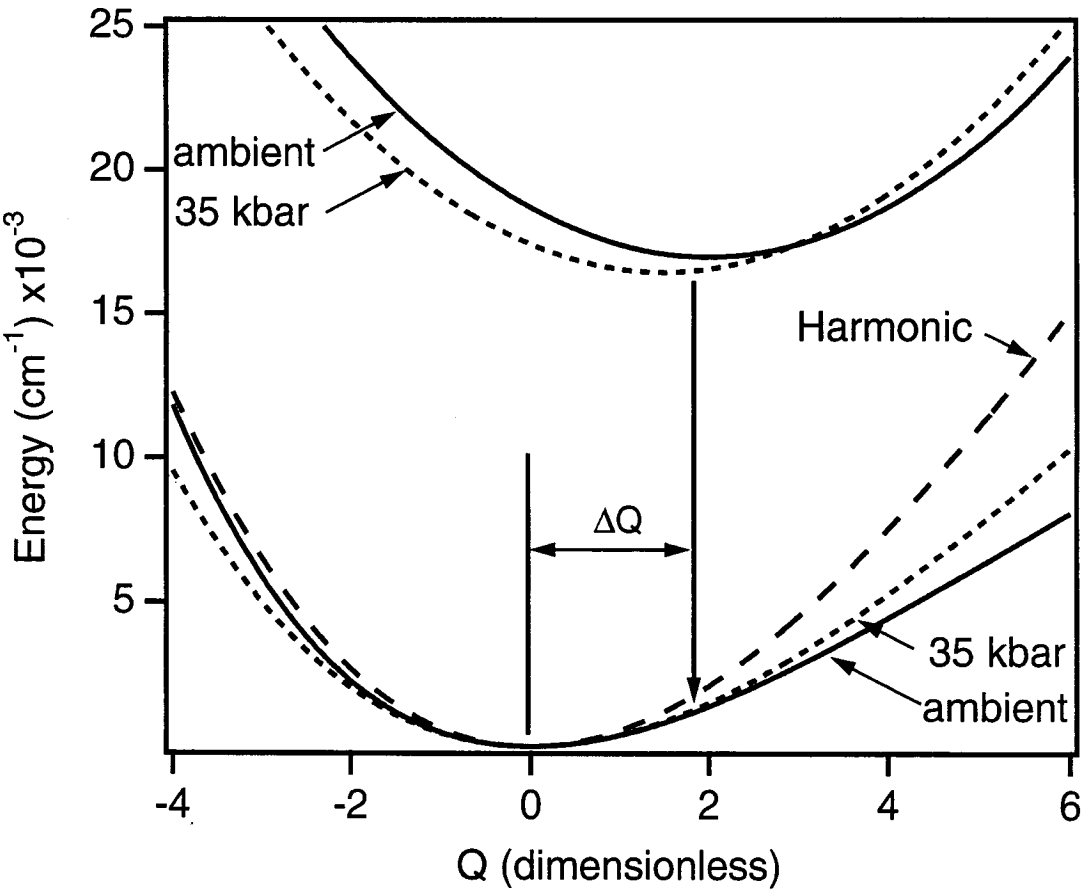

Figure 5.4. Potential energy surfaces for the ground and emitting states at ambient pressure (solid lines) and 35 kbar (dotted lines). The dashed line gives the harmonic ground state potential surface at ambient pressure.

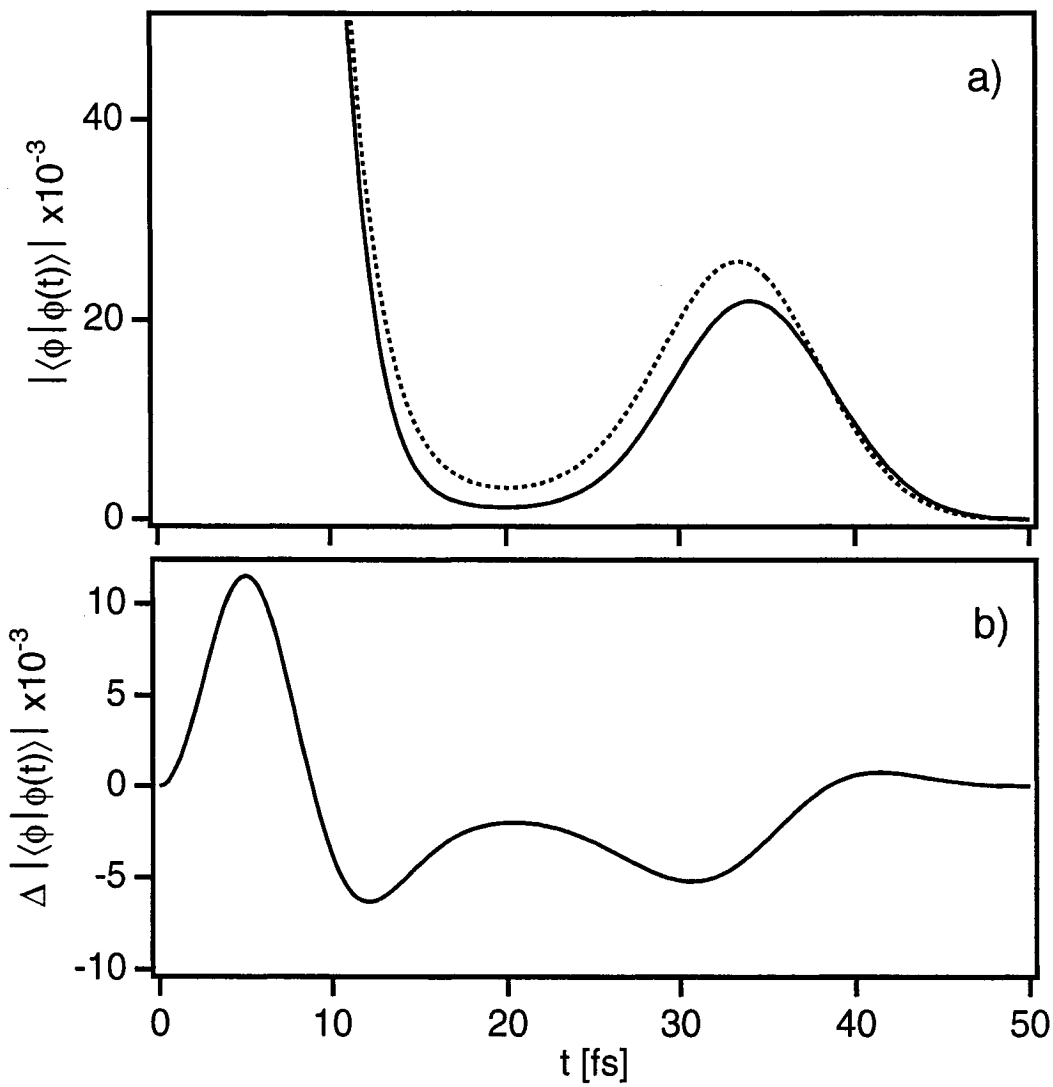

Figure 5.5. a) Absolute autocorrelation overlap functions calculated for ambient (solid) and 35 kbar (dotted) pressure-dependent spectra. b) change in autocorrelation between over the pressure range studied.

References

(1) Drickamer, H. G. In *Solids under pressure*; Warhauser, P. D., Ed.; McGraw-Hill: New York, 1963, p 357.

(2) Drickamer, H. G.; Frank, C. W. *Electronic Transitions and the High Pressure Chemistry and Physics of Solids*; Chapman and Hall: New York, 1973.

(3) Schäffer, C.; Lang, J. M.; Drickamer, H. G. *Inorg. Chem.* **1996**, *35*, 5072.

(4) Bray, K. L.; Drickamer, H. G.; Schmitt, E. A.; Hendrickson, D. N. *J. Am. Chem. Soc.* **1989**, *111*, 2849.

(5) Ferraro, J. R.; Basile, L. J.; Sacconi, L. *Inorg. Chim. Acta* **1979**, *35*, L317.

(6) Winkler, J. R.; Gray, H. B. *J. Am. Chem. Soc.* **1983**, *105*, 1373.

(7) Winkler, J. R.; Gray, H. B. *Inorg. Chem.* **1985**, *24*, 346.

(8) Miskowski, V. M.; Gray, H. B.; Hopkins, M. D. In *Adv. in Trans. Met. Coord. Chem.*; Che, C.-M., Yam, V. W.-W., Eds.; JAI Press: Greenwich, CT, 1996; Vol. 1, p 159.

(9) Savoie, C.; Reber, C.; Bélanger, S.; Beauchamp, A. L. *Inorg. Chem.* **1995**, *34*, 3851.

(10) Savoie, C.; Reber, C. *Coord. Chem. Rev.* **1998**, *171*, 387.

(11) Savoie, C.; Reber, C. *J. Am. Chem. Soc.* **2000**, *122*, 844.

(12) Kenney, J. W. I.; Clymire, J. W.; Agnew, S. F. *J. Am. Chem. Soc.* **1995**, *117*, 1645.

(13) Yersin, H.; Trümbach, D.; Wiedenhofer, H. *Inorg. Chem.* **1999**, *38*, 1411.

(14) Riesen, H.; Güdel, H. U. *J. Chem. Phys.* **1987**, *87*, 3166.

(15) Lock, C. J. L.; Turner, G. *Acta Cryst.* **1978**, *B34*, 923.

(16) Piermarini, G. J., Block, S., Barnett, J.D., Forman, R.A. *J. Appl. Phys.* **1975**, *46*, 2774.

(17) Heller, E. J. *J. Chem. Phys.* **1975**, *62*, 1544.

(18) Heller, E. J. *Acc. Chem. Res.* **1981**, *14*, 368.

(19) Zink, J. I.; Kim Shin, K.-S. In *Adv. Photochem.*; Volman, D. H., Hammond, G. S., Neckers, D. C., Eds.; John Wiley: New York, 1991; Vol. 16, p 119.

(20) Mayer, J. M. *Inorg. Chem.* **1988**, *27*, 3899.

(21) According to the split-operator algorithm developed by Feit et al. (Feit, M.D., Fleck Jr., J. A.; Steiger, A. *J. Comp. Phys.* **1982**, *47*, 412) the time-dependent wavepacket is given by,

$$\phi(t+\Delta t) = e^{\left(\frac{i\Delta t}{4M}\right)\nabla^2} e^{-i\Delta t V} e^{\left(\frac{i\Delta t}{4M}\right)\nabla^2} \phi(t) + O\left[\left(\Delta t^3\right)\right]$$

which has a maximum value of 1 at t =0. The autocorrelation function is the overlap of this time-dependent function, ϕ(t), with the initial function, ϕ, and the result ($\langle\phi|\,\phi(t)\rangle$ is Fourier-transformed to give the spectrum in the frequency domain.

Chapter 6

Effect of Pressure on Coupled Electronic Ground and Excited States Determined from Luminescence Spectra of *trans*-Dioxorhenium(V) Complexes

From the previous chapter, the ground electronic state of *trans*-$ReO_2(tmen)_2Cl$ was shown to be anharmonic along the O=Re=O symmetric stretching normal coordinate. This anharmonicity arises from avoided crossings between the ground state and excited states of the same symmetry. This chapter explores the effect of pressure on the avoided crossings using the pressure-dependent luminescence bandshapes of a series of substituted ethylenediamine complexes.

6.1 Introduction

The application of high external pressures to molecules in order to perturb electronic structures has found much use in chemistry, physics, and materials science.[1,2] These pressure-induced effects can be probed by electronic spectroscopy allowing the characterization of individual electronic states. Some of the most prolific work within this area has involved pressure-tuning of the absorption and luminescence spectra of transition metal complexes.[3,4] The effects of pressure on ligand-field parameters,[5-8] luminescence lifetimes,[3] the electronic ground state in spin-crossover compounds,[9] the correlation between changes in molecular structure (isomerizations) and electronic spectra (piezochromism),[10-12] and the Jahn-Teller effect[13] were investigated to obtain detailed information on the electronic structure of transition metal complexes. Despite the extensive studies in pressure-dependent electronic spectroscopy, there have been no previous comprehensive reports for the effects of pressure on coupling between ground and excited electronic states probed by luminescence spectroscopy.

* Slight modifications were made to the original manuscript for clarity and continuity.

Pressure-tuning spectroscopy studies aimed at interactions between excited states have been reported for doped chromium(III) systems. Ref. 3 presents pressure-dependent luminescence spectra and lifetimes indicating that the spin-orbit mixing of $^4T_2$ and ^2E excited states is sensitive to metal-ligand bond lengths. This excited state interaction shows an effect of pressure on both structural and electronic properties of the emitting states. The effect of pressure on the structure of the Jahn-Teller active $^4T_2$ emitting state of a chloride lattice doped with chromium(III)[13] is another recent example illustrating the characterization of an excited state through pressure-tuned luminescence spectroscopy with resolved vibronic structure. In order to investigate pressure-tuned interactions between the ground state and excited electronic states, we have applied high external pressures to molecular crystals of *trans*-dioxo rhenium(V) complexes. From the luminescence spectra, it is possible to determine quantitatively the influence of coupling between electronic states on electronic origins, luminescence band maxima, and offsets between ground and emitting-state potential minima. *trans*-Dioxo rhenium(V) complexes have found applications in monitoring host-guest interactions by intercalating these complexes into layered materials and recording absorption and luminescence spectra.[14] Ref. 14 presents various positions in which these chromophores can orient themselves within the interlamellar spaces of a host material and the electronic spectra reveal the effect of the environment on the rhenium(V) complexes. These host-guest interactions represent a chemical pressure on the intercalated molecule whose ground state properties are pressure-tuned. The results presented here are intended to show how pressure effects can be rationalized from models based on interacting electronic states.

Pressure decreases the volume of a solid sample and disrupts the balance between intra- and intermolecular forces. The pressure-dependent changes of the luminescence spectra reported in the following can therefore arise from both intra- and intermolecular effects. All properties, such as vibrational frequencies, vary smoothly with pressure providing no evidence for structural phase transitions. From the pure intramolecular standpoint, pressure leads to a reduction of metal-ligand bond lengths. Electronic spectroscopy has been used to analyze such effects, often described by pressure-dependent Racah parameters, B and C, and sets of ligand-field parameters such as Dq, Ds, and Dt.[5,15,16] The effect of external pressure on electronic transitions has been

explained with pure electronic energy levels defined by these parameters. This simple approach successfully describes pressure-induced variations of unresolved band maxima, but cannot rationalize vibronic bandshapes, which have to be characterized with potential energy surfaces. They lead to a more detailed description of the changes the molecules experience under external pressure.[3,13] The potential energy surfaces in Scheme 6.1 illustrate the effect of pressure on important observable spectroscopic quantities that define the ground and emitting states. As pressure increases, the metal-ligand bond lengths decrease and the potential minima shift to lower values of the normal coordinate, Q, in Scheme 6.1. The excited state potential energy surface in Scheme 6.1 has its minimum at a larger value of the normal coordinate and is likely to be more strongly affected by external pressure, leading to a decrease of ΔQ, the difference of potential minima along the normal coordinate. The energies of the two electronic states are also altered. This results in pressure-induced changes of the energy of the electronic origin, E_{00}, the band maximum, E_{max}, the offsets between ground and emitting states, ΔQ, and the vibrational frequencies, $\hbar\omega$, observed from Raman spectra or as the spacing of a vibronic progression.

The first spectroscopic studies on the *trans*-dioxorhenium(V) class of complexes were reported by Winkler and Gray[17,18] that revealed the rich optical properties in these materials where well-resolved, long vibronic progressions in the high frequency O=Re=O and low frequency Re-ligand modes are observed. The effect of pressure on the spectroscopic quantities outlined above was studied by monitoring the luminescence of crystalline chloride salts of *trans*-[ReO_2(*N,N,N',N'*-ethylenediamine)$_2$]$^+$, [ReO_2(*N,N,N',N'*-tetramethylethylenediamine)$_2$]$^+$, and [ReO_2(*N,N,N',N'*-tetraethylethylenediamine)$_2$]$^+$ complexes. These compounds will be denoted as $ReO_2(en)_2Cl$, $ReO_2(tmen)_2Cl$, and $ReO_2(teen)_2Cl$, respectively, throughout this report. The luminescence band maxima of the title complexes depend distinctly on the substitution of the ethylenediamine ligands, and vary by approximately 2,500 cm^{-1} between the three complexes studied here.[19-21] Low-temperature luminescence spectra of $ReO_2(en)_2Cl$ and $ReO_2(tmen)_2Cl$ complexes have been analyzed to show that the ground state is influenced by several excited states of the same symmetry through avoided crossings.[19] This electronic interaction gives rise to characteristic spectra with resolved vibronic progressions involving the O=Re=O

symmetric stretching mode (~900 cm^{-1}) even at room temperature and we present and apply a model based on potential energy surfaces as illustrated in Scheme 6.1 to describe quantitative changes with pressure. We use this series of closely related *trans*-dioxo rhenium(V) complexes to describe how the shapes of ground-state potential energy surfaces are influenced by pressure through interactions with excited states. This effect is important for all third-row transition metal complexes due to their large spin-orbit coupling constants.

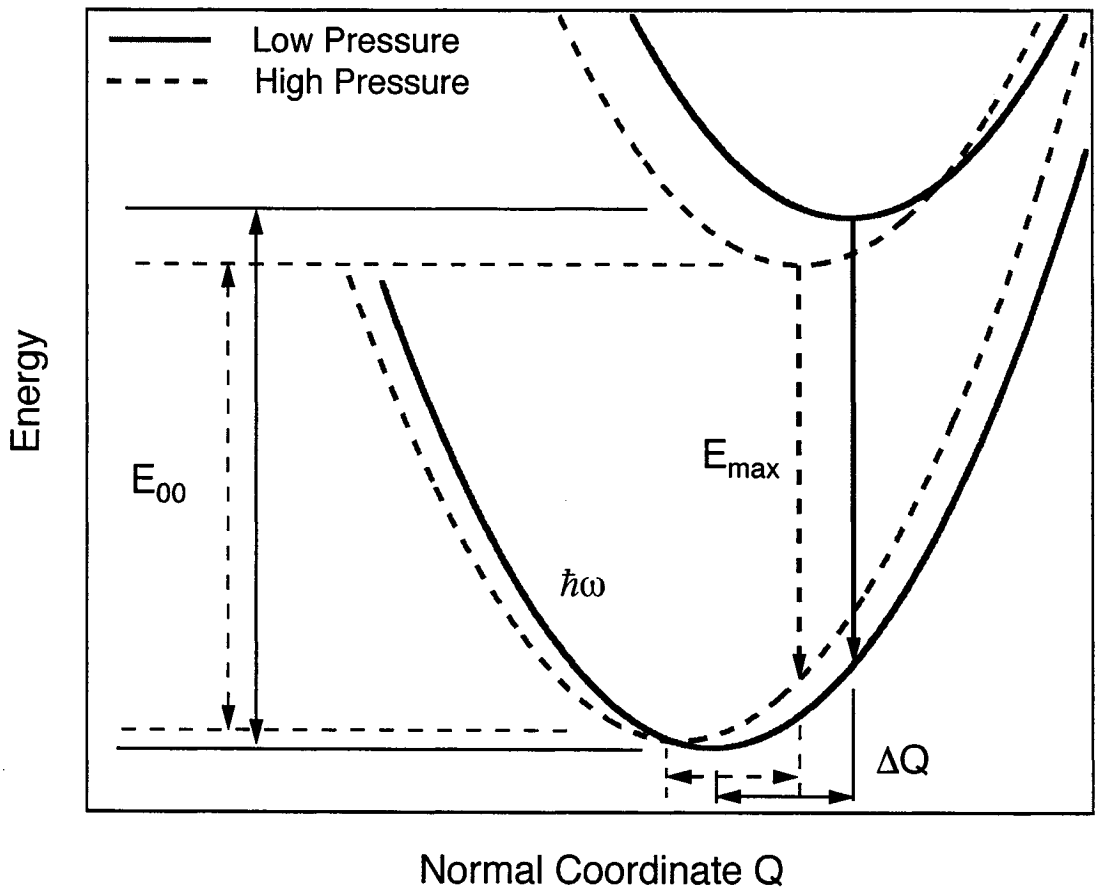

Scheme 6.1. Potential energy surfaces for ground and emitting states at low (solid lines) and high (dashed lines) pressures showing the pressure dependence of important spectroscopic parameters.

6.2 Experimental Section

The title complexes were synthesized and characterized using literature methods.[22,23] To apply pressure to the crystalline samples, diamond-anvil cell (DAC) techniques were used. Small crystals of the title compounds, a ruby chip, and Nujol were loaded into a gasketed DAC (300μm diameter sample chamber, High-Pressure Diamond Optics, Tucson, AZ) and pressure was raised mechanically. The R_1 peak of the ruby emission was used to calibrate pressures,[24] and Nujol was the pressure-transmitting medium. Pressure-dependent luminescence and Raman spectra were collected with a Renishaw 3000 Raman microscope (20× and 50× objectives) using Spectra Physics 163-C1210 and 163-C4210 argon-ion lasers (488 and 514.5 nm lines) or a Renishaw NIR 780 diode laser (782 nm) with the appropriate Renishaw notch filters as excitation sources. The pressure for experiments using the NIR diode laser was calibrated *in situ* by monitoring the shift of the t_{2g} phonon mode of the diamond anvils.[25] Since the excitation laser spot could be focused to approximately 1 μm in diameter, we were able to minimize superposition of the intense ruby $^2E \rightarrow {}^4A_2$ emission on the sample spectrum by strategically placing the ruby chip in the sample hole of the gasket.

A low-temperature luminescence spectrum of crystalline $ReO_2(teen)_2Cl$ was collected using the Renishaw 3000 Raman imaging microscope described above. Detailed low-temperature luminescence spectra for the $ReO_2(en)_2Cl$ and $ReO_2(tmen)_2Cl$ complexes have been reported before.[19] The Raman system was configured with an elbow objective that enabled the laser spot to be focused into an Oxford Instruments CF-1204 continuous flow helium cryostat. The luminescence spectrum of the $ReO_2(teen)_2Cl$ complex dissolved in DMSO (Aldrich, ACS reagent grade) was measured at 77 K using a Linkam THMS 6000 hot/cold stage. All luminescence spectra were corrected for spectrometer response using the procedure described previously.[26]

Luminescence lifetimes of $ReO_2(teen)_2Cl$ were measured using the tripled output (355 nm) of a Continuum mini-lite II Nd:YAG pulsed laser. The time-dependent luminescence intensities were detected with a Hamamatsu R928 photomultiplier tube and stored using a digital oscilloscope (Tektronix TDS 380) triggered by a silicon photodiode (Thorlabs FDS 100). The crystalline powder sample was cooled in the Oxford

Instruments cryostat described above and the emitted light was dispersed through a 0.5-m monochromator (Spex 500M) with a 600 lines/mm grating and filtered with a red longpass filter (Schott RG 630). Measurements were made at ambient temperature, 100 K, 50 K, and 5 K and decay curves were fitted with single exponential functions to obtain the lifetimes. Absorption and diffuse reflectance spectra of $ReO_2(teen)_2Cl$ were measured at room temperature with a Varian Cary 5E spectrometer.

6.3 Spectroscopic Results

Figure 6.1 shows luminescence spectra of all three complexes at a low and high pressure. The spectra illustrate the large variation of luminescence energies between the complexes and the effect of high pressure on the luminescence of each complex. All room-temperature spectra display a long progression involving the high-frequency O=Re=O symmetric stretching mode with a frequency of approximately 900 cm^{-1}. The luminescence spectra of the $ReO_2(tmen)_2Cl$ complex, shown as the middle traces in Figure 6.1, show the best resolution of vibronic progressions with well-separated members. This assignment of the vibronic progression to the O=Re=O symmetric stretching mode in the luminescence is confirmed by Raman spectroscopy and well-resolved low-temperature emission spectra from the literature.[17-21,27] Luminescence spectra of the $ReO_2(teen)_2Cl$ complex do not exhibit resolved vibronic structure, even at 5 K. A shoulder does appear in the blue region of the luminescence band with an energy separation of about 1400 cm^{-1} from the main maximum. Raman spectra of this complex show transitions at approximately 1400 cm^{-1} and a strong signal for the O=Re=O symmetric stretch at 1000 cm^{-1}. Luminescence lifetimes were measured across the band in order to determine if the shoulder resolved at low-temperature was not due to an emissive impurity or different sites of the complex in our crystalline sample. The excited state lifetime at 5 K is 153 ns, compared to 152 ns at 77 K, and does not change by more than 3% across the luminescence band. The luminescence spectrum of this complex dissolved in DMSO recorded at 77 K yields the same vibronic features as the luminescence spectrum of the crystalline complex at 5 K. These results provide evidence against multiple emitting states or luminescent impurities and allow us to include this complex in our study. Absorption and diffuse reflectance spectra of this complex at

ambient temperature show that the ligand-field absorption bands and the lowest energy charge transfer band strongly overlap. These spectroscopic results indicate that the emitting state of $ReO_2(teen)_2Cl$ is different in character than the complexes with lower energy luminescence bands.

Figure 6.2 shows two series of pressure-dependent luminescence spectra of the $ReO_2(en)_2Cl$ and $ReO_2(tmen)_2Cl$ complexes. Pressure-tuning of the title complexes leads to changes in the relative intensities and energies of vibronic bands, decreases in the overall intensity of the luminescence bands, and changes in the bandshapes. All pressure-induced spectroscopic changes are reversible. The magnitude of these pressure-induced changes depends strongly on the equatorial ethylenediamine ligands. Figure 6.2a corresponds to the least substituted complex of this series, $ReO_2(en)_2Cl$. This complex exhibits the lowest energy luminescence band. The luminescence becomes very weak at pressures above approximately 40 kbar. In these spectra, we have as much as three quanta of the O=Re=O symmetric stretching mode resolved and the intensity distribution of the vibronic bands changes with pressure. The most prominent spectral feature is the rapid decrease of the overall band intensity that is likely due to more efficient non-radiative pathways at higher pressures. Figure 6.2b show pressure-dependent luminescence spectra of the $ReO_2(tmen)_2Cl$ complex which display the most striking changes in the relative intensity distribution within the vibronic progression. We observe up to four resolved quanta of the O=Re=O symmetric stretching mode in these spectra and the most noticeable pressure effects are seen in the second and third members of the progression. The numbering of transitions is given below the bottom trace in Figure 6.2b. At low pressures, the relative intensity of the third member is higher than that of the second. As pressure increases, there is a gradual change in the intensities of the second and third peaks with the second peak becoming stronger. At pressures higher than 65 kbar, the vibronic structure is washed out and the overall intensity of the luminescence band decreases. Furthermore, as pressure increases, the luminescence onsets of the $ReO_2(en)_2Cl$ and $ReO_2(tmen)_2Cl$ complexes, on the high-energy side of the band, shift to lower energy. The overall luminescence band envelopes of the two complexes in Figure 2 also show a red shift that can be observed by following the vibronic peaks with increasing pressure. However, the red shift of the band maxima is not identical to that of

the onsets or any individual vibronic band. This will be discussed in detail in the next section. The largest change in energy of the luminescence maxima occurs with the lowest-energy emitting complex. The $ReO_2(teen)_2Cl$ complex shows a small blue shift of the luminescence band maximum at higher pressures, but virtually no changes in band shape with pressure or temperature. With the pressure-dependent vibronic features laid out here, we require a model based on potential energy surfaces, as presented in Scheme 6.1, that correctly describes the changes in the spectroscopic quantities for each pressure.

Figure 6.3 depicts the pressure-dependent Raman spectra of the $ReO_2(en)_2Cl$ complex in the O=Re=O symmetric stretching region. The frequency of the O=Re=O symmetric stretching mode shifts uniformly to higher wavenumber as a function pressure (+0.5 cm^{-1}/kbar), indicating an increase in the force constant of the rhenium-oxygen double bond. This trend is approximately the same for all the title complexes as illustrated by the inset in Figure 6.3, where we show the O=Re=O stretching frequency at various pressures for all complexes. Raman signals in the region of the Re-N(en) symmetric stretching modes show a shift to higher energy as well as a significant decrease in the area under the bands, a characteristic that is very common with the application of an external pressure.[28] Pressure-dependent Raman spectra of all complexes suggest that the local symmetry around the rhenium(V) center is not altered significantly, based on the smooth increases of the O=Re=O and Re-N(en) frequencies.

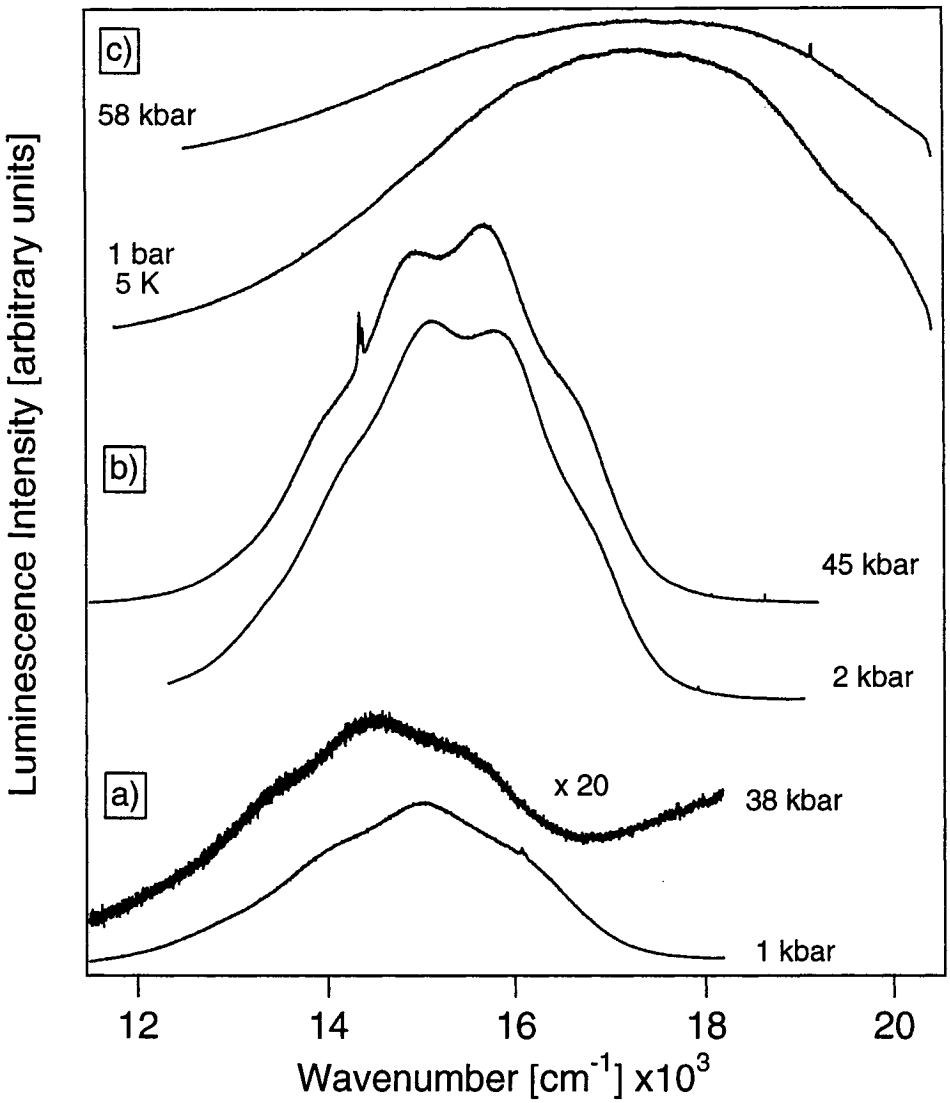

Figure 6.1. Low and high pressure luminescence spectra of a) $ReO_2(en)_2Cl$; b) $ReO_2(tmen)_2Cl$; c) $ReO_2(teen)_2Cl$. The vibronic structure corresponds to the frequency of the O=Re=O symmetric stretching mode. The ambient pressure spectrum of the $ReO_2(teen)_2Cl$ complex was measured at 5 K, showing little difference from that at room temperature.

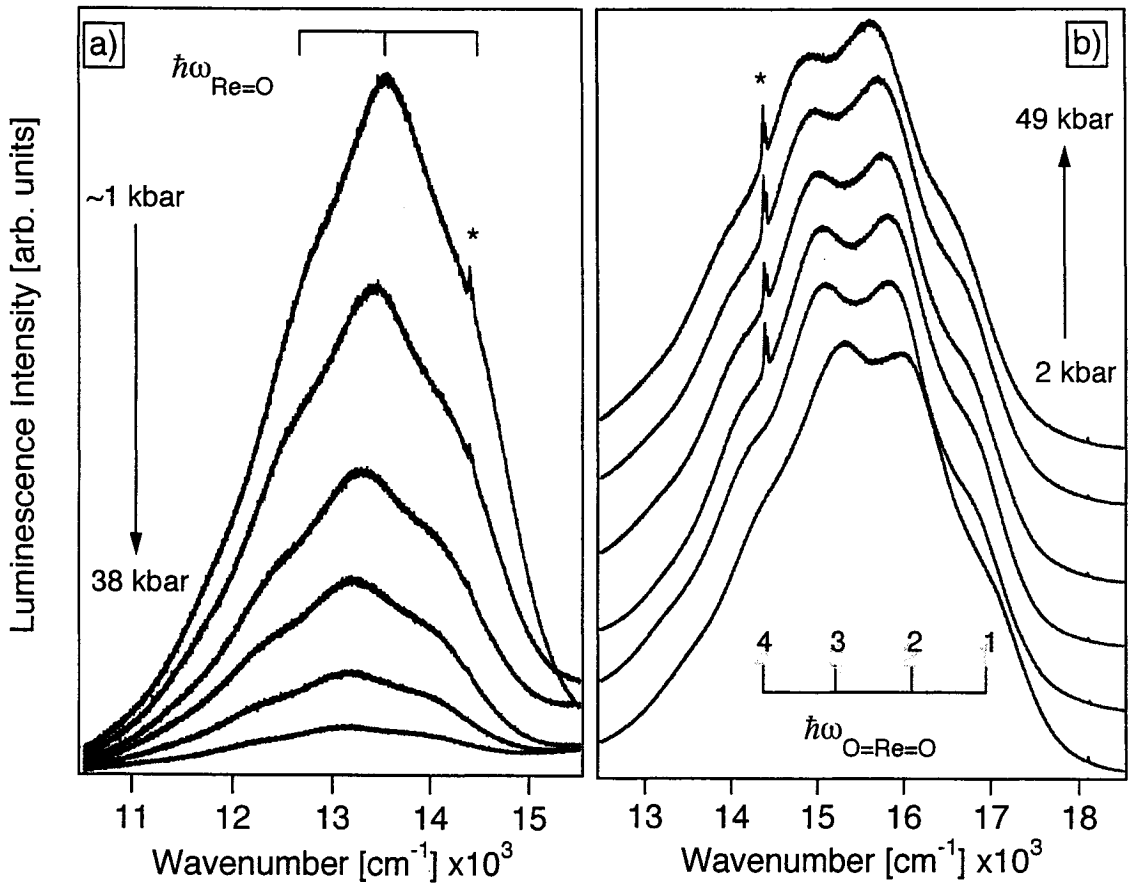

Figure 6.2. Examples of pressure-dependent luminescence spectra, a) $ReO_2(en)_2Cl$ from 1-38 kbar; b) $ReO_2(tmen)_2Cl$ from 2-49 kbar. The asterisk indicates the ruby luminescence used to calibrate pressure.

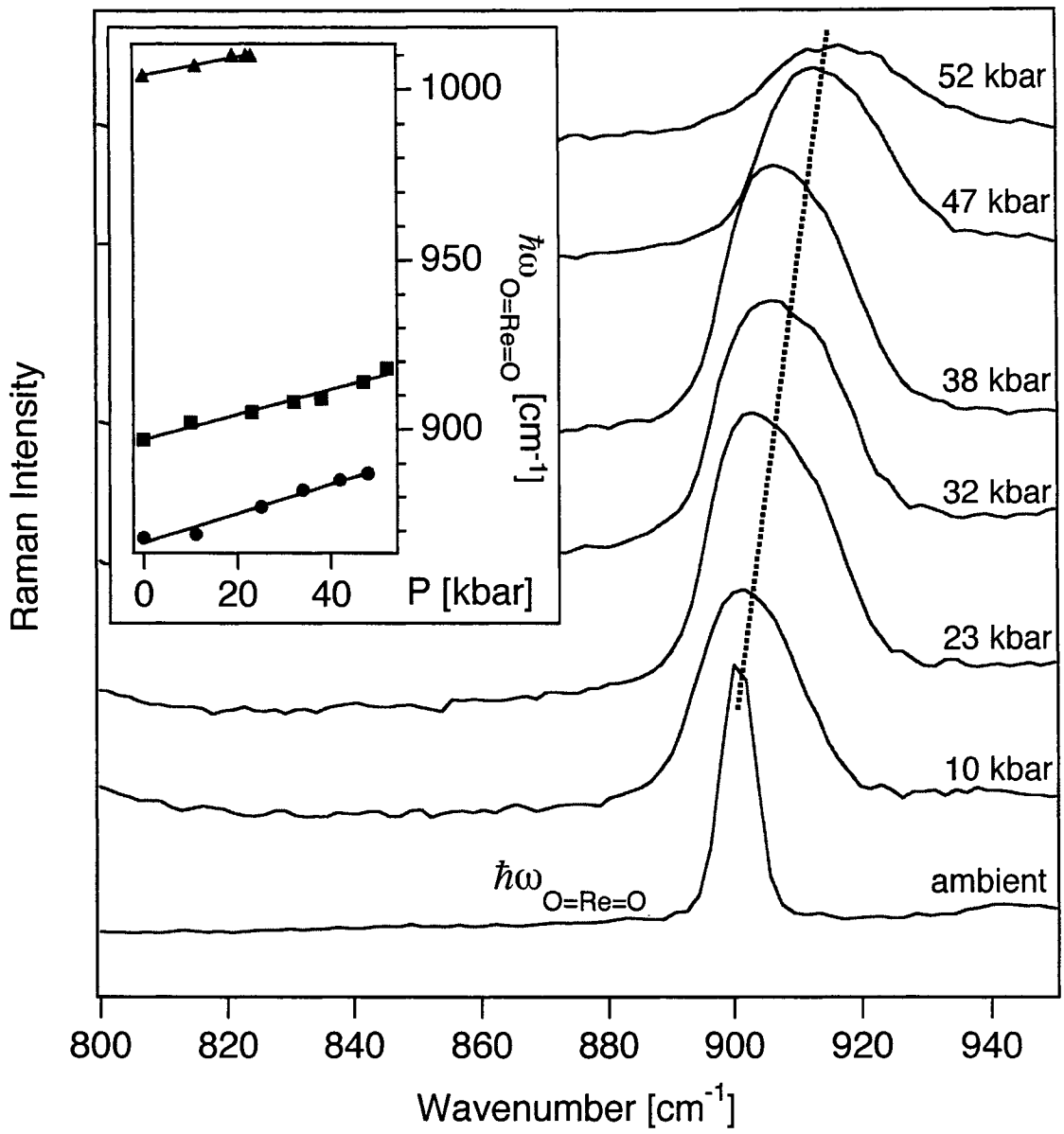

Figure 6.3. Ambient-temperature, pressure-dependent Raman spectra of solid $ReO_2(en)_2Cl$, showing the totally symmetric O=Re=O stretching region. The inset shows examples of the pressure dependence of the O=Re=O stretching mode from all complexes studied. Squares, circles, and triangles denote $ReO_2(en)_2Cl$, $ReO_2(tmen)_2Cl$, and $ReO_2(teen)_2Cl$, respectively.

6.4 Discussion

Our goal is to explain all of the pressure-dependent features for the three *trans*-dioxo rhenium(V) complexes. The experimental results show remarkably different luminescence properties for the closely related complexes, providing an ideal experimental data set that allows us to define and test theoretical models for pressure-tuning of third-row transition metal complexes. We base our model, as much as possible, on established models developed and applied to the title compounds.[19,27]

6.4.1 Coupled Electronic States of *trans*-$ReO_2(en)_2^+$ Complexes.

The electronic states of the title complexes have been well studied.[18,19,27] We will only briefly discuss some of the key points to give a background necessary to understand the effects of pressure on the luminescence spectra. Idealized D_{4h} symmetry labels are used for the electronic states even though the actual overall point group symmetry is lower for the title complexes. This approximation of the local symmetry around the rhenium(V) center has been justified from the previous low-temperature absorption and emission spectroscopy on *trans*-$[ReO_2L_4]^+$ complexes.[17-21,27] The rhenium(V) ion has the $[Xe]5d^2$ electron configuration which becomes $(b_{2g})^2$ (corresponding to d_{xy}^2) in D_{4h} symmetry and gives rise to a non-degenerate singlet electronic ground state, $^1A_{1g}$. The lowest unoccupied orbitals are the degenerate d_{xz}, d_{yz} (e_g) levels with metal-oxo π^* character. The first excited electronic state is a doubly degenerate triplet state, ^3E_g, corresponding to the $(b_{2g})^1(e_g)^1$ configuration. The energy separation of the HOMO and LUMO orbitals is described in terms of the AOM formalism by the parameter Δ_π.[27] Spin-orbit coupling splits the ^3E_g excited state into five components, one of which has the same A_{1g} symmetry as the ground state. The luminescence originates from the lowest energy [B_{1g}, B_{2g}] spin-orbit components of the ^3E_g state with electron density shifting from the e_g orbitals in the first excited state to the b_{2g} orbital. The long progression in the O=Re=O stretching mode shows that the molecule distorts strongly along this normal coordinate which suggests that the equilibrium molecular structure in the excited state is different than that of the ground state. Furthermore, there is a higher energy $^1A_{1g}$ excited state corresponding to the $(e_g)^2$ configuration as well as a A_{1g} spin-orbit component of a lower-lying $^3A_{2g}$ state arising from this configuration.[27] Due to the close proximity of

these two higher energy A_{1g} states and the fact that they cannot be observed spectroscopically,[18] we treat them as a single effective A_{1g} state. This situation leads to three states of A_{1g} symmetry that can interact through spin-orbit coupling and configuration interaction. Figure 6.4 shows the energies of the three A_{1g} states used in the model as a function of the spin-orbit coupling constant, ζ, for the $ReO_2(tmen)_2Cl$ complex. AOM calculations were performed using reasonable values for parameters describing bonding to the rhenium(V) metal center from the oxo and ethylenediamine ligands. It was assumed that π overlap from the tmen ligands was equal to zero, which is reasonable for saturated amine ligands.[27] The effect of the variation in spin-orbit coupling shows that the states interact strongly and, depending on the energy separation between the A_{1g} states, will have a large influence on the spectroscopic properties.

An important aspect of our model for the analysis of the pressure effects shown in Figures 6.1 and 6.2 are the avoided crossings of the A_{1g} states. These electronic states are coupled and their proximity has a large influence on the overall appearance of the emission bands. The non-zero off-diagonal matrix elements that define the coupling between states involve both the spin-orbit coupling and configuration interaction. In the literature formulation that we follow here, the configuration interaction between the lowest and highest energy $^1A_{1g}$ states is given as $\sqrt{2}K_{xy}$ where K_{xy} is defined in terms of the Racah parameters as $3B + C$.[27] Equations 6.1-6.3 give the crystal field energies of the A_{1g} states in terms of the parameters Δ_π and K_{xy} for the title complexes. All coupling constants are set to zero for these equations. Parameter values have been estimated from spectroscopic data[18,19,27] and serve as the basis from which we can understand the effect of external pressure on the spectra.

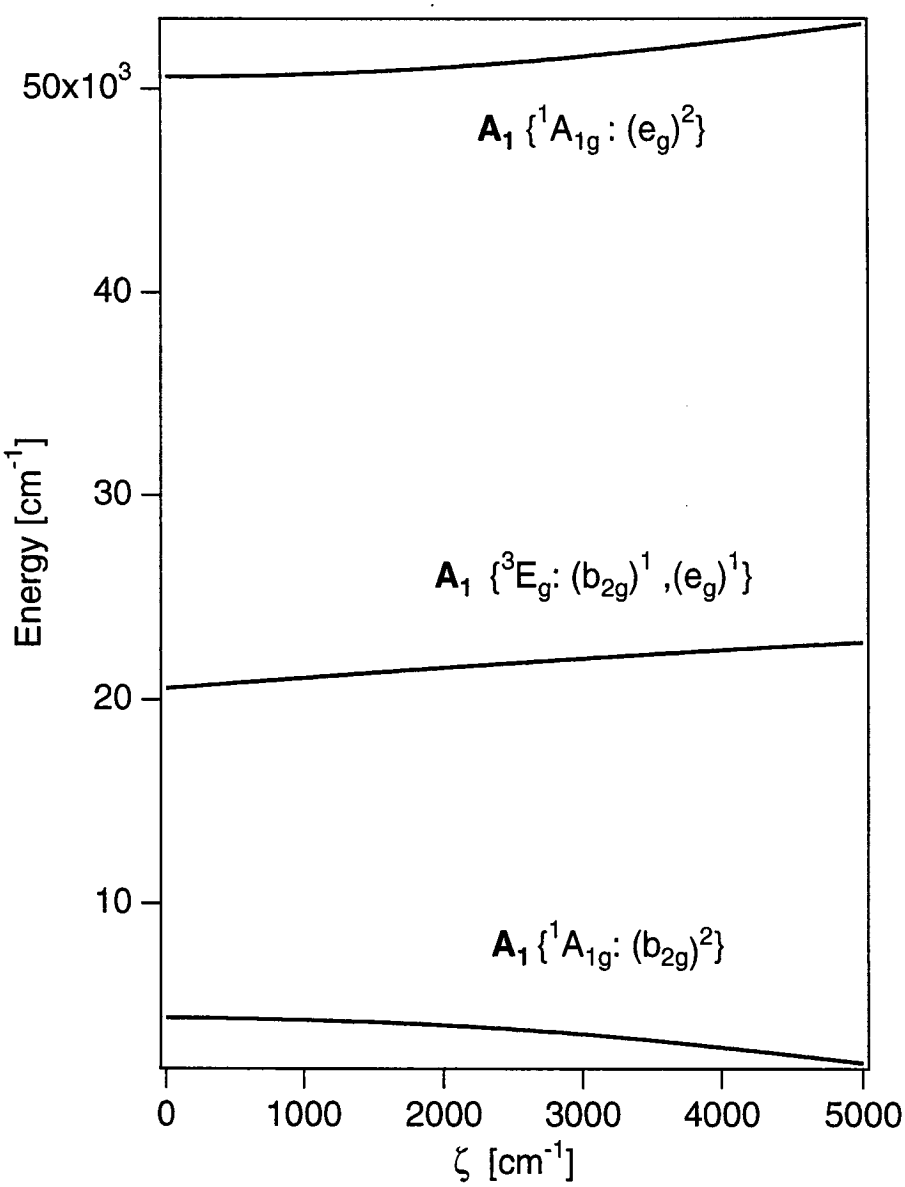

Figure 6.4. Calculated energies of the three coupled A_1 states (D_4 rotation group) of the $ReO_2(tmen)_2Cl$ complex using the AOM[29] with variable spin-orbit coupling. The following parameters were used as input for the calculations: $e_\pi(O)$ = 11,000 cm^{-1}, $e_\sigma(O)$ = 58,000 cm^{-1}, $e_\sigma(tmen)$ = 10,000 cm^{-1}, $e_\pi(tmen)$ = 0 cm^{-1}, B = 285 cm^{-1}, C = 1142 cm^{-1}.

$$E_1^{CF}\,[E(b_{2g})^2{:}^1A_{1g}] = 3K_{xy} \qquad \text{eq. 6.1}$$

$$E_2^{CF}\,[E(b_{2g})^1(e_g)^1{:}^3E_g] = \Delta_\pi \qquad \text{eq. 6.2}$$

$$E_3^{CF}\,[E(e_g)^2{:}^1A_{1g}] = 2\Delta_\pi + 4\,K_{xy} \qquad \text{eq. 6.3}$$

6.4.2 Theoretical Calculation of Emission Spectra.

Since we have vibronic structure resolved well enough to carry out a detailed theoretical analysis, we use the time-dependent theory of emission spectroscopy with potential energy surfaces defined by adjustable parameters to describe the electronic states of interest. This method has been covered extensively in the literature,[30-32] and we will only briefly summarize our application of this theoretical technique.

The vertical projection of the lowest energy vibrational eigenfunction of the initial state potential energy surface to the final state represents the first step of the emission process. This wavefunction is not an eigenfunction of the final potential surface and evolves with time. The time-dependent wavefunction, $\phi(t)$, is calculated on a one-dimensional grid representing the ground state potential energy surface using the split-operator method by Feit and Fleck.[33]

$$\phi(t+\Delta t) = e^{\left(\frac{i\Delta t}{4M}\right)\nabla^2} e^{-i\Delta t V} e^{\left(\frac{i\Delta t}{4M}\right)\nabla^2} \phi(t) + O\left[\left(\Delta t^3\right)\right] \qquad \text{eq. 6.4}$$

The vibronic luminescence spectrum is calculated as:[30-32]

$$I_{lum}(\omega) = C\omega^3 \int_{-\infty}^{+\infty} e^{i\omega t}\left\{\langle\phi|\phi(t)\rangle e^{-\Gamma^2 t^2 + \frac{iE_{00}}{\hbar t}}\right\} dt \qquad \text{eq. 6.5}$$

where ϕ is the wavefunction at time t=0. The most important component of equation 6.5 is the autocorrelation function, $\langle\phi|\,\phi(t)\rangle$. This term describes the time-dependent overlap of the propagating wave function on the final potential energy surface. The autocorrelation is Fourier transformed from time space to energy space to give the calculated spectrum. Γ represents a Gaussian phenomenological damping factor which is adjusted to fit the resolution of the experimental spectrum and E_{00} is the energy of the electronic origin. An attractive feature for the application of this method to our spectra is that potential energy functions of any form and even numerical potentials can be used as input for the states involved in the luminescence. It will be shown that the shape of the final potential energy surface is pressure-dependent leading to the vibronic features illustrated in Figures 6.1 and 6.2.

Because luminescence spectroscopy reveals information on ground-state properties, we define a model for the ground state that describes all spectral features with theoretical and spectroscopic parameters that are intrinsic to the title systems. As a first step, we start with the simplest possible model, the harmonic oscillator approximation. The harmonic potential energy surfaces calculated for the ground states from experimental vibrational frequencies did not reproduce the actual intensity distribution of the vibronic bands. To better account for the experimental vibronic bandshapes, Morse potentials were used to model the ground electronic states and were effective in reproducing the spectral features for $ReO_2(tmen)_2Cl$.[34] The Morse potential provides a good ad-hoc description of the pressure-dependent vibronic intensity distribution in the luminescence spectra of the title complexes. However, this description does not rationalize the different luminescence characteristics of the three complexes studied here. We develop in the following a model for the ground electronic states of the title complexes that explains all pressure-induced changes in vibronic structure and vibronic bandshapes using spectroscopic parameters.

6.4.3 Spectra arising from Coupled Electronic States under Variable External Pressure.

Previous low-temperature luminescence spectroscopic studies of the $ReO_2(en)_2Cl$ and $ReO_2(tmen)_2Cl$ showed that to reproduce non-replica intensity distributions of

vibronic progressions in the O=Re=O and Re-N(en) symmetric stretching modes, a model based on interacting electronic states was needed.[19] A similar model is also necessary to correctly describe the pressure-induced changes shown in Figures 6.1 and 6.2, namely, the change in the intensity distribution within the vibronic progression. Since we do not observe resolution of the Re-N(en) stretching modes, we limit the model to one-dimensional potential energy surfaces along the O=Re=O symmetric stretching coordinate and effectively treat the title complexes as tri-atomic, O=Re=O molecules. The potential energy surfaces of the three coupled A_{1g} states of all three *trans*-dioxo rhenium(V) complexes are given by:

$$V_{A_g} = \begin{bmatrix} E_1 & V_{12} & V_{13} \\ V_{12} & E_2 & V_{23} \\ V_{13} & V_{23} & E_3 \end{bmatrix} \qquad \text{eq. 6.6}$$

$$E_1 = E_1^{CF} + \frac{k_{Re=O}}{2} Q_{Re=O}^2 \qquad \text{eq. 6.7}$$

$$E_2 = E_2^{CF} + \frac{k_{Re=O}}{2} \left(Q_{Re=O}^2 - 2 Q_{Re=O} \Delta Q_{Re=O} \right) \qquad \text{eq. 6.8}$$

$$E_3 = E_3^{CF} + \frac{k_{Re=O}}{2} (Q_{Re=O}^2 - 4 Q_{Re=O} \Delta Q_{Re=O}) \qquad \text{eq. 6.9}$$

$k_{Re=O}$ is the force constant of the O=Re=O symmetric stretching mode in the ground and excited states, respectively, where $k = 4\pi^2 M(\hbar\omega)^2$; M is the mass of the mode (16 g/mole) and $\hbar\omega$ is the frequency of the O=Re=O stretching mode determined from Raman spectroscopy in cm^{-1} given in Table 6.1. $\Delta Q_{Re=O}$ is the offset of the potential energy minima of the A_{1g} state arising from the $(b_{2g})^1(e_g)^1$ configuration along the normal coordinate. We use 2 $\Delta Q_{Re=O}$ for the offset of the highest energy A_{1g} state, which arises from the $(e_g)^2$ configuration. The diabatic surfaces, E_1, E_2, E_3, represent three harmonic potential energy surfaces for A_{1g} states offset along the energy ordinate by the crystal field energies for each state and coupled through the off-diagonal elements, V_{12}, V_{13}, V_{23},

as illustrated in Figure 6.5. We obtain the lowest energy adiabatic potential energy of the ground state as the first eigenvalue of the 3×3 matrix in eq. 6.6. This anharmonic ground-state potential surface is shown in Figure 6.5 and used to calculate pressure-dependent luminescence spectra.

This model of three interacting states has three avoided crossings. Figure 6.5 only shows the lowest energy crossing, the others are off the figure at higher energy. We find that the lowest energy crossing is the most important due to the close proximity of the lower energy A_{1g} states, but neglecting the other two crossings leads to unsatisfactory calculated spectra. With the displacement of potential surfaces along the normal coordinate and the energy offset, the surface of the ground state is flattened for $Q_{Re=O} > 0$. The emitting state in this model is approximated as a harmonic potential energy surface that represents the lowest energy spin-orbit component of the ^3E_g excited state. Luminescence occurs from the lowest, most harmonic vibrational level of this state. We neglect the decrease of the force constant of the O=Re=O symmetric stretching mode in the excited state and set this value equal to the force constant of the ground state, $k_{Re=O}$. This approximation is sufficient for the resolution of the spectra in Figures 6.1 and 6.2.

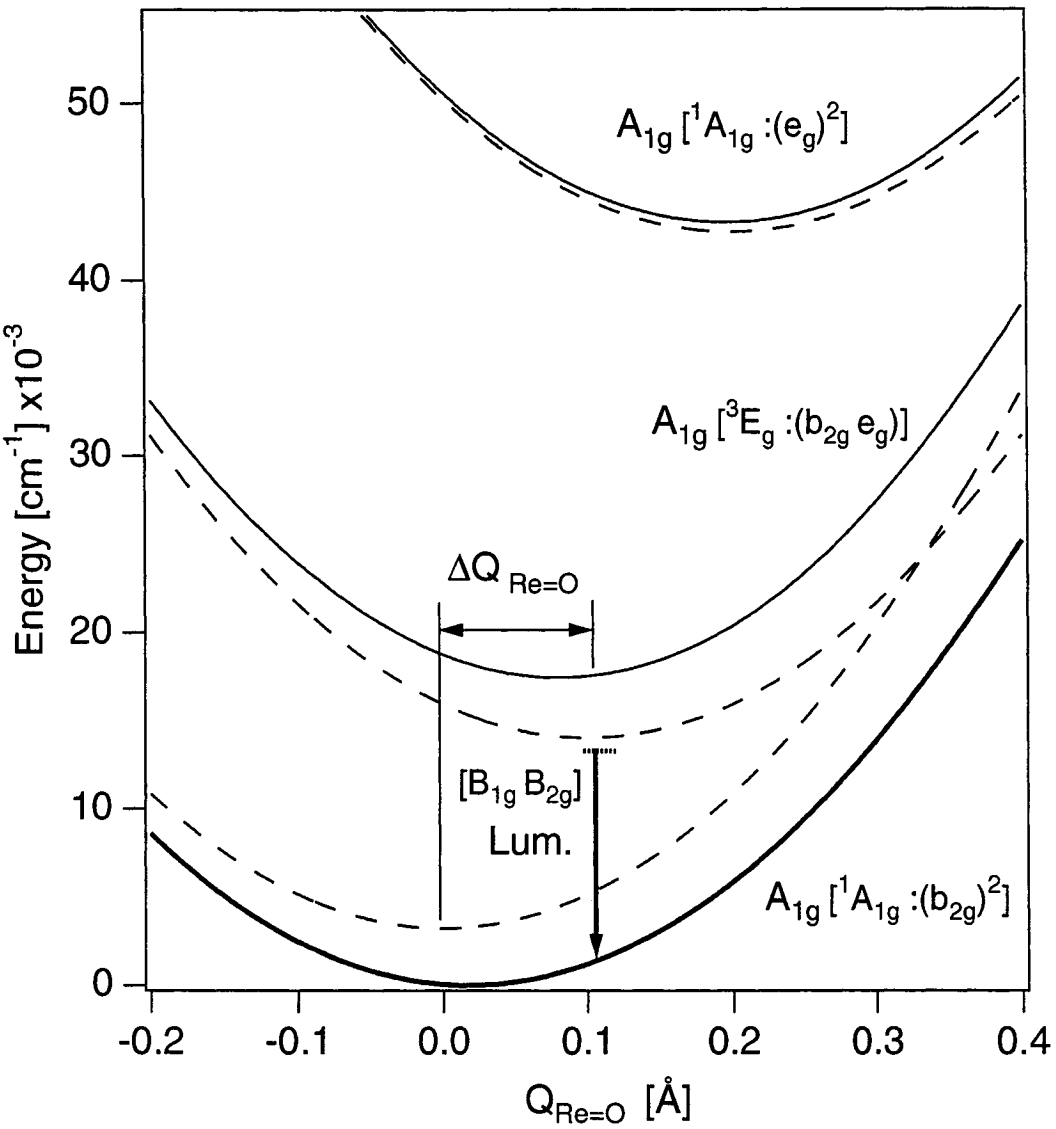

Figure 6.5 Coupled potential energy surfaces calculated from equation 6.6. Solid and dashed lines represent adiabatic and diabatic potentials, respectively. The lowest adiabatic surface corresponds to the electronic ground state used to calculate luminescence spectra. The crystal field energies E_i^{CF} (eqs. 6.1-6.3) for all three A_{1g} states are given along the vertical dashed line at Q=0.

We calculate spectra based on the model with three A_{1g} coupled states using eqs.(6.6-6.9). K_{xy} and Δ_π values for the $ReO_2(en)_2Cl$ and $ReO_2(tmen)_2Cl$ complexes are taken from previous low-temperature work.[19] We keep the K_{xy} and Δ_π parameters independent of pressure and vary only one coupling constant to replicate the experimental spectra. This choice is justified by the small variation of the energies of the luminescence maxima in Figures 6.1 and 6.2. It is on the order of 300 cm^{-1} between ambient pressure and 40 kbar and corresponds to approximately 2% of the luminescence energy. Such a small variation of K_{xy} and Δ_π is well within the error of these parameters, which we estimate to be on the order of 5%. The value of the parameter Δ_π is the same for all three *trans*-dioxo rhenium(V) complexes. Preliminary density functional theory (DFT) calculations show that the energy separation on the HOMO-LUMO gap, Δ_π, does not vary significantly between the three complexes studied.[35] The K_{xy} parameter varies by approximately 1000 cm^{-1} between the title complexes and this variation is the main reason for the variation of the luminescence energies in Figure 6.1. The coupling between the two lowest energy A_{1g} states, V_{12}, is varied to describe the pressure-dependent shape of the ground state potential surface. The other two coupling constants, V_{13} and V_{23}, are then set to equal values on the order of matrix elements coupling these states and are pressure independent. The pressure dependence of the coupling constant V_{12} is likely to reflect both intra- and intermolecular effects and we see that variation of this parameter best reproduces the flattening of the ground-state adiabatic surface and yields a better fit to experimental spectra on the "red" side of the luminescence band.

The offset, $\Delta Q_{Re=O}$, of the coupled potential energy surfaces along the O=Re=O stretching coordinate is adjusted to reproduce the pressure-induced changes in vibronic structure. This parameter shows a strong pressure dependence, which could again arise from both intra- and intermolecular effects, but it is the molecular electronic structure that leads to the distinct differences between the pressure-dependence of the luminescence spectra of the three complexes. For each calculation, we consider the first resolved, highest energy, member of the vibronic progression as the origin of the emission and use it to define E_{00}, the energy of electronic origin of the calculated spectra in eq. 6.5. We set the frequency of the O=Re=O stretching mode, $\hbar\omega$, in the calculated spectra to the value from the pressure-dependent Raman spectra. Figures 6.6-6.8 compare calculated and

experimental pressure-dependent luminescence spectra of the title complexes and Tables 6.1-6.3 contain all parameter values used. For $ReO_2(en)_2Cl$ and $ReO_2(tmen)_2Cl$ the agreement between experimental and calculated spectra is excellent and allows us to discuss the quantitative variation of $\Delta Q_{Re=O}$, E_{00}, and the energy of the band maxima, E_{max}, in the following.

The calculated spectra in best agreement with the experiment were obtained for $ReO_2(tmen)_2Cl$. This compound shows the relatively intense luminescence in Figures 6.2b and 6.7 making a baseline correction unnecessary and its well-resolved vibronic transition allow for an easy adjustment of the parameters in Table 6.2. The calculated spectra of $ReO_2(en)_2Cl$ were adjusted to compensate for the baseline by adding a linear function to the calculated spectrum. This baseline becomes important for the weak luminescence bands at high pressure. At higher pressures, the signal-to-noise ratio decreases as well, which made fitting the high-pressure spectra difficult. In spite of this problem, the intensity ratio of the first and second peaks is clearly seen to change with pressure in Figures 6.2a and 6.6, leading to reliable calculated spectra. The luminescence characteristics of the $ReO_2(teen)_2Cl$ complex shown in Figures 6.1 and 6.8 are markedly different from the other two complexes, forcing us to use a simplified version of the model described above. Coupling from the highest energy A_{1g} state to the others is neglected because of the large energy separation between A_{1g} states leading to a ground state potential surface that is almost harmonic. The calculated spectra are very similar to those obtained for a harmonic ground-state potential. Moreover, the luminescence spectrum of this complex was only weakly affected by pressure and the effective coupling between two A_{1g} states was held constant for all pressures. The lack of resolved vibronic structure in the luminescence of $ReO_2(teen)_2Cl$ leads to a situation with less constraints on model parameter values. We use the frequency of the O=Re=O symmetric stretching mode from the pressure-dependent Raman spectra. The energy of the electronic origin, E_{00}, was estimated and kept independent of pressure. A value for K_{xy} was chosen for this complex based on the established trend that interelectronic repulsion decreases for increased substitution on ethylenediamine ligands.[36,37] The offset $\Delta Q_{Re=O}$ was then adjusted to lead to an acceptable agreement between experiment and calculated spectra.

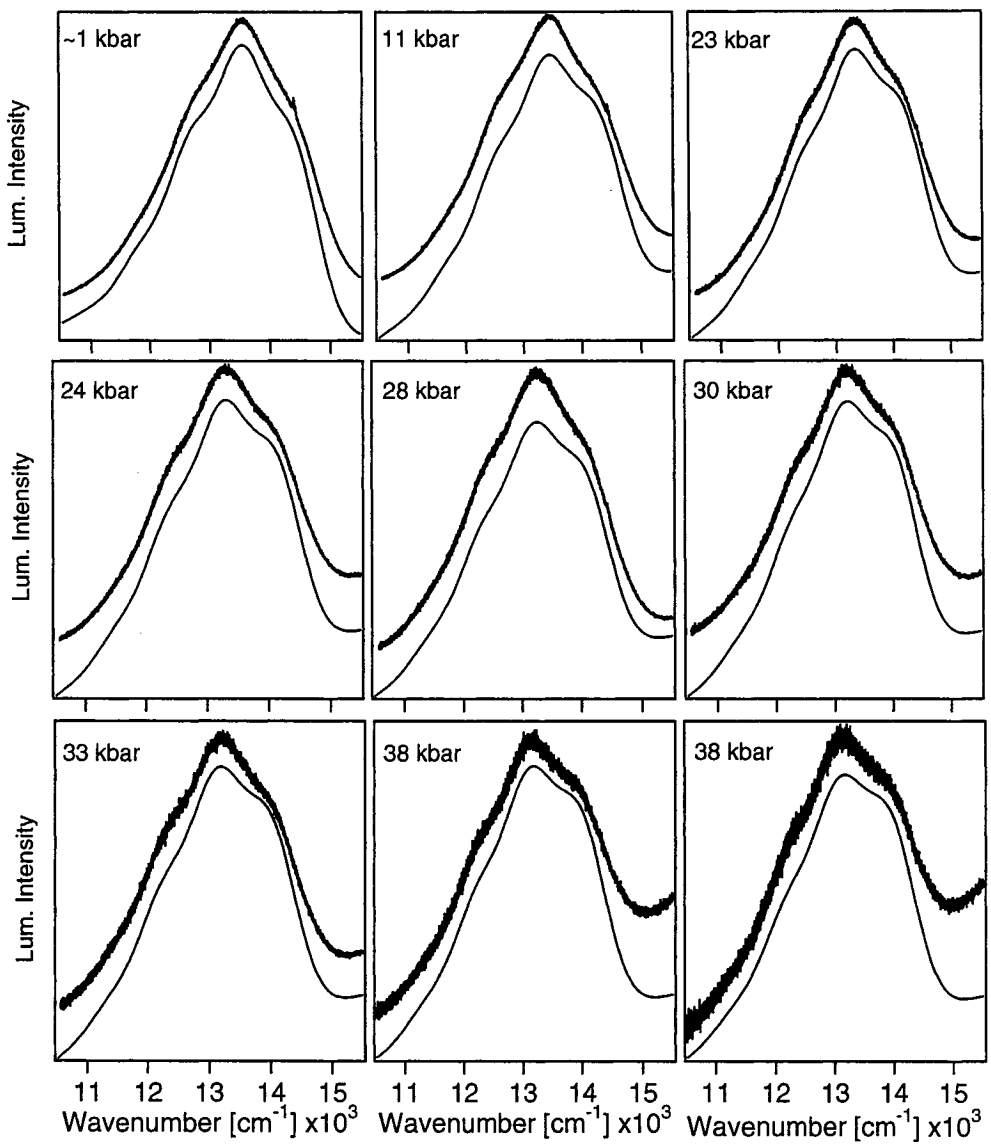

Figure 6.6. Examples of experimental pressure-dependent luminescence spectra compared to calculations obtained from the coupled potential energy surfaces for $ReO_2(en)_2Cl$ with the parameter values in Table 6.1. Top and bottom traces in each panel denote experimental and calculated spectra, respectively. Spectra are offset along the ordinate for clarity.

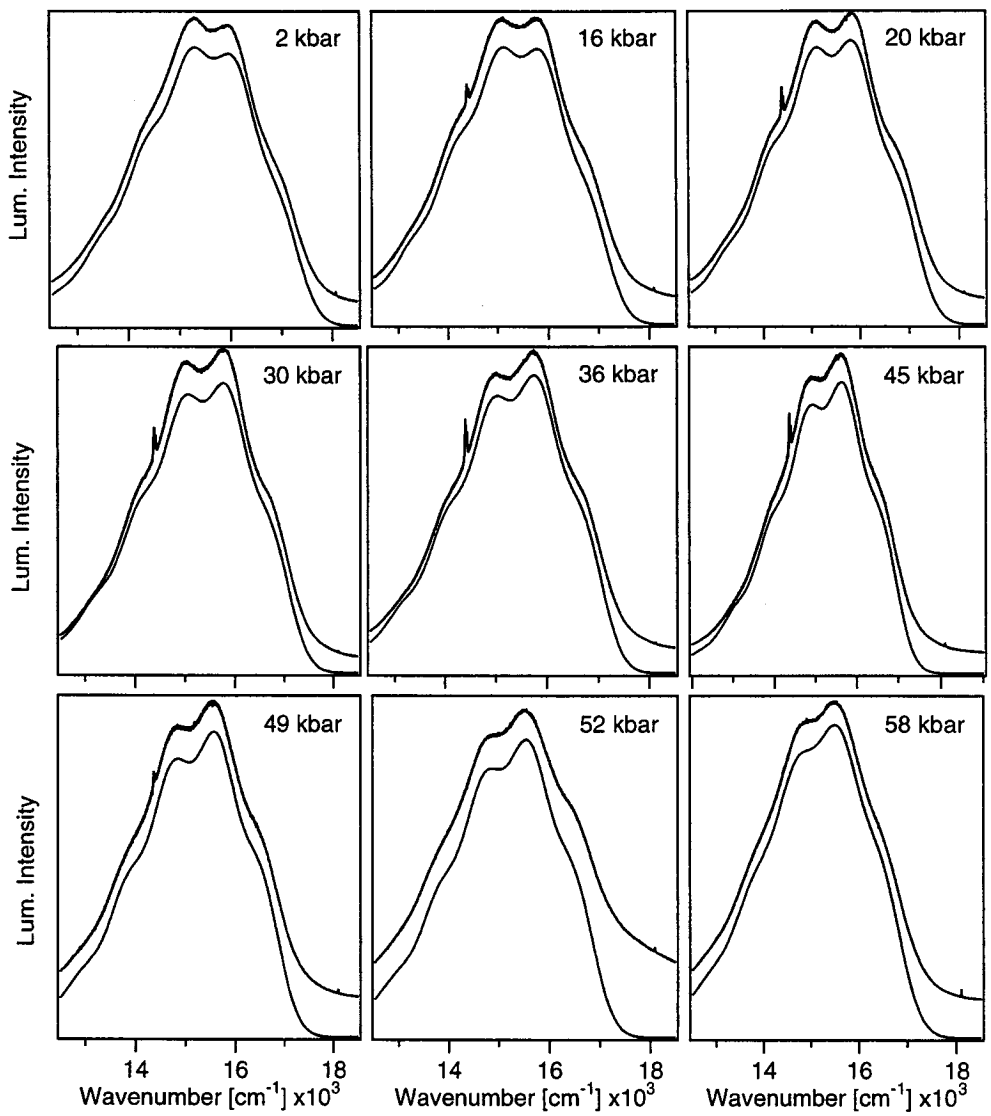

Figure 6.7. Examples of experimental pressure-dependent luminescence spectra compared to calculations obtained from the coupled potential energy surfaces for $ReO_2(tmen)_2Cl$ with the parameter values from Table 6.2. Experimental spectra are offset along the ordinate for clarity.

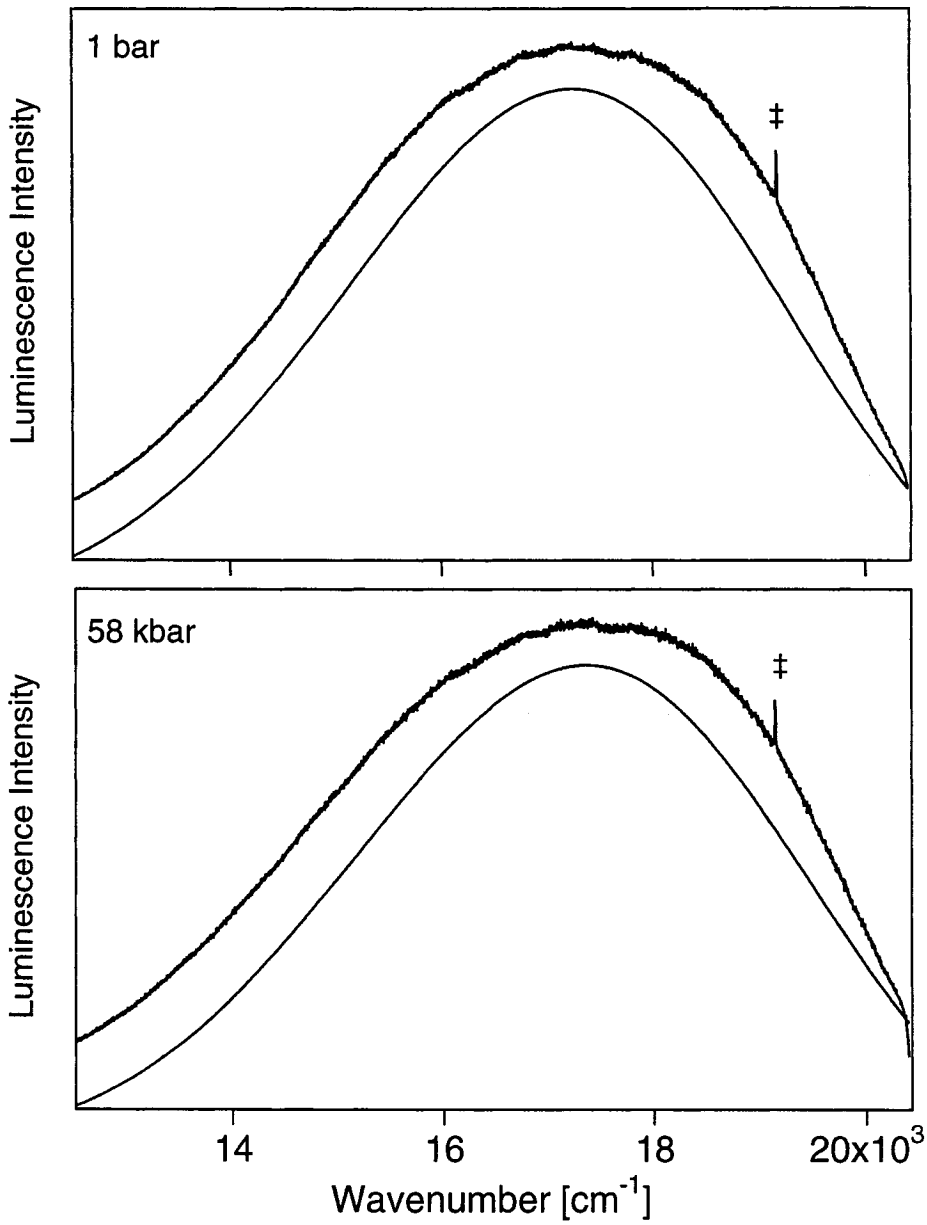

Figure 6.8. Pressure-dependent luminescence spectra of $ReO_2(teen)_2Cl$ compared to calculations obtained with the parameter values in Table 6.3. Experimental spectra are offset along the ordinate for clarity. The ‡ symbols denote the Raman active t_{2g} phonon mode of the diamond anvils.

P [kbar]	ΔQ [Å]	K_{xy} [cm^{-1}]	Δ_π [cm^{-1}]	$\hbar\omega_{O=Re=O}$ [cm^{-1}]	V_{12} [cm^{-1}]	V_{13} [cm^{-1}]	V_{23} [cm^{-1}]	E_{00} [cm^{-1}]	Γ [cm^{-1}]
1	0.110	3100	22,000	885	7250	2500	2500	14,545	285
11	0.107	3100	22,000	885	7215	2500	2500	14,421	290
23	0.106	3100	22,000	885	7215	2500	2500	14,330	290
24	0.105	3100	22,000	890	7170	2500	2500	14,270	290
28	0.105	3100	22,000	890	7150	2500	2500	14,204	295
30	0.103	3100	22,000	890	7135	2500	2500	14,172	295
33	0.103	3100	22,000	895	7115	2500	2500	14,147	295
38	0.102	3100	22,000	895	7105	2500	2500	14,127	295
38	0.100	3100	22,000	895	7080	2500	2500	14,097	300

Table 6.1. Parameters for potential energy surfaces and time-dependent calculations for $ReO_2(en)_2Cl$.

P [kbar]	ΔQ [Å]	K_{xy} [cm^{-1}]	Δ_π [cm^{-1}]	$\hbar\omega_{O=Re=O}$ [cm^{-1}]	V_{12} [cm^{-1}]	V_{13} [cm^{-1}]	V_{23} [cm^{-1}]	E_{00} [cm^{-1}]	Γ [cm^{-1}]
2	0.120	2000	22,000	880	5850	2500	2500	17,098	285
16	0.118	2000	22,000	885	5840	2500	2500	16,934	285
20	0.116	2000	22,000	890	5830	2500	2500	16,927	280
30	0.115	2000	22,000	890	5815	2500	2500	16,878	280
36	0.113	2000	22,000	895	5805	2500	2500	16,821	280
45	0.112	2000	22,000	895	5800	2500	2500	16,728	280
49	0.111	2000	22,000	900	5790	2500	2500	16,671	280
52	0.110	2000	22,000	900	5780	2500	2500	16,645	285
58	0.110	2000	22,000	900	5770	2500	2500	16,630	300

Table 6.2. Parameters for potential energy surfaces and time-dependent calculations for $ReO_2(tmen)_2Cl$.

P [kbar]	ΔQ [Å]	K_{xy} [cm^{-1}]	Δ_π [cm^{-1}]	$\hbar\omega_{O=Re=O}$ [cm^{-1}]	V_{12} [cm^{-1}]	$V_{13}{}^a$ [cm^{-1}]	$V_{23}{}^a$ [cm^{-1}]	E_{00} [cm^{-1}]	Γ [cm^{-1}]
0.001	0.150	400	22,000	1000	3500			21,077	600
23	0.150	400	22,000	1000	3500			21,077	600
28	0.148	400	22,000	1000	3500			21,077	600
35	0.148	400	22,000	1000	3500			21,077	600
42	0.148	400	22,000	1000	3500			21,077	600
46	0.147	400	22,000	1000	3500			21,077	600
52	0.147	400	22,000	1000	3500			21,077	600
55	0.147	400	22,000	1000	3500			21,077	600
58	0.147	400	22,000	1000	3500			21,077	600

[a] Coupling between the highest energy A_{1g} state to the lower energy A_{1g} states is neglected in calculating spectra for the $ReO_2(teen)_2Cl$ complex ($V_{13} = V_{23} = 0$).

Table 6.3. Parameters for potential energy surfaces and time-dependent calculations for $ReO_2(teen)_2Cl$.

We found that a model with only one avoided crossing and two coupled states is not sufficient to reproduce the experimental luminescence bands. Figures 6.9 and 6.10 show examples of calculated spectra of $ReO_2(en)_2Cl$ and $ReO_2(tmen)_2Cl$, respectively, using only two coupled states (i.e., one avoided crossing) for the lowest and highest pressure spectra. The large discrepancy on the lower energy side of the spectra between the calculated and experimental spectra highlight the necessity for including a third state at higher energy, which becomes increasingly important for lower energy luminescence where the close proximity of the avoided crossings to the Franck-Condon region have a large influence on the bandshapes. Traditional theoretical models for pressure-dependent electronic spectra involve analytical pressure-dependent terms that are added to the

potential energy surfaces.[38-41] We were not able to successfully apply these models to fit our spectra.

The most important results of the calculations shown in Figures 6.6-6.8 and Tables 6.1-6.3 are the quantitative pressure effects on the spectroscopic parameters of the *trans*-dioxo rhenium(V) complexes. The trend for normal coordinate offsets, $\Delta Q_{Re=O}$ in eqs. 6.7-6.9, at ambient pressure shows that as the ethylenediamine ligand becomes more substituted, the distortion along the O=Re=O stretching mode becomes larger. $\Delta Q_{Re=O}$ is adjusted to reproduce the changes in vibronic structure and Figure 6.11 shows its pressure dependences for all three complexes. We observe that this parameter decreases uniformly with pressure, which is expected as the rhenium-oxygen double bond lengths decrease with pressure. $\Delta Q_{Re=O}$ varies the most with pressure for $ReO_2(en)_2Cl$ at -3×10^{-4} Å/kbar, followed by $ReO_2(tmen)_2Cl$ at -2×10^{-4} Å/kbar, and, lastly, $ReO_2(teen)_2Cl$, which shows little change at -5×10^{-5} Å/kbar. These values illustrate how pressure changes metal-oxo bond distances with similar ancillary ligands by following the pressure-induced changes in the vibronic structure.

An experimental feature that is often reported in pressure-tuning spectroscopic studies is the shift of the band maximum with pressure. This particular observation can be explained most easily in terms of pure electronic energy diagrams for a molecule held frozen at its ground-state equilibrium geometry. Band maxima are not directly obtained for the spectra in Figures 6.1 and 6.2 because of the resolved vibronic structure. We determine this value by using the parameters in Tables 6.1-6.3 and increasing the phenomenological damping factor, Γ, until an unresolved calculated spectrum is obtained, for which the maximum is easily determined. The luminescence bands of $ReO_2(en)_2Cl$ and $ReO_2(tmen)_2Cl$ shift to lower energy by -8 cm^{-1}/ kbar and -6 cm^{-1}/ kbar, respectively. The $ReO_2(teen)_2Cl$ complex shows a slight blue-shift of +2 cm^{-1}/ kbar with increasing pressure. Figure 6.12 shows the pressure dependence of the band maximum, E_{max}, and the calculated value of the electronic origin, E_{00}.

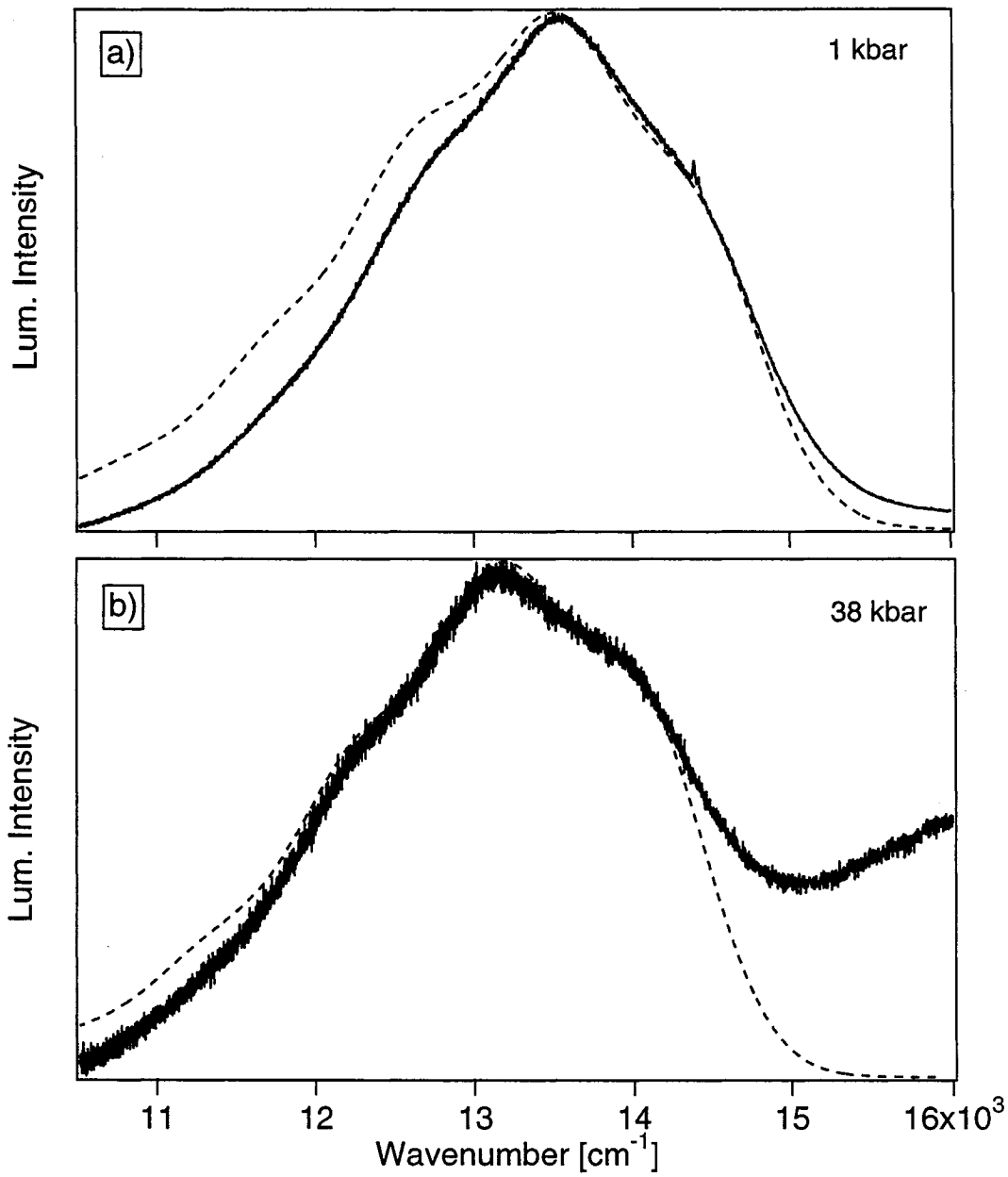

Figure 6.9. Pressure-dependent luminescence spectra of $ReO_2(en)_2Cl$ and calculated spectra using only two coupled states. a) 1 kbar: ΔQ = 0.096 Å, ΔE = 12700 cm^{-1}, E_{00} = 14545 cm^{-1}, V_{12} = 2000 cm^{-1}, $\hbar\omega$ = 885 cm^{-1}. b) 38 kbar: ΔQ = 0.086 Å, ΔE = 12700 cm^{-1}, E_{00} = 14015 cm^{-1}, V_{12} = 700 cm^{-1}, $\hbar\omega$ = 895 cm^{-1}.

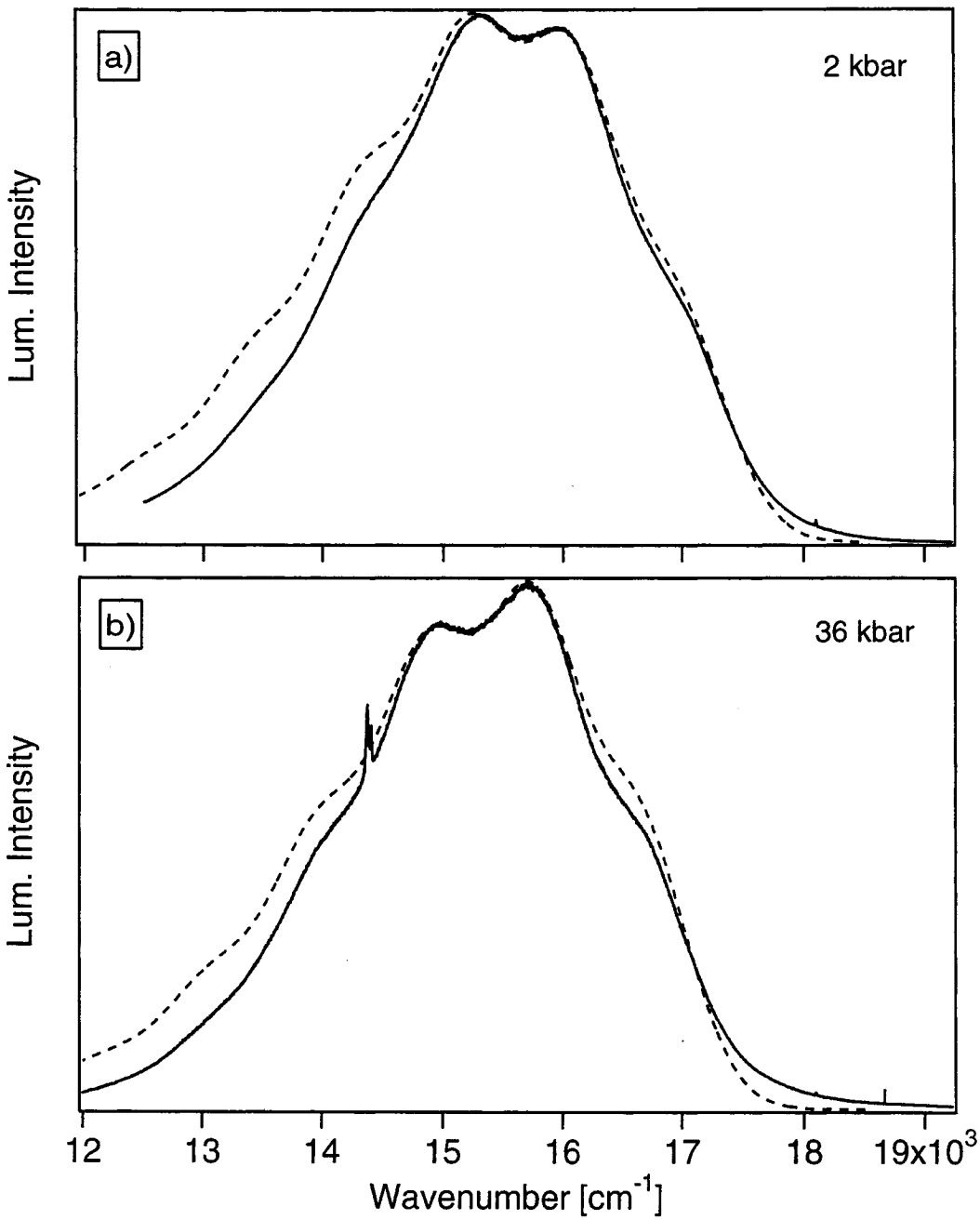

Figure 6.10. Pressure-dependent luminescence spectra of $ReO_2(tmen)_2Cl$ and calculated spectra using only two coupled states. a) 2 kbar: ΔQ = 0.110 Å, ΔE = 16000 cm^{-1}, E_{00} = 17098 cm^{-1}, V_{12} = 3200 cm^{-1}, $\hbar\omega$ = 880 cm^{-1}. b) 36 kbar: ΔQ = 0.102 Å, ΔE = 16000 cm^{-1}, E_{00} = 16821 cm^{-1}, V_{12} = 2100 cm^{-1}, $\hbar\omega$ = 895 cm^{-1}.

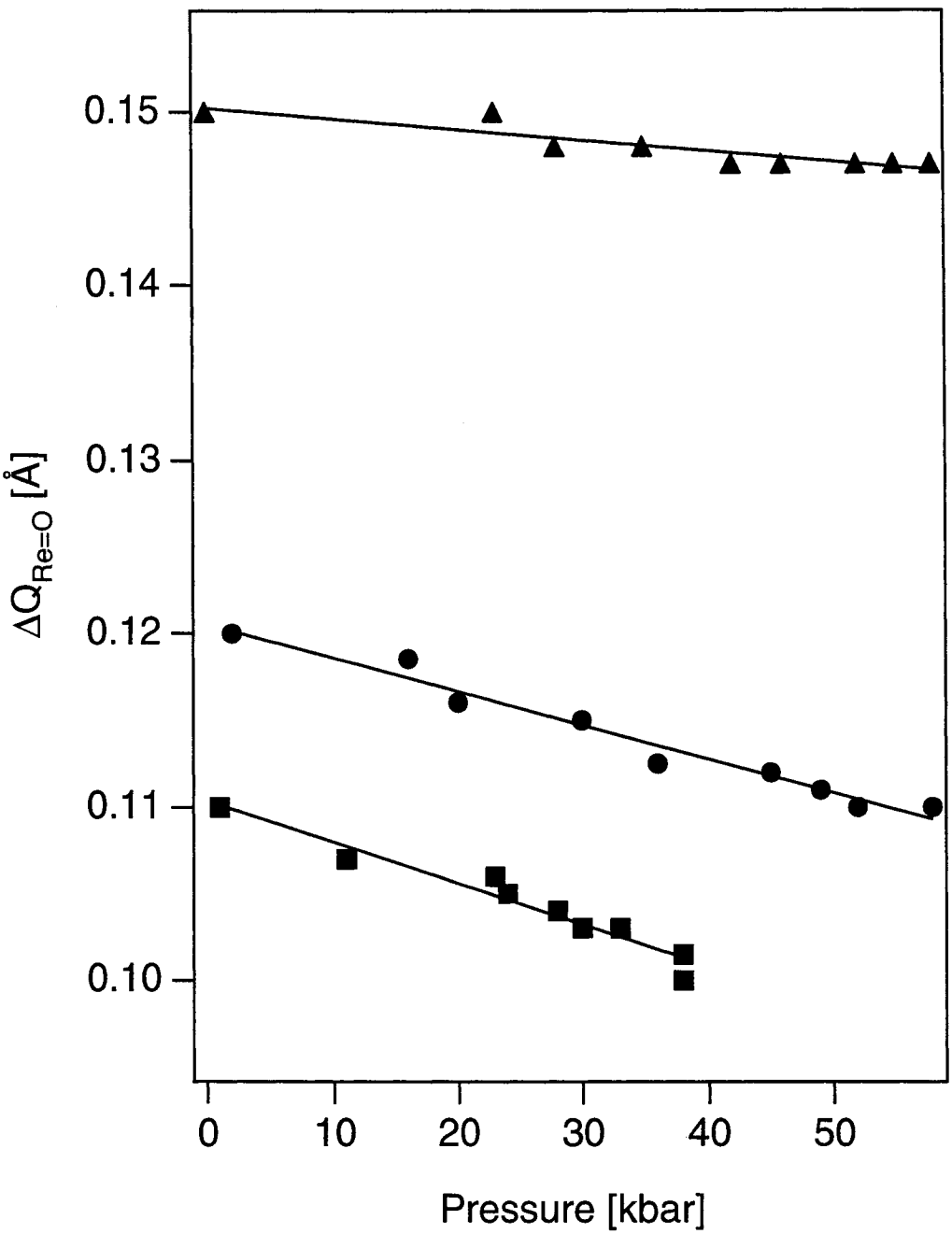

Figure 6.11. ΔQ *versus* pressure for $ReO_2(en)_2Cl$ (squares), $ReO_2(tmen)_2Cl$ (circles), and $ReO_2(teen)_2Cl$ (triangles) obtained from the potential energy surfaces used to calculate spectra.

The behavior of the calculated E_{max} and E_{00} values with pressure shows how the luminescence band maxima and onsets depend on the displacement of the emitting state potential surface relative to the ground-state potential surface both in energy and normal coordinate offset. We observe that these quantities do not have the same pressure dependence. The E_{00} values for both $ReO_2(en)_2Cl$ and $ReO_2(tmen)_2Cl$ decrease faster than the band maxima with pressure. This difference illustrates that the energy of the band maxima is not only influenced by the electronic energies, but also by the pressure-dependent displacement, $\Delta Q_{Re=O}$, of the potential minima along the normal coordinate. Since luminescence of $ReO_2(teen)_2Cl$ lacks well-resolved vibronic structure and shows only small shifts in band energies, the change in normal coordinate offset is sufficient to reproduce shifts in band maxima. This is accomplished by holding the E_{00} value of the emitting state constant and adjusting $\Delta Q_{Re=O}$, based on the range of frequency shift of this mode in the pressure-dependent Raman spectra, to replicate the energy shift of the band. The limits of the approach based on pure electronic levels are quantitatively illustrated here since these models cannot predict the different behavior of E_{max} and E_{00} with pressure.

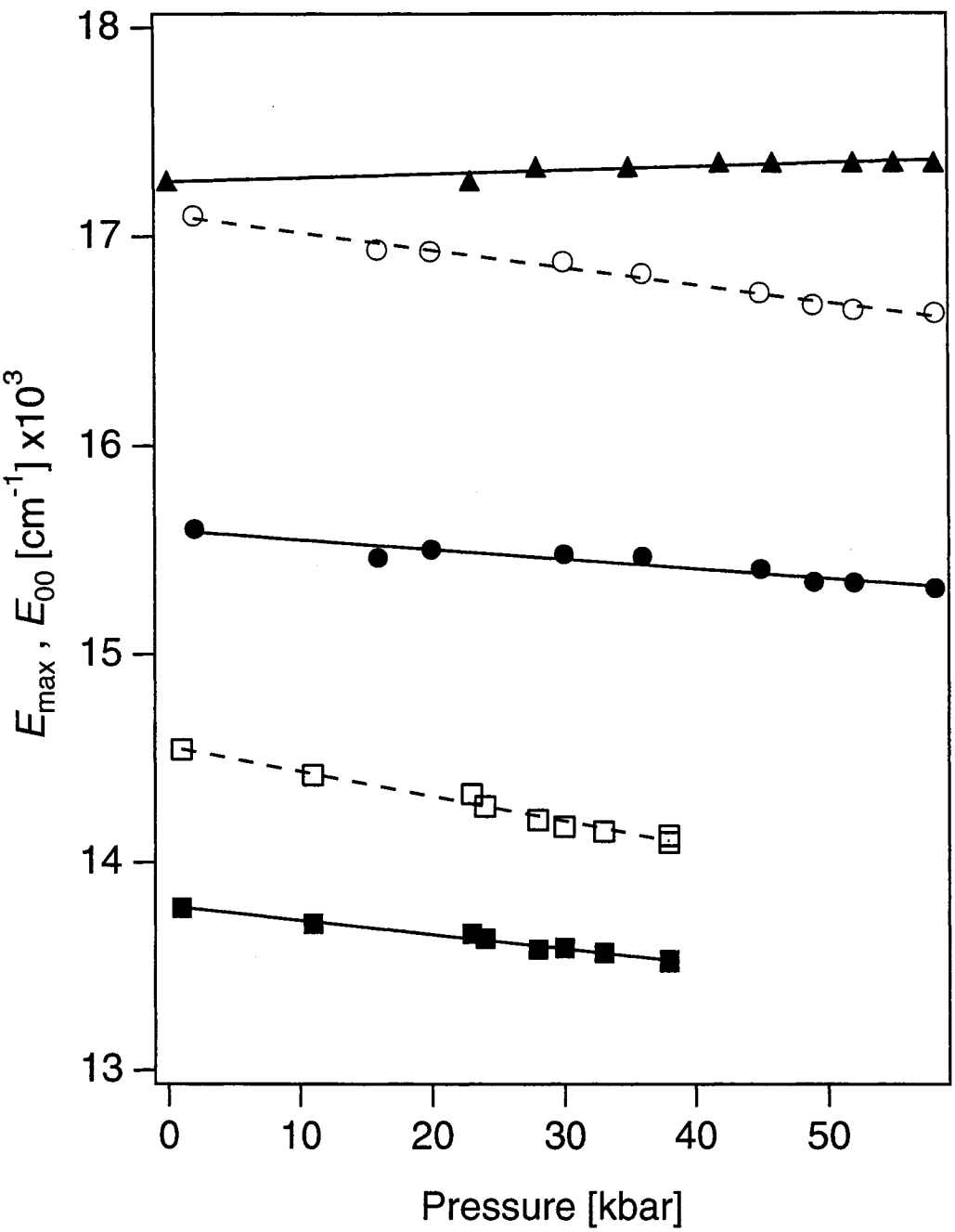

Figure 6.12. Emission energy maximum, E_{max}, (filled-in symbols) and energy of electronic origin, E_{00}, (open symbols) *versus* pressure, for $ReO_2(en)_2Cl$ (squares), $ReO_2(tmen)_2Cl$ (circles), $ReO_2(teen)_2Cl$ (triangles).

The ground-state potential energy surfaces show distinct changes that can be correlated with the proximity of avoided crossings. The overall qualitative trend found in all experimental luminescence spectra is that pressure "pushes up" the ground-state adiabatic potential at large values of $Q_{Re=O}$ so that it becomes more harmonic in character. Both intra- and intermolecular effects are likely responsible for this behavior. Figures 6.13a-c illustrate the effect of pressure-dependent coupling on the ground-state potential energy surfaces for all three *trans*-dioxo complexes at the lowest and highest pressure for which we obtained data. The difference between the lowest and highest pressure potential energy surfaces for the three complexes is shown on Figure 6.13d. These traces give the quantitative variations of the ground state potential as a function of pressure over a significant range of $Q_{Re=O}$, information that can only be obtained through luminescence spectroscopy. The pressure-induced changes to the shape of the ground state potential energy surface and the calculated spectra are most pronounced for the lower energy emitting complexes, because they have avoided crossings at low energies, as illustrated in Figure 6.5.

Our analysis shows that the ground-state potential energy surface is significantly altered by pressure as shown in Figure 6.13. It is interesting to note that the pressure-induced increase in vibrational frequency, illustrated in Figure 6.3, is not sufficient to explain the change of the potential energy surfaces in Figure 6.13. This change in the O=Re=O stretching frequency involves a small region of the ground-state potential energy surface near its minimum and far from the Franck-Condon region where the luminescence occurs, but the Raman results are important to define the effect of pressure on the vibrational frequency used in our calculations. The vibronic luminescence spectra provide insight into a much larger part of the ground-state potential energy surface than the fundamental vibrational transition probed by Raman spectroscopy, and the combination of electronic and vibrational spectroscopy under external pressure allows the identification of pressure-induced variations of all parameters, as illustrated in Scheme 6.1 and Tables 6.1-6.3.

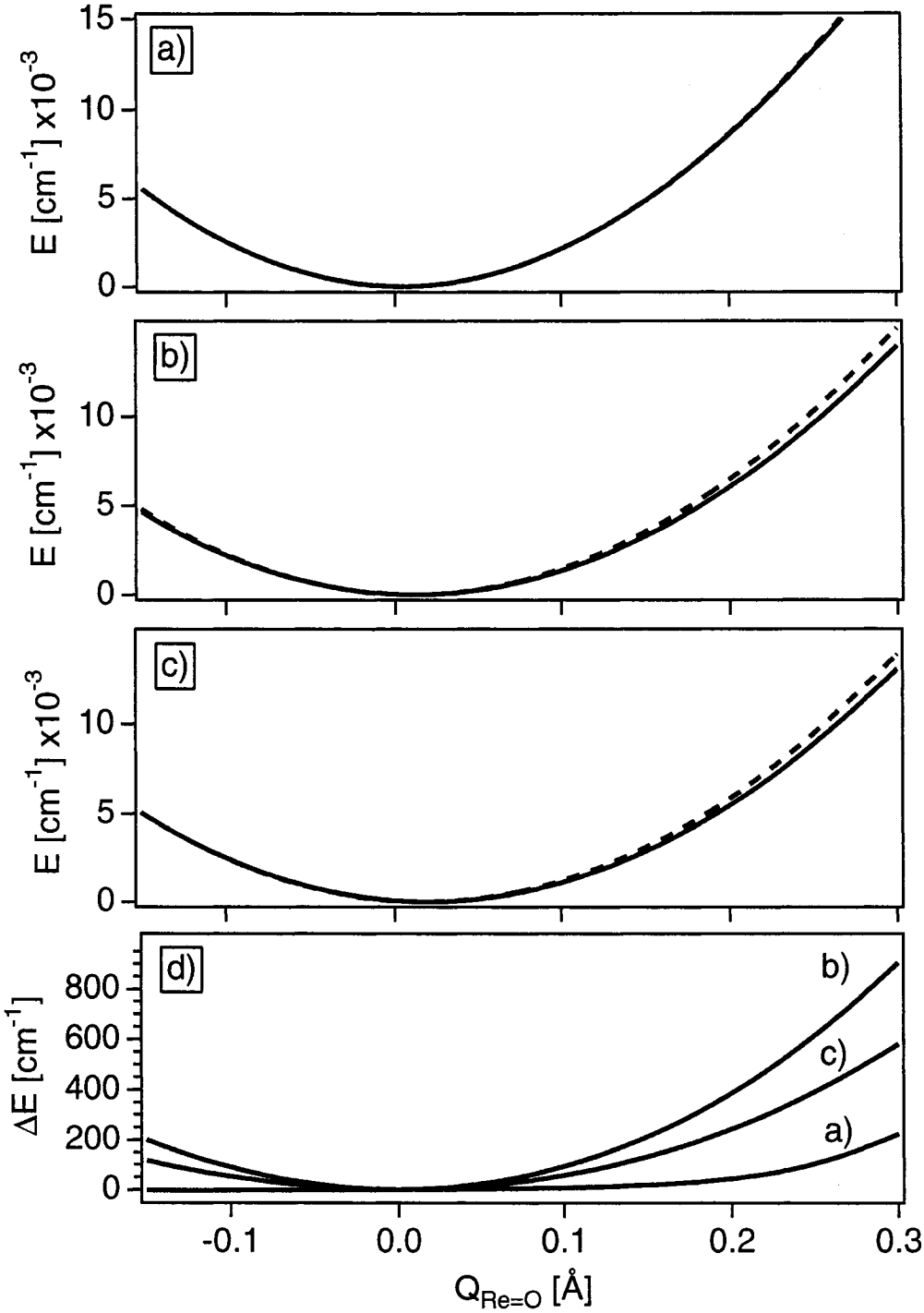

Figure 6.13. Ground state adiabatic potential energy surfaces at the lowest (solid) and highest (dashed) pressures for: a) $ReO_2(teen)_2Cl$: ambient (solid line) and 57 kbar (dashed line, b) $ReO_2(tmen)_2Cl$: 2 kbar (solid line) and 58 kbar (dashed line), and c) $ReO_2(en)_2Cl$: 1 kbar (solid line) and 38 kbar (dashed line). The bottom panel, d), shows the difference between the adiabatic ground state potential energy surfaces at the lowest and highest pressure for each complex.

6.5 Conclusion

Luminescence spectra of *trans*-dioxo complexes of rhenium(V) and a model based on coupled electronic states allow us to reproduce all of the pressure-dependent vibronic features observed in the luminescence bands and to compare quantitative pressure effects for a series of related complexes. The analysis provides new insight into the effect of pressure on interactions between electronic states. With resolved vibronic structure, it is feasible to determine the pressure dependence of molecular quantities. We observe that pressure-induced changes of the ground state potential energy surfaces depend on interactions with excited electronic states.

References

(1) Drickamer, H. G.; Frank, C. W. *Electronic Transitions and the High Pressure Chemistry and Physics of Solids*; Chapman and Hall: New York, 1973.

(2) Drickamer, H. G. *Acc. Chem. Res.* **1986**, *19*, 329.

(3) Bray, K. L. *Top. Curr. Chem.* **2001**, *213*, 1.

(4) Grey, J. K.; Butler, I. S. *Coord. Chem. Rev.* **2001**, *219-221*, 713.

(5) Schäffer, C.; Lang, J. M.; Drickamer, H. G. *Inorg. Chem.* **1996**, *35*, 5072.

(6) Parsons, R. W., Drickamer, H.G. *J. Chem. Phys.* **1958**, *29*, 930.

(7) Stephens, D. R., Drickamer, H.G. *J. Chem. Phys.* **1961**, *34*, 937.

(8) Stephens, D. R., Drickamer, H.G. *J. Chem. Phys.* **1961**, *35*, 429.

(9) Gütlich, P.; Hauser, A.; Spiering, H. *Angew. Chem. Intl. Ed. Engl.* **1994**, *33*, 2024.

(10) Bray, K. L.; Drickamer, H. G. *J. Phys. Chem.* **1991**, *95*, 559.

(11) Bray, K. L., Drickamer, H.G. *J. Phys. Chem.* **1990**, *94*, 2154.

(12) Bray, K. L.; Drickamer, H. G.; Schmitt, E. A.; Hendrickson, D. N. *J. Am. Chem. Soc.* **1989**, *111*, 2849.

(13) Wenger, O. S.; Valiente, R.; Güdel, H. U. *J. Chem. Phys.* **2001**, *115*, 3819.

(14) Newsham, M. D.; Giannelis, E. P.; Pinnavaia, T. J.; Nocera, D. G. *J. Am. Chem. Soc.* **1988**, *110*, 3885.

(15) Shen, Y. R.; Bray, K. L. *Phys. Rev. B* **1997**, *56*, R473.

(16) Ma, D.; Wang, Z.; Chen, J.; Zhang, Z. *J. Phys. C* **1988**, *21*, 3585.

(17) Winkler, J. R.; Gray, H. B. *J. Am. Chem. Soc.* **1983**, *105*, 1373.

(18) Winkler, J. R.; Gray, H. B. *Inorg. Chem.* **1985**, *24*, 346.

(19) Savoie, C.; Reber, C. *J. Am. Chem. Soc.* **2000**, *122*, 844.

(20) Savoie, C.; Reber, C. *Coord. Chem. Rev.* **1998**, *171*, 387.

(21) Savoie, C.; Reber, C.; Bélanger, S.; Beauchamp, A. L. *Inorg. Chem.* **1995**, *34*, 3851.

(22) Lock, C. J. L.; Turner, G. *Acta Cryst.* **1978**, *B34*, 923.

(23) Chatt, J.; Rowe, G. A. *J. Chem. Soc.* **1962**, 4019.

(24) Piermarini, G. J., Block, S., Barnett, J.D., Forman, R.A. *J. Appl. Phys.* **1975**, *46*, 2774.

(25) Markwell, R. D., Butler, I.S. *Can. J. Chem.* **1995**, *73*, 1019.

(26) Davis, M. J.; Reber, C. *Inorg. Chem.* **1995**, *34*, 4585.

(27) Miskowski, V. M.; Gray, H. B.; Hopkins, M. D. In *Adv. Trans. Met. Coord. Chem.*; Che, C.-M., Yam, V. W.-W., Eds.; JAI Press: Greenwich, CT, 1996; Vol. 1, p 159.

(28) Edwards, C. M.; Butler, I. S. *Coord. Chem. Rev.* **2000**, *199*, 1.

(29) Adamsky, H.; AOMX (www.aomx.de) Institut für Theoretische Chemie, Heinrich-Heine-Universität Düsseldorf: Düsseldorf, Germany, 1995.

(30) Heller, E. J. *J. Chem. Phys.* **1975**, *62*, 1544.

(31) Heller, E. J. *Acc. Chem. Res.* **1981**, *14*, 368.

(32) Zink, J. I.; Kim Shin, K.-S. In *Adv. Photochem.*; Volman, D. H., Hammond, G. S., Neckers, D. C., Eds.; John Wiley: New York, 1991; Vol. 16, p 119.

(33) Feit, M. D.; Fleck Jr., J. A.; Steiger, A. *J. Comp. Phys.* **1982**, *47*, 412.

(34) Grey, J. K.; Triest, M.; Butler, I. S.; Reber, C. *J. Phys. Chem. A* **2001**, *105*, 6269.

(35) Landry-Hum, J.; Tessier, V.; Ernzerhof, M.; Reber, C. *Coord. Chem. Rev.* **2002**, *233-234*, 63.

(36) Lever, A. B. P.; London, G.; McCarthy, P. J. *Can. J. Chem.* **1977**, *55*, 3172.

(37) Lever, A. B. P.; Walker, I. M.; McCarthy, P. J.; Mertes, K. B.; Jircitano, A.; Sheldon, R. *Inorg. Chem.* **1983**, *22*, 2252.

(38) Lin, S. H. *J. Chem. Phys.* **1973**, *59*, 4458.

(39) Tompkins, R. C. *J. Chem. Phys.* **1978**, *69*, 579.

(40) Tompkins, R. C. *J. Chem. Phys.* **1980**, *72*, 3449.

(41) Kesarwani, R. N., Varshni, Y.P. *J. Chem. Phys.* **1984**, *81*, 5508.

Chapter 7

Emitting-State Displacements in Ligand-Centered Vibrational Modes in the *trans*-$[OsO_2(NCS)_4]^{2-}$ Complex Determined from Near-Infrared Luminescence Spectroscopy

This chapter reports temperature-dependent luminescence properties of three salts of the *trans*-$[OsO_2(NCS)_4]^{2-}$ complex that show similar band envelopes to previous work on isoelectronic *trans*-dioxo rhenium(V) complexes. The low temperature (ca. 5 K) luminescence spectra have band maxima in the near-infrared region and are the best resolved to date in the *trans*-dioxo class of complexes. The spectra also show evidence for an emitting state displacement in a ligand-centered symmetric stretching mode, which has never been observed in this class of complexes.

7.1 Introduction

The lowest energy luminescence and absorption transitions in many transition metal complexes occur between states that are predominantly localized on the metal center. These ligand-field (d–d) transitions are often interconfigurational and involve an electron populating an orbital of markedly different bonding character than the original orbital. This situation gives rise to long vibronic progressions in metal-ligand vibrational modes corresponding to large emitting state displacements along metal-ligand normal coordinates. We study a series of *trans*-dioxo metal compounds with formal metal-oxo double bonds that show evidence for a displaced ligand-centered vibrational mode in a formal d–d luminescence transition and present results from quantitative analyses of the resolved low temperature spectra that reveal the contribution of this mode to the overall bandshape. The appearance of a ligand-centered vibrational mode is highly unusual in the luminescence spectroscopy of *trans*-dioxo metal complexes, which traditionally show progressions in metal-ligand modes only for their lowest energy electronic transitions.

The electronic structures for many metal-ligand multiply bonded systems are well-known and exhibit interesting and unique optical properties[1-8] and compounds with metal-ligand multiple bonds have been used extensively in synthetic applications.[9-11] We use luminescence spectroscopic methods on the *trans*-$[OsO_2(NCS)_4]^{2-}$ complex in three different crystalline environments and present low temperature spectra with highly resolved vibronic structure and distinctly different luminescence bandshapes and energies for the three compounds. This luminophore has idealized D_{4h} point group symmetry and we use these symmetry labels to describe the electronic states and vibrational modes. A recent X-ray crystal structure analysis of the TBA compound reveals that the ambidentate NCS^- ligand is coordinated through the nitrogen atom,[12] which is expected for the "hard" osmium(VI) metal center[13,14] and the NCS^- ligands are canted slightly out of the OsN_4 plane. The six-coordinate, *trans*-MO_2L_4 class of metal complexes represent the tetragonally compressed limit of the D_{4h} point group and is represented here with the Os=O bond lengths approximately 0.25 Å less than those of the Os—N bonds.[12]

The luminescence energies of *trans*-dioxo complexes depend strongly on the local environment around the metal center as well as the electronic configuration of the metal. The axially compressed nature of these, and other four-fold symmetric, systems leads to the following energetic ordering of the d-orbitals in increasing energy: d_{xy} (b_{2g}), d_{xz}, d_{yz} (e_g), $d_{x^2-y^2}$ (b_{1g}), d_{z^2} (a_{1g}). In the title compounds and other [Xe] $5d^2$ *trans*-dioxo complexes, the two d-electrons are paired in the metal d_{xy} $(b_{2g})^2$ HOMO orbital yielding an orbitally and spin nondegenerate $^1A_{1g}$ electronic ground state. The first ligand-field transition involves the promotion of an electron to the metal $d_{xz, yz}$ (e_g) LUMO orbitals yielding both singlet and triplet doubly degenerate $^{1,3}E_g$ excited states with the latter lower in energy by $2K_{xy}$, where K_{xy} is a two-electron interelectronic repulsion term ($K_{xy} = 3B + C$).[3] The energy of the e_g orbitals is defined by the ligand-field parameter Δ_π, which depends on the extent of overlap between the metal and ligand orbitals with π symmetry, and the energy of the b_{2g} orbital varies with K_{xy}.[3] The HOMO—LUMO energy separation between these crystal field orbitals depends on both of these parameters and optical transitions between states involving these orbitals are typically labeled as $n \rightarrow \pi^*$ transitions due to the predominantly nonbonding or weakly π^* character of the b_{2g} orbital and the strongly π^* (metal–oxo) character of the e_g orbitals that are largely localized on

the *trans*-$[MO_2]^{n+}$ moiety. Due to strong spin-orbit coupling effects present in 5d metal complexes, the lower energy ^3E_g state is split into five components and luminescence occurs from the lowest spin-orbit level(s). Previous spectroscopic work on isoelectronic osmium(VI) and rhenium(V) *trans*-dioxo complexes has revealed a wide variety of interesting features in both absorption and luminescence spectra, such as coupling between normal coordinates,[15,16] that arise from interactions between electronic states (i.e., spin-orbit coupling and configuration interactions).[17,18] The optical spectra of *trans*-dioxo systems are also quite unique in that there are usually two distinct and well-separated vibronic progressions corresponding to the totally symmetric (a_{1g}) high frequency O=M=O and lower frequency M—ligand stretching modes. The frequencies of these modes typically range from 850—900 cm^{-1} for the a_{1g} O=M=O mode and 175—400 cm^{-1} for the a_{1g} M—ligand modes, almost 4 times *less* in frequency. The high frequency of the O=M=O stretching mode is due to the greater strength of the metal–oxo double bonds and the long vibronic progressions often observed in both absorption and luminescence are indicative of large changes along the M=O coordinates upon absorption or emission of a photon.

trans-Dioxo complexes of osmium(VI) have received considerable attention for their use in photochemical oxidation processes, electrochemistry[19-23], and multielectron oxygen transfer catalysis.[24,25] Luminescence spectroscopic investigations on *trans*-dioxo osmium(VI) complexes with macrocyclic, nitrogen-donating ancillary ligands have revealed band maxima energies close to the near-IR region with relatively weak intensities and little or no resolved vibronic structure.[26] For comparison, the *trans*-$[OsO_2(CN)_4]^{2-}$ complex is the only closely related complex to the title compounds where the low temperature (77 K) luminescence spectrum shows a resolved, long vibronic progression in the totally symmetric O=Os=O stretching mode, but with low resolution of the lower frequency, M-CN modes and a higher energy luminescence band maximum (~14500 cm^{-1}).[27] Luminescence spectra from some *trans*-dioxo osmium(VI) complexes with nitrogen-donating and oxygen-donating bidentate ligands have also been reported and exhibit no resolved vibronic structure.[18] Osmium(VI) nitrido complexes with formal Os≡N triple bonds and simple halide ancillary ligands show highly resolved vibronic structure in the 5 K luminescence spectra with distinct progressions in the high frequency

Os≡N and Os—X (X=Cl^-, Br^-) stretching modes, including emitting state displacements in Jahn-Teller active vibrational modes.[28] The luminescence spectra of some rhenium(V) nitrido complexes have also been studied recently and they display the characteristic progression in the high frequency metal-ligand (Re≡N) symmetric stretching modes.[8]

The low temperature luminescence spectra of the *trans*-$[OsO_2(NCS)_4]^{2-}$ complex in three different crystalline environments presented in the following exhibit remarkable resolution of vibronic structure in both high and low frequency vibrational modes allowing for a full analysis of the resolved spectroscopic features. The most surprising characteristic is that the high frequency vibronic interval (855—880 cm^{-1}) resolved in the luminescence spectra does not exactly match the ground state Raman frequency for the totally symmetric O=Os=O stretching mode of 885 cm^{-1}. We present detailed spectroscopic and qualitative theoretical evidence for a significant displacement in the ligand-centered a_{1g} CS stretching vibration with a frequency of 858 cm^{-1}, only ~30 cm^{-1} lower than the metal-ligand O=Os=O symmetric stretching frequency. The emitting state displacement of both O=Os=O and CS high frequency modes leads to the observed discrepancy in the high frequency interval, which has been termed the "missing mode effect" or MIME.[29,30] All vibronic bandshapes are quantitatively analyzed using the time-dependent theory of spectroscopy assuming a two state system with the lowest spin-orbit component as the initial state and the ground state as the final state. We are then able to extract the individual contributions of both the O=Os=O and CS stretching modes to the high frequency interval.

7.2 Experimental

Three salts of the *trans*-$[OsO_2(NCS)_4]^{2-}$ complex were prepared using modified literature methods[12,31,32] and starting materials were used as received. The three compounds will be herein described using the following notation, 1) *trans*-$[OsO_2(NCS)_4](n\text{-}Bu_4N)_2$ **TBA**, 2) *trans*-$[OsO_2(NCS)_4](PPh_4)_2$ **PPH**, and 3) *trans*-$[OsO_2(NCS)_4](Ph_3PNPPh_3)_2$ **PPN** (PPN = *bis*-triphenylphosphoranylidene ammonium).

TBA. $K_2OsO_4 \cdot 2H_2O$ (0.04g: 0.1 mmol) was dissolved in methanol to which was added a methanolic solution of KSCN (0.1 g: 1 mmol) along with tetrabutylammonium

chloride (0.25 g). The pH of the solution was lowered by the dropwise addition of dilute glacial acetic acid that resulted in a color change from blue to a light brownish-yellow tint. The solution was then placed in an isopropanol/ dry ice mixture (~ -30 °C) for 4 hours where the compound precipitated as small, light beige crystals. Following filtration, the crystals were dissolved in dichloromethane and washed 3 times with distilled water then dried with calcium chloride. The dichloromethane was rotary evaporated yielding a reddish-brown residue that was dissolved in acetone and layered with diethyl ether. After 24 hours at 4 °C, small brown needle-like crystals formed. Anal. Calcd. for $OsO_2N_6C_{36}S_4H_{72}$: C, 46.02; N, 8.95; S, 13.60; H, 7.72. Found: C, 46.31; N, 8.99; S, 12.75; H, 7.85.

PPH. This compound was prepared by dissolving $K_2OsO_4 \cdot 2H_2O$ (0.07 g, 0.2 mmol) and PPh_4Br (0.36 g) in 2M HCl and upon addition, *trans*-$[OsO_2(Cl)_4](PPh_4)_2$ precipitated immediately as small beige colored crystals along with KBr. This compound was separated and dissolved in acetone to which was added a solution of KSCN (0.21 g: 2 mmol) in a minimum amount of distilled water. The solution was allowed to evaporate in air that yielded large dark brown crystals, which were recrystallized with acetone at 4 °C. Anal. Calcd. for $OsO_2N_4C_{52}S_4H_{40}$: C, 55.10; N, 4.96; S, 11.30; H, 3.56. Found: C, 54.63; N, 5.09; S, 11.08; H, 3.49.

PPN. This compound was prepared in the same manner as TBA except that *bis*-triphenylphosphoranylidene ammonium chloride (0.12 g) was substituted for tetrabutylammonium chloride.

7.2.1 Spectroscopic Methods

Luminescence spectra were measured using two different instruments. The first system was a single-channel, step-scan spectrometer and the 458, 488, and 514.5 nm lines of an argon ion laser (Spectra-Physics Stabilite 2017) were used to excite crystalline samples inside a continuous flow cryostat (Oxford CF1204). Luminescence was collected at 90° with a spherical mirror and dispersed by a 0.5 m monochromator (SPEX 500M, 600 lines/mm) with a long-pass filter to remove the excitation (Schott RG 645).

Emitted light was modulated with an optical chopper (400 Hz) and detected with a liquid N_2-cooled Ge photodiode (ADC 403UL) or photomultiplier tube (Hamamatsu R406) connected to a lock-in amplifier (Stanford Instruments SR 510 or SR 830). An in-house program was used to reject spikes in the luminescence signals measured with the Ge photodiode by sampling a preset number of data points and rejecting outlying values.[33] Due to low signal-to-noise ratios of the photodiode detector of wavelengths longer than 800 nm, a microscope-based system with a sensitive CCD camera was employed with argon ion (488 nm and 514.5 nm) and He–Ne (633 nm) laser excitation. Samples were placed under vacuum and cooled in a liquid helium micro-cryostat (Janis ST 500). Each compound has identical overall bandshapes when excited with different wavelengths and spectra recorded with both spectrometers can be superposed to compare overlapping features. This is important since both spectrometers have largely varying spectral sensitivities over the wavelength range studied. All spectra were corrected for instrument response with a tungsten lamp (Oriel 63350) using a procedure described in detail before.[34]

Raman spectra of the *trans*-dioxo osmium(VI) complexes were obtained from the microscope spectrometer and excitation sources described previously. Resonance Raman spectra of **PPH** at room temperature were measured on a double monochromator (SPEX 14018, 0.75 m) system with single-photon counting detection (SPEX DPC-2). The 458, 476, 488, and 514.5 nm lines of the argon-ion laser were used as excitation sources and the scattered light was collected at 90° and focused onto the slits of the monochromator. The excitation wavelengths are on, or near resonance with the $^1A_{1g} \rightarrow {}^1E_g$ band (D_{4h}) and excitation profiles were obtained for the O=Os=O and CS totally symmetric stretching vibrations from the integrated areas of the Raman bands with the 995 cm^{-1} vibration of the PPh_4^+ counterion as an internal intensity standard. Infrared spectra of the title compounds were measured with an FT instrument (BioRad FTS 3000FX) and samples were dispersed in KBr and pressed into a pellet.

Luminescence lifetime measurements were obtained using a Nd^{3+}:YAG pulsed laser (Continuum Minilite II, 5—10 ns pulse width) operating in either doubled (532 nm) or tripled (355 nm) output. The luminescence was collected and detected using the step-scan spectrometer described above. Decay traces were averaged and saved on a digital

oscilloscope (Tektronix TDS 380) and least-squares routines were used to fit and assign decay. Absorption spectra were obtained with a Varian Cary 5E spectrometer operating in double beam mode. Samples were cooled in the continuous flow cryostat mentioned above and all spectra reported are unpolarized. Neutral density filters were placed in the reference beam in order to keep the optical densities at a measurable level.

7.3 Spectroscopic Results

Low temperature single crystal luminescence spectra of the *trans*-$[OsO_2(NCS)_4]^{2-}$ complex in three different crystalline environments are shown in Figure 7.1: **TBA**, top panel; **PPH**, middle panel; **PPN**, bottom panel. All spectra have weak intensities, even at low temperature, which indicates efficient nonradiative deactivation of the emitting state, and show well-resolved vibronic progressions in a high frequency interval (870 ± 5 cm^{-1} for **TBA**, 855 ± 8 cm^{-1} for **PPH**, 880 ± 5 cm^{-1} for **PPN**) and a low frequency interval (ca. 255 cm^{-1}) is also resolved. The latter is in good agreement with the ground state Raman band for the totally symmetric (a_{1g}) Os—N stretching vibration of 250—255 cm^{-1} whereas the high frequency interval does not exactly match any frequency in the Raman spectra of all three compounds. Normally, in the optical spectra of d^2 *trans*-dioxo complexes, this progression interval best corresponds to the O=M=O symmetric (a_{1g}) stretching frequency. However, in the title compounds there are two high frequency vibrational modes observed in the Raman spectra, the a_{1g} O=Os=O stretching mode of 885 cm^{-1} and the a_{1g} vibration of the ligand-centered CS stretching mode at 858 cm^{-1}, which are identical for all three compounds. The mode of coordination of the ambidentate NCS^- ligand was also checked by Raman spectroscopy where the frequencies of the CN stretching modes (2095—2100 cm^{-1}) were smaller than those of other complexes where the NCS^- ligand is coordinated to the metal via the sulfur atom,[13,14] thus in good qualitative agreement with previous observations for both possible linkage isomers. There are no reported complexes for S-bonded isomers of the NCS^- ligand to osmium(VI), making a quantitative comparison of the CN frequencies impossible. Temperature-dependent luminescence lifetimes (λ_{exc} = 532 nm) for all three compounds reveal relatively short (~1 μs) emitting state decay times, which is in qualitative agreement with previous observations in lower-energy emitting *trans*-dioxo complexes.[16]

Excitation with 355 nm pulses, which correspond to populating the ligand-to-metal charge transfer (LMCT) states, result in shorter lifetimes by approximately 15 % than those excited by 532 nm light.

One of the most striking features of the spectra in Figure 7.1 is the markedly different luminescence bandshapes and energies for the same complex with different counterions. Previous low temperature (5—77 K) luminescence measurements reported for *trans*-dioxo osmium(VI) systems have often shown broad and unresolved bands or weakly resolved vibronic structure with intervals corresponding to the O=Os=O mode. The resolution of vibronic structure and overall band envelope characteristics enables a detailed study and characterization of multi-mode emitting state distortions in these types of complexes for the first time. Each panel of Figure 7.1 shows the high-resolution spectrum as the top trace and the bottom trace shows the complete luminescence band for all three compounds studied. Both spectra are recorded with different detectors and intensities are not equivalent whereas luminescence energies are identical. All relevant spectroscopic parameters are listed in Table 7.1 and we discuss the spectral features for each compound separately below.

parameter	**TBA**	**PPH**	**PPN**
lum. maximum [cm^{-1}]	11550	9900	11700
lum. origin [cm^{-1}]	12975	11650	13000
abs. maximum [cm^{-1}] ($^1A_{1g} \rightarrow {}^3E_g$)	18500	17850	
Stokes shift [cm^{-1}]	6950	7950	
lum. lifetime [μs]	1.4 (9 K)	0.89 (10 K)	0.82 (85 K)
	1.3 (100 K)	0.79 (100 K)	0.65 (250 K)
	1.2 (200 K)	0.80 (200 K)	
vibronic intervals [cm^{-1}]	870 [a] (885 $\hbar\omega_{O=Os=O}$ and 858 $\hbar\omega_{CS}$) [b, c]	855 [a] (885 $\hbar\omega_{O=Os=O}$ and 858 $\hbar\omega_{CS}$) [b, c]	880 [a] (885 $\hbar\omega_{O=Os=O}$ and 858 $\hbar\omega_{CS}$) [b, c]
	255 [a] (240, 251 [c] $\hbar\omega_{Os-N}$) [b]	255 [a] (258 $\hbar\omega_{Os-N}$) [b]	250 [a] (251 $\hbar\omega_{Os-N}$) [c]

[a] Luminescence. [b] Ground state Raman frequency (300 K). [c] Raman ref. 12.

Table 7.1. Spectroscopic quantities determined from luminescence data shown in Figures 7.1–7.4, and 7.6.

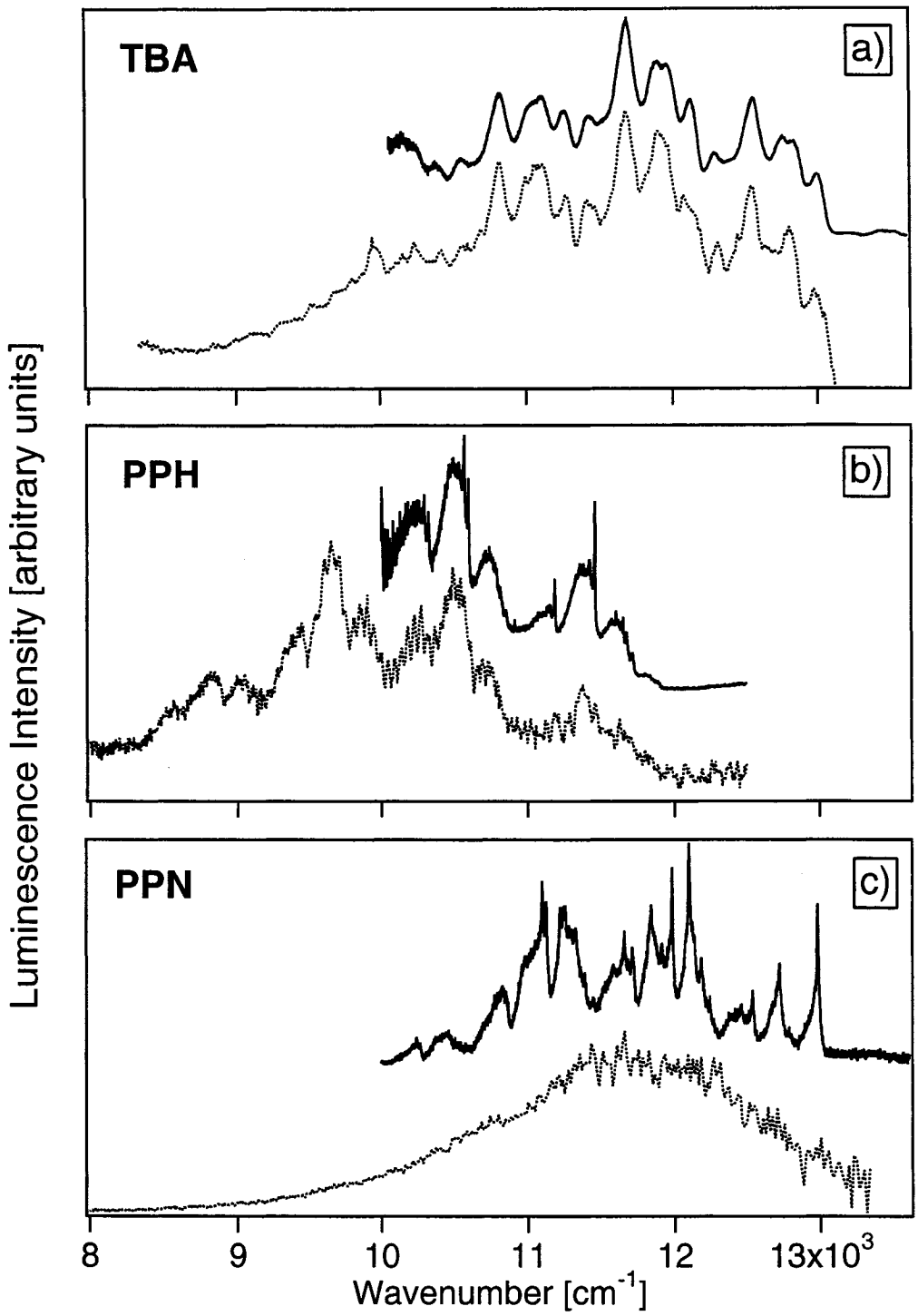

Figure 7.1. High-resolution 6 K luminescence spectra (top traces) and 5 K luminescence spectra showing the complete band (bottom traces) of: a) *trans*-$[OsO_2(NCS)_4](n\text{-}Bu_4N)_2$; **TBA**, b) *trans*-$[OsO_2(NCS)_4](PPh_4)_2$; **PPH**, c) *trans*-$[OsO_2(NCS)_4](Ph_3PNPPh_3)_2$; **PPN**.

TBA. Figure 7.1a (top panel) shows the luminescence spectra recorded for the **TBA** compound at ca. 5 K on the two different instruments described previously. The high-resolution spectrum reveals a peculiar feature where the second peak of each cluster has a double maximum. This gives rise to frequency intervals of 170 and 255 cm^{-1}, with the latter in good agreement with both literature and ground state Raman values for the totally symmetric Os—N stretching mode. The former interval is not repeated across the entire band and does not correspond to any frequency observed in the experimental Raman spectrum, however, is in good agreement with the frequency of an E_u vibration (171 cm^{-1}) reported in the literature IR spectrum of this compound.[12,32] Figure 7.2a shows the high-resolution luminescence spectrum with the single crystal absorption spectrum at 5 K. The lowest energy absorption band corresponds to the characteristic $^1A_{1g} \rightarrow {}^3E_g$ transition (18500 cm^{-1}), which is masked on the higher energy side of the band by the more-intense $^1A_{1g} \rightarrow {}^1E_g$ band. Figure 7.2b highlights a region of the absorption spectrum where it is also revealed that the overall spectrum consists of two overlapping spectra separated by approximately 80 cm^{-1}. The high frequency interval in this excited state is approximately 615 cm^{-1}, which amounts to a 30 % reduction from the 870 cm^{-1} interval observed in the luminescence spectrum and the 230 cm^{-1} interval in the absorption spectrum corresponds to the emitting state Os—N frequency. Interestingly, there is another resolved interval in a low frequency mode of ~150 cm^{-1} that is similar to the 170 cm^{-1} frequency interval observed in the luminescence spectrum. Due to the congestion arising from overlapping vibronic transitions and relatively weak oscillator strength at lower energy (toward the origin region) it is difficult to interpret these features as either genuine progressions or transitions to close-lying spin-obit levels of the ^3E_g state. The effect of temperature on the **TBA** luminescence spectrum is shown in Figure 7.3a (λ_{exc} = 514.5 nm) and the spectra do not show an appreciable change in the overall luminescence band intensity with increasing temperature. However, there is a noticeable change in the intensity distribution in the second member in each cluster (i.e., double maximum), possibly due to a transition built on a vibronic origin or either a second emitting state or different emitting species. As temperature increases, the double maximum coalesces into one peak and blue-shifts by approximately 40 cm^{-1} between 6—100 K, indicating

possible hot band transitions consistent with progressions built on a vibronic origin. A high-resolution scan of the origin region of the luminescence is shown in Figure 7.3a (×5 bottom right) that reveals two very weak bands that may correspond to transitions allowed by a magnetic dipole mechanism. Figure 7.3b demonstrates the effect of excitation wavelength on the luminescence bandshapes where the first discernible feature (indicated by dotted arrows) changes as a function of wavelength. Additionally, there are other weak transitions flanking the highest energy peak slightly lower in energy before the main band begins at approximately 13000 cm^{-1}. Furthermore, the intensity distribution of the double maximum (highlighted with sloping lines) varies slightly as a function of wavelength. Despite these minor wavelength- and temperature-dependent features, the position of the origin transition of the main band (13000 cm^{-1}) does not change with these variables and the crystal structure for this compound reveals only one site for the *trans*-$[OsO_2(NCS)_4]^{2-}$ complex in the unit cell.[12] The appearance of a single quantum of the 170 cm^{-1} E_u mode leading to the double maximum on the second peak in each cluster strongly suggests a vibronic coupling mechanism whereby the formally spin and parity forbidden d–d luminescence borrows intensity from intense LMCT [E_u: $p_\pi(O)$] transitions (300—400 nm) as well as by spin-orbit coupling. This is further supported by temperature-dependent luminescence lifetime measurements where no discontinuities are observed as a function of temperature and all luminescence decay curves can be reproduced by a single-exponential function, thus not supporting the presence of a second emitting state or species.

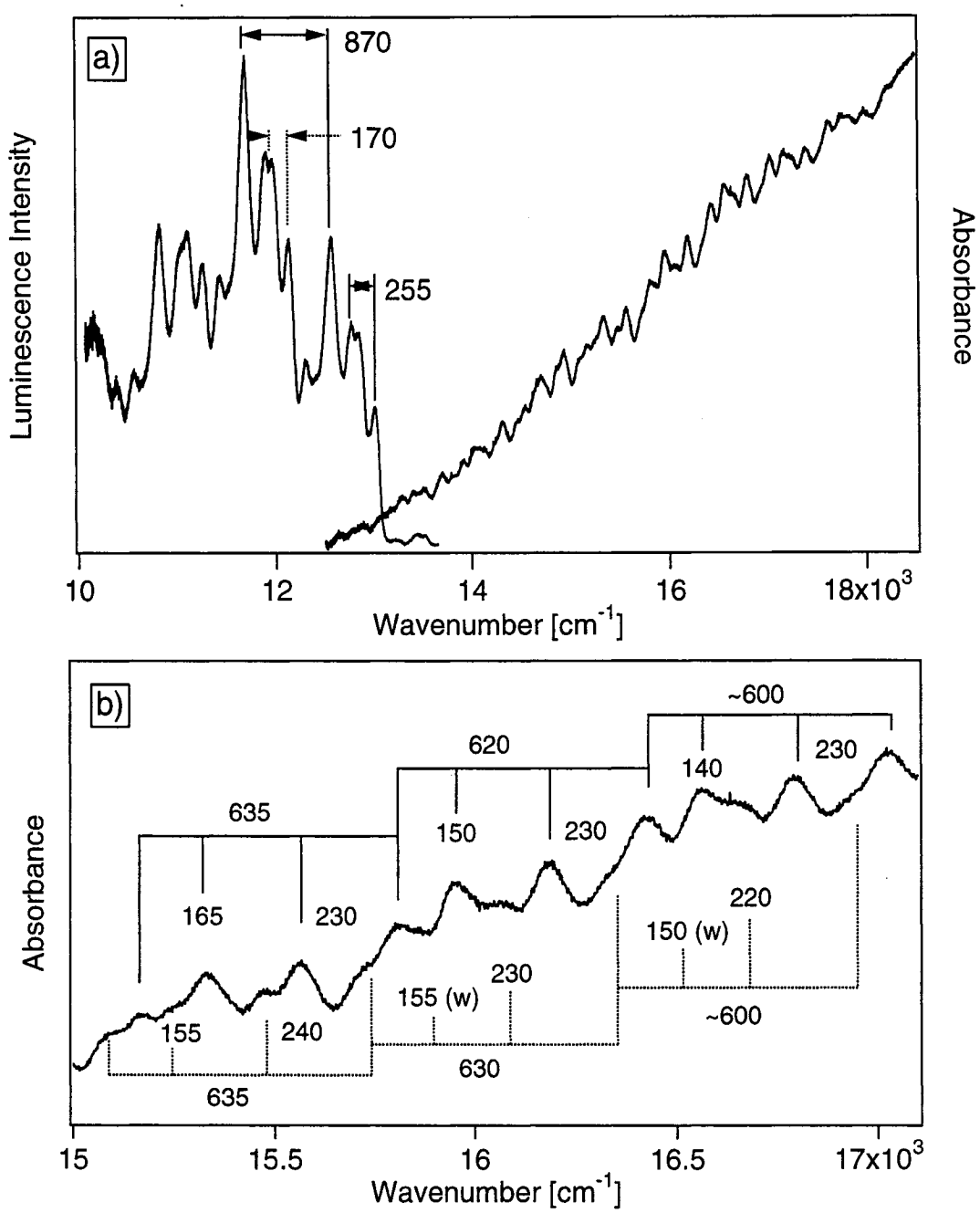

Figure 7.2. a) High-resolution 6 K luminescence spectrum of **TBA** (λ_{exc} = 633 nm) with the resolved intervals indicated and 5 K single crystal unpolarized absorption spectrum. b) region of the 5 K absorption spectrum with vibronic intervals highlighted. The total spectrum consists of two separate bands separated by 80 cm^{-1}.

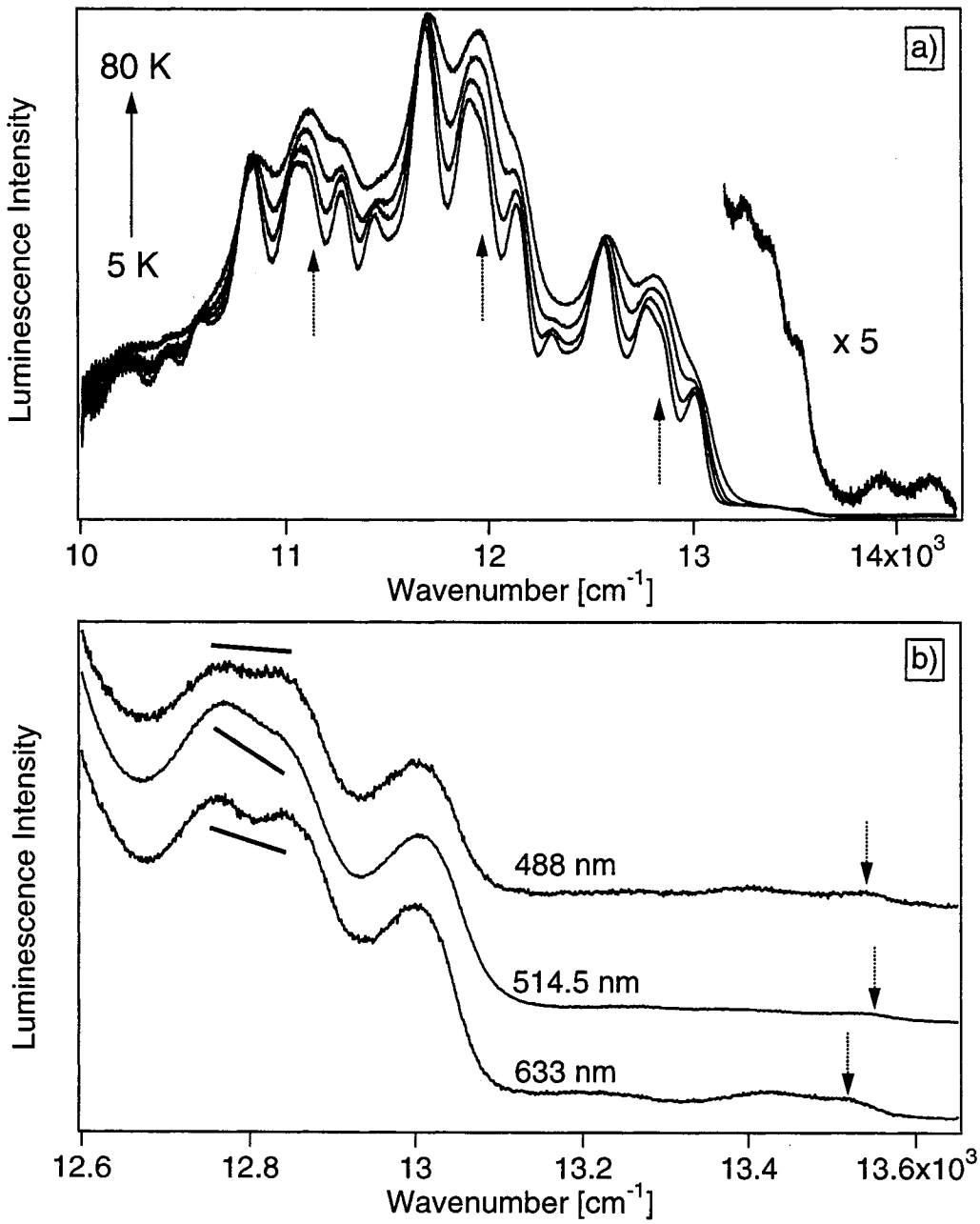

Figure 7.3. a) Temperature-dependent luminescence spectra (λ_{exc} = 514.5 nm) of **TBA** at 6 K, 30 K, 50 K, and 80 K. Arrows show the increase of the intensity of the second peak with increasing temperature and a high-resolution scan of the origin region is included (×5). b) Wavelength-dependent luminescence spectra of **TBA** at 6 K with excitation wavelengths indicated on each spectrum. Arrows are used to show the position of the first discernible feature at each wavelength.

PPH. Figure 7.1b shows the low temperature luminescence spectra of the **PPH** compound. The low signal-to-noise ratio in the full spectrum (bottom trace) illustrates the very low quantum yields intrinsic to the *trans*-$[OsO_2(NCS)_4]^{2-}$ luminophore. Figure 7.4a shows the 6 K high-resolution luminescence spectrum and 5 K single-crystal unpolarized absorption spectrum of **PPH**. This first absorption band corresponds to the formal $^1A_{1g} \rightarrow {}^3E_g$ transition and average vibronic intervals of 755 and 280 cm^{-1} are observed, which are most likely the emitting state O=Os=O or CS and Os—N vibrational frequencies. The slight increase in the Os—N frequency interval is consistent with the decrease of Os—N bond lengths often observed in other *trans*-dioxo complexes due to the removal of electron density from the Os—N π^* b_{2g} (HOMO) orbital to the O=Os=O π^* e_g (LUMO) orbitals. The average frequency interval of the dominant progression-forming mode in the ca. 5 K luminescence spectra is 855 cm^{-1}, which is in excellent agreement with the ground state Raman frequency of 858 cm^{-1} for the a_{1g} CS stretching mode. The overall spectral profile and band maximum energy is also different from the other two compounds. For example, the third cluster of vibronic bands is the most intense for this compound compared to the second cluster for the **TBA** and **PPN** complexes in Figure 7.1 and the luminescence energy is lower by almost 1500 cm^{-1}. Figure 7.4b shows a high-resolution scan near the luminescence origin, which reveals low frequency (40-100 cm^{-1}) phonon sidebands close to the beginning of each quantum of the lower frequency progression. Similar features have also appeared in luminescence spectra of osmium(VI) nitrido complexes and the isoelectronic *trans*-$[ReO_2(CN)_4]^{2-}$ complex, revealing strong coupling between intramolecular and intermolecular motions. The intensity distributions of the 255 cm^{-1} progressions are not the same across the entire band (i.e., non-replicas) that can be observed by comparing the relative intensities of the first and second quanta of the first and fourth clusters of vibronic bands in Figure 7.1b. The inset of Figure 7.4b shows a corresponding region in the 5 K absorption spectrum where similar phonon structure can be observed. Because the high frequency interval in this compound more closely matches the CS frequency than in the other compounds, we use resonance Raman spectroscopy to determine if the scattering intensity of this mode is enhanced with variable wavelength excitation. The 514.5, 488, 476, and 458 nm lines of

an argon ion laser were used as excitation sources and these lines are on, or near, resonance with the $^1A_{1g} \rightarrow {}^1E_g$ absorption band. However, due to the relatively low oscillator strength of this transition ($\varepsilon \sim 10\ M^{-1}\ cm^{-1}$), enhancements were small (< 2). Figure 7.5 consists of resonance Raman excitation profiles for the O=Os=O (top panel) and CS (bottom panel) a_{1g} stretching modes and the CC stretching vibration (995 cm^{-1}) of the PPh_4^+ counterion was used as an internal intensity standard. Resonance Raman (^1E_g) and luminescence (^3E_g) spectra involve states arising from the same orbital configuration and have very similar metal-ligand bonding properties. Normal coordinate offsets for these two transitions can therefore be compared. The insets on both panels show results obtained from the microscope spectrometer where the 633 nm excitation line provides a reference point from the $^1A_{1g} \rightarrow {}^3E_g$ absorption band ($\varepsilon \sim 1\ M^{-1}\ cm^{-1}$) that shows negligible enhancements compared to data obtained from 514.5 and 488 nm lines of this instrument. Both vibrational modes show noticeable increases in Raman scattering intensity with decreasing excitation wavelength and the excitation profile for the CS mode provides further evidence for the displacement of this vibration in the emitting state and the necessity for including it in the analysis of the vibronic structure in the luminescence spectrum.

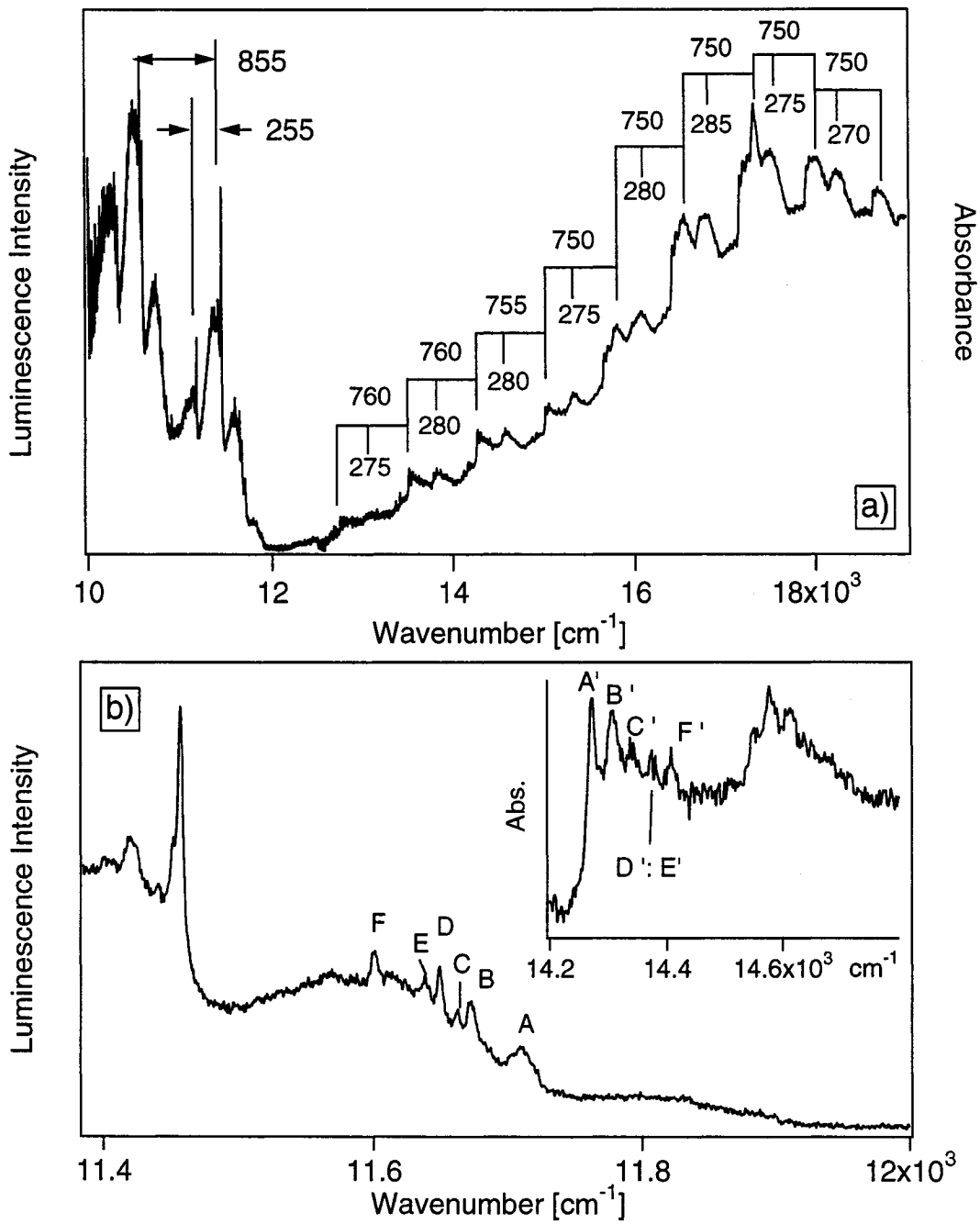

Figure 7.4. a) High-resolution 6 K luminescence spectrum of **PPH** (λ_{exc} = 633 nm) with the resolved intervals indicated and 5 K single crystal unpolarized absorption spectrum showing the resolved frequency intervals of this state. b) Origin region of the 6 K luminescence spectrum showing resolved phonon sidebands A-F and the inset shows the corresponding region in the 5 K absorption spectrum with resolved phonon bands A′-F′.

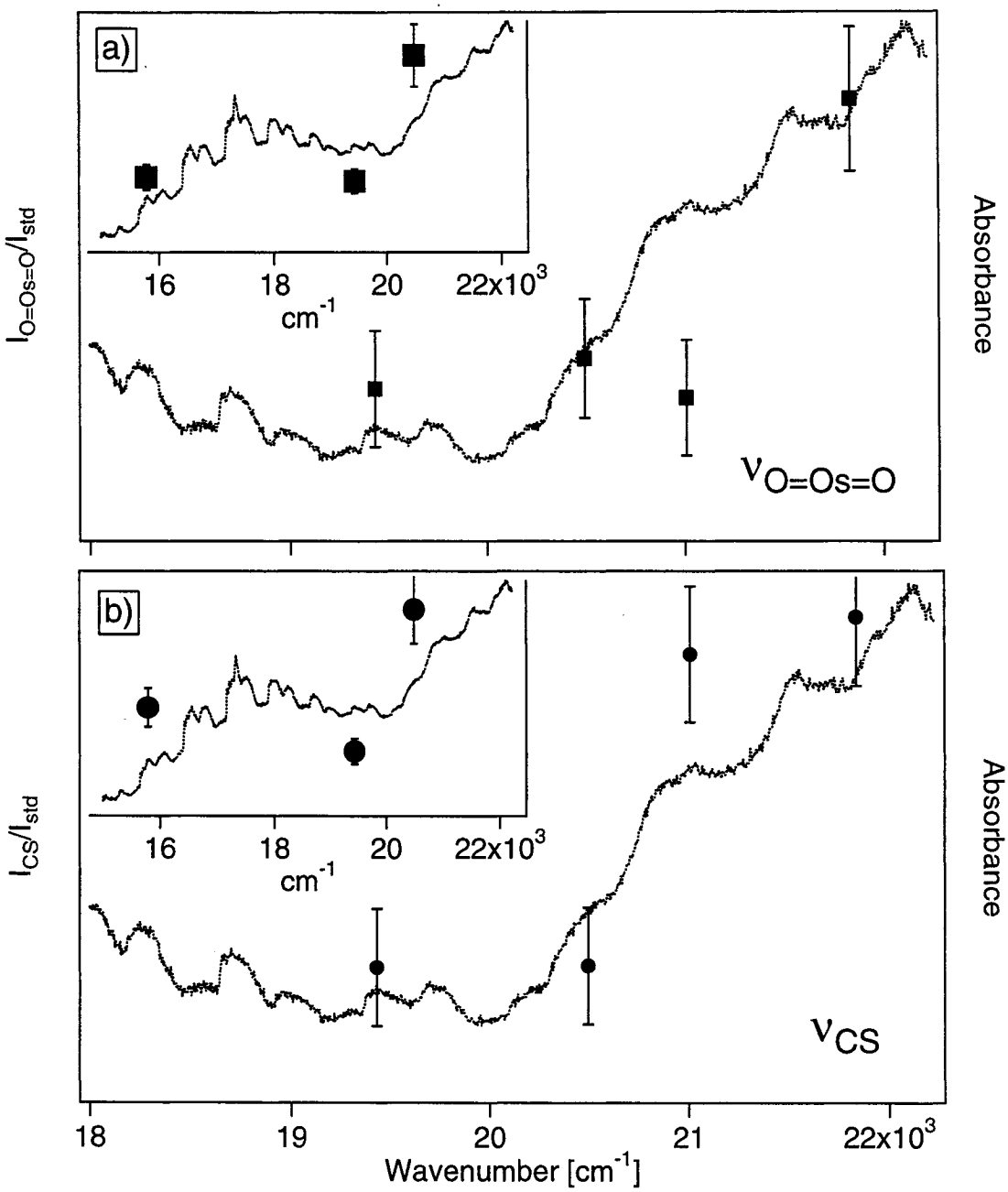

Figure 7.5. Resonance Raman excitation profiles of **PPH** measured from single crystal samples at 300 K using the 458 nm, 476 nm, 488 nm and 514.5 nm lines of an argon ion laser as excitation. Inset: excitation profiles generated from Raman spectra measured on the microscope system using 488 nm, 514.5 nm and 633 nm excitation. a) O=Os=O totally symmetric (a_{1g}) mode (885 cm^{-1}) and, b) CS totally symmetric (a_{1g}) stretching mode (858 cm^{-1}).

PPN. Figure 7.1c shows both the high-resolution (top trace) and the complete luminescence spectra (bottom trace) at ca. 5 K. The high-resolution spectrum of this compound shows the best resolved vibronic structure. The dominant progression interval is approximately 880 cm^{-1} with a lower frequency progression of 255 cm^{-1}. The high frequency progression interval is in good agreement with the ground state Raman frequency of the a_{1g} O=Os=O stretching mode of 885 cm^{-1}. The high-resolution 6 K spectrum (Figure 7.1c) also shows evidence of phonon sideband structure, however, the spectrum is quite congested making it difficult to definitively assign peaks to genuine progressions in low frequency intermolecular modes or transitions from multiple origins. Further comparison of the band envelope with the **TBA** and **PPH** complexes shows that, despite the similar energy range with **TBA**, the intensity distribution of the 255 cm^{-1} progression is noticeably different where the first maximum in each cluster is the most intense, indicating smaller emitting state displacements along the Os—N normal coordinate.

Figure 7.6a shows the 6 K luminescence spectrum, with the 880 cm^{-1} and 255 cm^{-1} intervals indicated. The first transition originates at 12975 cm^{-1} and after the second quantum of the 255 cm^{-1} mode, an additional interval appears at 12540 cm^{-1} with progressions in the 880 and 255 cm^{-1} intervals built on this transition. The difference from the origin at 12975 cm^{-1} is 435 cm^{-1} (12540 cm^{-1}) and the Raman and IR spectra of this compound in Figure 7.6b show weak bands corresponding to this frequency. Continuing across the band, there is another transition at 11980 cm^{-1} (~1000 cm^{-1}), near the band maximum, with progressions in the 880 and 255 cm^{-1} modes built on this transition. Raman and IR spectra also reveal a peak corresponding to this frequency and both the 435 and 1000 cm^{-1} frequencies are not repeated across the luminescence band. Furthermore, the progressions built on these origins have different temperature-dependent behavior. The 435 cm^{-1} mode is in reasonable agreement with an asymmetric (e_u) Os—NCS bending vibration of 470 cm^{-1} reported for the **TBA** compound[12] and the 1000 cm^{-1} closely matches a C=C vibration in the phenyl ring of the PPN^+ counterion. Comparison of these frequencies in the IR spectrum shows corresponding bands, thus indicating that the *trans*-$[OsO_2(NCS)_4]^{2-}$ luminophore is not exactly centrosymmetric in this crystal lattice although crystallographic information is not available for this

compound. Temperature-dependent luminescence spectra show a rapid broadening of vibronic transitions leading to an overall decrease in resolution and intensity (shown in the inset of Figure 7.6a). There are also noticeable changes in the positions of resolved vibronic maxima, however, the signal-to-noise ratios also decrease rapidly with increasing temperature, making an analysis of these features very difficult. Figure 7.6b shows the ground state Raman spectrum of this compound where the a_{1g} O=Os=O, CS, and Os—N stretching vibration bands are indicated and asterisks highlight the 435 and 1000 cm^{-1} frequencies that correspond to the irregular intervals in the luminescence spectra described above. The appearance of a possible enabling mode in the Raman spectrum may be indicative of minor structural perturbations of the *trans*-$[OsO_2(NCS)_4]^{2-}$ luminophore in this compound where comparison of both IR and Raman spectra reveal the presence of both modes.

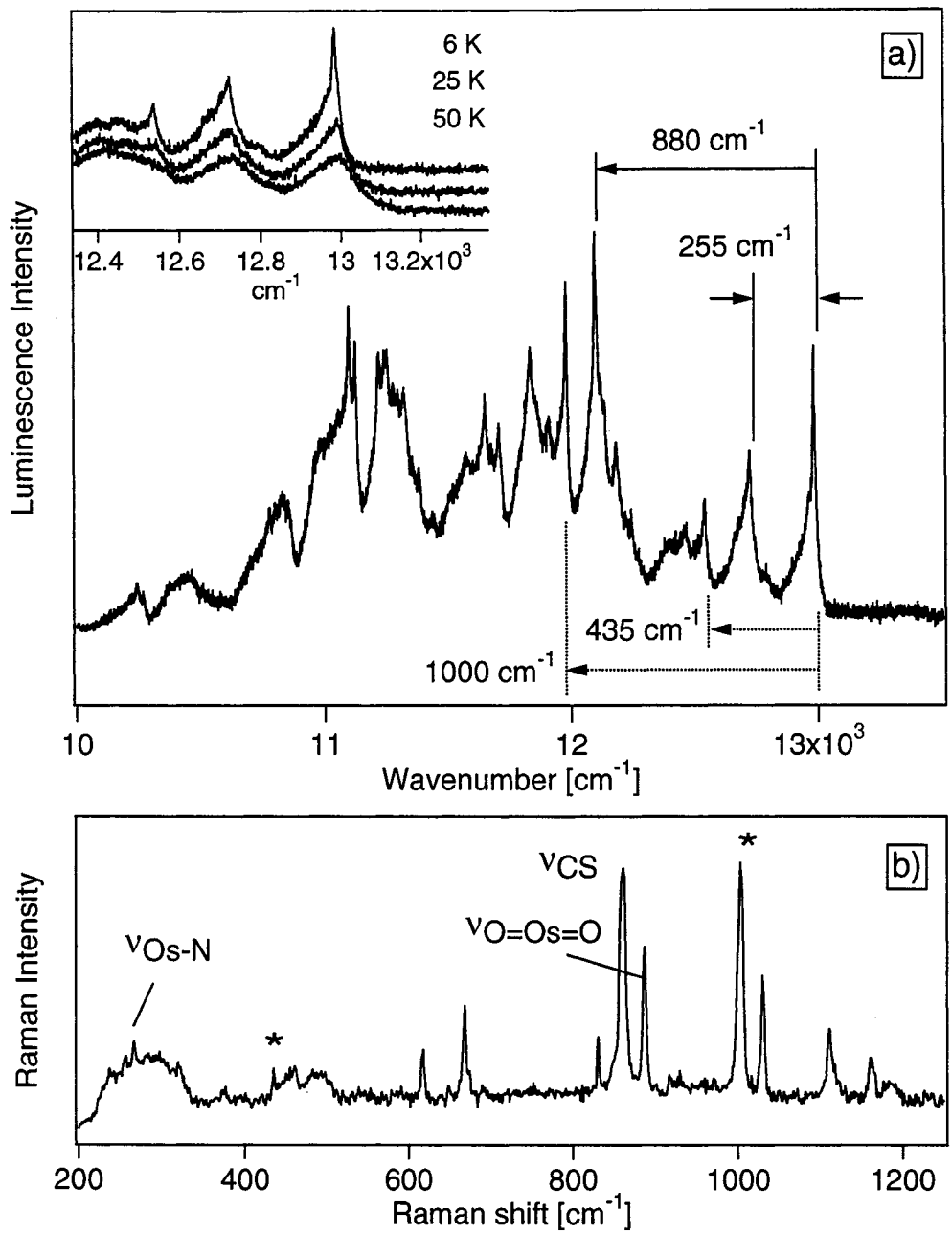

Figure 7.6. a) 6 K high-resolution luminescence spectrum of **PPN** (λ_{exc} = 514.5 nm) with the resolved frequency intervals indicated with solid lines. Anomalous intervals appearing at 435 cm^{-1} and 1000 cm^{-1} are indicated with dotted lines. The inset shows temperature-dependent luminescence spectra of this compound at 6 K, 25 K, and 50 K. b) Room temperature Raman spectrum (λ_{exc} = 633 nm) of **PPN** with the a_{1g} O=Os=O, CS and Os—N bands labeled and asterisks indicate the 435 and 1000 cm^{-1} intervals.

7.4 Discussion

7.4.1 Vibronic Progressions in Metal-Ligand and Ligand-Centered Vibrational Modes.

The low temperature luminescence spectra in Figures 7.1—7.4 and 7.6 show well-resolved high and low frequency vibronic progressions that are in good agreement with previous spectroscopic observations in other *trans*-dioxo systems where most complexes show vibronic structure in high frequency O=M=O and lower frequency M—ligand symmetric stretching modes in either absorption or luminescence. The lower frequency vibronic progression in the three *trans*-$[OsO_2(NCS)_4]^{2-}$ compounds closely matches the a_{1g} Os—N stretching mode of 255 cm^{-1} whereas the high frequency progression does not exactly match the a_{1g} O=Os=O stretching mode frequency of 885 cm^{-1} in all compounds. The high frequency intervals range between 855—880 cm^{-1} and this discrepancy between the O=Os=O mode frequency and the resolved high frequency intervals strongly suggests a contribution from another high frequency mode. From the ground state Raman spectra of all three compounds, the a_{1g} CS stretching mode is only ~30 cm^{-1} lower in frequency than the O=Os=O stretching mode which is in good agreement with the lower limit of the high frequency progression interval frequency range above. The presence of two a_{1g} modes differing by a small amount suggests that the discrepancy between the resolved high frequency interval in the luminescence spectra and the ground state Raman frequencies is due to the displacement of both modes in the emitting state. This is clearly unexpected for a formal ligand-field transition that is largely localized on the osmium(VI) d-orbitals and, to our knowledge, this case represents the first piece of spectroscopic evidence for a Franck-Condon active ligand-centered vibrational mode in this class of complexes. Resonance Raman excitation profiles measured for the **PPH** compound showed enhancements for both high frequency modes, further confirming that both of these modes are displaced in the emitting state. This trend represents a significant deviation from the accepted physical picture of optical transitions in *trans*-dioxo metal complexes where the $(d_{xy}) \rightarrow (d_{xz}, d_{yz})$ transitions are localized on the metal center, hence only emitting state displacements in metal-ligand modes are expected.

The emitting state displacement in the a_{1g} CS stretching mode implies that there must be significant electronic coupling between the ligand- and metal-centered orbitals involved in the luminescence transition. We use DFT methods to calculate the molecular orbital surfaces for the HOMO and LUMO as well as vibrational frequencies in order to gain additional insight into the origin of this effect. These calculations are performed using the Gaussian 98 suite[35] and the point group symmetry of the *trans*-$[OsO_2(NCS)_4]^{2-}$ complex is approximated as exactly D_{4h} but we do not impose symmetry constraints in the geometry optimization process. Figure 7.7 shows the results for the HOMO and LUMO surfaces generated in the DFT calculations with the coordinate systems indicated on both surfaces. These surfaces correspond well to the $d_{xy}(b_{2g}$: HOMO) and d_{xz}, $d_{yz}(e_g$: LUMO) orbitals. Based on the large change in π^* electron density between the HOMO and LUMO levels, most notably on the *trans*-$[O=Os=O]^{2+}$ moiety, a large normal coordinate displacement along the metal-oxo bonds is expected. Additionally, there are changes in π^* electron density on the CS fragments of the NCS^- ligand. In the HOMO surface shown in Figure 7.7, the π^* density on CS is in the *xy* (equatorial) plane of the molecule whereas in the LUMO the electron density has changed significantly (i.e., much less in amplitude) and perpendicular to this plane, indicating changes in CS bond lengths in the lowest energy (emitting) state.

Calculation of vibrational frequencies yields an 887 cm^{-1} Raman-active band that is in excellent agreement with the experimental Raman frequency of the a_{1g} O=Os=O stretching mode of 885 cm^{-1}. Analysis of the individual bonding coordinate displacements in this mode reveals a predominant contribution from Os=O oscillators with significant, but smaller, Os—N and CS stretching character as well. The DFT frequency calculation also predicts other Raman bands at 806 cm^{-1} that involve predominantly the CS oscillators with contributions from both Os=O and Os—N coordinates and a vibration at 247 cm^{-1} that corresponds to the symmetric Os—N breathing mode, in very good agreement with the experimental frequency of ca. 255 cm^{-1}. Interestingly, these calculations predict an IR-active asymmetric (e_u) N—Os—N bending vibration of 171 cm^{-1} as observed in the luminescence spectra of the **TBA** compound, which agrees exactly with the reported value in the literature IR spectrum. The DFT results (molecular orbital shapes and calculated frequencies) qualitatively confirm the

emitting state displacement of the ligand-centered a_{1g} CS mode, which is also strongly supported by the resonance Raman excitation profiles for this mode in Figure 7.5. The enhancement of Raman intensities for the O=Os=O mode is expected and enhancement in the CS mode further demonstrates that a ligand-centered vibrational mode plays an important in bringing the molecule to its emitting state equilibrium geometry.

The title complexes exhibit, to our knowledge, the first known example of a nonzero emitting state displacement in a ligand-centered vibrational mode in the *trans*-dioxo class of metal complexes. Other known cases where evidence of displacements in ligand-centered vibrational modes has been observed in the spectroscopy of d–d electronic transitions involve some tetragonal first-row transition metal complexes. Low temperature absorption spectroscopic studies on *trans*-$[MCl_2(H_2O)_4]^{n+}$ complexes (M= Ni^{2+}, Co^{2+}, V^{3+}, and Cr^{3+}) has shown evidence for vibronic progressions based on the high frequency O—H stretching modes of the water ligands, but only a very small displacement in the excited states is observed.[36] Additionally, recent low temperature luminescence measurements on the organometallic $[Ta(CO)_6]^-$ complex show two resolved progressions in the symmetric Ta—C stretching mode, where one of the progressions was based on a high frequency CO vibronic origin.[37] However, the detailed experimental spectroscopic data and qualitative theoretical calculations presented here demonstrate that a symmetric ligand-centered stretching mode has a significant emitting state displacement and its inclusion in the analysis of vibronic structure is necessary.

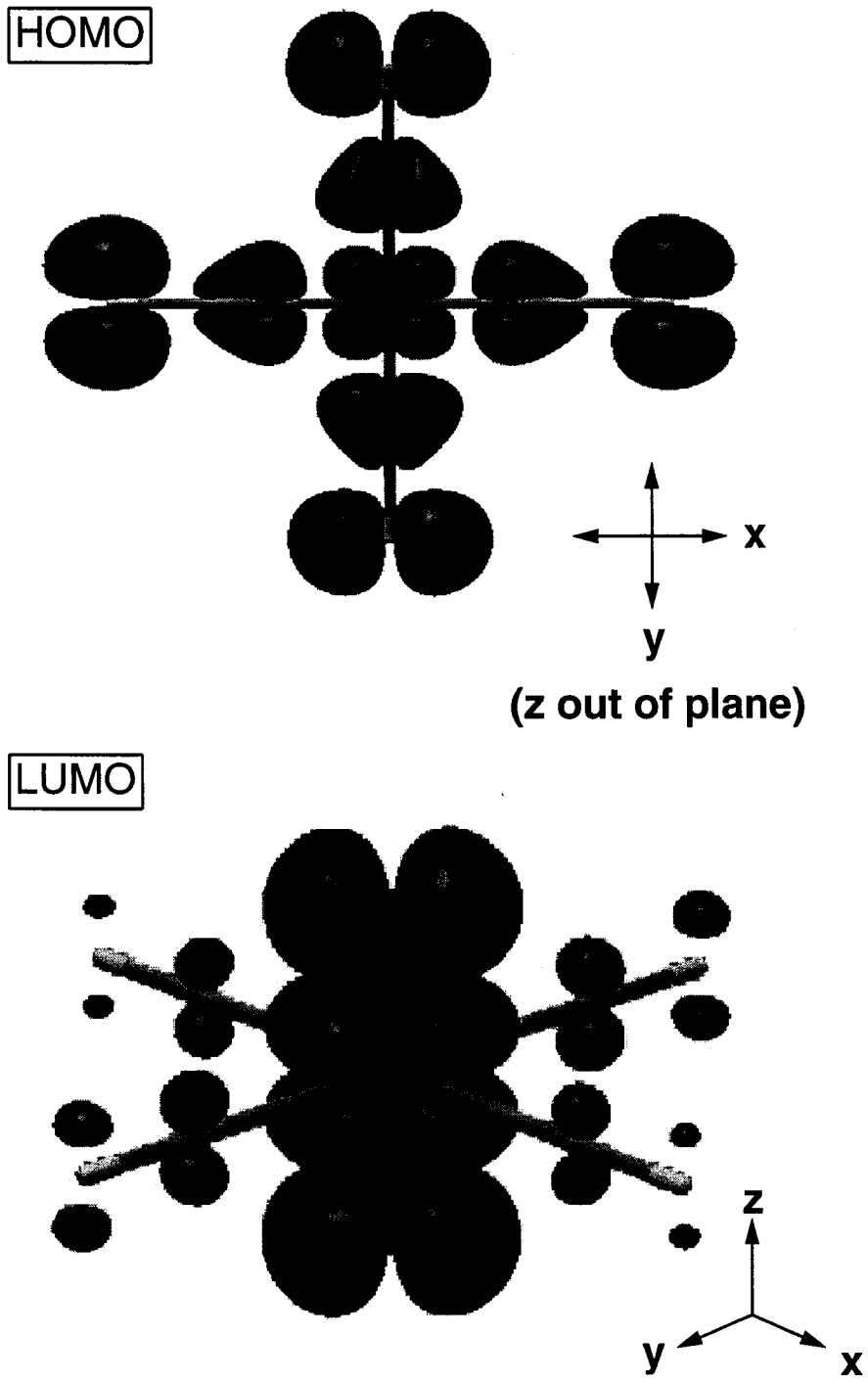

Figure 7.7. Molecular orbital surfaces generated from DFT calculations with Cartesian coordinate references given for each surface. The top picture is of the highest occupied molecular orbital (HOMO) and the bottom picture is the lowest unoccupied molecular orbital (LUMO).

7.4.2 Calculation of the Vibronic Structure in the Luminescence Spectra.

The well-resolved vibronic structure in the low temperature luminescence spectra of the title compounds enables a detailed analysis of each displaced normal coordinate and the vibronic features of each compound. We use the time-dependent theory of luminescence spectroscopy[38-40] to calculate the experimental bandshapes by fitting the intensity distributions. The parameters used in the calculations are the normal coordinate offsets, Δ_i (dimensionless units), energy of electronic origin, E_{00} (cm^{-1}), vibrational frequency for each displaced mode, $\hbar\omega_i$ (cm^{-1}) and the phenomenological damping factor, Γ (cm^{-1}), that defines the bandwidth of individual vibronic transitions. The values for Δ_i are adjusted to reproduce the individual intensity distributions for each displaced mode. We assume one emitting state and include three vibrational modes in these calculations: the a_{1g} O=Os=O, CS, and Os—N stretching modes and the frequencies are taken from both our own experimental and literature Raman spectra. E_{00} is chosen as the first resolved peak in each progression and, in the **TBA** and **PPN** complexes, multiple origins are used to fit the experimental spectrum with progressions in the a_{1g} modes built on these origins. The initial and final states are represented as harmonic potential energy surfaces where it is assumed that: (a) the vibrational frequencies, $\hbar\omega_i$, in the ground and excited states are identical, (b) there is no coupling between normal coordinates, and (c) the transition dipole moment is constant. Previous work on *trans*-dioxo rhenium(V) ethylenediamine and imidazole complexes displayed luminescence bandshapes which were dependent on the energy of the luminescence and the magnitude of the O=Re=O and Re—ligand normal coordinate offsets.[17,18] This feature arises from coupling between the a_{1g} O=Re=O and Re—N stretching modes induced by interactions between the ground and excited states of the same A_{1g} symmetry.[18] When the Franck-Condon region of the luminescence transition is near an avoided crossing, such as between the ground state and the A_{1g} spin-orbit component of the ^3E_g excited state, this effect is more pronounced in the experimental spectrum where clusters of vibronic transitions are not replicas of each other across the entire band. The luminescence spectra in Figures 7.1—7.4 and 7.6 reveal similar behavior where intensity distributions of the lower frequency Os—N progressions change as a function of decreasing wavenumber. In spite of what seems to be a case for

coupled coordinates, we are able to use the simpler harmonic models to successfully reproduce all relevant spectroscopic features outlined in the previous section.

Initially, calculations were performed by using only the O=Os=O and Os—N modes, however, agreement with experiment was poor due to the inability of the model to reproduce the high frequency interval and intensity distributions of the low frequency progressions in each compound. In order to account for the variations in the high frequency interval between compounds, the ligand-centered, a_{1g} CS stretching mode must be included. The relative contribution of the O=Os=O and CS modes can be estimated by calculating only the high frequency interval using these high two modes. Figure 7.8a shows an example for the **TBA** compound where the Δ values of both the a_{1g} O=Os=O (885 cm^{-1}) and CS (858 cm^{-1}) are varied to reproduce the "effective" high frequency interval of 870 cm^{-1} in the 5 K spectrum. The appearance of a resolved frequency interval in luminescence spectra that does not have a matching value in the ground state Raman spectrum has been termed the missing mode effect or, MIME. The MIME arises from the displacement of at least two Franck-Condon active vibrations that are usually close in frequency where the individual maxima combine to give the appearance of only one frequency. This effect is not observed for the **PPN** compound where the resolution is much higher than that of the other two compounds, i.e., the vibronic linewidth Γ is less than the difference between both implicated frequencies. This frequency difference dictates the range of the MIME frequency and the individual contribution of each displaced mode is determined largely by their Δ_i values[41] and in the simple two-mode calculation of the **TBA** compound, $\Delta_{CS} = 1.91$ ($\Delta Q_{CS} = 0.067$ Å) and $\Delta_{O=Os=O} = 1.14$ ($\Delta Q_{O=Os=O} = 0.055$ Å). The time-dependent theory of spectroscopy provides an intuitive means for understanding this effect in the time-domain and, in Figure 7.8b, we show the autocorrelation function[42] for the individual modes (dotted and hatched traces) and the overlap for the two-mode calculation in Figure 7.8b (solid trace). The recurrence times for each mode are 39 fs for the CS mode and 37 fs for the O=Os=O mode and the total overlap is generated by multiplying the individual overlap functions for each mode which makes it possible to visualize the MIME in this case. Ref. 41 presents a simple formula for estimating the MIME frequency which we determine to be 866 cm^{-1} based on the frequencies of the CS and O=Os=O modes and values for Δ_{CS} and $\Delta_{O=Os=O}$ ($\Gamma = 25$ cm^{-1}).

This preliminary calculation involving two high frequency modes differing by less than 30 cm^{-1} (Figure 7.8a) reveals that Δ_{CS} can make a sizable contribution to the observed frequency and further justifies its inclusion in the calculation of vibronic structure. We now calculate the full luminescence bandshapes and vibronic features for each compound and all numerical values used in the fits are collected in Table 7.2.

The luminescence band envelope of the **TBA** compound shows what superficially appears to be strong evidence for coupled motions of the displaced normal coordinates with the intensity distribution of the cluster of lower frequency (Os—N) vibronic bands varying across the band. This is most apparent upon comparison of the first and third clusters where the intensity of the third quantum is less in the third cluster beginning at 11260 cm^{-1} (third quanta of O=Os=O/ CS modes) than in the first cluster beginning at 13000 cm^{-1}. Additionally, the irregular interval causing the double maximum on the second member of each cluster is a strong indication that this feature arises from a transition built on a different origin. Evidence for two different origins comes from the temperature-dependent luminescence spectra (Figure 7.2a) where the intensity and energy of the second member, i.e., the double maximum, changes as a function of temperature. It is not possible to reproduce this and other features using only a simple model with one origin and three vibrational modes. We had attempted to calculate the double maximum by including a 170 cm^{-1} mode, but this did not lead to a reasonable fit because only one quantum of this mode appears in the spectrum. In order to explain the unusual bandshapes of the **TBA** compound we interpret this interval as a vibronic origin built on the first peak of the double maximum starting at 12833 cm^{-1}. Figure 7.9a compares two spectra that are calculated using the three a_{1g} modes mentioned previously and the same values for Δ_i, $\hbar\omega_i$, and Γ (Table 7.2) with the high-resolution 6 K luminescence spectrum. The origin of the first calculated spectrum (dotted trace) is taken as the first peak in the main band (13000 cm^{-1}) and the first peak of the double maximum (12833 cm^{-1}) is the second origin (hatched trace). The first spectrum (E_{00} = 13000 cm^{-1}) is multiplied by an appropriate factor to reproduce the overall intensity ratio of the first peak relative to that of the second spectrum, which phenomenologically accounts for the total intensities of both electronic transitions and the two spectra are added to obtain the total calculated spectrum. Figure 7.9b shows the best-fit total spectrum using the two–origin model

(bottom trace) with the high-resolution 6 K spectrum (middle trace) and the 5 K overall spectrum (top trace). The best-fit spectrum shows excellent agreement with both experimental spectra where the intensity distribution of the double maximum is replicated across the entire luminescence band (indicated by the small sloping solid lines) and the intensity distributions of each cluster are in very good agreement with the overall band envelope upon comparison with the 5 K total spectrum (illustrated with the hatched sloping lines for the third cluster). Upward pointing arrows on the 5 K spectrum point out small resolved shoulders on the lower energy side of the third member of the 255 cm^{-1} progression that are also reproduced in the best-fit spectrum.

Figure 7.10a shows the 5 K luminescence spectrum (top trace) and calculated spectrum of **PPH** (bottom trace). The calculated spectrum was carried out using the totally symmetric O=Os=O, CS and Os—N modes with one origin. We do not attempt to reproduce the fine structure corresponding to phonon sidebands in the high-resolution spectrum and calculate only the overall band envelope. The intensity distribution of the low frequency Os—N interval changes quite noticeably across the entire luminescence band. However, the simple harmonic three-mode model is able to reproduce the bandshape very well, which is highlighted by the sloping lines on the first and fourth clusters. Because there was no apparent evidence for multiple transitions from different origins, a single origin model was used to calculate the total spectrum. Figure 7.10b shows the experimental 6 K luminescence spectrum (top trace) and the best-fit calculated spectrum (bottom trace) of the **PPN** compound. This spectrum was calculated using the same a_{1g} vibrational modes as before and three origins based on the first peak of the main spectrum (12975 cm^{-1}) and at 12540 cm^{-1} and 11980 cm^{-1}, which correspond to the 435 and 1000 cm^{-1} intervals discussed earlier. The total spectrum was obtained in a similar manner as for **TBA** where the relative intensity of the first peak in each spectrum was adjusted by multiplying the spectrum by an appropriate factor to reproduce the overall spectral band envelope, which qualitatively accounts for the intensities of each transition. The individual spectra are added to give the total calculated spectrum with the proper intensity ratios for each of the constituent spectra. Agreement between the experimental and calculated spectra are very good, however, all of the fine resolved features, such as lattice modes, cannot be reproduced entirely.

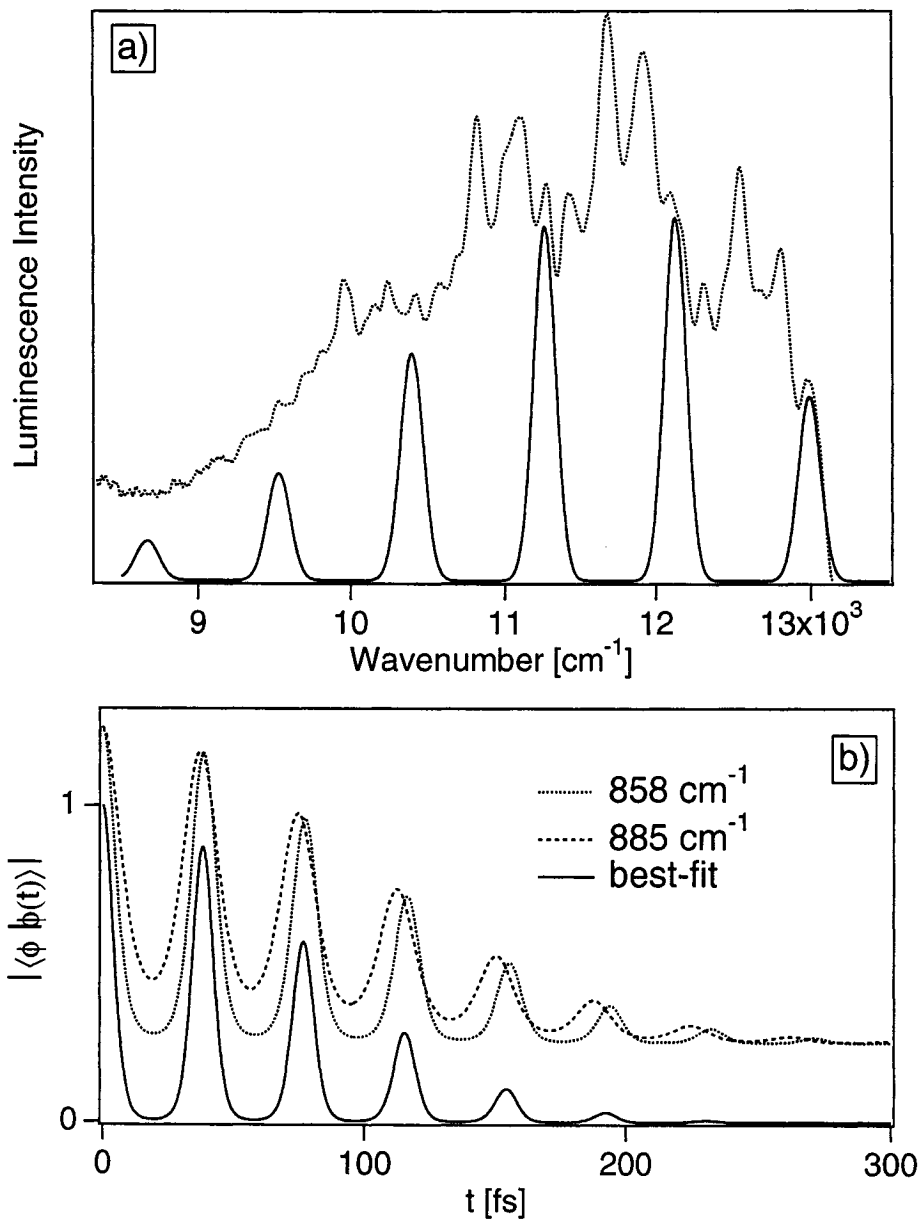

Figure 7.8. a) Experimental 5 K luminescence spectrum of **TBA** (dotted trace) and 2-mode calculated fit. b) Autocorrelation overlaps of the 2-mode spectrum in a) (solid trace) and overlap for the 858 cm^{-1} CS mode (···) and 885 cm^{-1} O=Os=O mode (---).

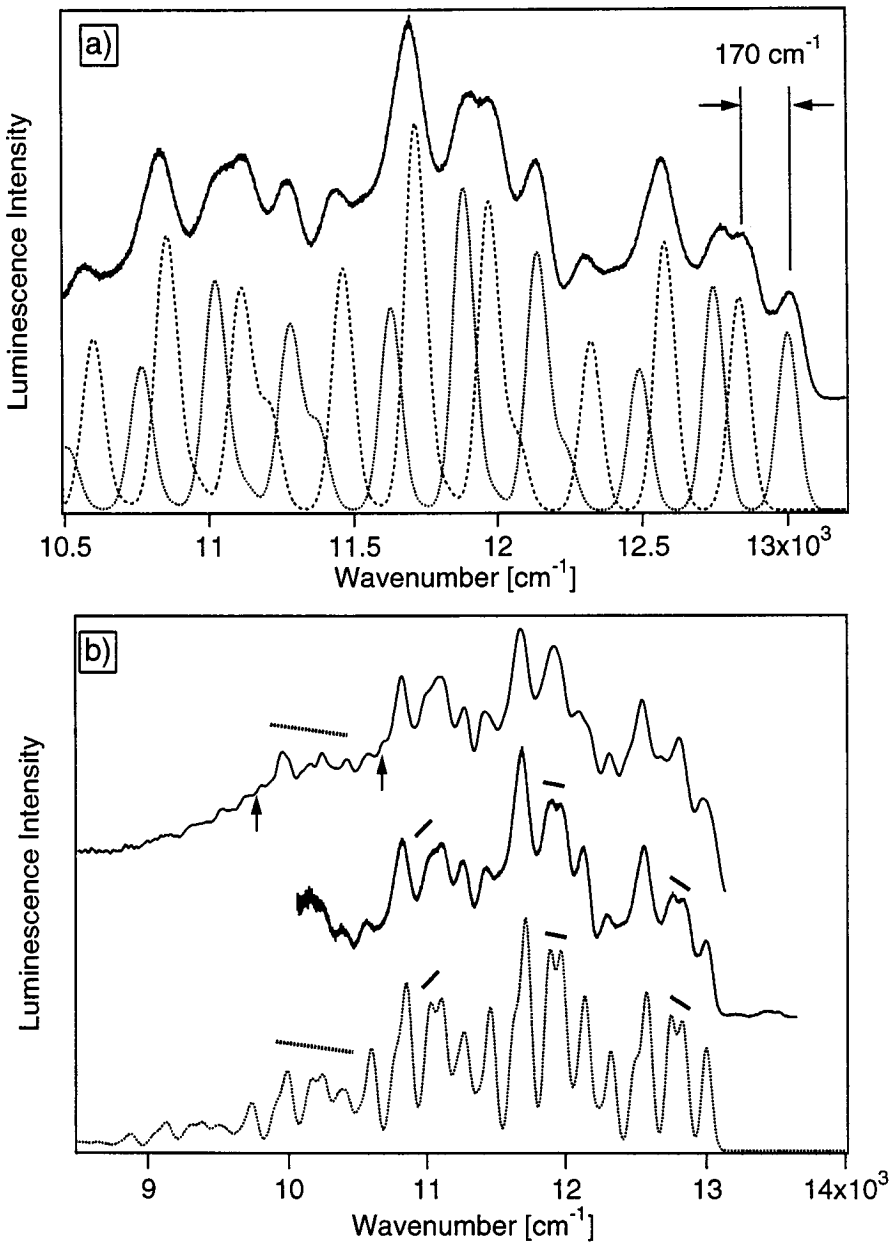

Figure 7.9. a) Comparison of 6 K high resolution luminescence spectrum of **TBA** (top trace) and 3-mode (O=Os=O, CS, Os—N) calculated spectra. Two spectra are calculated based on different origins of 13000 cm^{-1} (···) and 12833 cm^{-1} (---) using identical offsets for each spectrum. b) Comparison of 5 K luminescence spectrum (top trace), high-resolution 6 K luminescence spectrum (middle trace) and best-fit, 3-mode, 2-origin calculated spectrum (bottom trace). Small solid sloping lines on the calculated spectrum and the high-resolution spectrum show the agreement between experiment and the calculated spectrum of the double maximum appearing on the second member of each cluster. Hatched sloping lines on the 5 K spectrum and the calculated spectrum show the effect of varying intensity distribution of the 255 cm^{-1} Os—N progression. Arrows on the 5 K spectrum highlight shoulders that are reproduced in the best-fit calculated spectrum.

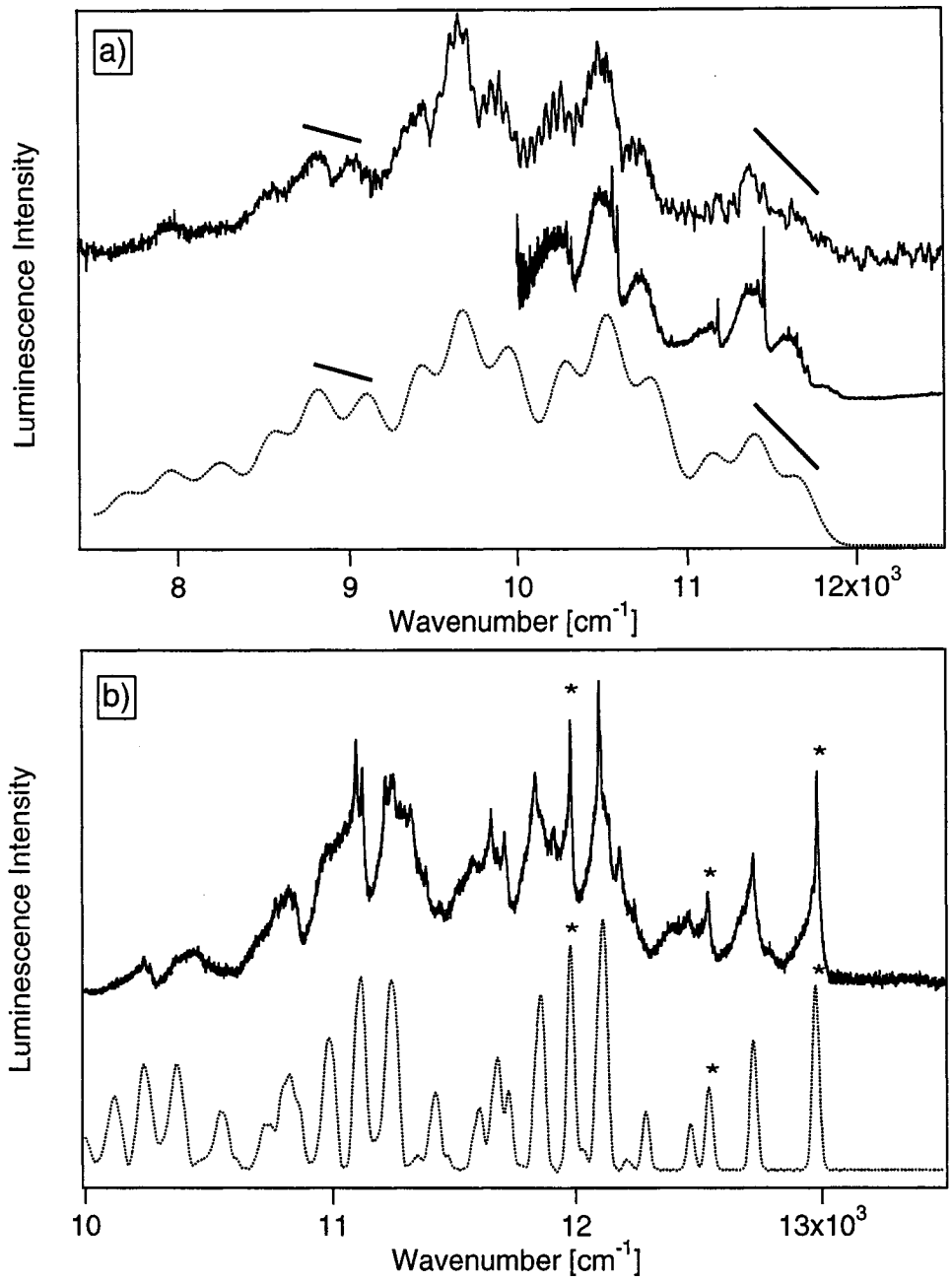

Figure 7.10. a) Comparison of the 5 K luminescence spectrum (top trace) and the high-resolution spectrum (middle trace) of **PPH** with the best-fit calculated spectrum consisting of progressions in the a_{1g} O=Os=O, CS and Os—N modes (bottom trace) with one origin at 11650 cm^{-1}. Sloping solid lines on the first and fourth clusters show the agreement between the calculated spectrum and experimental spectra. b) Comparison of the 6 K high-resolution spectrum of **PPN** and the best-fit 3-mode calculated spectrum. Three spectra are calculated with each origin indicated with an asterisk and are multiplied by an appropriate factor to obtain the proper intensity ratio between each spectrum.

7.4.3 Emitting State Displacements in the O=Os=O and CS High Frequency Vibrational Modes.

The normal coordinate offsets used in the calculations are listed in Table 7.2 for each compound and are given in dimensionless units (Δ) and converted to Ångstrom (ΔQ). We now compare the ΔQ values between each of the title compounds and other d^2 *trans*-dioxo complexes. The values for the emitting state offset along the a_{1g} CS mode (ΔQ_{CS}) and the a_{1g} O=Os=O stretching mode ($\Delta Q_{O=Os=O}$) were 0.038 and 0.062 Å, respectively, for **TBA** and 0.060 and 0.065 Å, respectively, for **PPH** thus demonstrating that the dominant displacement occurs along the CS mode. These larger offsets along the CS modes lead to a high frequency interval closer to the CS frequency, which is a consequence of the MIME. Because the high frequency interval in the **PPN** complex (880 cm^{-1}) was closer to the O=Os=O stretching frequency of 885 cm^{-1}, it is expected that the $\Delta Q_{O=Os=O}$ should be larger than that of ΔQ_{CS}. The $\Delta Q_{O=Os=O}$ for this compound was found to be 0.063 Å, for progressions built on I and II, compared to the value of 0.061 Å determined for ΔQ_{CS}, yielding a larger observed frequency interval in the low temperature luminescence spectra than for the other two compounds. For highly resolved vibronic structure, the MIME is not observed since individual vibronic maxima are well-resolved, which may also explain why the high frequency interval in the **PPN** compound is much closer to that of the O=Os=O frequency as opposed to the others where the maxima are much less resolved (i.e., larger values of Γ). The value of $\Delta Q_{O=Os=O}$ for **TBA** was considerably smaller than those obtained from the other compounds. It is not apparent from the crystal structure of this compound if intermolecular packing forces impede motion along this coordinate, thus leading to smaller offsets. This large difference is difficult to interpret since all compounds have very different luminescence bandshapes and our choice of model excludes other effects, such as coupling between normal coordinates, which may contribute to the observed bandshapes to a varying degree.

compound	**TBA**	**PPH**	**PPN**
E_{00} [cm^{-1}]	**I.** 13000	11650	**I.** 12975
	II. 12830		**II.**[b] 12540
			III.[b] 11980
$\Delta_{O=Os=O} : \Delta Q_{O=Os=O}$	**I.**[b] 0.77: 0.038	1.22: 0.060	**I.** 1.30: 0.063
[dimensionless: Å][a]	**II.** 0.77: 0.038		**II.**[c] 1.30: 0.063
($\hbar\omega_{O=Os=O}$ = 885 cm^{-1})			**III.**[c] 1.18: 0.058
$\Delta_{CS} : \Delta Q_{CS}$	**I.**[b] 1.76: 0.062	1.87: 0.065	**I.** 1.73: 0.061
[dimensionless: Å][a]	**II.** 1.76: 0.062		**II.**[c] 1.73: 0.061
($\hbar\omega_{CS}$ = 858 cm^{-1})			**III.**[c] 1.34: 0.047
$\Delta_{Os\text{-}N} : \Delta Q_{Os\text{-}N}$	**I.**[b] 1.64: 0.078	1.87: 0.089	**I.** 1.22: 0.058
[dimensionless: Å][a]	**II.** 1.64: 0.078		**II.**[c] 1.22: 0.058
($\hbar\omega_{Os\text{-}N}$ = 255 cm^{-1})			**III.**[c] 0.87: 0.030
Γ [cm^{-1}]	25	70	10

[a] The formula for converting from dimensionless units is given by: $\Delta Q_k = \sqrt{\frac{N_A \hbar}{4\pi^2 c \hbar \omega_k M}} 10^8 \Delta_k$ where N_A is Avogodro's number, $\hbar$ is Planck's constant in erg s, c is the speed of light in cm s^{-1}, $\hbar\omega_k$ is the frequency of the vibration in cm^{-1}, and M is the mass of the mode in g mol^{-1}.

[b] The intensity of band **I** is scaled to 80% of its original value.

[c] Intensities of bands **II** and **III** are scaled to 50% of their original vales to fit the experimental spectra.

Table 7.2. Parameters used for the calculation of luminescence spectra in Figures 7.9 and 7.10.

Emitting state normal coordinate displacements along the low frequency a_{1g} Os—N stretching mode were substantially larger than the offsets determined for the high frequency modes in the **TBA** and **PPH** compounds with values of 0.078 Å and 0.089 Å, respectively whereas the **PPN** compound shows a much smaller offset of 0.058 Å in this mode. This can be seen directly in the experimental spectra where the first quantum of this mode is the most intense followed by less intense transitions in higher quanta of this mode, indicating a smaller emitting state displacement. It is also interesting to note that the largest displacement along Q_{Os-N} coincides with the largest value of ΔQ_{CS}, which leads to a high frequency interval that more closely matches the frequency of the CS mode, such as in the **PPH** compound with a resolved high frequency interval of 855 cm^{-1}. The **PPN** compound is at the other limit where smaller values of ΔQ_{Os-N} and smaller ΔQ_{CS} are obtained and a high frequency interval (880 cm^{-1}) that is closer to the frequency of the O=Os=O mode of 885 cm^{-1}. This correlation between the CS and Os—N stretching coordinates illustrates the importance of ligand-centered vibrational modes on the d–d luminescence transition.

Comparison of ΔQ values determined here with other *trans*-dioxo complexes of both osmium(VI) and rhenium(V) reveals similar trends as well as some differences in the established emitting state properties of these systems. The only other reported case in *trans*-dioxo osmium(VI) complexes where resolved vibronic structure in both the O=Os=O and Os—ligand stretching modes are both resolved is in the 77 K luminescence spectrum of the *trans*-$[OsO_2(CN)_4]^{2-}$ complex. We calculate normal coordinate displacements in the a_{1g} O=Os=O and Os—CN stretching modes of 860 cm^{-1} and 400 cm^{-1}, respectively, with experimental data taken from Sartori and Preetz.[27] The values determined for $\Delta Q_{O=Os=O}$ and ΔQ_{Os-CN} were 0.12 and 0.076 Å, respectively, the former being in good agreement with the range reported by Sartori and Preetz of 0.1—0.13 Å. Other work on osmium(VI) complexes with bidentate, oxygen-donating oxalate ligands and nitrogen-donating ethylenediamine ligand reported emitting state displacements in the a_{1g} O=Os=O stretching mode (~910 cm^{-1}) of 0.085 and 0.10 Å, respectively.[18] These values are slightly larger than those for $\Delta Q_{O=Os=O}$ and ΔQ_{CS} reported here. Vibronic structure in the Os-ligand modes in this earlier work was not sufficiently resolved to

permit the inclusion of these lower frequency modes in the calculation.[18] The values reported for $\Delta Q_{Os\text{-}N}$ in Table 7.2 are therefore the first of their kind reported from resolved low temperature luminescence spectra of *trans*-dioxo osmium(VI) complexes. Further comparison with isoelectronic *trans*-dioxo rhenium(V) complexes with monodentate and bidentate nitrogen-donating ancillary ligands, such as imidazoles, reveals somewhat larger emitting state offsets along the high frequency O=Re=O normal coordinate that have similar vibrational frequencies as the two displaced high frequency modes in the title compounds. In a series of rhenium(V) complexes with substituted imidazole ligands the $\Delta Q_{O=Re=O}$ values were found to range between 0.10—0.11 Å whereas complexes with substituted ethylenediamine ligands showed slightly larger offsets between 0.12—0.13 Å.[16,18] Displacements in the Re-ligand modes were also determined, which were in a similar range as those reported here (0.08—0.1 Å) with the exception of the **PPN** complex that showed a much smaller value of $\Delta Q_{Os\text{-}N}$. The sign of $\Delta Q_{M\text{-}L}$ is also important where loss of electron density in the *xy* plane upon promotion of an electron to the d_{xz}, d_{yz} orbitals leads to a decrease in M—L bond lengths (i.e., increase in M—L vibrational frequency) and thus a negative sign of the normal coordinate offset. Because harmonic potential energy surfaces are used to represent the ground states in the calculated spectra, only the absolute values of $\Delta Q_{Os\text{-}N}$ are obtained from our calculations.

The detailed analysis of vibronic structure and extraction of emitting state offsets for each displaced normal coordinate provides a valuable insight into the excited state geometries of these and related *trans*-dioxo complexes. However, there is no conclusive evidence from these calculations why the luminescence bandshapes change so much between the compounds. Based on the invariance of Raman frequencies for the O=Os=O, CS and Os—N modes in all three compounds, the ligand sphere around the metal center is practically identical. The effect of the environment on the optical properties of these compounds appears to have a significant influence on what is formally a metal-centered electronic transition. This interaction between intra- and intermolecular properties has also been observed in different salts of the *trans*-$[ReO_2(pyridine)_4]^+$ complex where luminescence bandshapes and energies change somewhat as a function of counterion.[5, 43] The degree of phonon band structure also indicates the degree of coupling

between lattice and intramolecular vibrations, which (as shown in Figure 7.1) can be tuned by choice of counterions.

7.5 Conclusions

The nonzero offsets of the emitting state potential energy minima along a ligand-centered vibrational mode are illustrated in the *trans*-dioxo class of complexes for the first time. From the values of normal coordinate offsets extracted from the calculated spectra, it appears that the magnitude of the low frequency (Os—N) normal coordinate offset is related to that of the high frequency CS mode. This interdependence of both metal-ligand and ligand-centered stretching motions is also supported by theoretical calculations where calculated O=Os=O, CS, and Os—N symmetric stretching frequencies closely matched those observed in experimental vibrational spectra and all contained varying contributions from the O=Os=O, CS, and Os—N coordinates. The intramolecular luminescence transition also appears to be influenced by the environment of the *trans*-$[OsO_2(NCS)_4]^{2-}$ luminophore where the magnitude of normal coordinate offsets and luminescence energies change noticeably between compounds.

References

(1) Ballhausen, C. J.; Gray, H. B. *Inorg. Chem.* **1962**, *1*, 111.

(2) Jørgensen, C. K. *Acta. Chem. Scand.* **1957**, *11*, 73.

(3) Miskowski, V. M.; Gray, H. B.; Hopkins, M. D. In *Adv. in Trans. Met. Coord. Chem.*; Che, C.-M., Yam, V. W.-W., Eds.; JAI Press: Greenwich, CT, 1996; Vol. 1, p 159.

(4) Winkler, J. R.; Gray, H. B. *J. Am. Chem. Soc.* **1983**, *105*, 1373.

(5) Winkler, J. R.; Gray, H. B. *Inorg. Chem.* **1985**, *24*, 346.

(6) Stanislas, S.; Reber, C.; Beauchamp, A. L. *Inorg. Chem.* **2000**, *39*, 2152.

(7) Da Re, R. E.; Hopkins, M. D. *Inorg. Chem.* **2002**, *41*, 6973.

(8) Bailey, S. E.; Eikey, R. A.; Abu-Omar, M. M.; Zink, J. I. *Inorg. Chem.* **2002**, *41*, 1755.

(9) Espenson, J. H. *Adv. Inorg. Chem.* **2003**, *54*, 157.

(10) Nugent, W. A.; Mayer, J. M. *Metal-Ligand Multiple Bonds*; John Wiley: New York, 1988.

(11) Du Bois, J.; Tomooka, C. S.; Hong, J.; Carreira, E. M. *Acc. Chem. Res.* **1997**, *30*, 364.

(12) Stumme, M.; Preetz, W. *Z. Anorg. Allg. Chem.* **2000**, *626*, 1367.

(13) Pearson, R. G. *J. Am. Chem. Soc.* **1963**, *85*, 3533.

(14) Pearson, R. G. *Science* **1966**, *151*, 172.

(15) Savoie, C.; Reber, C.; Bélanger, S.; Beauchamp, A. L. *Inorg. Chem.* **1995**, *34*, 3851.

(16) Savoie, C.; Reber, C. *Coord. Chem. Rev.* **1998**, *171*, 387.

(17) Landry-Hum, J.; Tessier, V.; Ernzerhof, M.; Reber, C. *Coord. Chem. Rev.* **2002**, *233-234*, 63.

(18) Savoie, C.; Reber, C. *J. Am. Chem. Soc.* **2000**, *122*, 844.

(19) Che, C.-M.; Cheng, W. K. *J. Am. Chem. Soc.* **1986**, *108*, 4644.

(20) Che, C.-M.; Yam, V. W.-W.; Cho, K.-C.; Gray, H. B. *Chem. Comm.* **1987**, 948.

(21) Yam, V. W. W.; Che, C.-M. *J. Chem. Soc., Chem. Comm* **1988**, 100.

(22) Yam, V. W. W.; Che, C.-M. *New. J. Chem.* **1989**, *13*, 707.

(23) Yam, V. W.-W.; Che, C.-M. *Coord. Chem. Rev.* **1990**, *97*, 93.

(24) Maiboroda, A.; Rheinwald, G.; Lang, H. *Eur. J. Inorg. Chem.* **2001**, *9*, 2263.

(25) Dobson, J. C.; Meyer, T. J. *Inorg. Chem.* **1989**, *28*, 2013.

(26) Che, C.-M.; Cheng, W. K.; Yam, V. W. W. *J. Chem. Soc., Dalton Trans.* **1990**, 3741.

(27) Sartori, C.; Preetz, W. *Z. Naturforsch.* **1988**, *43a*, 239.

(28) Hopkins, M. D.; Miskowski, V. M.; Gray, H. B. *J. Amer. Chem. Soc.* **1986**, *108*, 6908.

(29) Tutt, L.; Tannor, D.; Heller, E. J.; Zink, J. I. *Inorg. Chem.* **1982**, *21*, 3858.

(30) Tutt, L.; Zink, J. I. *J. Amer. Chem. Soc.* **1986**, *108*, 5830.

(31) Griffith, W. P.; Jolliffe, J. M. *J. Chem. Soc., Dalton Trans.* **1992**, 3483.

(32) Sartori, C.; Preetz, W. *Z. Anorg. Allg. Chem.* **1988**, *565*, 23.

(33) Oetliker, U.; Reber, C. *J. Near Infrared Spectr.* **1995**, *3*, 63.

(34) Davis, M. J.; Reber, C. *Inorg. Chem.* **1995**, *34*, 4585.

(35) a) Frisch, M.J.; Trucks, G.W.; Schlegel, H.B.; Scuseria, G.E.; Robb, M.A.; Cheeseman, J.R.; Montgomery Jr., J.A.; Stratmann, R.E.; Burant, J.C.; Dapprich, S.; Millam, J.M.; Daniels, A.D.; Kudin, K.N.; Strain, M.C.; Farkas, O.; Tomasi, J.; Barone, V.; Cossi, M.; Cammi, R.; Mennucci, B.; Pomelli, C.; Adamo, C.; Clifford, S.; Ochterski, J.; Petersson, G.A.; Ayala, P.Y.; Cui, Q.; Morokuma, K.; Malick, D.K.; Rabuck, A.D.; Raghavachari, K.; Foresman, J.B.; Cioslowski, J.; Ortiz, J.V.; Stefanov, B.B.; Liu, G.; Liashenko, A.; Piskorz, P.; Komaromi, I.; Gomperts, R.; Martin, R.L.; Fox, D.J.; Keith, T.; Al-laham, M.A.; Peng, C.Y.; Nanayakkara, A.; Gonzalez, C.; Challacombe, M.; Gill, P.M.W.; Johnson, B.G.; Chen, W.; Wong, M.W.; Andres, J.L.; Head-Gordon, M.; Replogle, E.S.; Pople, J.A. *Gaussian 98*, Gaussian Inc. Pittsburgh PA 2001. b) The LanL2DZ pseudopotential and basis set functionals and the RB3LYP method were used for the exchange-correlation energy term in the Kohn-Sham calculation.

(36) Bussière, G.; Beaulac, R.; Cardinal-David, B.; Reber, C. *Coord. Chem. Rev.* **2001**, *219-221*, 549.

(37) Bitner, T. W.; Zink, J. I. *J. Am. Chem. Soc.* **2000**, *122*, 10631.

(38) Zink, J. I.; Kim Shin, K.-S. In *Adv. Photochem.*; Volman, D. H., Hammond, G. S., Neckers, D. C., Eds.; John Wiley: New York, 1991; Vol. 16, p 119.

(39) Heller, E. J. *J. Chem. Phys.* **1975**, *62*, 1544.

(40) Heller, E. J. *Acc. Chem. Res.* **1981**, *14*, 368.

(41) Tutt, L.; Zink, J. I.; Heller, E. J. *Inorg. Chem.* **1987**, *26*, 2158.

(42) The expression for the autocorrelation overlap function is given by,

$$\langle \phi_k | \phi_k(t) \rangle = \exp\left[-\frac{\Delta_k^2}{2}(1-\exp(-i\omega_k t)) - \frac{i\omega_k t}{2}\right]\exp\left(\frac{-iE_{00}t}{\hbar} - \Gamma^2 t^2\right)$$

where Δ_k is the normal coordinate offset of the *k*th mode in dimensionless units, ω_k is the frequency of the *k*th mode in cm^{-1}, E_{00} is the energy of electronic origin transition in cm^{-1}, and Γ is the phenomenological damping factor in cm^{-1}. This

expression is then Fourier-transformed into the frequency domain to give the calculated spectrum.

(43) Grey, J.K.; Butler, I.S.; Reber, C. Can J. Chem. Accepted for publication.

Chapter 8

Large Pressure-Induced Increase in Luminescence Intensity for the $[Pd(SCN)_4]^{2-}$ Complex

This chapter explores the luminescence properties of square-planar Pd(II) complexes, which represent the tetragonally elongated limit of D_{4h} point group symmetry. Temperature- and pressure-dependent luminescence intensities and lifetimes of the $[Pd(SCN)_4]^{2-}$ complex show a dramatic variation over the range studied. Pressure-dependent luminescence intensities at room temperature show an unusual enhancement by several orders of magnitude from ambient values and this effect is compared to other Pd(II) complexes with different ligands. Chapter 9 systematically studies the origin of this effect.

8.1 Introduction

Broad-band luminescence in the red to near-infrared wavelength range from transition metal complexes is usually weak at room temperature.[1,2] The luminescence intensity of $[Pd(SCN)_4](n\text{-}Bu_4N)_2$ single crystals[3] at room temperature shows an unprecedented pressure-induced increase by several orders of magnitude. Other square-planar d^8 complexes, such as the well-studied $[Pt(CN)_4]^{2-}$, do not show comparable increases,[4] and compounds such as $[Ru(bpy)_3]^{2+}$,[5] or *trans*-$[ReO_2(tmen)_2]^+$,[6] show an intensity decrease with pressure. A recent study on manganese(II) ions doped into $Ca_{0.25}Sr_{0.75}F_2$ documents an increase of the luminescence lifetime by a factor of four at 40 kbar.[7] This effect is orders of magnitude lower than the effect described here.

In order to verify the effect of pressure on the luminescence properties of the title complex, other Pd(II) complexes are studied with different ligands. The

* Modifications were made to the original manuscript to broaden the scope of the article and for the overall continuity of the thesis.

tetrabromopalladate(II) complex has exact D_{4h} point group symmetry and serves as a spectroscopic benchmark for comparison with other complexes. In addition, a pyrrolidene dithiocarbamate complex of Pd(II) is studied where the bidentate nature of the sulfur-donating ligand effectively 'clamps' the metal center. These additional complexes have somewhat similar temperature-dependent luminescence characteristics, but the different ligand structures are expected to lead to a different response of the luminescence properties with pressure.

8.2 Experimental

$[Pd(SCN)_4](n\text{-}Bu_4N)_2$ was prepared using literature procedures.[3] K_2PdBr_4 was purchased from Aldrich and used as received. $[Pd(pdtc)_2]$ (pdtc = 1-pyrroleidinecarbodithioate was synthesized from the addition of DMSO solutions of 1-pyrroleidinecarbodithioate (100 mg, 0.6 mmol) to $PdCl_2$ (55 mg, 0.3 mmol) at 0 °C. A color change from yellow-brown to bright orange color and upon rotary evaporation of DMSO, a bright orange solid was collected. The solid was dissolved in acetonitrile and recrystallized by diffusion into water.

The spectroscopic instrumentation has been described before.[6] All luminescence spectra were corrected for system response. Microscope optics (Renishaw 3000) allowed us to verify and adjust the sample position and obtain reliable intensities as pressure is varied. Pd-S raman bands were used as internal intensity standards leading to estimated errors less than ± 40 units on the intensity scale. Luminescence lifetimes as a function of pressure were measured using the doubled output of a Nd:YAG pulsed laser (532 nm), a photomultiplier tube (Hamamatsu R928) and a digital oscilloscope. All pressure-induced phenomena presented here are reversible.

8.3 Results

Figure 8.1 illustrates the variation of the luminescence intensities of $[Pd(SCN)_4](n\text{-}Bu_4N)_2$ as a function of pressure and temperature. The room temperature luminescence at the lowest pressure shown is very weak. At higher pressures, the luminescence intensities increase rapidly and become up to three orders of magnitude larger at 29 kbar than at ambient pressure. Band maxima show a significant blue-shift of 29 cm^{-1}/kbar.

The luminescence intensity also varies strongly with temperature, increasing by a factor of five between 70 K and 10 K. Vibronic progressions involving both the totally symmetric Pd-S stretching mode (a_{1g}, D_{4h}) and the non-totally symmetric, in-plane Pd-SCN bending mode (b_{2g}, D_{4h}) are resolved as indicated in Figure 8.1b. The vibrational assignments are based on a normal coordinate analysis and the frequencies of these modes are 274 cm^{-1} and 147 cm^{-1}.[3] Figure 8.2 shows pressure-dependent Raman spectra of this complex with monotonic frequency increases of 0.7 cm^{-1}/kbar for both modes. The absence of any abrupt changes in the pressure-dependent Raman and luminescence spectra indicates that there are no drastic structural changes of the title complex in the pressure range shown in Figure 8.1a.

Figure 8.3a shows luminescence lifetimes and integrated band intensities as a function of pressure. The most intense spectrum, observed at 29 kbar, is more intense by a factor of 1500 than the spectrum at 1 kbar. The luminescence lifetimes increase from 330 ns at ambient pressure to 53 μs at 29 kbar, an increase by a factor of 160. Figure 8.3b shows the effect of pressure on experimental luminescence decay data. By comparison, luminescence lifetimes for complexes with a pressure-induced change of the emitting state, such as $[VCl_6]^{3-}$,[8] or many chromium(III) compounds,[9] show an increase that is smaller by at least an order of magnitude than for the title complex over the pressure range in Figure 8.3a. Pressure-dependent measurements were also performed on $[Pt(SCN)_4](n\text{-}Bu_4N)_2$, and we observe a lifetime increase from 750 ns at atmospheric pressure to 17 μs at 27 kbar and an intensity increase by almost two orders of magnitude (data not shown). All luminescence intensities begin to decrease steadily at pressures above 30 kbar, an effect that is well-established when energy transfer between molecules becomes more efficient at higher pressures.[10]

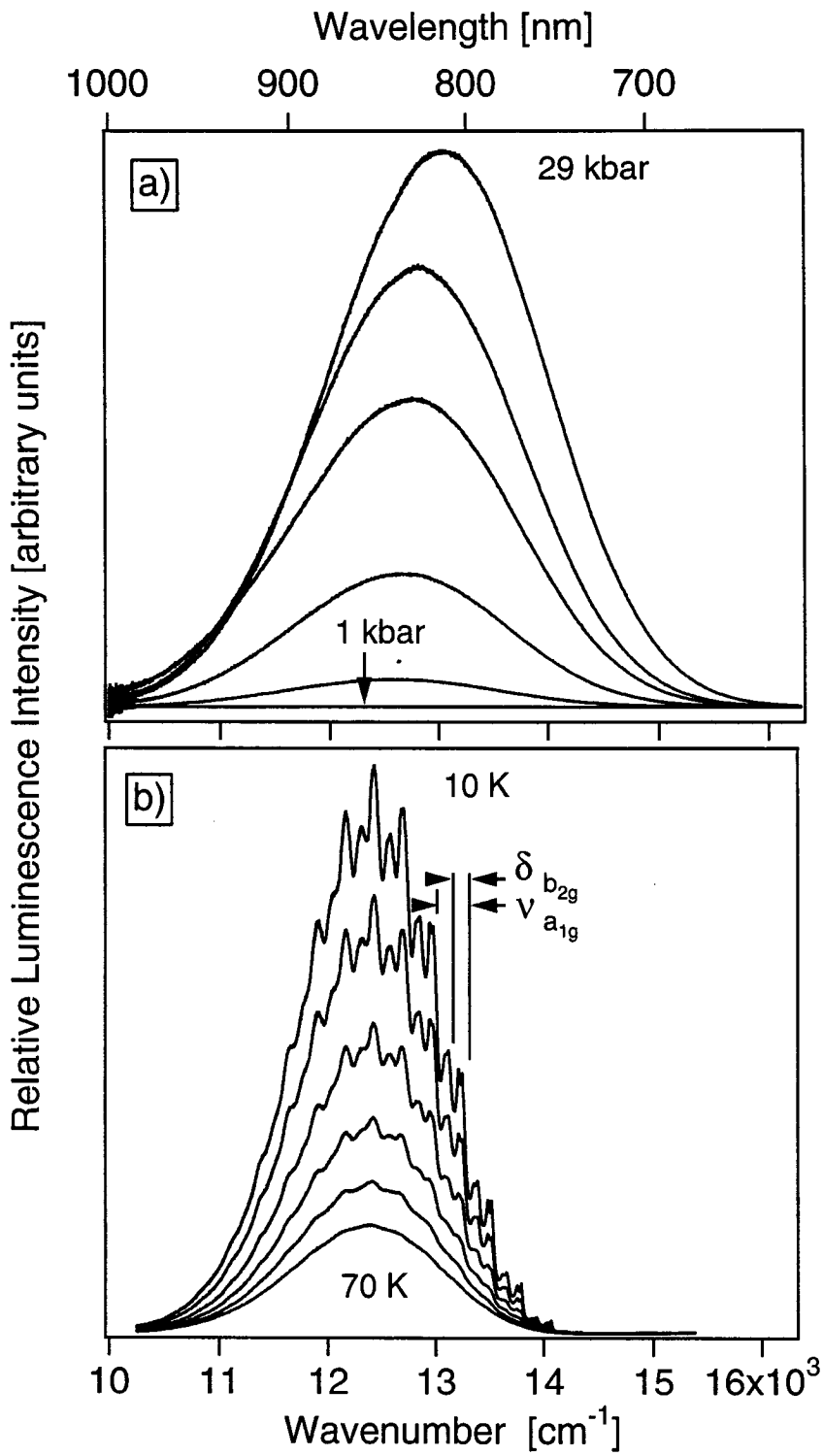

Figure 8.1. a) Pressure-dependent luminescence spectra of $[Pd(SCN)_4](n\text{-}Bu_4N)_2$ at 300 K and 1 kbar (bottom trace), 2 kbar, 5 kbar, 13 kbar, 17 kbar, and 29 kbar (top trace). b) Temperature-dependent luminescence of $[Pd(SCN)_4](n\text{-}Bu_4N)_2$ at 70 K (bottom trace), 50 K, 40 K, 30 K, 20 K, and 10 K (top trace). Modes defining vibronic progression intervals are identified by labels in the D_{4h} idealized point group.

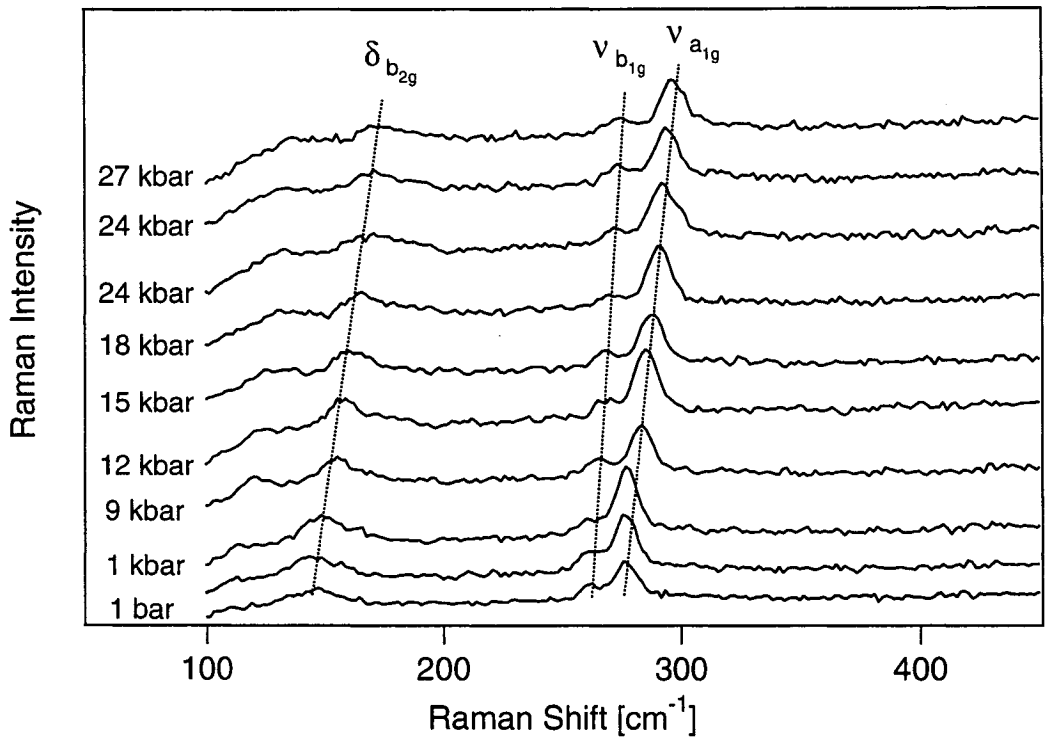

Figure 8.2. Pressure-dependent Raman spectra of the $[Pd(SCN)_4](n\text{-}Bu_4N)_2$ complex measured at room temperature with bands in the a_{1g}, b_{1g}, and b_{2g} metal-ligand modes indicated.

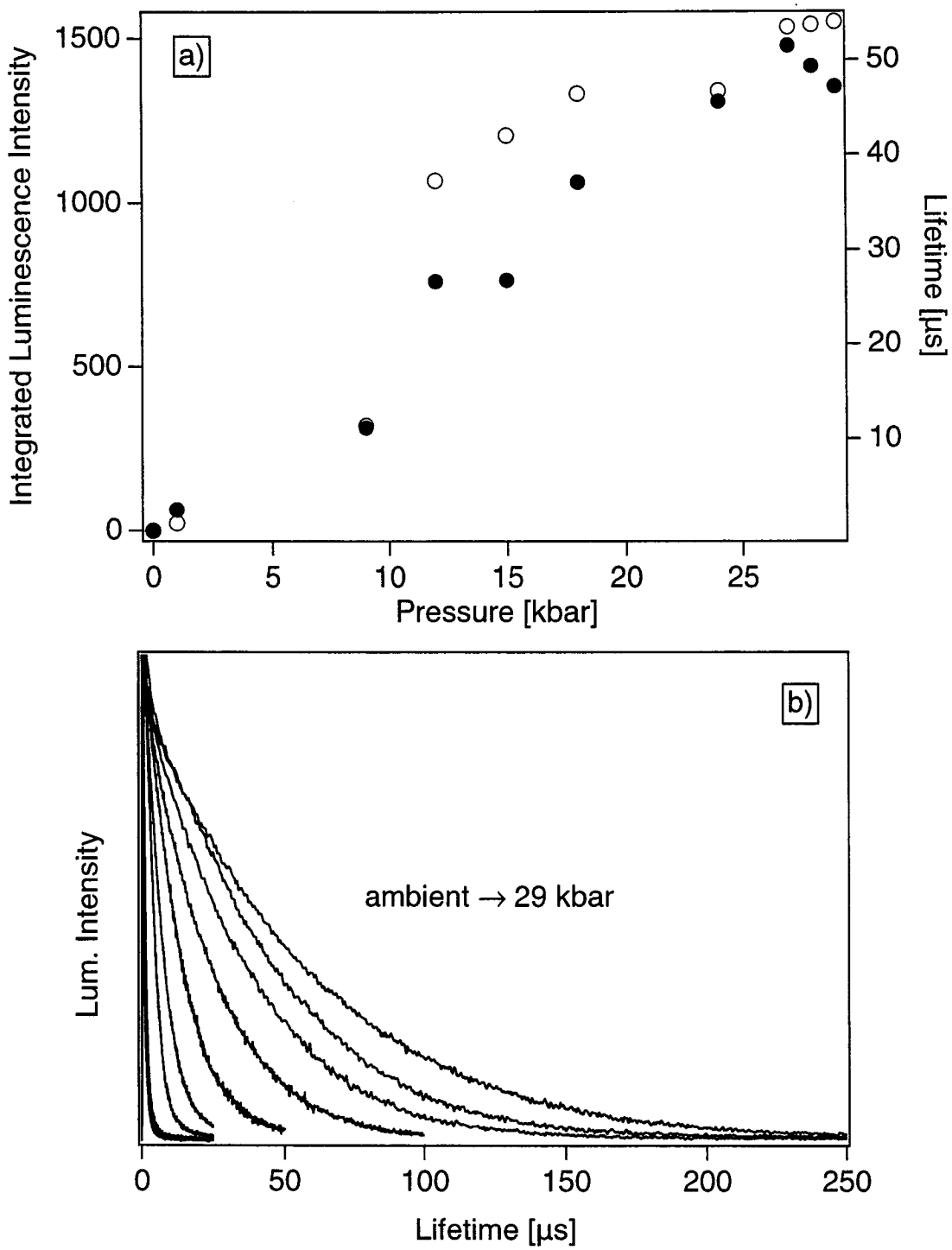

Figure 8.3. a) Pressure-dependent luminescence lifetimes (○) and intensities (●) for $[Pd(SCN)_4](n\text{-}Bu_4N)_2$ at 300 K. The integrated intensity at 1 kbar was scaled to 1 and the same scaling factor has been applied to integrated intensities at other pressures. b) Experimental pressure-dependent luminescence decay kinetics of $[Pd(SCN)_4](n\text{-}Bu_4N)_2$ (T = 300 K).

Figure 8.4 shows pressure-dependent integrated luminescence intensities (8.4a) and integrated a_{1g} Pd-S Raman bands (8.4b) for the $[Pd(SCN)_4](n\text{-}Bu_4N)_2$ compound for three independent runs. In order to compare the pressure-induced luminescence enhancements between separate sets of data, the Raman intensities were normalized and the respective luminescence intensities are scaled by an appropriate factor to estimate the order of magnitude of pressure-induced luminescence intensity enhancement for the title complex. This was necessary due to minor fluctuations in laser power with time and because the position of the diamond anvil cell changed with variation of pressure.

The effect of ligand substitution on the metal-centered luminescence is tested and we compare room temperature, pressure-dependent luminescence spectra from two other Pd(II) compounds. The optical spectra of the tetrabromopalladate(II) complex has been well-characterized by temperature-dependent methods where it was shown that the molecule undergoes a significant displacement in a Jahn-Teller active non-totally symmetric metal-ligand stretching mode (b_{1g}). The luminescence at room temperature is very weak, similar to the title complex, and shows no comparable enhancement of luminescence intensity with increasing pressure. The $[Pd(pdtc)_2]$ complex contains the bidentate sulfur-donating 1-pyrroleidinecarbodithioate ligand which effectively clamps the metal center, thus preventing metal-ligand bending vibrations as observed in the low temperature luminescence spectra of the title compound. Figure 8.5 shows the effect of temperature and pressure on single crystals of $[Pd(pdtc)_2]$. Low temperature luminescence spectra no resolution of vibronic structure and temperature-dependent intensities decrease rapidly with increasing temperature, similar to the behavior of the title complex. Temperature-dependent luminescence lifetimes show a steady decrease from 660 μs at 5 K to 4 μs at 125 K and lifetimes monitored at different wavelengths across the luminescence band do not vary more than 2 %. Pressure-dependent luminescence spectra (Figure 8.5b) show enhancements of luminescence intensity as a function of pressure, but much smaller than those obtained for the title complex. At pressures greater than 30 kbar, the intensities decrease rapidly. The luminescence band maxima also show a small blue-shift of 3 cm^{-1}/ kbar, almost 10 times smaller than that observed in the title complex.

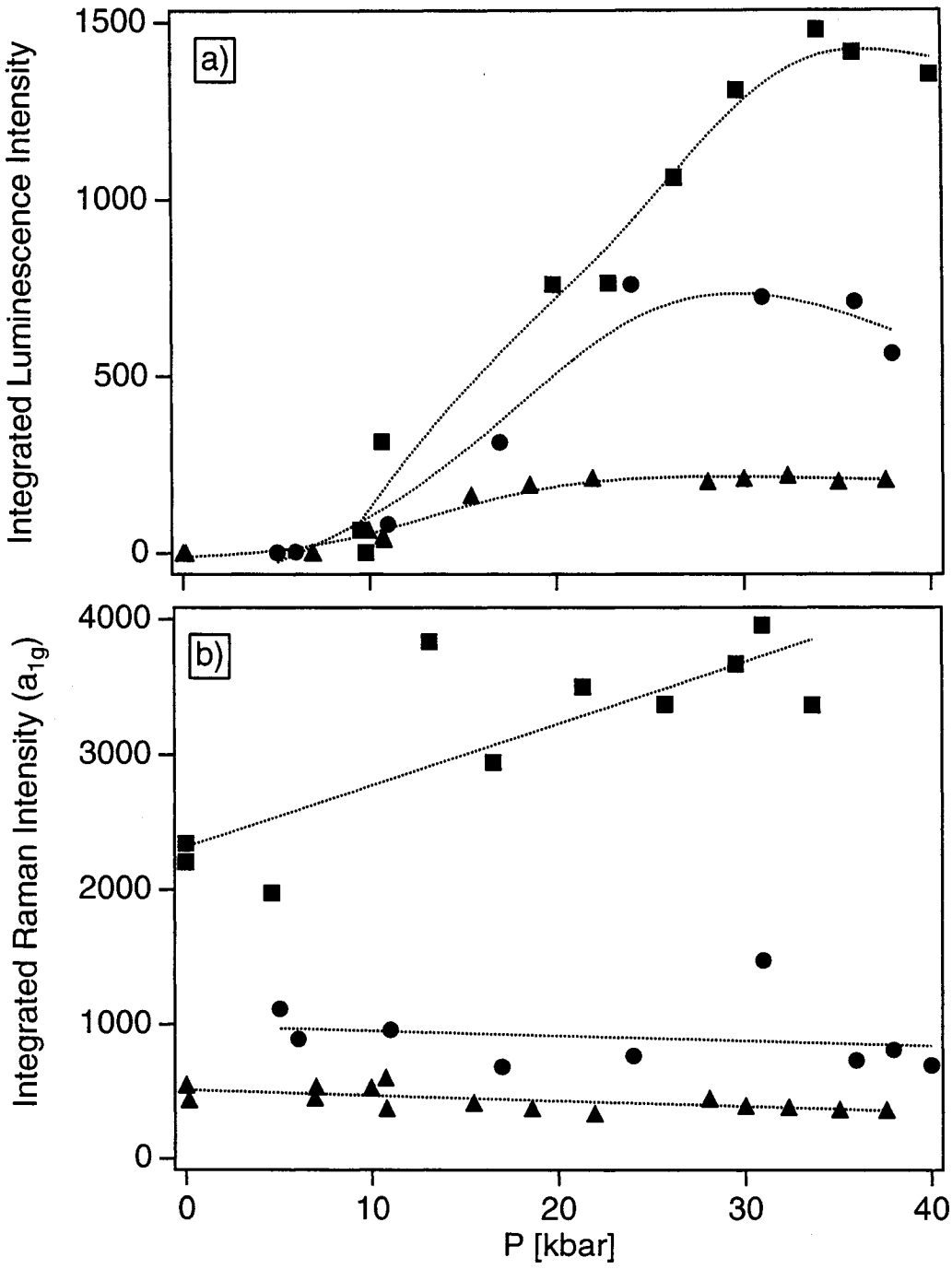

Figure 8.4. a) Pressure-dependent luminescence integrated intensities and, b) corresponding a_{1g} Pd—S integrated Raman intensities. Dotted lines are included as a guide for the eye.

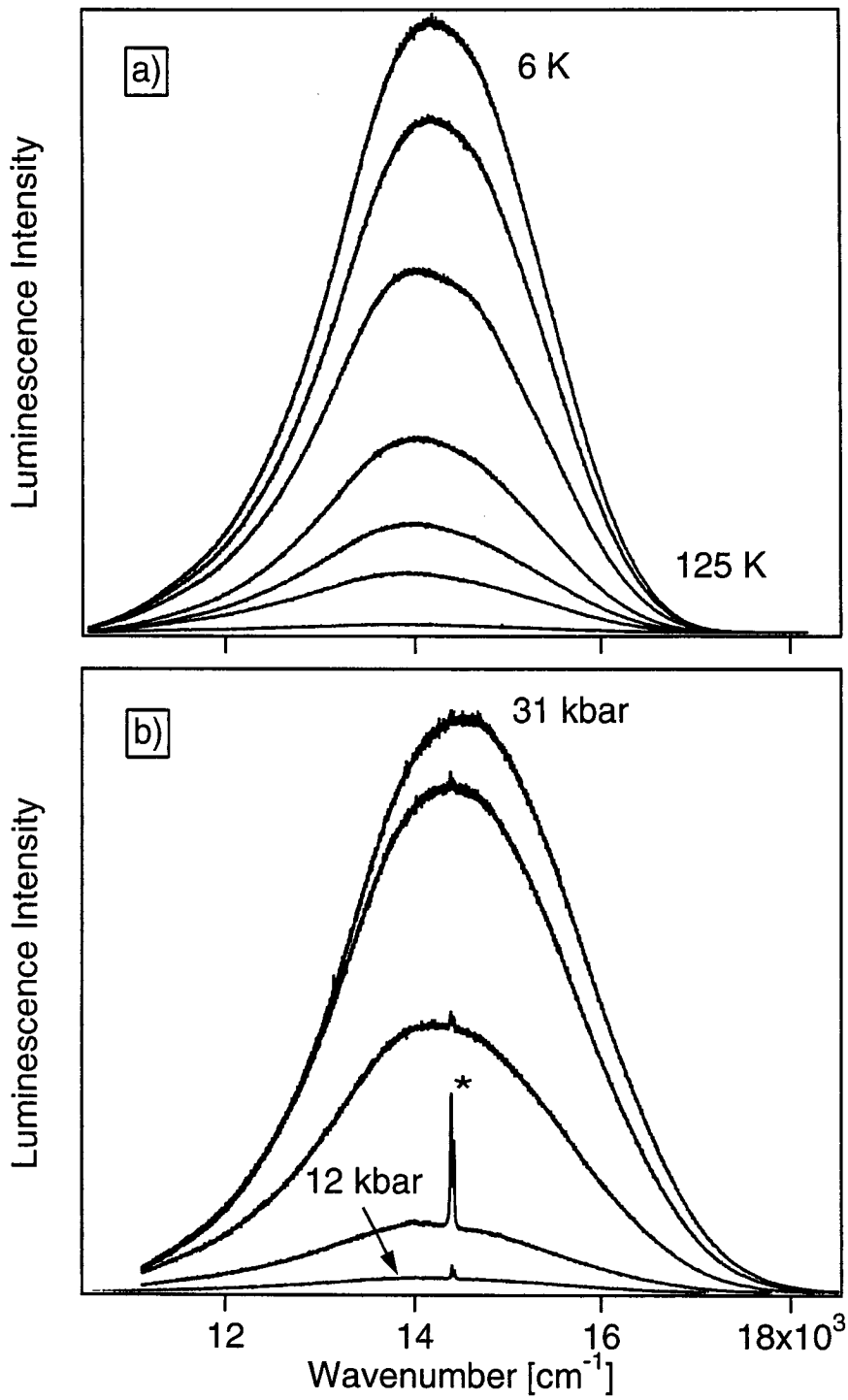

Figure 8.5. a) Temperature-dependent luminescence spectra of $[Pd(pdtc)_2]$ at 6 K (top trace), 15 K, 30 K, 50 K, 75 K, 100 K, and 125 K (bottom trace). b) Pressure-dependent luminescence spectra of $[Pd(pdtc)_2]$ measured at 300 K: 12 kbar (bottom trace), 18 kbar, 25 kbar, 30 kbar, and 31 kbar (top trace). * denotes emission from ruby.

8.4 Discussion

We qualitatively consider four effects that contribute to the large and unexpected increase in luminescence intensity of the $[Pd(SCN)_4]^{2-}$ complex with increasing pressure shown in Figures 8.1 and 8.3. This effect occurs because radiative and non-radiative relaxation rate constants are competitive in magnitude. They are not observed if either one completely dominates. The effect of molecular structure on the luminescence properties as a function of both temperature and pressure are also discussed.

In the title complex, the point group symmetry of the PdS_4 fragment is D_{4h}.[3] External pressure can break the inversion symmetry, for example by slightly bending some of the SCN^- ligands out of the plane of the complex, leading to a more allowed luminescence transition in a lower symmetry and to shorter luminescence lifetimes. The fact that both lifetimes and intensities *increase* with increasing pressure suggests that the non-radiative rate constant decreases significantly.

The blue-shift of the luminescence band indicates that the gap between the ground and emitting states increases with pressure. The number of vibrational quanta needed to bridge this energy gap also increases and the non-radiative rate constant is expected to decrease according to the energy gap law.[11] For the title complex, the number of 2100 cm^{-1} CN stretching quanta increases from 6.0 to 6.2 between ambient pressure and 29 kbar, leading to a decrease of the non-radiative rate constant at high pressure by less than a factor of two. This reveals that the blue-shift is a likely contribution to the observed increase of lifetimes and intensities in Figure 8.3, but not sufficient to fully account for the effect.

The luminescence spectra of $[Pd(SCN)_4]^{2-}$ in Figure 8.1b show that the offsets between the ground and emitting potential energy surfaces along several metal-ligand normal coordinates are large.[1] The activation energy for non-radiative rate constant increases when pressure reduces these large displacements. Literature reports indicate that pressure effects on bending modes of four-coordinate complexes lead to larger changes in the electronic spectra[12] than effects on stretching modes, and we therefore expect that the offset along the b_{2g} bending coordinate decreases most with pressure and leads to a much higher activation energy for non-radiative relaxation. This is corroborated by preliminary pressure-dependent luminescence spectra of $K_2[PdBr_4]$

where the published analysis of the low temperature spectra shows that the only nonzero offsets occur for stretching normal coordinates.[2] A very small pressure-induced luminescence intensity increase by a factor of four is observed for $[PdBr_4]^{2-}$, followed by a rapid decrease at higher pressures. When the Pd(II) metal center is coordinated by the bidentate 1-pyrroleidinecarbodithioate ligand, relatively small pressure-induced luminescence enhancements are observed that becomes quenched rapidly at higher pressures (> 30 kbar). Furthermore, the blue-shift of the luminescence band is much less than that observed in the title complex, which would result in a smaller decrease of the nonradiative rate constant based on the energy gap law. The other major difference between the three compounds studied is the environment of the luminophore. The crystal structure analysis for the title compound shows that the $[Pd(SCN)_4]^{2-}$ molecules are not stacked directly on top of each other, unlike in the well-studied salts of the tetracyanoplatinate(II) system. Therefore metal-metal interactions are probably negligible in this compound. However, the $[Pd(pdtc)_2]$ compound is neutral and therefore the molecules are in close proximity and excitation energy transfer should become more efficient with higher pressure. From the preliminary spectroscopic results and comparison with related Pd(II) complexes, it appears that this unusual pressure effect is not restricted to only one type of structure.

These experimental results imply that the nature of the ligands and the emitting-state distortions play an important role in the increase of luminescence intensities with pressure. In the title complex, the spatial arrangement of the thiocyanate ligands appears to be significantly altered by intermolecular effects, in which these ligands act as efficient levers that pressure-tune the metal-centered luminescence transition. This characteristic is a major contribution to the pressure effects in Figures 8.1 and 8.3 and may rationalize the comparatively smaller or negligible pressure-induced enhancements observed for the other complexes.

Previous work on D_{4h} *trans*-dioxo rhenium(V) complexes has demonstrated that pressure can change the shape of the ground state potential energy surface by "pushing up" areas at larger values along the coordinates with nonzero offsets.[6] This effect is a manifestation of an avoided crossing between coupled electronic states and depends strongly on the energies and normal coordinate offsets of the potential energy minima.

Electronic states can be coupled through spin-orbit and configuration interactions, which are strong for second- and third-row transition metal complexes and therefore amplify the effect of pressure on the potential energy surfaces beyond the simple shifts discussed in the preceding paragraph, resulting in even higher activation energies for non-radiative transitions. This effect is most important for lower energy transitions, as illustrated by the comparison with $[Pt(SCN)_4]^{2-}$, where we observe a luminescence maximum higher in energy by approximately 2000 cm^{-1} than for the title complex and, consequently, less dramatic pressure effects on luminescence intensities and lifetimes.

It is likely that all four effects described above contribute to the surprising pressure-induced luminescence properties of the title complex. The large enhancement, at relatively modest pressures, of the near-infrared luminescence properties of $[Pd(SCN)_4]^{2-}$ complex is unprecedented and may lead to new applications as a remote sensor for pressure.

References

(1) Pelletier, Y.; Reber, C. *Inorg. Chem.* **2000**, *39*, 4535.

(2) Pelletier, Y.; Reber, C. *Inorg. Chem.* **1997**, *36*, 721.

(3) Rohde, J.-U.; von Malottki, B.; Preetz, W. *Z. Anorg. Allg. Chem.* **2000**, *626*, 905. The shortest Pd—Pd distance perpendicular to the plane of the $[Pd(SCN)_4]^{2-}$ complexes is 13.09 Å, preventing significant metal-metal interactions in this compound.

(4) a) Gliemann, G.; Yersin, H. *Struct. Bond.* **1985**, *62*, 87. b) Pt—Pt distances of 3.1—3.6 Å lead to metal-metal interactions in this compound.

(5) Yersin, H.; Gallhuber, E. *inorg. Chem.* **1984**, *23*, 3745.

(6) Grey, J. K.; Triest, M.; Butler, I. S.; Reber, C. *J. Phys. Chem. A* **2001**, *105*, 6269.

(7) Gutierrez, R. E.; Rodriguez, F.; Moreno, M.; Alcala, R. *Radn. Eff. Def. Sol.* **2001**, *154*, 287.

(8) Wenger, O. S.; Güdel, H. U. *Chem. Phys. Lett.* **2002**, *354*, 75.

(9) Bray, K. L. *Top. Curr. Chem.* **2001**, *213*, 1.

(10) Dreger, Z. A.; Lang, J. M.; Drickamer, H. G. *J. Phys. Chem.* **1996**, *100*, 4637. b) Dreger, Z. A.; Lang, J. M.; Drickamer, H. G. *J. Phys. Chem.* **1996**, *100*, 4646

(11) Englman, R.; Jortner, J. *Mol. Phys.* **1970**, *18*. 145.

(12) Drickamer, H. G.; Bray, K. L. *Acc. Chem. Res.* **1990**, *23*, 55.

Chapter 9

Pressure-Induced Enhancements of Luminescence Intensities and Lifetimes Determined from Emitting State Distortions in Thiocyanate and Selenocyanate Complexes of Platinum(II) and Palladium(II)

Reproduced with permission from *Inorg. Chem.* **2003**, *42*, 6503-6518.

Square-planar thiocyanato and selenocyanato complexes of platinum(II) and palladium(II) exhibit large variations of luminescence properties as a function of both temperature and pressure. Pressure-dependent luminescence intensities and lifetimes show increases of over two orders of magnitude from ambient pressure values. This large pressure effect can be correlated to the total emitting state distortions.

9.1 Introduction

Square planar, d^8, platinum(II) and palladium(II) complexes show a wide range of luminescence properties that depend strongly on the structural and electronic characteristics of the ligands. It is well known that the nature of the emitting state and luminescence energies of these compounds can be tuned by substitution of ligands, by modification of ligand substituent groups, and by changes in the surrounding medium of the luminescent molecule, i.e., solvent, counterions, and neighboring complexes.[1-7] In addition to this chemical tuning, variation of temperature and pressure provides insight into the extent of tunability of electronic and vibronic transitions for a variety of transition metal complexes.[8-17] These variables can be used to characterize the effects of small changes in molecular geometry on kinetic competition between radiative and nonradiative excited state relaxation,[18-21] coupling between potential energy surfaces,[22,23] or changes in the ground state electronic structure, such as spin-crossover transitions.[24,25] We present a new pressure effect leading to large increases of luminescence intensities

* Slight modifications were made to the original manuscript for clarity and continuity.

and lifetimes. It is specific to square-planar complexes with a Jahn-Teller active emitting state.

The title complexes have some unique traits relevant for the spectroscopic effects presented and discussed in the following. The ambidentate ligands, denoted as XCN^- (X: S, Se), may coordinate to the metal *via* the sulfur or selenium atom or *via* the nitrogen atom depending on the hardness or softness of the metal center.[26-30] All complexes studied here are coordinated through the X atom and have exact D_{4h} point group symmetry for the MX_4 fragment. Crystal structures for the title complexes show M-X-C angles of approximately 109° and 105-107° for the thiocyanate and selenocyanate complexes, respectively, and it was determined that the anionic complexes occupy only one site throughout the monoclinic lattice.[31] A recent normal coordinate analysis for the title complexes[31] has assigned the vibrational modes in idealized D_{4h} point group symmetry and we use these labels for the ground state metal-ligand vibrational modes (a_{1g}, b_{1g}, and b_{2g}) to characterize the resolved structure in the low temperature luminescence spectra. The typical ranges of these frequencies are: 274-303 cm^{-1} (a_{1g} totally symmetric stretching), 260-290 cm^{-1} (b_{1g} non-totally symmetric stretching), and140-150 cm^{-1} (b_{2g} non-totally symmetric bending) for the SCN^- complexes, and 180-195 cm^{-1} (a_{1g}), 170-187 cm^{-1} (b_{1g}), and 100-110 cm^{-1} (b_{2g}) for the $SeCN^-$ complexes. We then determine if this difference in metal-ligand vibrational frequencies between the thiocyanate and selenocyanate complexes affects the variation in luminescence properties brought on by increasing pressure.

The electronic configuration of all title complexes is $a_{1g}(d_{z^2})^2b_{2g}(d_{xy})^2e_g(d_{xz,yz})^4b_{1g}(d_{x^2-y^2})^0$, leading to a non-degenerate $^1A_{1g}$ ground state and all one-electron excitations populate the b_{1g} σ^* orbital and are therefore interconfigurational. The lowest energy excited state is degenerate (^3E_g), originating from the promotion of an electron from the e_g orbitals to the b_{1g} orbital.[32-35] This state is split into five components by spin-orbit coupling. Low temperature absorption spectra of the potassium salts of platinum(II) and palladium(II) thiocyanate complexes show broad and unresolved bands for the transition to this excited state, suggesting a superposition of the energetically close spin-orbit states.[32,36,37] Polarized absorption spectra of these complexes also show weak dichroisms for this transition.[36] Similar absorption features are observed for the title

complexes and the luminescence transition studied occurs from the lowest energy spin-orbit component of this state.[38]

The luminescence bands of the title complexes are broad, indicating large displacements of the emitting state potential energy minimum along Franck-Condon active metal-ligand vibrational modes. These large structural distortions lead to weak luminescence at higher temperatures due to efficient nonradiative deactivation of the emitting state. At ambient temperature and pressure, the luminescence intensities of the title complexes and related compounds are very low and almost unobservable.[32,37] As temperature is lowered, the efficiency of nonradiative decay pathways is reduced and all title complexes show rapidly increasing luminescence intensities and lifetimes. Below 50 K, all luminescence spectra exhibit resolved vibronic structure with progressions in multiple vibrational modes, including the b_{2g} and b_{1g} metal-ligand non-totally symmetric bending and stretching modes. The vibronic structure is richer than for square-planar palladium(II) and platinum(II) halide complexes, where distortions only occur along a single non-totally symmetric mode.[37,39] The well-resolved vibronic structure of the title complexes allows for a detailed analysis of emitting state distortions that may be used to rationalize the large pressure-induced effects on luminescence properties.

We have reported in a recent communication that the luminescence intensities and lifetimes of the $[Pd(SCN)_4](n\text{-}Bu_4N)_2$ complex show large increases under external pressures at room temperature.[40] The degree to which this effect depends on the nature of the metal center and ligands is now determined. All pressure-dependent luminescence intensities and lifetimes measured at room temperature show large increases in intensities and lifetimes, by almost three orders of magnitude, with the application of relatively modest pressures up to 30 kbar. The palladium(II) complexes show the largest pressure-induced increases. The effects for the platinum(II) complexes are significant, but weaker than the palladium(II) compounds. Similar pressure-dependent lifetime measurements on doped chromium(III) ions in various oxide, chloride, and fluoride lattices also show large increases, typically by two orders of magnitude, due to a change in emitting state from a spin-allowed $^4T_{2g}$ to a spin-forbidden ^2E_g, but no intensity increases have been reported.[41] Other studies have been carried out on molecular transition metal complexes that maintain the same emitting state with increasing pressure, such as polypyridyl complexes

of ruthenium(II) and osmium(II).[18,19] These systems show only small variations of pressure-dependent luminescence lifetimes at constant temperature by less than a factor of two within similar pressure ranges as studied here.

Theoretical models are employed for calculating luminescence spectra as well as the trends of the temperature- and pressure-dependent luminescence decay behavior. The low-temperature luminescence spectra are analyzed using the time-dependent theory of spectroscopy,[42-45] which allows for the quantitative determination of the emitting state distortions along all relevant normal modes and provides an intuitive means of understanding the detailed spectroscopic features. The experimental temperature-dependent luminescence decay rate constants were analyzed with an analytical expression for the nonradiative rate constant in the strong-coupling limit of radiationless decay theory derived by Englman and Jortner.[46] We use experimental information determined directly from the resolved low-temperature spectra, such as vibrational energies, the energy of the electronic origin transition, and emitting state distortions to calculate nonradiative rate constants for each complex. Only a single adjustable parameter in the pre-exponential factor remains to fit the experimental luminescence decay rate constant at all temperatures studied. We are then able to rationalize the different magnitudes of the pressure-induced increase in luminescence lifetimes for all title complexes with the parameters determined from the low-temperature luminescence spectra and temperature-dependent luminescence lifetimes.

9.2 Experimental

Single crystals of $[Pt(SCN)_4](PPh_4)_2$ (**1**), $[Pt(SCN)_4](n\text{-}Bu_4N)_2$ (**2**), $[Pd(SCN)_4](n\text{-}Bu_4N)_2$ (**3**), $[Pt(SeCN)_4](n\text{-}Bu_4N)_2$ (**4**), and $[Pd(SeCN)_4](n\text{-}Bu_4N)_2$ (**5**) were prepared following literature methods.[31,47-49] Starting materials were purchased from Sigma-Aldrich and used without further purification. Complexes **1-3** were also prepared by dissolving crystals of $K_2[PtCl_4]$ or $K_2[PdBr_4]$ in water and adding an aqueous solution of KSCN in excess followed by gentle refluxing for 2 hours. After rotary evaporation of water, the potassium salts of the thiocyanate compounds were recrystallized three times from hot 1-butanol. The compounds were then dissolved in acetonitrile to which an excess of $(n\text{-}Bu_4N)Cl{\cdot}2H_2O$ or $(PPh_4)Br$ in acetonitrile was added. All compounds were

recrystallized several times by slow evaporation of acetonitrile and analyzed by Raman, luminescence, absorption, and excitation spectroscopy. Raman spectra of the title complexes were measured at 295 K and 77 K and bands in the metal-ligand stretching and bending region show strong and sharp peaks with frequencies in excellent agreement with literature values.[31] The mode of ligation for the thiocyanate and selenocyanate ligands was confirmed from Raman spectroscopy by monitoring the CN stretching frequencies and all compounds show strong and sharp single peaks between 2100 and 2110 cm^{-1} (Table 9.1), indicative that ligands are *not* coordinated through the nitrogen atom of the XCN^- ligands and are oriented around the metal center in a nearly equivalent fashion.[31]

9.2.1 Temperature and pressure dependent spectra

Luminescence spectroscopic measurements were carried out using two different instruments. Samples were cooled in a micro-cryostat system (Janis ST-500) by pumping off liquid helium. The 488 nm and 514.5 nm lines of argon ion lasers (~ 2 mW) were focused onto the crystals using a Renishaw 3000 imaging microscope system. The luminescence was collected and detected with a Peltier-cooled CCD camera. The other system used to record the luminescence spectra was a single channel scanning spectrometer.[50] A continuous flow helium cryostat (Oxford CF 1204) was used to cool samples down to 5 K. Excitation sources were again the 488 nm and 514.5 nm lines of an argon ion laser (Spectra Physics Stabilite 2017) using the appropriate interference filters. Excitation was focused onto samples with a quartz lens and the luminescence collected at 90° by a spherical mirror, then dispersed through a 0.5 m monochromator (Spex 500M, 600 lines/mm grating) with a longpass filter (Schott OG 550, RG 610) positioned at the entrance slit. The detection system was a cooled photomultiplier tube (Hamamatsu R928 or R406/ Products for Research TE 177RF cooler) connected to a photon counter (Stanford SR 400) or lock-in amplifier (Stanford SR 510) with the luminescence signal modulated with an optical chopper (Stanford SR 540) and the intensities were saved on a computer also used to control the wavelength. Luminescence spectra of complexes **2** and **3** in a glassy matrix (1:1 toluene-acetone) were measured at 5 K with concentrations on the order of 10^{-4} M. All luminescence spectra are corrected for

instrument response[50] by calibration with a tungsten lamp (Oriel 63350). The corrected luminescence bandshapes obtained with the two instruments are identical. Detector response characteristics vary strongly over the wavelength range of interest and it is therefore important to compare results recorded with different instruments.

Pressure-dependent luminescence and Raman spectra were recorded using the microscope system described above. Pressure was applied to the solid samples by loading crystals into a gasketed diamond-anvil cell (DAC, High Pressure Diamond Optics). The ruby (R_1) method was used to calibrate pressures[51] and paraffin oil was the pressure-transmitting medium. All pressure effects reported here are reversible where, upon gradual release of external pressures, all quantities return to their normal values at ambient pressure.

9.2.2 Luminescence lifetime measurements

Temperature-dependent lifetimes were measured using the doubled output (532 nm) of a Nd:YAG pulsed laser (Continuum Mini-Lite II, ~5 ns pulse width). Laser pulse energy was kept at approximately 1 mJ/pulse measured at the laser head. The luminescence was dispersed by the 0.5 m monochromator and detected using the same cooled photomultiplier tube described above. The signal was averaged and saved on a digital oscilloscope (Tektronix TDS 380) triggered by a photodiode (Thorlabs FDS 100). Luminescence lifetimes of all complexes were recorded at multiple wavelength intervals as a function of temperature and these values vary by 2% or less across the luminescence bands. Decay traces were fitted with single- and double exponential functions using least squares methods. Decay was assigned as single exponential when χ^2 was less than 0.003 for a single exponential function otherwise with a double exponential function was fitted to the experimental data. Measurements were recorded between 5 K and 275 K. At higher temperatures an accurate determination of lifetimes was difficult due to low signal-to-noise ratios of the luminescence intensities.

Pressure-dependent lifetime measurements were carried out using the same pulsed laser source. The excitation was focused into the DAC with a short focal length quartz lens and the emitted light was detected with the cooled R928 photomultipler tube with either a red (Schott RG 610) or orange (Schott OG 590) longpass filter. These

measurements take advantage of the entire luminescence band and good signal-to-noise ratios were obtained. Signals were acquired using the same detection equipment described above. To avoid heating effects on the sample and possible damage to the DAC, the laser was used in low-energy mode and the output power was approximately 500 μJ/pulse.

9.2.3 Excitation and absorption spectra

A Xe lamp filtered through water to remove IR radiation was used as the excitation source. The 0.5 m monochromator was used to scan the excitation wavelength and the emitted light was dispersed through a 0.75 m monochromator (Spex 1800 II, 600 lines/mm grating).[50] A KV 418 UV cutoff filter was placed at the exit slit of the excitation monochromator and either OG 550 (compounds **2** and **4**), or, RG 645 filters (compounds **3** and **5**) were placed at the entrance slit of the luminescence monochromator. Excitation spectra were measured at the luminescence band maximum as well as other wavelengths across the luminescence bands. The detection systems were the same as that used in the luminescence measurements.

Absorption measurements were carried out with a Varian Cary 5E spectrometer. Samples **2-5** were dissolved in a 1:1 toluene/acetone solution and spectra were recorded at 300 K and 77 K and the concentrations were on the order of 10^{-4} M.[52]

9.3 Spectroscopic Results

The luminescence spectra from single crystals of the title complexes are broad, spanning up to 4500 cm^{-1}. Low temperature data reveal well-resolved long vibronic progressions in multiple vibrational modes. The band maxima are ca. 14500 cm^{-1} for platinum(II) complexes (**1**,**2**,**4**) and ca. 12500 cm^{-1} for the palladium(II) complexes (**3**,**5**). These characteristics are comparable to luminescence spectra for other square-planar transition metal compounds reported in the literature.[32,36,37,39,53]

The 5 K luminescence and absorption spectra of **1** are shown in Figures 9.1 and 9.2 and serve as representative examples for typical luminescence and absorption spectral profiles of the title complexes at low temperature. The luminescence band has well-resolved vibronic structure with a main progression in the a_{1g} mode and an easily visible,

but less intense progression matching the frequency of the b_{2g} non-totally symmetric bending mode. Additional structure is observable near the origin region, as shown in Figure 9.2a, and the frequencies of all relevant vibrational modes determined from the luminescence spectra are listed in Table 9.1. The high-resolution spectrum in Figure 9.2a reveals that the dominant progressions are separated by small frequency intervals of 10, 35, and 70 cm^{-1}. These fine features are lost toward the band maximum where the intensities of the main vibronic bands are much higher. Up to seventeen quanta of the a_{1g} stretching mode with an average frequency interval of 295 cm^{-1} on the blue side of the band are resolved in the 5 K luminescence spectrum with the band maximum at the 9th member of this progression. Starting from this member, the vibronic spacings decrease gradually by 11 cm^{-1} to 284 cm^{-1} at the 15th quantum. Polarized luminescence spectra of **1** were recorded at 20 K and show the same relative intensity distributions throughout the spectrum as in the unpolarized spectrum in Figure 9.1. The dichroic ratio of the total intensities is approximately two. Luminescence intensities and lifetimes are strongly temperature dependent. Lifetimes increase by up to a factor of 300 between ambient temperature and 5 K, demonstrating efficient nonradiative relaxation processes at higher temperatures. The 5 K unpolarized absorption spectrum in Figure 9.1 has a weak and unresolved band for the lowest energy transition that corresponds to overlapping transitions to multiple spin-orbit components of the ^3E_g excited state.[34,35] However, there is another band starting at 19960 cm^{-1} that shows resolved vibronic structure in four discernible modes, as shown in detail in Figure 9.2b. The largest frequency interval in this resolved band is 250 cm^{-1}, which is most likely the frequency of the a_{1g} vibrational mode in this excited state. The Stokes shift between the luminescence band maximum and the center of the first absorption band in Figure 9.1 is approximately 4900 cm^{-1}, indicative of large structural changes along the metal-ligand vibrational modes. Estimated energy gaps between the onsets of the luminescence and absorption bands are found to be approximately 500 cm^{-1}, much smaller than those found in platinum(II) and palladium(II) complexes with simple halide ligands.[37,39] This energy gap probably arises from vibronic origins involving low frequency odd-parity promoting modes.

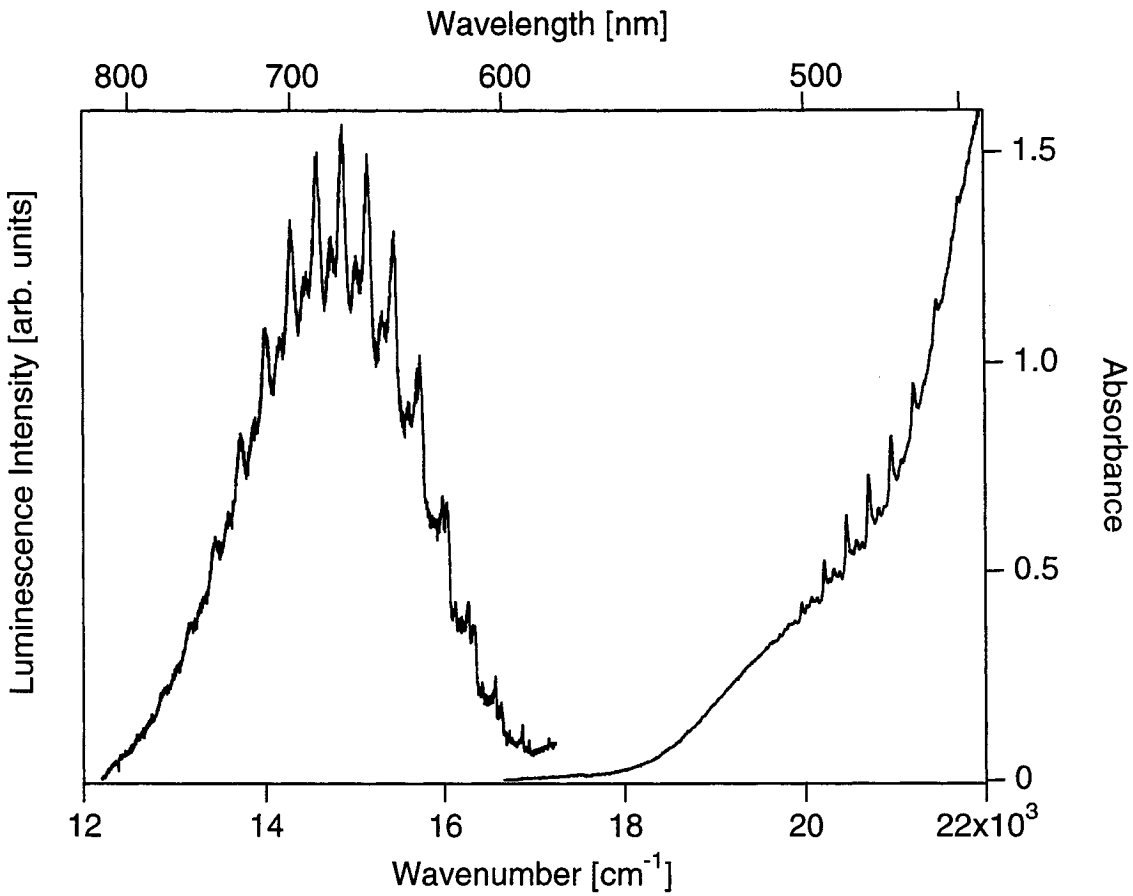

Figure 9.1. Single crystal luminescence and unpolarized absorption spectra of $[Pt(SCN)_4](PPh_4)_2$ **1** at 5 K (unpolarized).

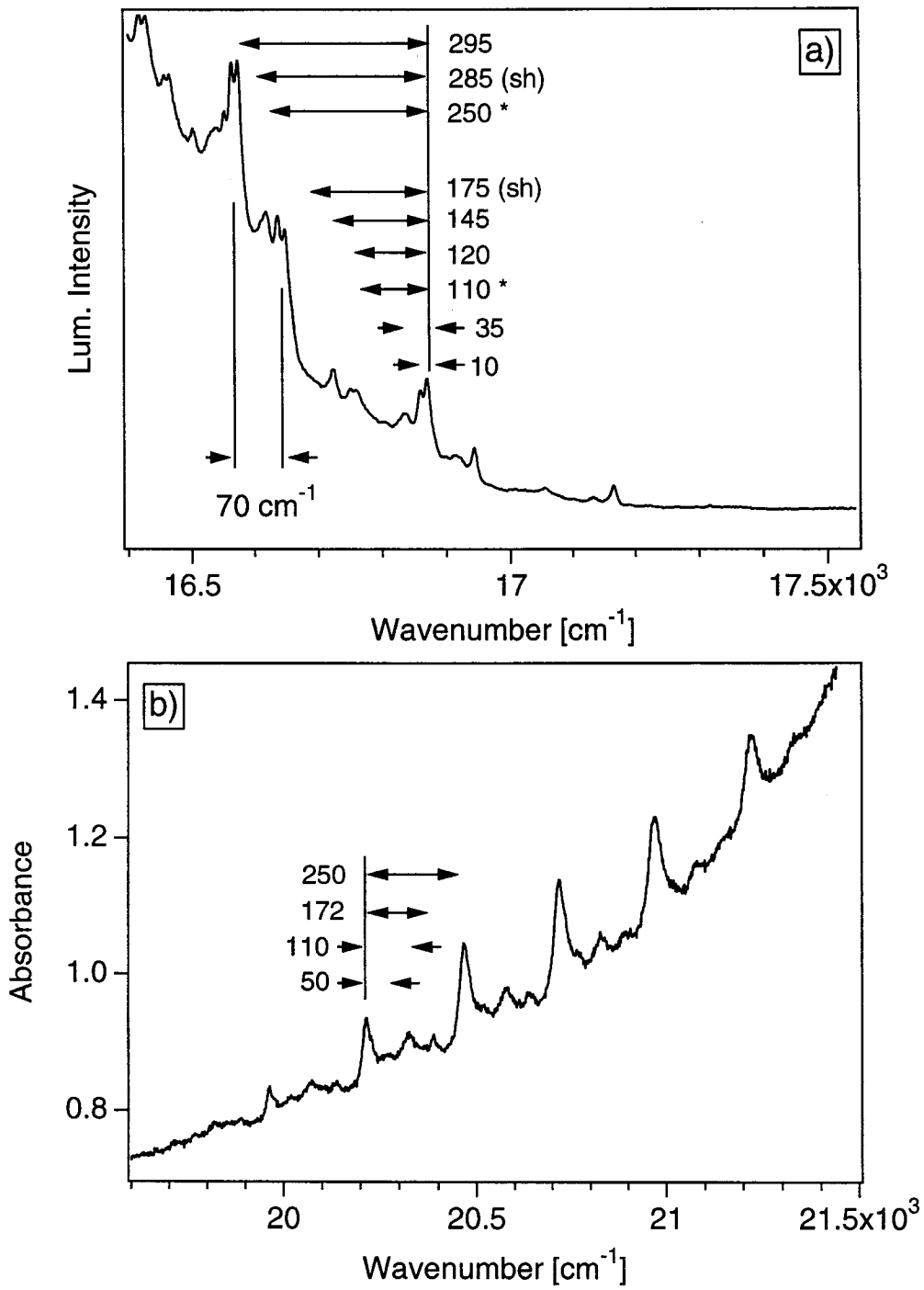

Figure 9.2. a) High resolution luminescence spectrum of $[Pt(SCN)_4](PPh_4)_2$ **1** at 5 K near the luminescence origin (E_0). The spectrum consists of two progressions that are separated by approximately 70 cm^{-1} and by additional small frequency intervals of 35 cm^{-1} and 10 cm^{-1}. Vibronic intervals in wavenumber (cm^{-1}) units are indicated on the spectrum; * corresponds to vibrational quanta that also appear in the 5 K absorption spectrum and (sh) stands for shoulder. b) 5 K absorption spectrum of **1** showing details of the vibronic structure in the second, higher energy band in Figure 9.1.

9.3.1 Temperature Dependent Luminescence Intensities and Lifetimes

Figures 9.3 and 9.4 show the temperature dependent luminescence spectra and 5 K excitation spectra of the platinum(II) complexes (**2** and **4**) and palladium(II) complexes (**3** and **5**), respectively, and all relevant spectroscopic quantities referred to in the following are collected in Table 9.1. The luminescence spectra of these complexes exhibit well-resolved vibronic structure at temperatures below 50 K with the dominant progression-forming frequencies corresponding to the a_{1g} metal-ligand stretching mode in addition to prominent lower frequency progressions including the b_{2g} non-totally symmetric bending mode. Progressions in the b_{1g} non-totally symmetric stretching modes appear as weak shoulders on the blue side of a_{1g} vibronic bands. The low temperature luminescence of **2**, Figure 9.3a, shows similar features to that of **1** with the luminescence band maximum shifted to lower energy by 330 cm^{-1}. This complex exhibits a more noticeable decrease in the main progression interval toward higher quanta of the a_{1g} mode than what is observed in the 5 K luminescence spectrum of **1** with the interval decreasing by as much as 30 cm^{-1} across the band. At the band maximum, close to the 10th member of the a_{1g} progression, the frequency interval is approximately 285 cm^{-1} and by the 15th quantum the interval decreases to 270 cm^{-1}. The luminescence origin region is less resolved than for complex **1** in Figure 9.2a. However, a weak shoulder (~ 33 cm^{-1}) is observed on the red side of the a_{1g} interval near the luminescence origin and is subsequently lost toward the band maximum, as illustrated in Figure 9.4a with dotted vertical lines. To determine if the vibronic patterns persisted in a different medium, the luminescence spectra of **2** in a glassy matrix were measured at 5 K and 77 K and gave broad and unresolved bands, however, the overall spectral profiles and band maxima were similar to the data obtained for single crystal samples. When the $SeCN^-$ ligand replaces SCN^- on the metal centers, the luminescence spectrum becomes narrower as a result of the lower frequency Pt-SeCN modes that form vibronic progressions. The band maximum does not show an appreciable shift in energy, indicating very similar ligand fields for the two different ligands.[54] Figure 9.3b shows the luminescence of $[Pt(SeCN)_4](n\text{-}Bu_4N)_2$ (**4**) as a function of temperature. The 6 K luminescence spectrum exhibits well-resolved progressions in the 195 (a_{1g}) and 105 (b_{2g}) cm^{-1} modes in addition to less intense progressions in 160 cm^{-1}

and 65 cm^{-1} modes that are not resolved toward the lower energy side of the band. The positions of the band maxima were also found to change as a function of temperature. At 225 K the band is centered at 13690 cm^{-1}, it then blue shifts gradually by approximately 600 cm^{-1} at 50 K. From 50 K to 6 K, the band red shifts by 150 cm^{-1}. Excitation spectra of both **2** and **4** at 5 K show a weak and unresolved first absorption band, similar to that observed in the 5 K lowest energy absorption band of **1** and excitation spectra monitored at different wavelengths across the luminescence bands all give the same results as shown in Figure 9.3. The Stokes shifts for complexes **2** and **4** are 5020 cm^{-1} and 4520 cm^{-1}, respectively, and energy gaps between luminescence and excitation onsets are both comparable to the value determined for $[Pt(SCN)_4]^{2-}$ (**1**) in Figure 9.1.

Figure 9.4 shows the temperature dependent luminescence spectra of $[Pd(SCN)_4](n\text{-}Bu_4N)_2$ (**3**) and $[Pd(SeCN)_4](n\text{-}Bu_4N)_2$ (**5**). The temperature dependent luminescence spectra of the palladium(II) complexes behave in a manner similar to that of the platinum(II) complexes showing weak bands at high temperature. Vibronic structure in **3** is more resolved than spectra previously reported using different counterions.[32] Progressions in the b_{1g} non-totally symmetric stretching modes, in addition to the long progressions in the b_{2g} bending mode, are resolved as shoulders close to the maxima of the a_{1g} vibronic peaks. It is not possible to conclusively determine if there is an experimentally significant decrease in the a_{1g} progression interval for complex **3**, as was observed in the low temperature luminescence spectra of platinum(II) complexes **1** and **2**. The number of resolved peaks on the red side of the spectra is lower than for the platinum(II) analogs, preventing a detailed comparison to these compounds. Near the luminescence origin, complex **3** exhibits the most distinguishable repetitive patterns at temperatures below 20 K with well resolved frequency differences of 35 cm^{-1} on each member of the dominant progressions. Luminescence spectra of this complex in a glassy matrix were measured at 5 K to observe this feature in a different environment, however, the results revealed broad and featureless bands. Vibronic structure in the selenocyanate analog **5** is not as resolved as in the other complexes except near the origin region where small intervals of approximately 65 cm^{-1} are barely resolved. On the red side of the band, resolved structure is completely absent, similar to the platinum(II) complex **4**. In an

attempt to achieve better resolution of vibronic structure by further separating the $[Pd(SeCN)_4]^{2-}$ luminophores in the crystal lattice, the tetrabutylammonium counterion was exchanged for the larger *bis*-(triphenylphosphonium)phosphoranylidene ammonium $(PPN)^+$ cation, but the resulting 6 K luminescence spectrum showed no significant improvement. The excitation spectra of **3** and **5** show band shapes similar to the platinum(II) complexes **2** and **4** and vibronic structure is virtually absent. Excitation maxima are 16450 cm^{-1} for **3** and 16610 cm^{-1} for **5**, both lower in energy by approximately 2000 cm^{-1} than in the platinum(II) complexes. Stokes shifts for these two palladium(II) complexes are similar with values of 4060 cm^{-1} for **3** and 4080 cm^{-1} for **5**. The energy gaps between luminescence and excitation onsets are approximately 800 cm^{-1} for both palladium(II) complexes, somewhat larger than the literature value of 300 cm^{-1} for the $[Pd(SCN)_4]^{2-}$ luminophore in different crystalline environments.[32]

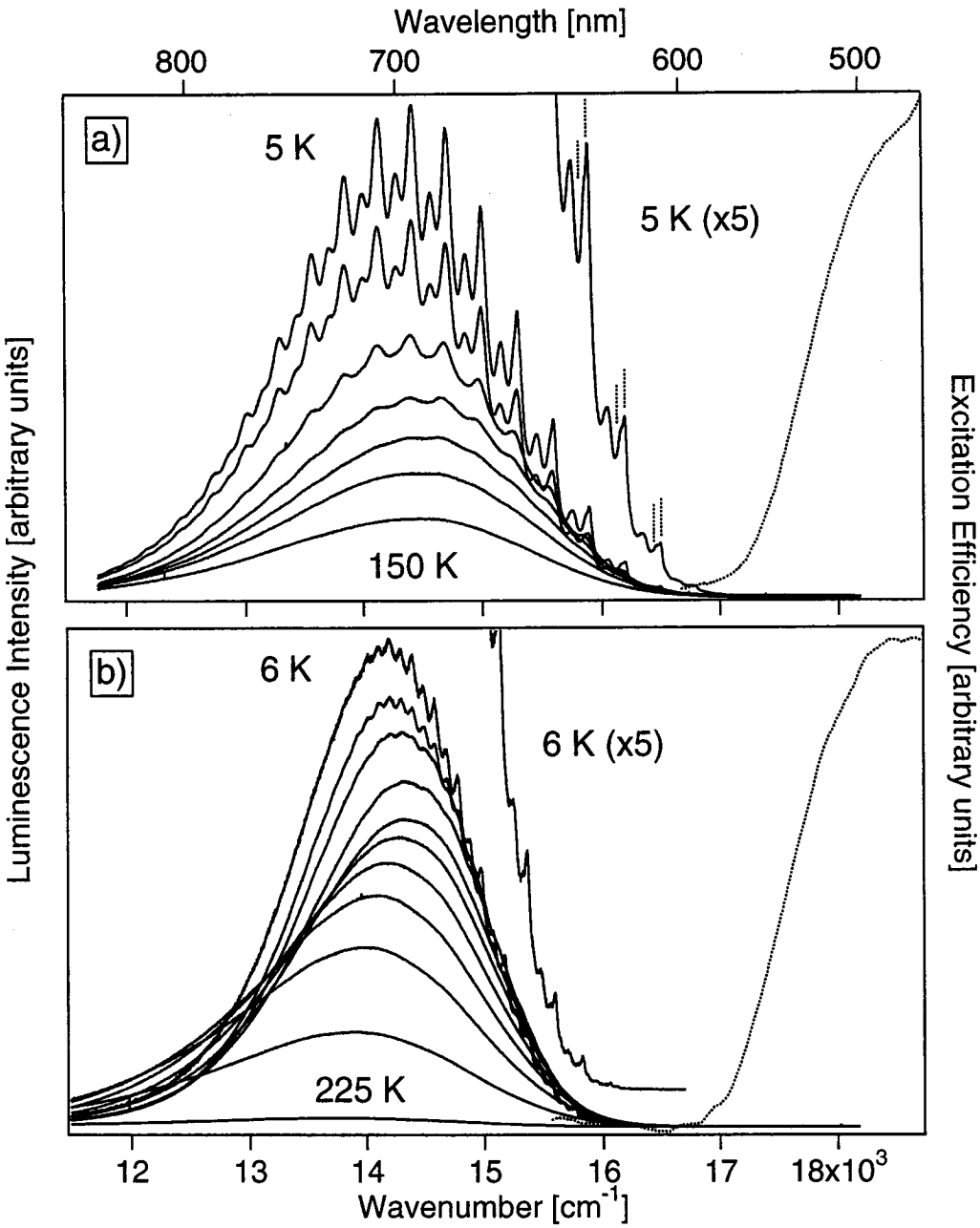

Figure 9.3. a) Luminescence and excitation spectra of $[Pt(SCN)_4](n\text{-}Bu_4N)_2$ **2**. Temperature dependent luminescence spectra are shown at 5 K, 25 K, 50 K, 75 K, 100 K, 125 K, and 150 K (top to bottom). The excitation spectrum at 5 K (dotted trace) shows the first absorption transition. The luminescence spectrum at 5 K is enlarged by a factor of 5 to show detailed features near the origin. Dotted vertical lines show the small experimental energy separation (35 cm^{-1}) resolved near the origin, but not across the entire band. b) Luminescence and excitation spectra of $[Pt(SeCN)_4](n\text{-}Bu_4N)_2$ **4**. Temperature dependent luminescence spectra at 6 K, 15 K, 30 K, 50 K, 75 K, 100 K, 125 K, 150 K, 175 K, 200 K, and 225 K are shown top to bottom. The excitation spectrum at 5 K (dotted trace) shows the first absorption transition. The luminescence spectrum at 6 K is enlarged by a factor of 5 and offset along the ordinate for clarity.

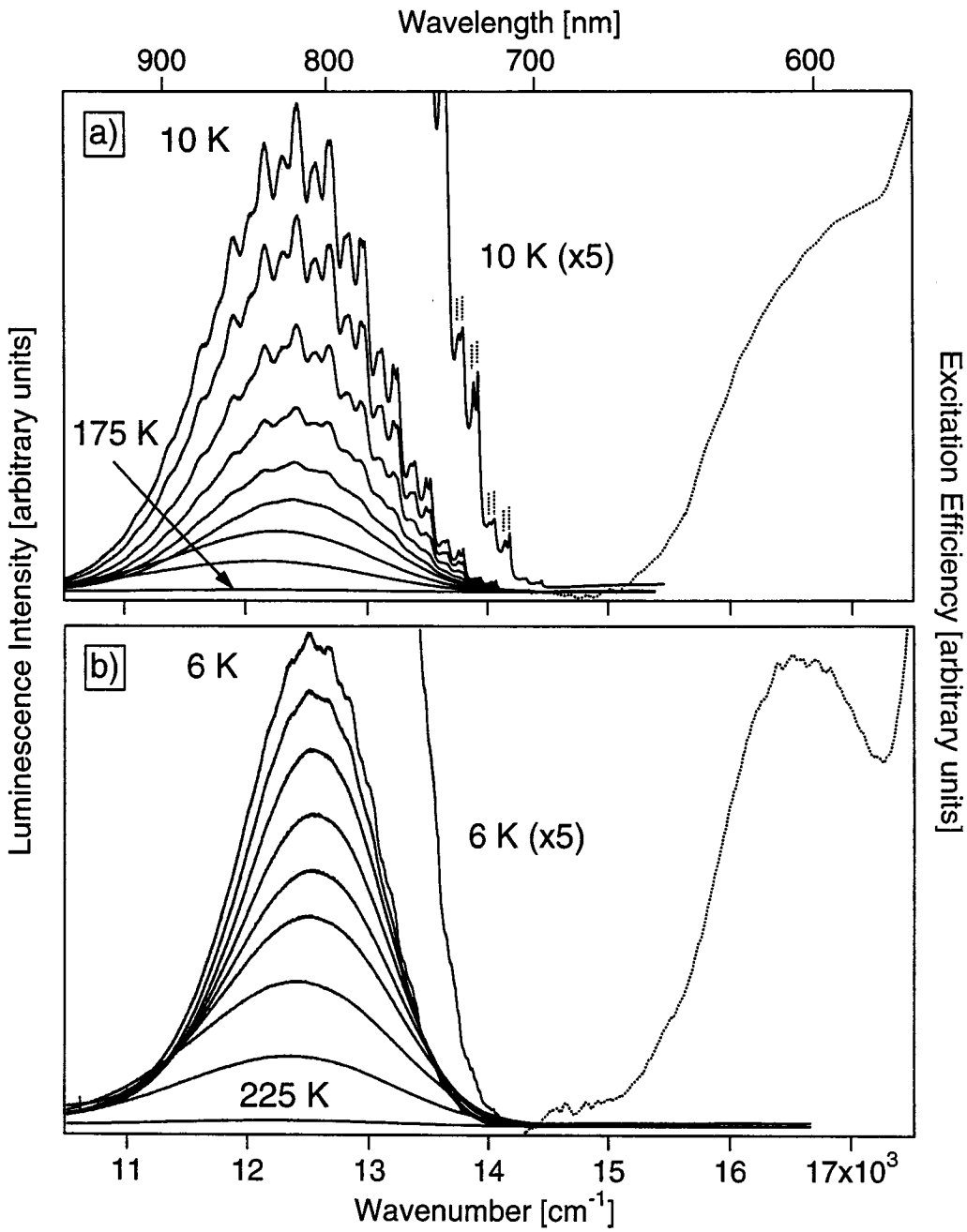

Figure 9.4. a) Luminescence and excitation spectra of $[Pd(SCN)_4](n\text{-}Bu_4N)_2$ **3**. Temperature dependent luminescence spectra are shown at 10 K, 20 K, 30 K, 45 K, 50 K, 60 K, 70 K, 100 K, 125 K, and 175 K (top to bottom). The luminescence spectrum at 5 K is enlarged by a factor of 5 to show the small repetitive spacings near the origin. Dotted vertical lines illustrate this separation of 35 cm^{-1} for this complex. b) Luminescence and excitation spectra of $[Pd(SeCN)_4](n\text{-}Bu_4N)_2$ **5**. Temperature dependent luminescence spectra at 6 K, 15 K, 30 K, 50 K, 75 K, 100 K, 125 K, 150 K, 175 K, and 225 K are shown top to bottom. The luminescence spectrum at 5 K is enlarged by a factor of 5 to show detailed features near the origin. The excitation spectra at 5 K (dotted traces) shows the first absorption transition for both complexes **3** and **5**.

Figure 9.5 shows the temperature dependent integrated luminescence intensities and lifetimes for complexes **2-5**. All luminescence lifetimes reported in Figure 9.5 and Table 9.1 were measured near the luminescence band maximum and all show a similar increase, by up to a factor of 300, when temperature is decreased from 250 K to 5 K. Complex **3** (Figure 9.5c) shows a slightly different behavior: its luminescence lifetimes increase drastically at temperatures lower than 50 K. The platinum(II) thiocyanates (**1**,**2**) exhibit double exponential excited state decay behavior with a fast component accounting for approximately 5 % of the total intensity at 5 K which is followed by a steady increase of the fast component to 50 % at 150 K. This type of decay behavior is wavelength dependent and appears predominantly on the blue sides of the luminescence spectra of **1** and **2**. The fast component is assigned as a luminescent trap.

Normalized integrated luminescence intensities for complexes **2-5** show steady decreases with increasing temperature, the exception again being complex **3** where, similar to the lifetimes, the intensity shows a large increase at temperatures lower than 50 K. The temperature-dependent integrated intensities all have weak shoulders in the temperature range of 100 K to 150 K. This feature is not seen in the lifetime data and is most evident in the intensity data of complex **4** (Figure 9.5b) where the integrated intensities change little between 75 K and 150 K and then decrease rather suddenly at higher temperatures. Differences in the temperature-dependent luminescence intensities may be attributed to subtle changes in radiative and nonradiative relaxation rate constants and energy transfer rate constants. All compounds show a strong decrease of their luminescence intensity and lifetime at high temperatures, a key condition for the observation of the unusual pressure effects presented in the next section.

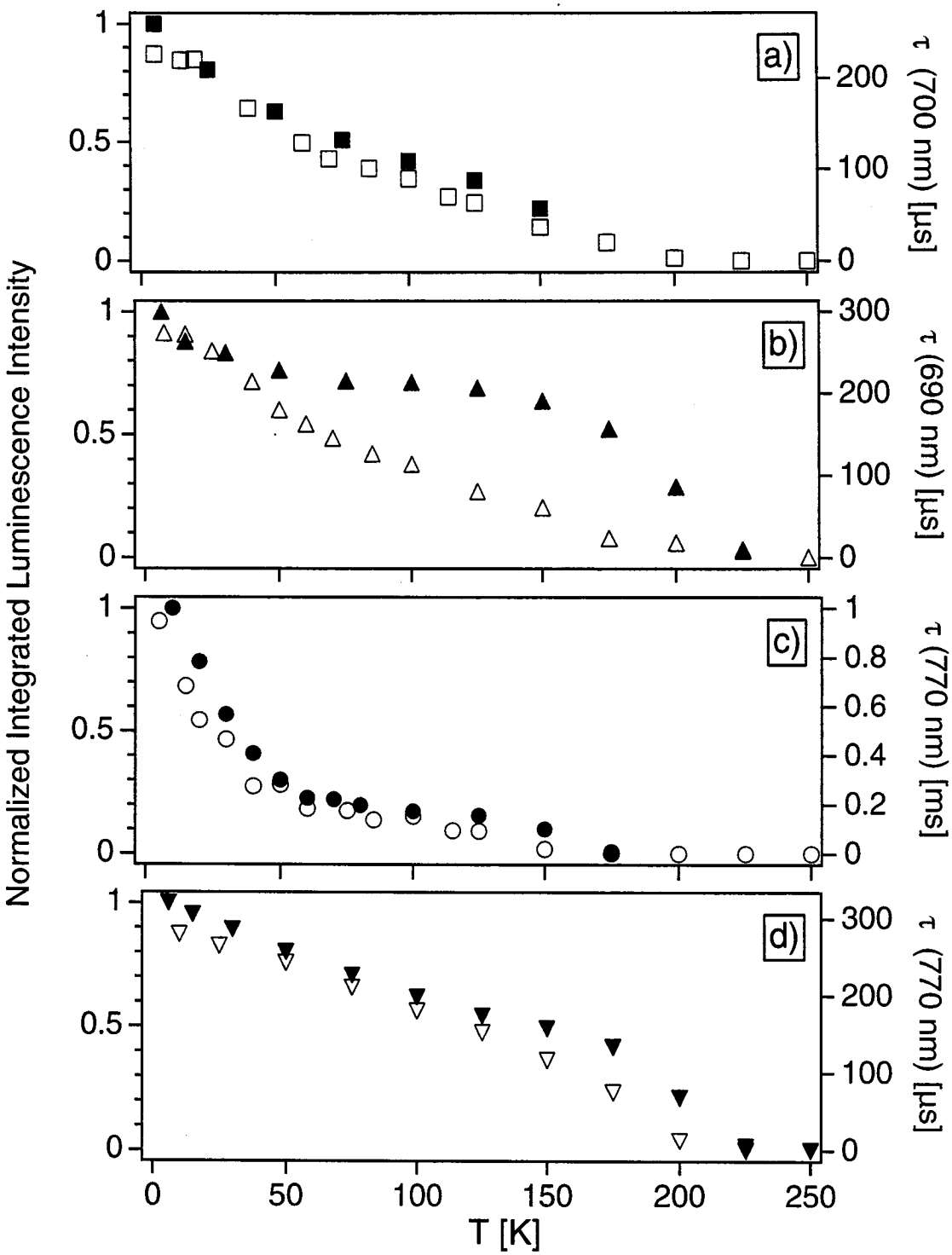

Figure 9.5. Normalized integrated luminescence intensities (solid symbols) and single exponential luminescence lifetimes (open symbols) at wavelengths near the luminescence band maxima. a) $[Pt(SCN)_4](n\text{-}Bu_4N)_2$ **2** (squares) at 700 nm; b) $[Pt(SeCN)_4](n\text{-}Bu_4N)_2$ **4** (triangles) at 690 nm; c) $[Pd(SCN)_4](n\text{-}Bu_4N)_2$ **3** (circles) at 770 nm; d) $[Pd(SeCN)_4](n\text{-}Bu_4N)_2$ **5** (inverted triangles) at 770 nm.

quantity	$[Pt(SCN)_4]$ $(PPh_4)_2$ (**1**)	$[Pt(SCN)_4]$ $(n\text{-}Bu_4N)_2$ (**2**)	$[Pd(SCN)_4]$ $(n\text{-}Bu_4N)_2$ (**3**)	$[Pt(SeCN)_4]$ $(n\text{-}Bu_4N)_2$ (**4**)	$[Pd(SeCN)_4]$ $(n\text{-}Bu_4N)_2$ (**5**)
E_{max} (cm^{-1})	14770	14440	12390	14180	12530
luminescence origin (cm^{-1})	17464	16806	14343	16330	14445
τ (μs)	(700 nm)	(700 nm)	(770 nm)	(740 nm)	(780 nm)
	285, 4K	320, 5K	947, 5K	300, 5K	279, 5K
	173, 50K	207, 50K	282, 50K	149, 75K	180, 100K
	81, 125K	102, 100K	153, 100K	86, 125K	75, 175K
	41, 175K	49, 150K	19, 150K	27, 200K	12, 200K
		0.3, 200K			
main progression interval (cm^{-1})	295	303	274	195	185
absorption† / excitation‡ maximum (cm^{-1})	19660†	19460‡	16450‡	18700‡	16610‡
Stokes Shift (cm^{-1})	4895	5020	4060	4520	4080

Table 9.1. Spectroscopic quantities from the temperature-dependent luminescence spectra in Figures 9.1-9.5.

Table 9.1 contd.

frequency intervals in luminescence spectra (cm^{-1}) [Raman freqs. (cm^{-1})]	295 [303, a_{1g}][a,b]	300 [303, a_{1g}][a,b]	274 [274, a_{1g}][a,b]	195 [195, a_{1g}][a,b]	185 [179, a_{1g}][a,b]
	250 [b_{1g}][b]	150 [151, b_{2g}][a,b]	260 [260, b_{1g}][a,b]	160 [b_{1g}]	145 [b_{1g}]
	230	33	165	105 [102, b_{2g}][a,b]	110 [113, b_{2g}][a,b]
	220		135 [144, b_{2g}][a,b]	65	65
	175		113 [115][b]		
	145 [151, b_{2g}][a,b]		35		
	108 [b_{2g}][c]				
	70 [77, Π]				
	35				
	10				
$\hbar\omega_{CN}$ (cm^{-1})	2101, 2126	2107	2103	2108	2105
	(strong, sharp)	(strong, sharp)	(sharp)	(strong, sharp)	(strong, sharp)

[a] Ref. 31. [b] This work. [c] Observed in absorption spectrum at 5 K in Figure 9.2b.

9.3.2 Pressure dependent luminescence intensities and lifetimes

Figures 9.6-9.9 show pressure-dependent luminescence spectra and lifetimes of complexes **2-5** in a similar crystalline environment.[55] The pressure-induced changes in important spectroscopic quantities are summarized in Table 9.2. All complexes show large increases of luminescence intensities and lifetimes as a function of pressure, by almost three orders of magnitude between ambient pressure and 35 kbar at room temperature. This effect is accompanied by significant blue shifts of the luminescence band maxima by up to 29 cm^{-1}/kbar. Pressure-dependent Raman spectra are monitored concomitantly to determine if changes in molecular structure accompany the unusual intensity and lifetime increase. Most spectra show similar smooth shifts of the metal-ligand vibrational bands to higher frequency as a function of pressure.

quantity	$[Pt(SCN)_4]$ $(n\text{-}Bu_4N)_2$ (**2**)	$[Pd(SCN)_4]$ $(n\text{-}Bu_4N)_2$ (**3**)	$[Pt(SeCN)_4]$ $(n\text{-}Bu_4N)_2$ (**4**)	$[Pd(SeCN)_4]$ $(n\text{-}Bu_4N)_2$ (**5**)
ΔE_{max} (cm^{-1}/ kbar)	+24	+29	+12	+25
$\Delta\hbar\omega_{a_{1g}}$ (cm^{-1}/ kbar)	+0.60	+0.68	+0.46	+0.57
$\Delta\hbar\omega_{b_{2g}}$ (cm^{-1}/ kbar)	+0.88	+0.72	*a*	*a*
τ	750 ns (5 kbar)	541 ns (7 kbar)	2 μs (5 kbar)	4 μs (7 kbar)
	9 μs (14 kbar)	36 μs (15 kbar)	3 μs (16 kbar)	55 μs (16 kbar)
	13 μs (30 kbar)	48 μs (30 kbar)	6 μs (32 kbar)	62 μs (28 kbar)

[a] $\hbar\omega_{b_{2g}}$ peaks are too close to the Rayleigh cutoff filter used in the pressure-dependent Raman measurements.

Table 9.2. Spectroscopic quantities obtained from the pressure-dependent luminescence and Raman spectra of the title complexes (Figure 9.10).

Figure 9.6 shows pressure-dependent luminescence spectra of **2** (Figure 9.6a) and **3** (Figure 9.6b) at pressures up to 30 kbar. The ambient pressure spectrum is very weak and appears as a flat trace at the bottom of each panel. As pressure is increased on the crystalline samples, the luminescence intensities show a fast, but continuous increase followed by a slow decrease at pressures over 30 kbar. The luminescence band maxima show a steady blue shift as a function of pressure with values of 24 cm^{-1}/ kbar (**2**) and 29 cm^{-1}/ kbar (**3**) (Table 9.2).[56] These shifts are opposite to those observed in the well-studied tetracyanoplatinate(II) complexes where there are strong metal-metal stacking interactions between the closely spaced $[Pt(CN)_4]^{2-}$ chromophores.[2,57] In the title systems, the closest distance for the metal centers to interact in a stacking fashion is approximately 13 Å,[31] larger by more than a factor of three than typical metal-metal distances of 3.1-3.7 Å in tetracyanoplatinate(II) complexes,[58] immediately ruling out metal-metal interactions as a cause for the pressure effects reported here. The effect of pressure on the luminescence spectrum of $K_2[Pt(SCN)_4]$ has been previously studied at 100 K and a blue-shift of the band maximum of 10±3 cm^{-1}/kbar was found,[59] almost three times smaller than the blue shift reported for **2**. This literature study also reports a very significant decrease of the luminescence intensity at 57 kbar. The linearly polarized luminescence spectra at 100 K exhibit a small dichroism, comparable to the polarized spectrum of **1** measured at 20 K, indicating that the nature of the luminescence transition is similar in $K_2[Pt(SCN)_4]$ and the $[Pt(SCN)_4]^{2-}$ complexes **1** and **2**. Figure 9.7 shows pressure-dependent luminescence spectra of the selenocyanate complexes, $[Pt(SeCN)_4](n\text{-}Bu_4N)_2$ (**4**) and $[Pd(SeCN)_4](n\text{-}Bu_4N)_2$ (**5**). Increases in luminescence intensities are similar to the thiocyanate analogs with the notable exception of complex **4** whose enhancement of the signal is much smaller than all other complexes studied. The pressure-induced blue shifts for band maxima of the selenocyanates are 12 cm^{-1}/ kbar (**4**) and 25 cm^{-1}/ kbar (**5**). It is also interesting to note that the blue shift for complex **4** is lower by a factor of 2 than the observed blue shifts for the other complexes and more comparable to the literature value found for the $[Pt(SCN)_4]^{2-}$ complex with the smaller K^+ counterion.

Figure 9.8 shows the pressure-dependent luminescence lifetimes and Figure 9.9 compares increases in lifetimes with intensities of complexes **2**-**5**. All experimental

excited state decay kinetics are single exponential and all luminescence lifetimes increase with pressure. The largest enhancement occurs for the palladium(II) complexes where the lifetimes increase by almost three orders of magnitude from their ambient pressure values of approximately 350-400 ns up to 62 μs at 28 kbar. The platinum(II) complexes show much smaller increases in lifetimes, up to 15 μs at high pressures (ca. 30 kbar) from approximately 1 μs at ambient pressure. Complex **4** exhibits the smallest increase in lifetimes of all complexes studied, similar to the trends observed in luminescence intensities and blue shift of the band maxima as a function of pressure. At pressures greater than 30 kbar, all complexes tend to show slight decreases in both intensity and lifetime. Decreases in pressure-dependent luminescence intensity are quite common due to more efficient energy transfer processes between luminophores and to deep traps when the sample volume becomes smaller. Pressure increases inhomogeneity and possibly also the number of deep traps, further reducing the observed luminescence intensity. Evidence for this effect comes from pressure-dependent Raman spectra where measurements of **2** show noticeable changes in the intensities and number of bands in the metal-ligand stretching region (280 to 300 cm^{-1}). We rationalize the pressure effects using the detailed spectroscopic information obtained at low temperature.

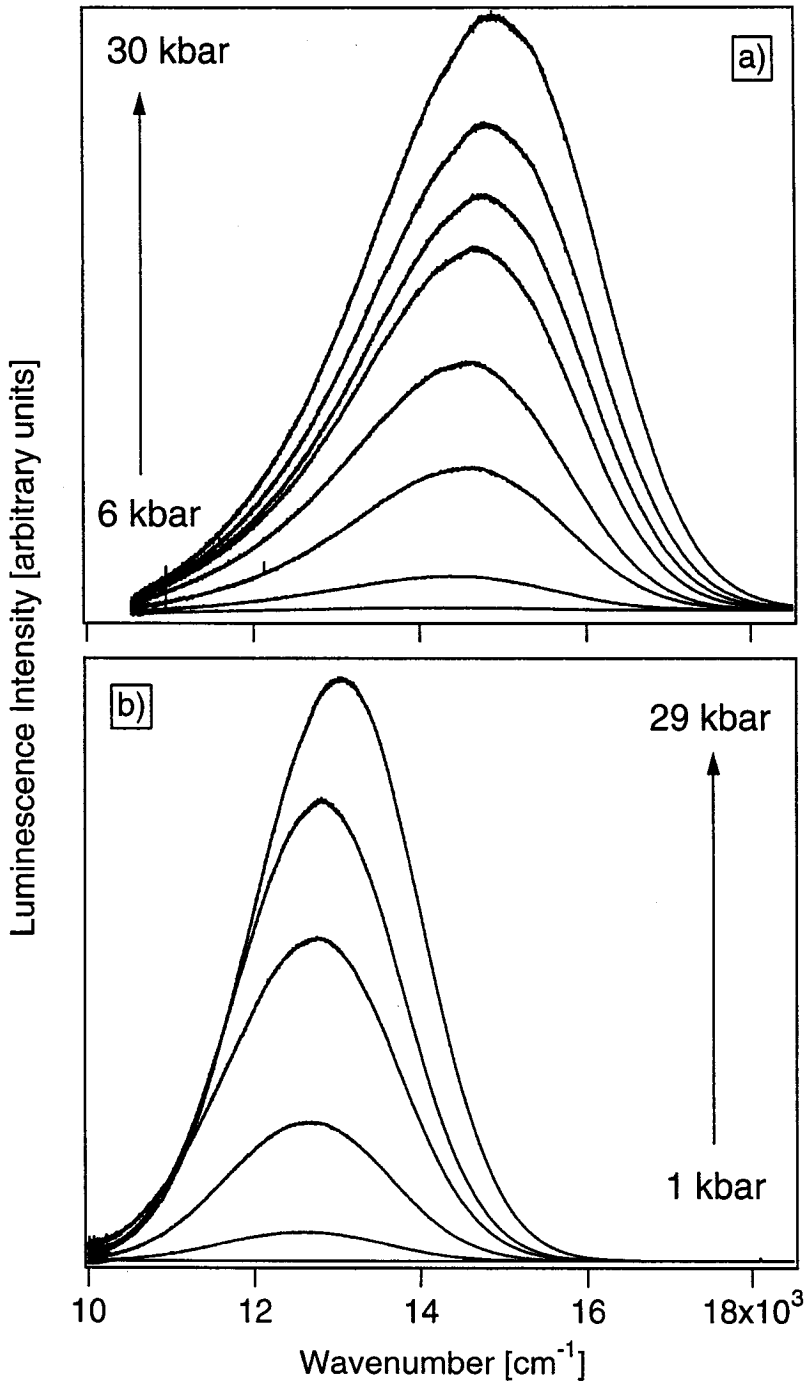

Figure 9.6. Representative pressure dependent luminescence spectra for thiocyanate complexes. a) $[Pt(SCN)_4](n\text{-}Bu_4N)_2$ **2** at 6 kbar, 10 kbar, 16 kbar, 17 kbar, 21 kbar, 24 kbar, 26 kbar, 28 kbar, and 30 kbar (bottom to top). b) $[Pd(SCN)_4](n\text{-}Bu_4N)_2$ **3** at 1 kbar, 9 kbar, 12 kbar, 18 kbar, 27 kbar, and 29 kbar (bottom to top).

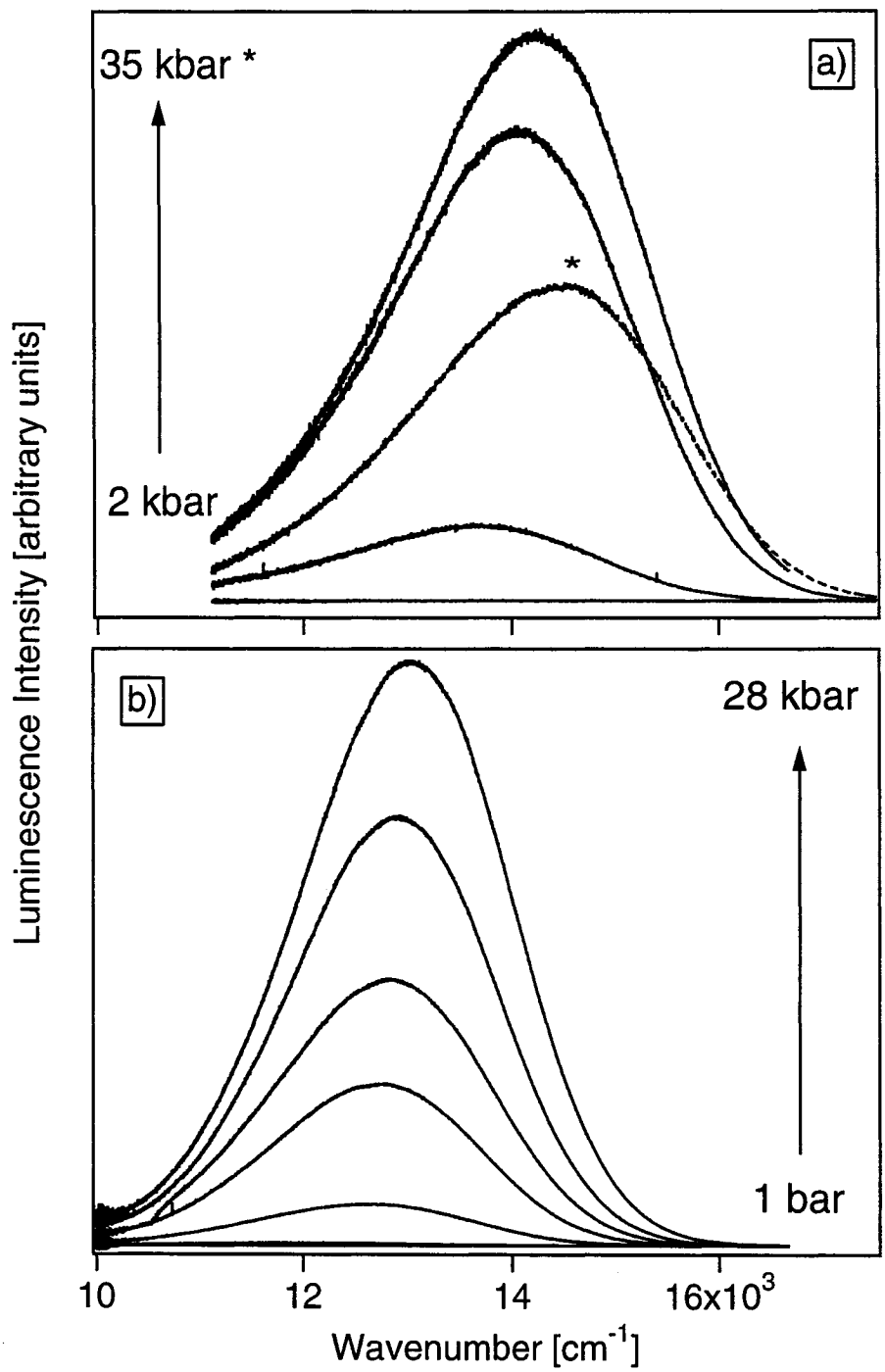

Figure 9.7. Representative pressure dependent luminescence spectra for selenocyanate complexes. a) $[Pt(SeCN)_4](n\text{-}Bu_4N)_2$ **4** at 2 kbar, 5 kbar, 16 kbar, 23 kbar, 25 kbar, and 35 kbar (bottom to top). The highest pressure spectrum (35 kbar) is indicated by an asterisk. b) $[Pd(SeCN)_4](n\text{-}Bu_4N)_2$ **5** at 1 bar (ambient pressure), 2 kbar, 5 kbar, 11 kbar, 13 kbar, 20 kbar, and 28 kbar (bottom to top).

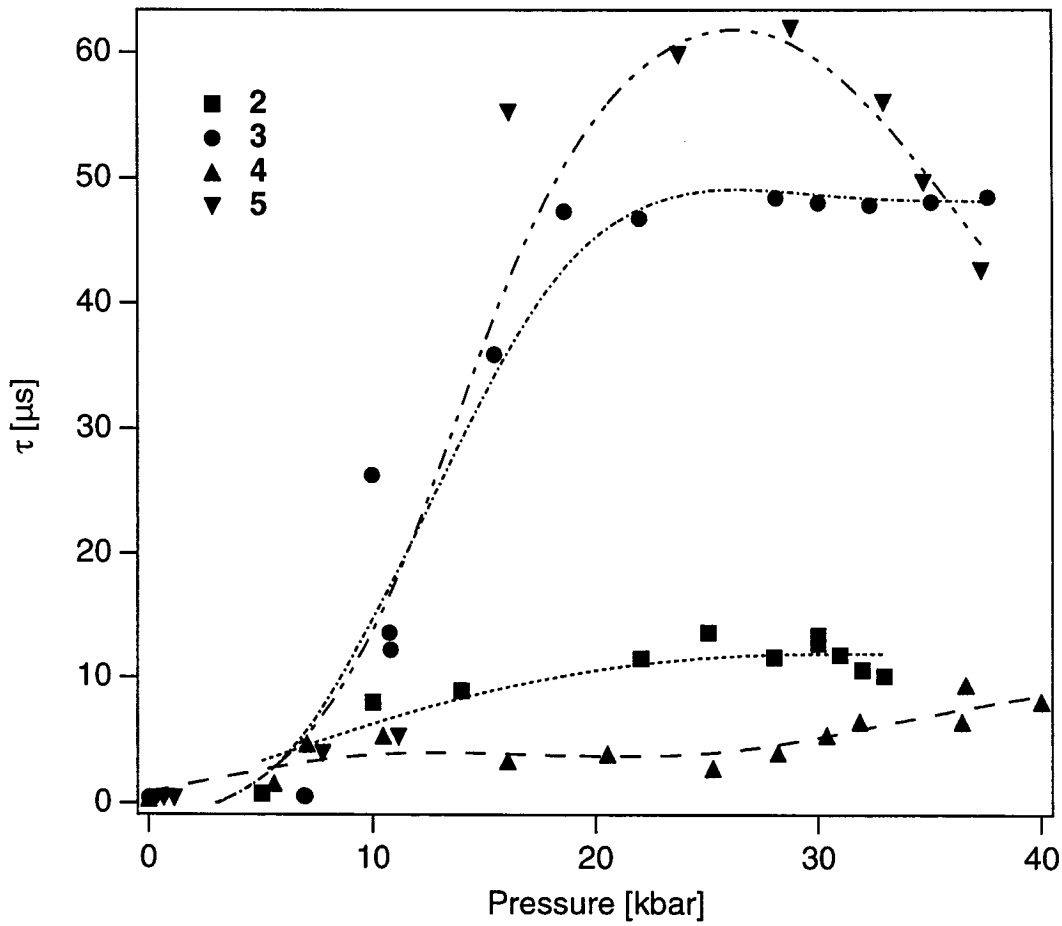

Figure 9.8. Pressure dependent luminescence lifetimes: a) $[Pt(SCN)_4](n\text{-}Bu_4N)_2$ **2** (squares); b) $[Pd(SCN)_4](n\text{-}Bu_4N)_2$ **3** (circles); c) $[Pt(SeCN)_4](n\text{-}Bu_4N)_2$ **4** (triangles); d) $[Pd(SeCN)_4](n\text{-}Bu_4N)_2$ **5** (inverted triangles). The accompanying curves for each data set are included as a guide for the eye.

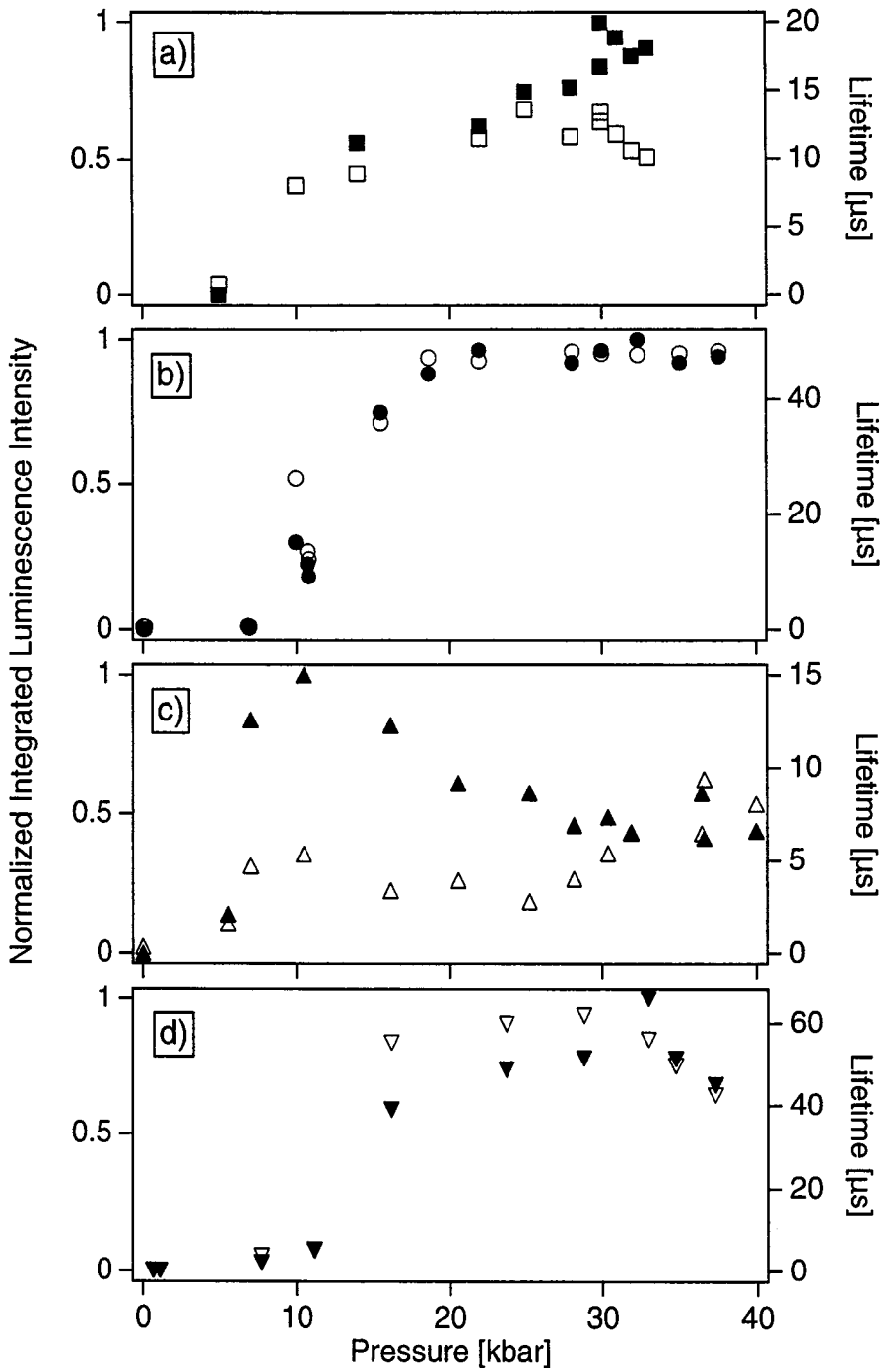

Figure 9.9. Normalized integrated luminescence intensities (solid symbols) and single exponential luminescence lifetimes (open symbols) of the pressure-dependent luminescence. a) $[Pt(SCN)_4](n\text{-}Bu_4N)_2$ **2** (squares); b) $[Pd(SCN)_4](n\text{-}Bu_4N)_2$ **3** (circles); c) $[Pt(SeCN)_4](n\text{-}Bu_4N)_2$ **4** (triangles); d) $[Pd(SeCN)_4](n\text{-}Bu_4N)_2$ **5** (inverted triangles).

9.4 Discussion

9.4.1 Vibronic Structure in Low Temperature Luminescence Spectra

The well-resolved vibronic structure in the luminescence spectra presented in Figures 9.1-9.4 provides detailed insight into the structural changes, which the title complexes undergo upon emission of a photon. We discuss the most important features, which are: a) long progressions in multiple modes, namely the a_{1g} and b_{2g} stretching and bending modes, respectively, b) vibronic origins arising from odd-parity vibrational modes, and c) the small repetitive spacings near the luminescence origins. The low temperature luminescence spectroscopy of **1** was used a benchmark for illustrating the previous points because it shows the best resolution of the vibronic structure.

Long progressions in non-totally symmetric vibrational modes, as shown in Figures 9.1-9.4, are rare for square-planar complexes. The appearances of prominent frequency intervals in the b_{2g} bending mode and the b_{1g} stretching mode mean that the emitting state geometry has a lower point group symmetry than the ground state.[60] The most plausible rationale for long progressions in a bending mode comes from previous low temperature luminescence spectra of the $[Pd(SCN)_4]^{2-}$ luminophore in different crystalline environments than of those studied here, showing evidence of a progression in the b_{2g} mode.[32] DFT calculations qualitatively confirm the activity of the b_{2g} mode from the electron density on the highest occupied d-orbitals on the metal center, e_g (d_{xz}, d_{yz}), being tilted off-axis due to repulsive effects from the proximity of lone-pair electron density on the sulfur atoms of the thiocyanate ligands. By exciting an electron to the higher-lying b_{1g} ($d_{x^2-y^2}$) orbital, whose lobes are oriented on the bonding axes, this repulsive effect is altered thereby favoring a scissor (b_{2g}) motion. Another possibility is that the b_{2g} interval appears due to progressions in the totally symmetric (a_{1g}) stretching mode built on vibronic (false) origins of promoting modes that differ by approximately the b_{2g} vibrational frequency. In D_{4h} point group symmetry the components of the electric dipole transform under the a_{2u} and e_u irreducible representations and a vibronically allowed transition will require one quantum of either a_{2u} and e_u vibrations. In the title complexes one of the two e_u modes has a frequency difference with the a_{2u} mode that could give rise to an interval between vibronic origins matching the b_{2g} frequency if both types of

promoting modes are active.[61] For the thiocyanate complexes, the appropriate e_u mode has a frequency difference between the a_{2u} mode within 5 cm^{-1} of the b_{2g} bending frequencies whereas this difference for the selenocyanate complexes is up to 30 cm^{-1} larger than the actual frequency interval observed in the resolved luminescence spectra in Figures 9.3b and 9.4b. The inclusion of the b_{2g} bending modes is therefore justified based on the experimental luminescence spectra in Figures 9.1-9.4.

It is important to point out that there is another e_u mode approximately 25 to 35 cm^{-1} higher in frequency than the a_{2u} mode for all complexes and the frequency difference between these two possible promoting vibrations may account for the repetitive spacings observed in the thiocyanate complexes in Figures 9.2a, 9.3a, and 9.4a. We first consider all other possibilities for the appearance of these small spacings, such as low frequency lattice vibrations and "beats" corresponding to the frequency difference between two Franck-Condon active vibrational modes.[62] Beating arises from the nonzero displacements of two vibrational modes whose frequency difference is much smaller than the sum of the two frequencies. Because the a_{1g} stretching mode is the highest frequency, progression-forming mode in the title systems, there must be a vibrational mode that is approximately 25 to 35 cm^{-1} higher in frequency to achieve the small repetitive spacing effect observed in the spectra of the thiocyanate complexes. Raman spectra measured at 300 K and 77 K and those reported in literature studies,[31] reveal that there are no modes that match this description. If such a mode existed, its inclusion in our model would result in a calculated spectrum with a large discrepancy in the vibronic intervals on the red side of the spectra, i.e., an increase of the a_{1g} interval as opposed to the observed decrease for the platinum(II) thiocyanates **1** and **2**. The 5 K luminescence of **1** (Figure 9.2a) exhibits the same small frequency interval of ca. 35 cm^{-1} as observed in the spectra of **2** and **3** (Figures. 9.3a and 9.4a), in addition to other intervals of 70 cm^{-1} and 10 cm^{-1}. In the 10 K luminescence spectrum of complex **3** the small repetitive spacings of 35 cm^{-1} are the most resolved and persist close to the band maximum. Because small spacings in the same approximate interval are present in different complexes and in the same complexes in different crystalline environments, lattice vibrations with large displacements are probably not responsible for these features. We rationalize the small repetitive spacings based on the previous considerations of odd-parity vibrational modes,

i.e., a_{2u} and the lower frequency e_u, producing two vibronic origins separated by a small frequency interval ($\Delta\hbar\omega \approx 25$ to 35 cm^{-1}). It has also been demonstrated on theoretical grounds that such unusual spectroscopic features can be present in the electronic spectra square-planar complexes with second- or third-row transition metal centers, i.e., large spin-orbit coupling constants.[63]

9.4.2 Calculated Emitting State Distortions from Progressions in Luminescence Spectra

We use a model for the luminescence spectra of the title complexes with multiple displaced vibrational modes based on two vibronic origins. The interval between these origins is ca. 35 cm^{-1}, corresponding to the difference between the a_{2u} and the lower frequency e_u promoting vibrations. Two spectra are calculated with significant displacements in totally and non-totally symmetric even-parity metal-ligand vibrational modes and added for the resulting fitted spectrum. The time-dependent theory of luminescence spectroscopy is used to calculate the vibronic patterns in the low temperature luminescence spectra of the title complexes and determine the magnitudes of excited state displacements along multiple vibrational modes.[43-45] Here we only briefly discuss our application and the choice of model that we use to calculate our spectra.

Upon emission of a photon from a molecule in the emitting state at t = 0, a wavepacket is created on the final potential energy surface. Because the wavepacket is not an eigenfunction of this surface, it evolves in time according to the time-dependent Schrödinger equation. In many transition metal compounds, there are nonzero displacements of the initial and final state potential surfaces along multiple vibrational modes. The wavepacket will then follow the path of steepest descent, which governs the overall width of the luminescence band. The intensity of the luminescence transition is given by eq. 9.1,

$$I_{lum}(\omega) = C\omega^3 \int_{-\infty}^{+\infty} e^{i\omega t} \langle \phi | \phi(t) \rangle dt \qquad \text{eq. 9.1}$$

where $I_{lum}(\omega)$ is the luminescence intensity per unit volume, area at the frequency ω, C is a constant, and $\langle\phi|\,\phi(t)\rangle$ is the autocorrelation function, which is the overlap of the initial wavepacket, $\phi(t = 0)$, with the time-dependent wavepacket , $\phi(t)$.

The latter quantity is calculated from a closed-form analytical equation[43-45] and several assumptions have to be made in order to calculate the overlap in a multidimensional case; (a) there are no changes in the vibrational force constants in the excited state, (b) there is no mixing of normal coordinates, and (c) the transition dipole moment, μ, is constant. The overlap for the *k*th mode is then given by eq. 9.2,

$$\langle\phi_k|\phi_k(t)\rangle = \exp\left[-\frac{\Delta_k^2}{2}(1-\exp(-i\omega_k t)) - \frac{i\omega_k t}{2}\right]$$

eq. 9.2

for harmonic potential energy surfaces Δ_k and ω_k are the displacement and frequency of the *k*th mode in dimensionless units and cm^{-1}, respectively. For many displaced modes, the total overlap is the product of overlaps for each individual mode,

$$\langle\phi|\phi(t)\rangle = \prod_k \langle\phi_k|\phi_k(t)\rangle \exp\left(\frac{-iE_0 t}{\hbar} - \Gamma^2 t^2\right)$$

eq. 9.3

where E_0 is the energy of the electronic origin and Γ is a Gaussian damping factor, both in cm^{-1}. After calculating the total overlap, the result is Fourier transformed (eq. 9.1) to give the spectrum.

The primary goal of calculating the luminescence spectra is to determine excited state distortions, Δ_k, along the displaced vibrational modes and to rationalize the apparent anharmonicity effects. Vibrational frequencies are obtained from ground state Raman spectra of the title compounds, which are shown in Figure 9.10 for **2-5**.

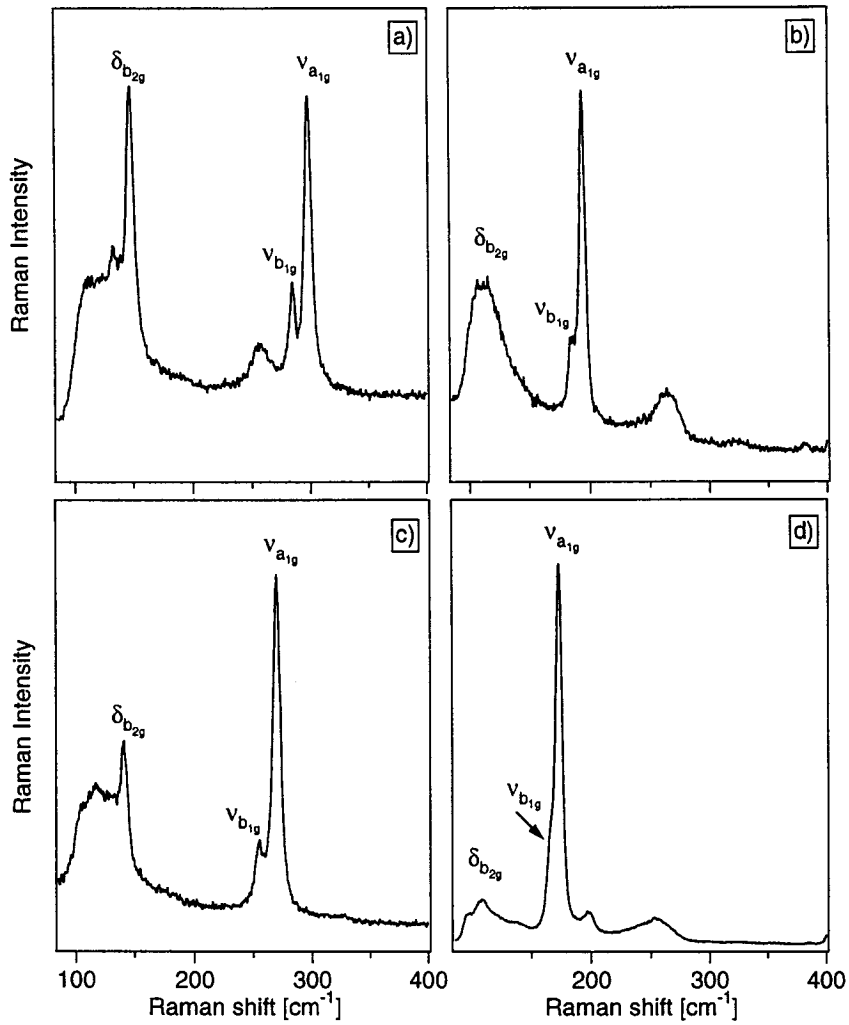

Figure 9.10. Room temperature Raman spectra in the metal-ligand region (i.e., a_{1g}, b_{1g}, and b_{2g} modes) of; a) **2**, b) **4**, c) **3**, d) **5**.

Table 9.3 shows the numerical values used in the calculation of luminescence spectra of the title complexes. In complexes **1-3**, we calculate luminescence spectra using two origins separated by the frequency difference of two promoting modes whose frequency difference corresponds to the small repetitive spacing observed in the luminescence spectra of these complexes (ca. 35 cm^{-1}). The calculated spectra shown in Figures 9.11-9.14 are obtained by first fitting one progression (progression **I** in Table 9.3) followed by calculating the second progression (progression **II**) and scaling it by appropriate factors, which are 0.15 (**1**), 0.35 (**2**), and 0.70 (**3**). Values used for the individual offsets, Δ_k, of both progressions are varied independently to obtain reasonable fits for the experimental spectra. The final result is obtained by adding the two calculated spectra. In cases where the luminescence is vibronically allowed, the propagating wavepacket is multiplied by the transition dipole and along each displaced mode the cross sections explored are not necessarily identical. The procedure used to calculate spectra is justified by the need to reproduce the highly resolved features in Figures 9.1-9.4 and we obtain the differences between progressions on different vibronic origins by using individual offsets for both the calculated spectra. This does not lead to substantial differences in offsets between the largest displaced modes. Spectra calculated using exactly identical offsets for progressions built on both vibronic origins **I** and **II** resulted in noticeable discrepancies between the best-fit spectrum and the experimental data. Low temperature luminescence spectra of complexes **4** and **5** have a much narrower spectral profile and vibronic structure is not as resolved near the origin. We use only one origin to calculate the luminescence spectra for these compounds, which leads to very good agreement with the experimental spectra as shown in Figure 9.14. All vibrational frequencies used in the calculations are determined from experimental Raman spectra. The percentage of the a_{1g} displacement to the sum of all normal coordinate offsets is listed at the bottom row of Table 9.3. The variance of this value between complexes with the same ligand is small, which shows that all complexes, despite the differences in band-widths, have similar displacements along the dominant progression-forming mode. The values used for the damping factor, Γ, in the calculated luminescence spectra for complexes **1-3** are smaller than the actual vibronic bandwidths. This was necessary due to the "filling in" effects by

the large number of displaced modes of closely spaced progressions and to show the small doubling effect near the origin region. The choice of Γ does not influence the values of Δ_k used to calculate the spectra in Figures 9.11-9.14.

Figure 9.11 shows the fit for complex **1**. A larger frequency interval, 70 cm^{-1}, is used between the two vibronic origins **I** and **II** corresponding to the largest separation between dominant progressions observed in the experimental spectrum in Figures 9.1 and 9.2a. The inset in Figure 9.11 is the origin region showing the good agreement between the calculated and experimental spectra. Some of the detailed features, such as the small spacings of 10 cm^{-1}, cannot be reproduced in the calculated spectra due to the overlapping of several peaks and the value of the damping factor, Γ. Figure 9.12a shows the low energy side of **1** with the calculated spectrum (Γ = 15 cm^{-1}) below the experimental spectrum. The vertical lines correspond to constant frequency intervals in the a_{1g} mode (295 cm^{-1}), illustrating the effect of a gradually decreasing frequency interval of the main progression in the experimental spectrum. Figure 9.12b shows the experimental (top trace) and calculated (bottom and middle traces) spectra of **2** with the arrows at the maxima of selected vibronic peaks on the low energy side. When using a simpler model based on one origin with only the two predominant displaced modes (a_{1g} and b_{2g}), the calculated spectrum (bottom trace) cannot reproduce the experimental spectrum, as shown by the vertical lines that match the largest frequency interval in the experimental spectrum. The best-fit calculated spectrum with two vibronic origins can better reproduce the decrease in the largest progression interval on the red side as well as the small doubling effect near the luminescence origin. Figure 9.13 contains the experimental (top trace) and calculated (bottom and middle traces) luminescence spectra of **3** and the inset shows the origin region in detail. The two-vibronic origin model is able to reproduce the small repetitive spacing and the intensity distributions of the individual progressions. We include a best fit to the overall band profile using a single origin spectrum with the same vibrational modes involved as a comparison. Figure 9.14 shows the experimental (top traces) and calculated (bottom traces) of the selenocyanate complexes **4** and **5**. It was found that a model based on one origin, considering the number of vibrational modes involved, was sufficient to calculate the luminescence

spectra. Preliminary calculations with the two-origin model lead to congested spectra and poor agreement between calculated and experimental spectra. This discrepancy is attributed to the fact that the luminescence spectra of the selenocyanates are much narrower than the thiocyanate analogs making the fit procedure difficult with the two-origin model due to the many overlapping vibronic bands.

Phenomenological spectroscopic effects reminiscent of those analyzed here have been observed for other compounds. The low temperature luminescence spectrum of *bis*-(maleonitriledithiolato)palladate(II) shows highly resolved vibronic structure that is "modulated" by a small frequency interval of 26 cm^{-1}.[53] The origin of this small repetitive spacing arises from a beating effect and the two modes with largest displacements have a frequency difference of 26 cm^{-1}. Another illustrative example is the low temperature luminescence spectrum of ruthenocene, which exhibits two well-defined progressions in the totally symmetric (a_{1g}) Ru-cp stretching mode with the main vibronic peaks separated by 165 cm^{-1}.[62] Similar beating effects occur in this spectrum with well resolved shoulders appearing on the two main progressions. The beat frequency comes from differences between the totally symmetric stretching mode and higher frequency non-totally symmetric modes. In both the above cases, we find that similar models applied to the spectra in Figures. 9.1-9.4 do not yield good fits or are physically meaningless. Overall, the calculated fits are able to reproduce the important and prominent spectral features observed in the experimental luminescence spectra and we now use the time-dependent theory to explain the effect of the decreasing main progression interval across the luminescence bands.

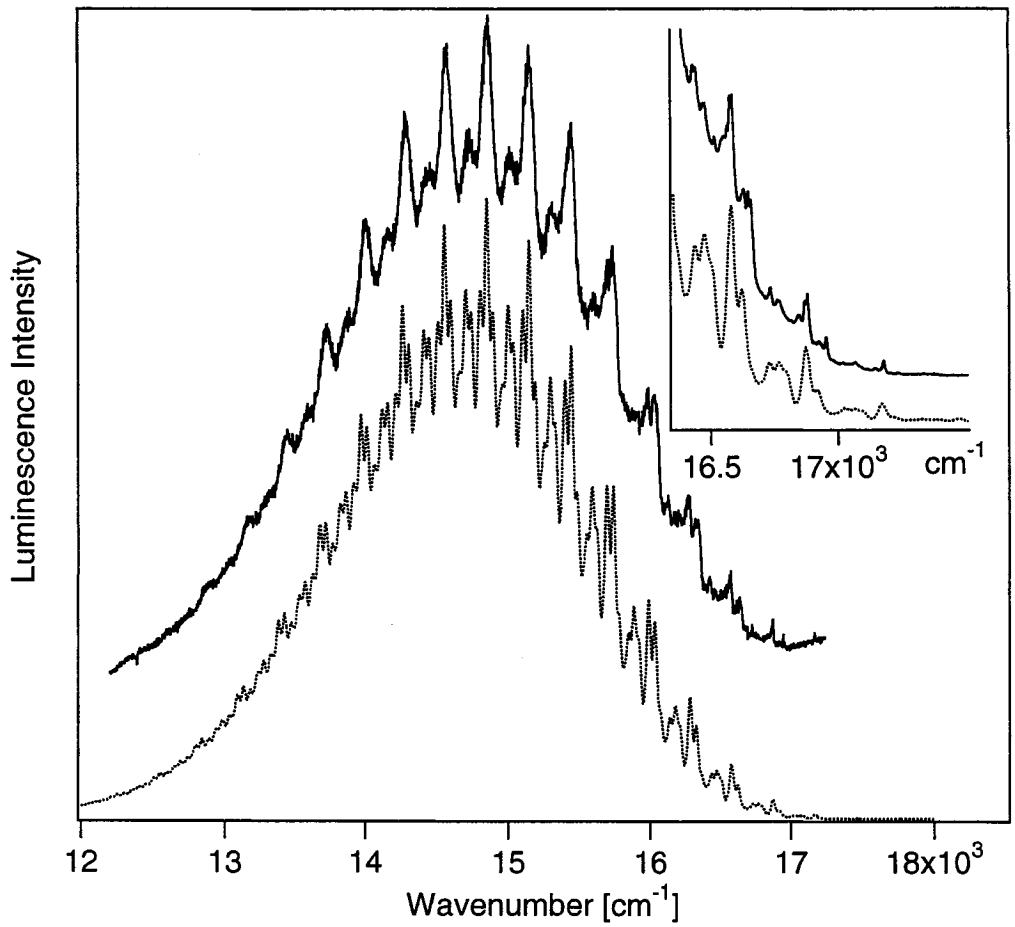

Figure 9.11. Calculated and experimental (5 K) luminescence spectra of **1**. The experimental spectrum is offset along the ordinate and the calculated spectrum is given by the dotted trace. The inset shows features near the origin. All parameters used for the calculated spectrum are listed in Table 9.3.

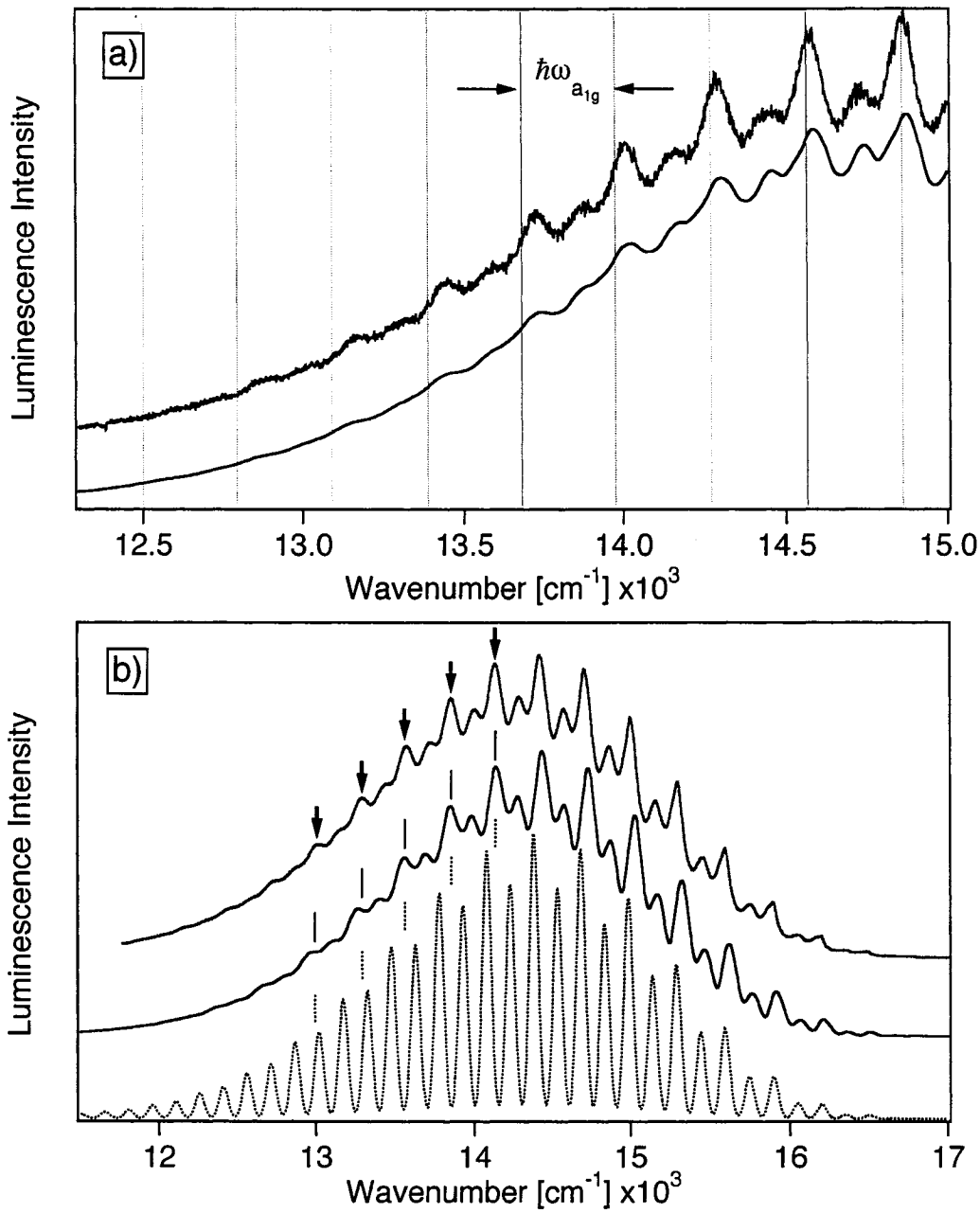

Figure 9.12. a) Calculated (Γ = 15 cm^{-1}) and experimental (5 K) luminescence spectra of **1** on the lower energy half of the spectrum. The experimental spectrum is offset and the vertical lines represent intervals of the totally symmetric Pt-S stretching mode (a_{1g}, 295 cm^{-1}). b) Calculated and experimental luminescence spectra of **2**. The top trace is the experimental spectrum at 5 K, the middle trace represents the 5-mode calculated spectrum with two vibronic origins (Γ = 10 cm^{-1}) using the parameters in Table 9.3, and the bottom trace is a 2-mode model (Γ = 20 cm^{-1}) calculated spectrum. To illustrate the decrease of the high frequency progression interval on the low energy side of the spectrum, the intervals of the highest frequency are indicated on the experimental spectrum by arrows. Corresponding lines are given on the calculated spectra for comparison to the experimental trace.

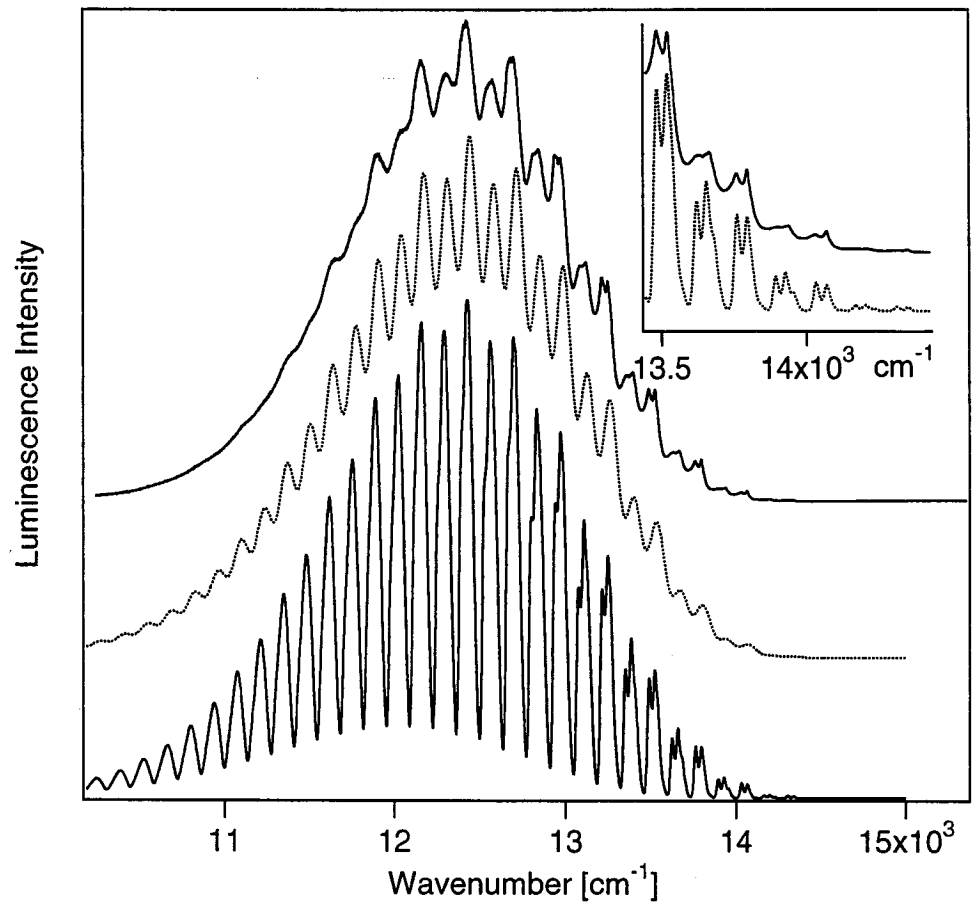

Figure 9.13. Calculated and experimental spectra of $[Pd(SCN)_4](n\text{-}Bu_4N)_2$ **3**. The top trace denotes the 10 K experimental spectrum, the dotted (middle) trace is a 4-mode calculated spectrum (Γ = 32 cm^{-1}) with one origin, and the solid (bottom) trace is the best-fit high resolution 4-mode calculated spectrum with two vibronic origins (Γ = 4 cm^{-1}). Both calculated spectra use the same vibrational modes. The offsets (Δ) for the single origin calculated spectrum are as follows: Δ_{274} = 3.36, Δ_{260} = 1.76, Δ_{140} = 1.52, and Δ_{113} = 1.00 (E_0 =14343 cm^{-1}) and parameters for the 2-origin fit are listed in Table 9.3. The inset shows the experimental spectrum (solid trace) and 2-origin calculated spectrum (dotted trace) highlighting the small doubling effect.

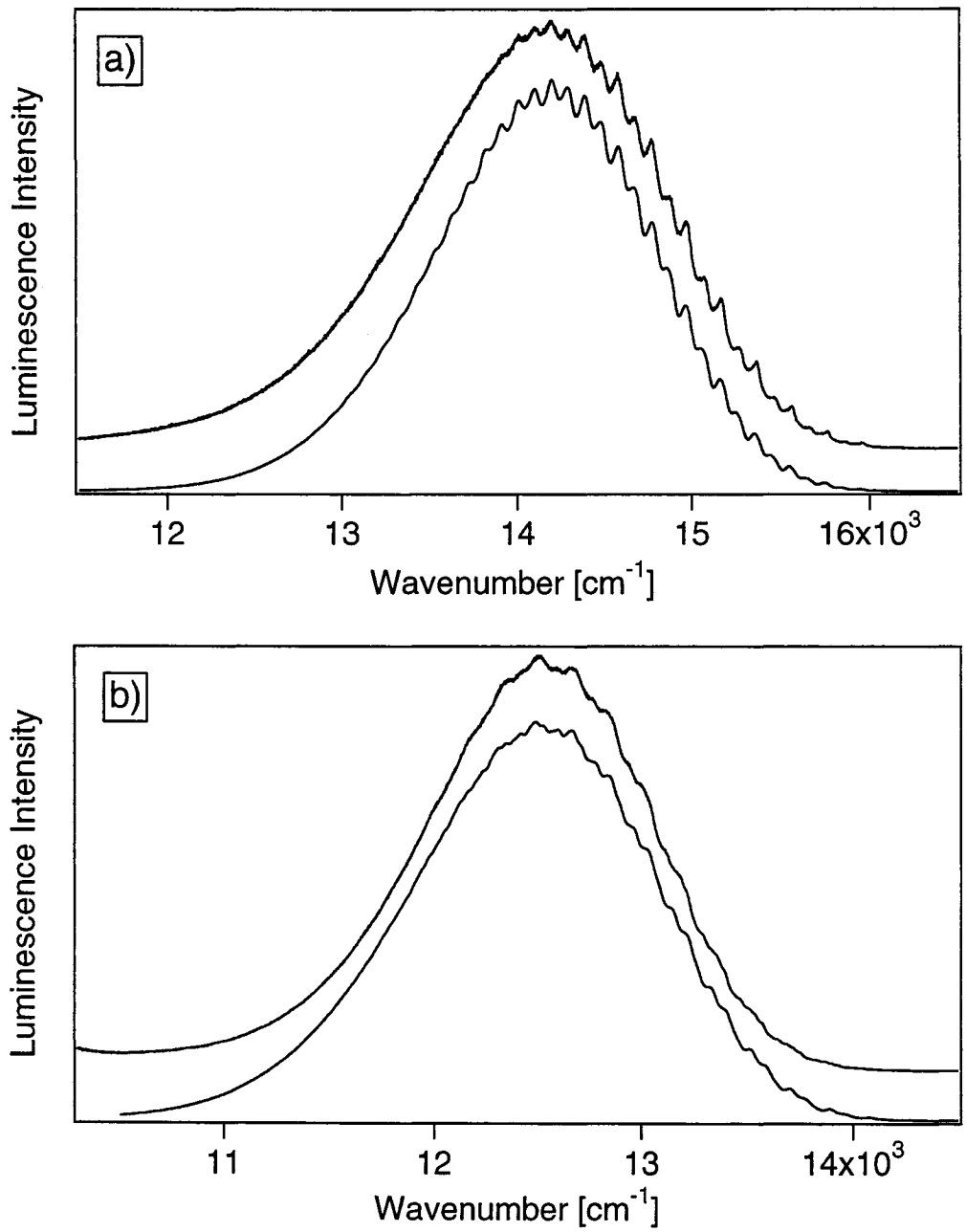

Figure 9.14. a) Calculated spectrum (bottom trace) and experimental spectrum (top trace) of $[Pt(SeCN)_4](n\text{-}Bu_4N)_2$ **4** at 6 K. b) Calculated spectrum (bottom trace) and experimental spectrum (top trace) of $[Pd(SeCN)_4](n\text{-}Bu_4N)_2$ **5** at 6 K. Parameters used in the calculated spectrum are listed in Table 9.3.

parameter	$[Pt(SCN)_4]$ $(PPh_4)_2$ (**1**)	$[Pt(SCN)_4]$ $(n\text{-}Bu_4N)_2$ (**2**)	$[Pd(SCN)_4]$ $(n\text{-}Bu_4N)_2$ (**3**)	$[Pt(SeCN)_4]$ $(n\text{-}Bu_4N)_2$ (**4**)	$[Pd(SeCN)_4]$ $(n\text{-}Bu_4N)_2$ (**5**)
Progression	**I, II**[d]	**I, II**[d]	**I, II**[d]	**I**	**I**
vibrational energies [ground and emitting state (cm^{-1}) : Normal coordinate offset (dimensionless)	295[a,b]:4.01, 3.87 285[b,c]:1.00, 1.00 250[a]: 1.64, 1.52 175[b]: 0.71, 0 145[a,b]:1.18, 1.00 110[a]: 1.05, 0.71	303[a,b]:3.75, 3.67 290[a,b]:0.71, 0.55 257[b] : 1.92, 1.55 151[a,b]:1.22, 1.22 132[b] : 1.05, 0.84	274[a,b]:3.55, 3.53 260[b,c]:1.48, 1.45 140[a,b]:1.67, 1.64 113[b]: 1.14, 0.84	195[a,b] : 4.36 160[a,b] : 1.73 105[a,b] : 1.87 65[c] : 1.0	185[a,b] : 4.22 145[a,b] : 1.79 110[a,b] : 1.84 65[c]: 0.89
E_0 (cm^{-1})	**I** 17464 **II** 17387	**I** 16806 **II** 16771	**I** 14343 **II** 14307	**I** 16330	**I** 14445
Γ (cm^{-1})	10	10	6	15	15
% $\Delta_{a_{1g}} / \Delta_T$	42 (I), 48 (II)	43 (I), 47 (II)	45 (I), 47 (II)	49 (I)	48 (I)

[a] From luminescence. [b] Experimental Raman frequency measured at 295 K. [c] Raman and IR.[31] [d] Progression II is scaled by an appropriate factor and added to progression I; (**1**) 0.15, (**2**) 0.35, (**3**) 0.70.

Table 9.3. Parameters used to calculate luminescence spectra of the title complexes.

9.4.3 Non-constant progression intervals

From the high resolution luminescence spectra of **1-3**, we have found that there are significant displacements in non-totally symmetric vibrational modes, including the b_{1g} and b_{2g} stretching and bending modes. Near the luminescence band maxima, the resolution decreases and only the dominant progressions are visible. In this region, transitions near the maxima of the a_{1g} progression coalesce and appear as one peak. In the model defined by eqs. 9.1 to 9.3, this effect corresponds to a damping factor, Γ, that increases as the luminescence energy decreases. Multiple individual maxima for the narrow vibronic peaks are resolved near the origin, but only a single maximum is observed for the broader vibronic peaks at lower energy that does not exactly correspond to any ground state vibrational frequency, as indicated by the arrows in Figure 9.12b. This effect causes a gradual decrease of the experimental energy interval separating maxima of the main apparent progression in the spectra of the thiocyanate complexes, giving the overall impression of anharmonicity. A well-established and related effect has been reported for $K_2[PtCl_4]$ where large displacements along the a_{1g} mode and smaller displacements along the lower frequency b_{1g} mode give an overall progression frequency that does not match the frequency of any ground state vibrational mode.[39] This is known as the "missing mode effect" or, MIME, and is observed when vibronic progressions are not highly resolved. The decrease of the progression interval on the low energy side of the luminescence spectra of **1** and **2** (Figures 9.1, 9.2, 9.3a, and 9.4a) is different from the MIME effect, but can be rationalized with the concepts underlying the MIME. From the calculations using the harmonic approximation with multiply displaced vibrational modes we are able to show that the decrease in the main progression interval comes from changes in the relative intensities of individual vibronic transitions and *not* from an anharmonic shape of the potential energy surface.

The time dependent theory allows for an intuitive understanding of these features. Figure 9.15 shows calculated absolute autocorrelation functions for the spectra in Figures 9.11-9.14. The top panel (Figure 9.15a) shows the total overlap used for the calculated spectrum of **1** (Figure 9.11) with the overlap of the single a_{1g} mode (295 cm^{-1}) using the average displacement value from the calculated spectrum. The second recurrence of the

overlap shows a small mismatch with the expected recurrence time of the 295 cm^{-1} mode. The middle panel (Figure 9.15b) shows the absolute overlaps used in the calculated spectra of Figure 9.12b. The inset of Figure 9.15b is the difference in absolute autocorrelation functions ($\Delta \left| \langle \phi \mid \phi(t) \rangle \right|$) between a two-mode model and the model for the best-fit calculated spectrum. The recurrence mismatch can be clearly seen in the second recurrence, where the best-fit spectrum has a longer recurrence time compared to what would be expected for progressions with constant energy spacings between members. This mismatch is the result of two vibrational modes close in frequency, i.e., a_{1g} and b_{1g} modes, that combine to yield a frequency that does not correspond to any ground state vibration, as is illustrated in Figure 9.12a. The actual MIME frequency is then mediated within the range of each implicated mode by the individual offsets for these modes. The bottom panel (Figure 9.15c) contains the absolute autocorrelation used to calculate the spectrum of **3** (Figure 9.13). The overlap is modulated by beats that are illustrated by the dotted trace. The beat frequency arises out of the difference between the two highest frequency modes with the largest displacements. It corresponds to 136 cm^{-1}, which is the difference of the a_{1g} and b_{2g} frequencies. The b_{1g} mode also has a significant distortion, but its beat with the a_{1g} modes is only 14 cm^{-1} and may only manifest itself at longer timescales than necessary for our calculations. Figure 9.16 shows similar beat effects from calculated spectra of the selenocyanate complexes where the a_{1g} and b_{2g} modes also have the largest displacements.

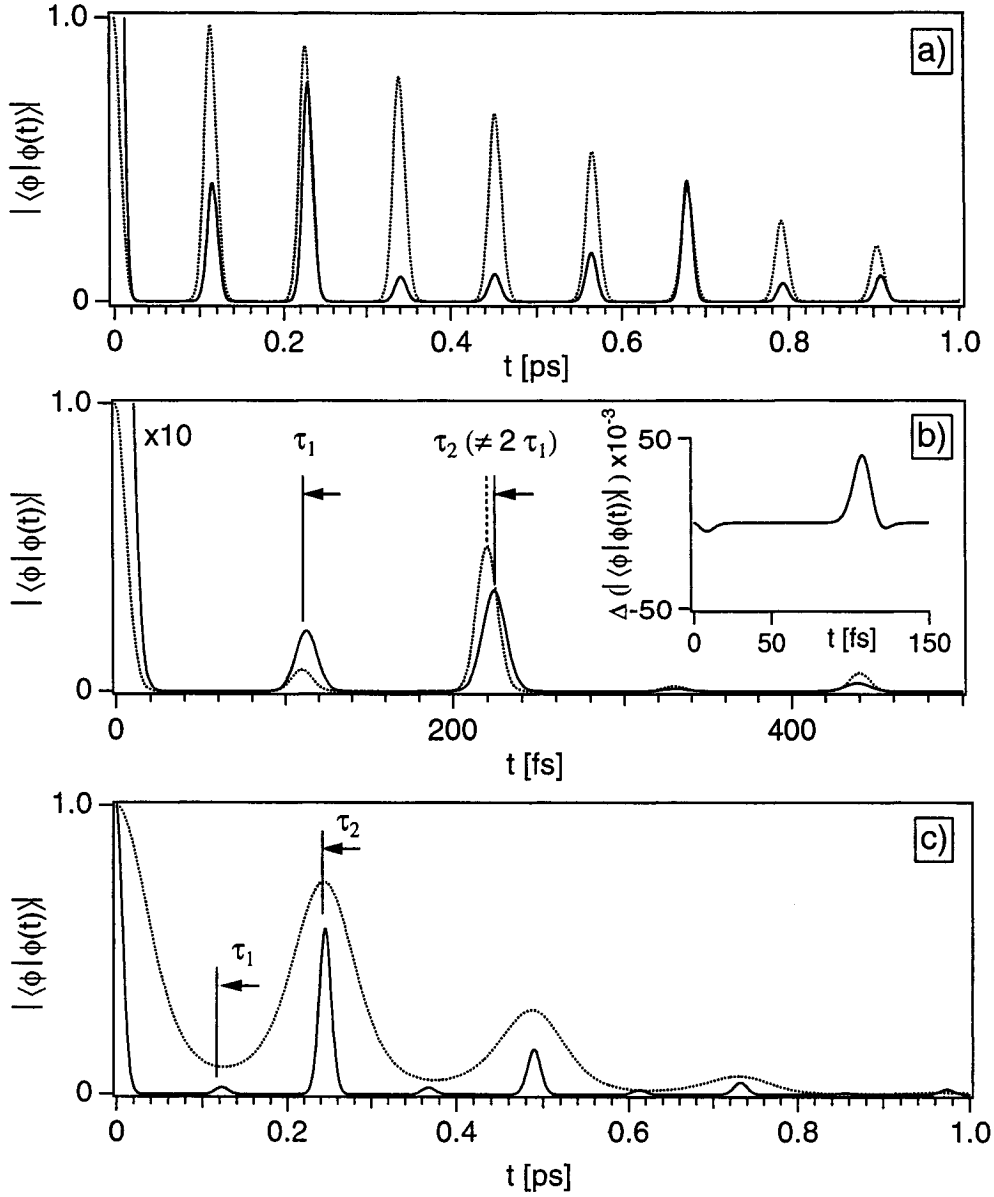

Figure 9.15. a) Absolute autocorrelation functions for **1**. Dotted trace: autocorrelation function for the 295 cm^{-1} mode (Γ = 10 cm^{-1}). Solid trace: total autocorrelation used to calculate the best-fit spectrum and enlarged by a factor of 10. b) Total autocorrelation functions for calculated spectra of **2**. Solid trace: total autocorrelation of the two vibronic origin best-fit spectrum enlarged by a factor of 5. Dashed trace: 2-mode total autocorrelation. The first two recurrence times are indicated (τ_1, τ_2) showing that $\tau_2 \neq 2\tau_1$. Inset: difference plot showing the mismatch in the second recurrence times for the total autocorrelation of the best-fit spectrum. c) Total autocorrelation functions for calculated spectra of **3**. Solid trace: total autocorrelation used in the high-resolution two-vibronic origin model calculated spectrum (Γ = 6 cm^{-1}). The dotted line is included as a guide for the eye to show the modulation of the overlap.

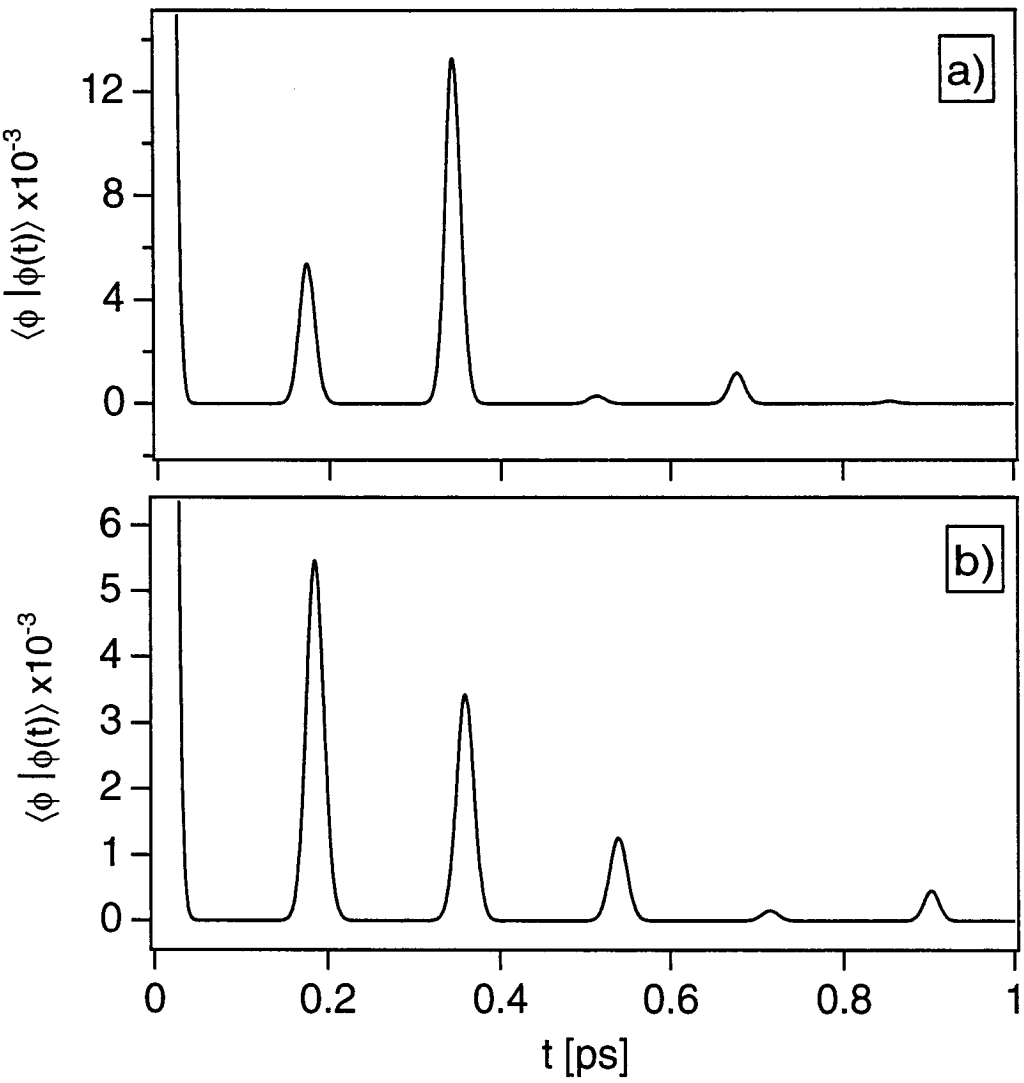

Figure 9.16. a) Absolute autocorrelation functions for **4** with a beat recurrence time of 340 fs. b) Absolute autocorrelation functions for **5** with a modulation of 900 fs, corresponding to a shorter beat frequency.

9.4.4 Temperature and pressure dependent luminescence decay behavior

Large displacements of the emitting state potential energy surface along multiple normal coordinates favor nonradiative decay mechanisms because the potential surfaces of the ground and excited states cross at energies close to the lowest vibrational level of the emitting state. At room temperature (ca. 300 K) efficient nonradiative relaxation processes lead to short luminescence lifetimes and weak luminescence intensities. This situation corresponds to the strong-coupling limit[46] of radiationless decay theory where the transition probability for nonradiative decay depends exponentially on the activation energy between the two states in the luminescence transition. One of the classical spectroscopic characteristics for the strong-coupling case is when the Stokes shifts are much larger than the largest accepting vibrational frequency, as observed for the title complexes in Figures 9.1-9.4 and summarized in Table 9.1. We use an analytical expression for the nonradiative rate constant, k_{NR}, derived by Englman and Jortner[46] to model the temperature-dependent luminescence decay behavior.

$$k_{NR} = \frac{C_{ij}^2 \sqrt{2\pi}}{\hbar \sqrt{E_m k_B T^*}} e^{\left(\frac{-E_A}{k_B T^*}\right)} \qquad \text{eq. 9.4}$$

C_{ij} is a pre-exponential frequency factor, k_B is the Boltzmann constant in cm^{-1}/ K, $\hbar$ is in units of $cm^{-1} \cdot s$,

$$k_B T^* = \frac{1}{2} \hbar \omega_{eff} \coth\left(\frac{\hbar \omega_{eff}}{2 k_B T}\right) \qquad \text{eq. 9.5}$$

and

$$E_A = \frac{(\Delta E - E_m)^2}{4E_m} \qquad \text{eq. 9.6}$$

where ΔE is the energy difference between the lowest vibrational levels of the ground and emitting states, (E_0) in Table 1, and E_m is half the Stokes shift,

$$E_m = \frac{1}{2}\sum_i^N \hbar\omega_{eff}\Delta_k^2 \cong \frac{1}{2}\hbar\omega_{eff}\Delta_{total}^2 \qquad \text{eq. 9.7}$$

The effective accepting mode, $\hbar\omega_{eff}$, is calculated as the weighted sum of all displaced metal-ligand vibrational frequencies (in cm^{-1}), listed in Table 9.3. Δ_{total} is the offset between the ground and excited state potential minima (dimensionless units) which is taken as the sum of all Δ_k used to calculate the spectra (Table 9.3). For the thiocyanate complexes (**2** and **3**) we use the average Δ_k values for progressions **I** and **II** then sum over these averaged offsets for Δ_{total}. Identical frequencies for the accepting mode in the ground and emitting states are assumed in the Englman-Jortner formalism provided that the energy difference between these states is sufficiently large. The only non-empirical parameter in eq. 9.4, C_{ij}, is assumed to be a constant and adjusted to obtain good fits with experimental decay rate data as a function of temperature. The observed luminescence decay rate constants are then modeled with eq. 9.4 assuming that the radiative rate constant, k_R, is equal to the observed rate at 5 K ($k_{NR} = 0$) and is invariant of temperature. The parameters used in the calculations are collected in Table 9.4. Figure 9.17 shows good agreement between the one-parameter fits with the observed temperature-dependent decay rate constants for complexes **2**-**5**. Some discrepancies arise between 150 to 200 K for complexes **2** and **4**, where the calculated rate constant increases faster than the experimental data for the former, and slower for the latter. However, experimental rates for both complexes show a rather sudden increase at 225 K and this large change may contribute to the difficulty of reproducing these trends in the data at higher temperatures. Because the title complexes undergo multiple and substantial distortions in the excited states, this simple one-dimensional model cannot fully account for all possible

contributions to the observed luminescence decay rate constants. This is most obvious in the large differences between individual values used for C_{ij} and due to the inherent difficulty of accurately estimating such coupling factors, we do not attempt to interpret these quantities. The most important aspect of this model is that reliable calculated decay rate constants can be obtained by using parameters determined directly from resolved experimental spectra and quantitative calculated luminescence spectra. The Englman-Jortner expression (eq. 9.4) is now used to rationalize the pressure-dependent luminescence decay behavior of complexes **2-5** in Figures 9.6-9.9.

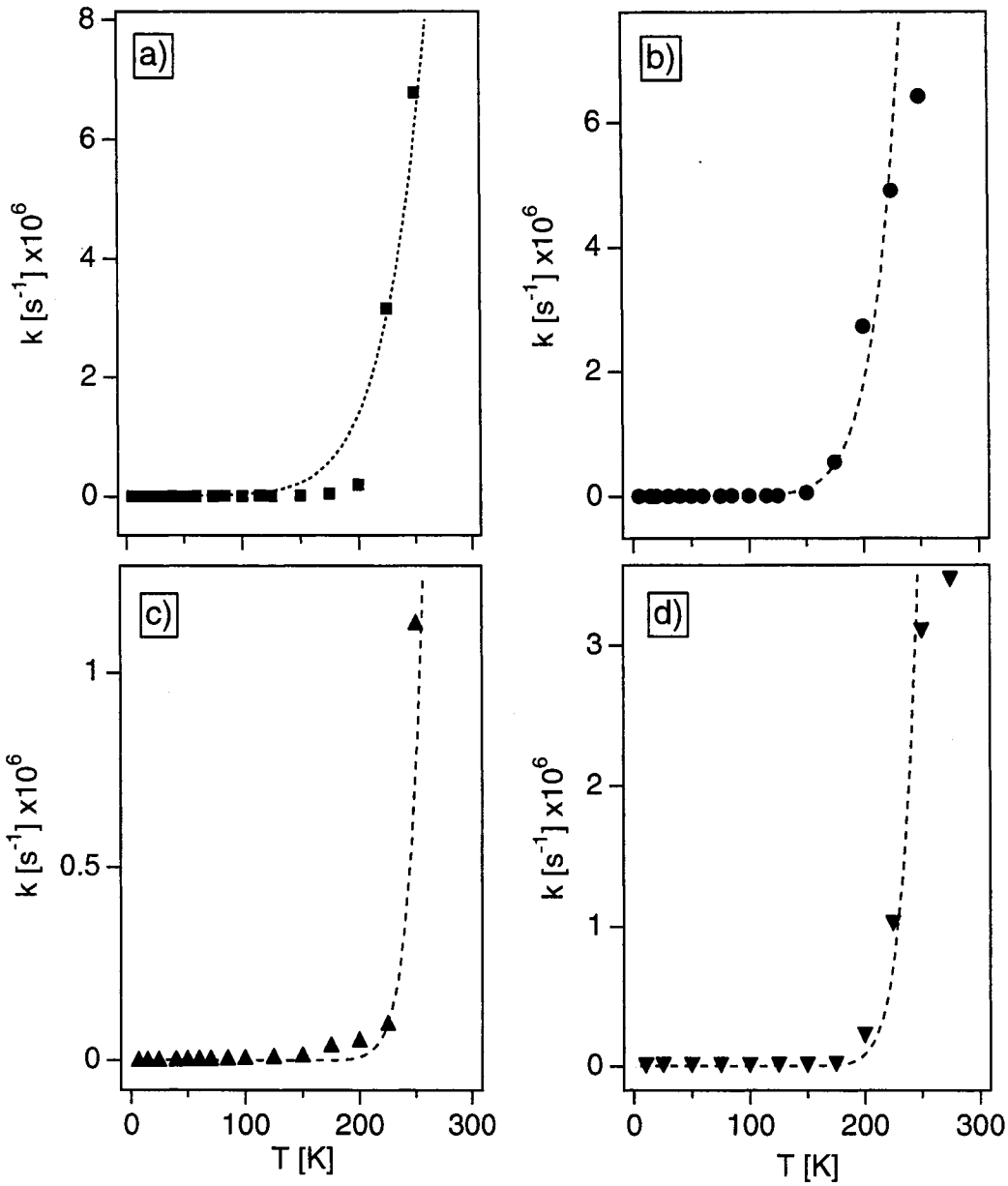

Figure 9.17. Experimental luminescence decay rate constants (solid symbols) with calculated fits using equation 9.4 (dashed lines) as a function of temperature. a) $[Pt(SCN)_4](n\text{-}Bu_4N)_2$ **2**. b) $[Pt(SeCN)_4](n\text{-}Bu_4N)_2$ **4**. c) $[Pd(SCN)_4](n\text{-}Bu_4N)_2$ **3**. d) $[Pd(SeCN)_4](n\text{-}Bu_4N)_2$ **5**.

9.4.5 Pressure dependent luminescence intensities and lifetimes

At room temperature and ambient pressure the luminescence spectra of the title complexes are very weak. The large pressure-induced enhancements of the luminescence intensities observed for the title complexes are unexpected and they can principally arise from both increasing radiative relaxation rate constants or decreasing nonradiative relaxation rate constants. The trends observed here are comparable to some organic chromophores that show enhancements of luminescence intensities and lifetimes with increasing pressure.[16] A possible contribution to the increase in intensity as a function of pressure may be caused by the removal of the center of inversion, thereby making the electronic transition more allowed in a non-centrosymmetric molecular geometry. The nature of the metal-ligand geometry and specific vibrational modes may also play an important role in this process. For example, by compressing the crystals the bending motions (b_{2g}) can gain "leverage" through intermolecular forces acting on the SCN^- and $SeCN^-$ ligands. This effect would enable the metal-centered luminescence transition to be tuned through these largely displaced, low frequency bending vibrations in the emitting state. To test the validity of this conjecture, we have measured the pressure dependent luminescence spectra of $K_2[PdBr_4]$, a compound that does not show a progression in the b_{2g} mode.[37] The room temperature luminescence of this compound is weak, similar to the title complexes and there was virtually no pressure-induced enhancement of the signal.

The luminescence lifetimes also exhibit a considerable increase from ambient pressure values as shown in Figure 9.8 and Table 9.2. If the pressure-induced changes in molecular structure removes the center of inversion around the metal ion, the luminescence transition becomes more allowed and the lifetime is expected to decrease as the radiative rate constant, k_R, increases. In contrast, the measured decay rate constant decreases significantly. The decrease of the rate constant by more than two orders of magnitude indicates therefore a very large decrease of the nonradiative rate constant, k_{NR}, with pressure. To better understand the trend in pressure dependent lifetimes, we apply the strong-coupling model discussed in the previous section to the pressure-dependent decay rates.

The model described by eq. 9.4 treats the title complexes as isolated molecules. At pressures greater than 30 kbar it is obvious that intermolecular effects are increasingly

important since the spectra show steady decreases in intensity due to quenching by efficient energy transfer to nonluminescent traps. This situation is not addressed by eq. 9.4 and we instead focus on the rise in luminescence intensities and lifetimes with pressure below 30 kbar. The most relevant pressure-dependent parameter in the strong-coupling model is the offset along the effective accepting mode, Δ_{total}. Figure 9.18a shows the effects of varying Δ_{total} on k_{NR} at a constant temperature of 300 K for complexes **2-5** to simulate the effect of pressure-induced decreases in normal coordinate offsets between the ground and emitting states. Figure 9.18b shows the surface generated by varying both temperature, T, and Δ_{total} for complex **3**.

From Figure 9.18a, it is clear that the variation of k_{NR} with Δ_{total} near the values of Δ_{total} used in the calculation of temperature dependent decay rate constants (indicated by the downward vertical arrows) is greater for the palladium(II) complexes **3** and **5** than for the platinum(II) complexes **2** and **4**, resulting in a larger decrease in k_{NR} for similar decreases in Δ_{total}. This result is consistent with the trends of the experimental pressure-dependent luminescence decay rate constants and intensities in Figures 9.6-9.9. The variations of k_{NR} calculated with eq. 9.4 are similar for complexes of the same metal ion, despite the very different C_{ij} values used for different ligands. The most important differences between the platinum(II) and palladium(II) complexes that influence the dependence of k_{NR} as a function of Δ_{total} are the vibrational frequencies, the offsets Δ_{total}, and the luminescence energies (ΔE in eq. 9.6). Each of these parameters alone is not sufficient to explain the pressure-induced luminescence effect. For example, a large value of Δ_{total} leads to a lower activation barrier for nonradiative relaxation than a small value of Δ_{total}, suggesting a large rate constant for identical $\hbar\omega_{eff}$ and luminescence energy. Figure 9.18a shows that the platinum(II) complexes have larger Δ_{total} values than their palladium(II) analogs, but their k_{NR} values are lower and vary less than those of the palladium(II) complexes. The observed variations are determined by all these parameters simultaneously. The lower vibrational frequencies of the palladium(II) complexes lead to wider potential energy surfaces and crossings at lower activation energy for identical Δ_{total} and luminescence energy, and their lower luminescence energies also lead to lower activation energy barriers, assuming identical Δ_{total} and $\hbar\omega_{eff}$ values. The influence of all

these parameters determines the slope of the surface shown for one compound (**3**) in Figure 15b and for three others (**2**,**4**, and **5**). An alternative, qualitatively appealing rationalization of the pressure effect on luminescence properties is given by the variation of the activation energy, defined in eq. 9.6 as the difference between the minimum of the emitting state potential energy curve and the crossing point of the ground- and emitting state potential curves given by the parameters in Table 9.4. For identical variations of Δ_{total}, a larger change of the activation energy is obtained for the palladium(II) complexes than for the platinum(II) complexes, confirming that the trends summarized in Figures 9.6-9.9. This comparison illustrates that the analysis of the pressure effects reported here does not depend on the mathematical formalism chosen to describe the nonradiative rate constants, but that their physical origin can be understood from the emitting state potential energy surfaces derived from the low temperature luminescence spectra.

Transitions between states with small Δ_k along metal-ligand vibrational modes, such as intraconfigurational d-d and some charge transfer transitions, are expected to show small changes in the pressure-dependent luminescence lifetimes at a constant temperature. For example, the pressure-dependent excited state decay kinetics for $[Ru(bpy)_3]Cl_2$ and $[Ru(phen)_3]Cl_2$, both metal-to-ligand charge transfer (MLCT) emitters, were successfully modeled using an expression in the weak-coupling limit of radiationless decay theory (energy gap law) and do not show large changes of k_{NR} with pressure. The increases in pressure dependent lifetimes of these systems are less than a factor of two,[18,19] much smaller than those reported here. It is also expected that the role of the b_{2g} bending mode in the pressure-induced enhancements of luminescence intensities and lifetimes is important given the large displacements that occur along this mode in the emitting state. Figure 9.18b also shows that at lower temperatures the values of k_{NR} decrease significantly and vary much less with Δ_{total} than at room temperature. We therefore expect smaller changes of luminescence intensity at low temperatures, which might explain why $K_2[Pt(SCN)_4]$ does not appear to show an enhancement of luminescence intensity with increasing pressure at 100 K. By using eq. 9.4 and varying Δ_{total} to simulate the effect of pressure, it is also possible to explain the pressure-induced blue shifts of all luminescence band maxima. A significant decrease in Δ_{total} can lead to a significant blue shift of the band maxima without any change in the energy of the

potential minimum since the more nested emitting state surface would shift vibronic intensities toward higher energy. We suspect that energy differences between potential energy minima (electronic origins) do not change with pressure because they are similar for thiocyanate and selenocyanate complexes of the same metal ion, a much larger "spectrochemical change" than the shifts induced by the pressures used here.

parameter	$[Pt(SCN)_4]$ $(n\text{-}Bu_4N)_2$ (**2**)	$[Pd(SCN)_4]$ $(n\text{-}Bu_4N)_2$ (**3**)	$[Pt(SeCN)_4]$ $(n\text{-}Bu_4N)_2$ (**4**)	$[Pd(SeCN)_4]$ $(n\text{-}Bu_4N)_2$ (**5**)
ΔE (cm^{-1})[a]	16806	14343	16330	14445
C_{ij} (cm^{-1})	18	85	2700	1400
Δ_{total}	8.25	7.66	8.96	8.74
$\hbar\omega_{eff}$ (cm^{-1})[b]	251	220	155	146

[a] line 2 (E_0) in Table 9.1. [b] The contribution to $\hbar\omega_{eff}$ from each displaced mode is weighted by the individual offsets in Table 9.3.

Table 9.4. Parameters used in the calculation of the nonradiative rate constant within the strong-coupling model in eq. 9.4.

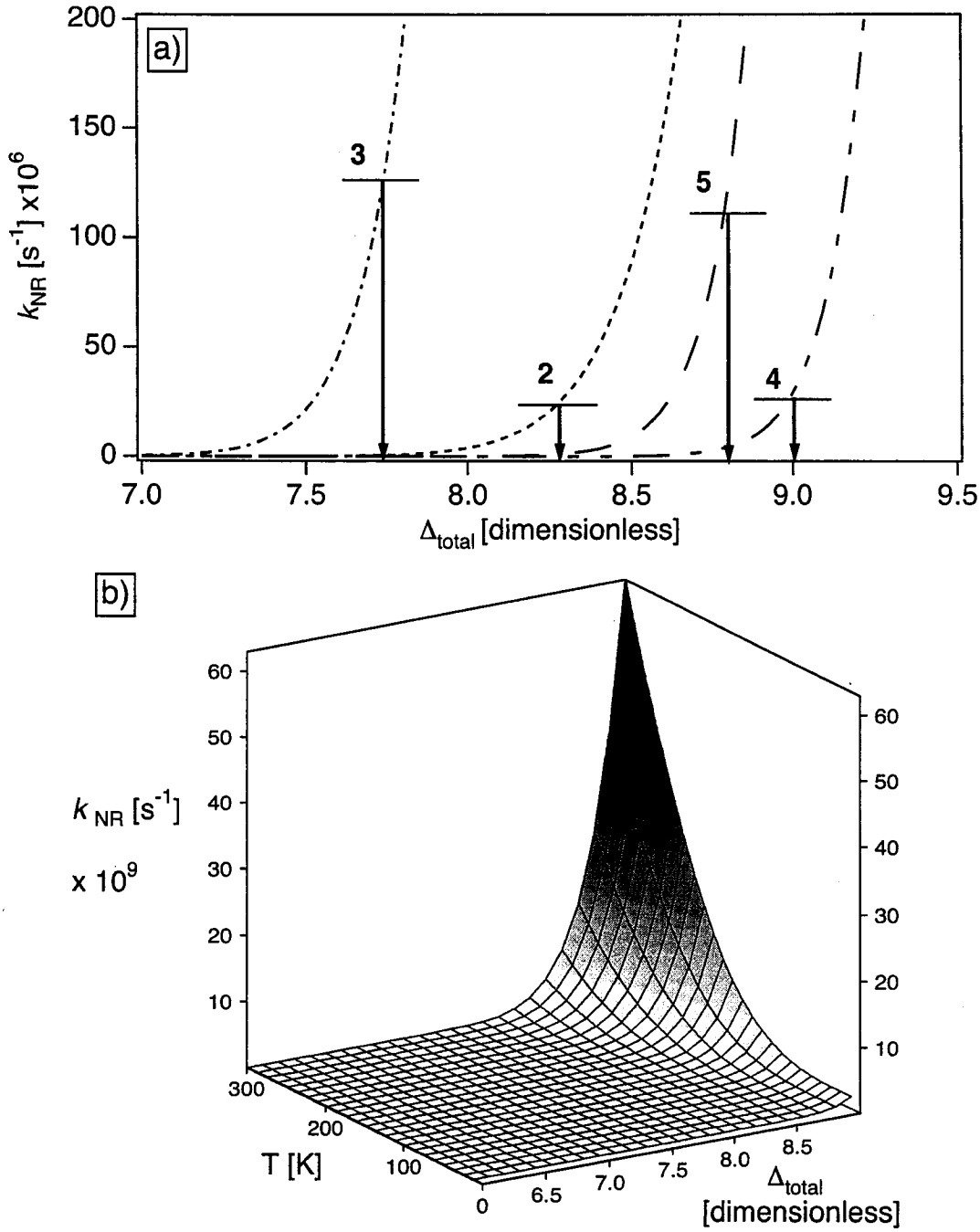

Figure 9.18. a) Calculated nonradiative rate constants (k_{NR}) as a function of the normal coordinate offset (Δ_{total}) along the $\hbar\omega_{eff}$ at 300 K. The downward arrows indicate the value of Δ_{total} used for the calculation of temperature dependent rate constants in Table 9.4. b) k_{NR} calculated as a function of temperature, T, and emitting state offset, Δ_{total}, along the effective mode, $\hbar\omega_{eff}$, of complex **3**.

9.5 Conclusions

The temperature- and pressure dependent spectroscopic results show large variations from ambient conditions. Analysis of the vibronic structure in the low temperature luminescence spectra shows that the largest displacements occur along the totally symmetric (a_{1g}) metal-ligand stretching vibration. Significant distortions in the b_{2g} bending modes occur in all complexes and the pressure effects on luminescence properties are most likely dependent on the pressure-induced displacement of this mode. The strong-coupling model can be used to rationalize the temperature and pressure dependence of the nonradiative decay rate constant using physically meaningful parameters determined from spectroscopic experiments.

References

(1) (a) Cummings, S. D.; Eisenberg, R. *J. Am. Chem. Soc.* **1996**, *118*, 1949. (b) Zuleta, J.A.; Bevilacqua, J.M.; Eisenberg, R. *Coord. Chem. Rev.* **1991**, *111*, 237.

(2) Gliemann, G.; Yersin, H. *Struct. Bond.* **1985**, *62*, 87.

(3) Martin, D. S. *Inorg. Chim. Acta Rev.* **1971**, *5*, 107.

(4) (a) Connick, W. B.; Henling, L. M.; Marsh, E. M.; Gray, H. B. *Inorg. Chem.* **1996**, *35*, 6261. (b) Yang, F.; Fanwick, P.E.; Kubiak, C.P. *Inorg. Chem.* **2002**, *41*, 4805.

(5) Barigelletti, F.; Sandrini, D.; Maestri, M.; Balzani, V.; von Zelewsky, A.; Chassot, L.; Jolliet, P.; Maeder, U. *Inorg. Chem.* **1988**, *27*, 3644.

(6) Aldridge, T. K.; Stacy, E. M.; McMillin, D. R. *Inorg. Chem.* **1994**, *33*, 722.

(7) Yersin, H.; Trümbach, D.; Wiedenhofer, H. *Inorg. Chem.* **1999**, *38*, 1411.

(8) Ferraro, J. R. *J. Chem. Phys.* **1970**, *53*, 117.

(9) Bray, K. L.; Drickamer, H. G.; Schmitt, E. A.; Hendrickson, D. N. *J. Am. Chem. Soc.* **1989**, *111*, 2849.

(10) Bray, K. L., Drickamer, H.G. *J. Phys. Chem.* **1990**, *94*, 2154-2159.

(11) Bray, K. L.; Drickamer, H. G. *J. Phys. Chem.* **1991**, *95*, 559.

(12) Gutierrez, R. E.; Rodriguez, F.; Moreno, M.; Alcala, R. *Radn. Eff. Def. Sol.* **2001**, *154*, 287.

(13) Wenger, O. S.; Valiente, R.; Güdel, H. U. *J. Chem. Phys.* **2001**, *115*, 3819.

(14) Wenger, O. S. G., H. U. *Chem. Phys. Lett.* **2002**, *354*, 75-81.

(15) Willett, R. D.; Haugen, J. A.; Lebsack, J.; Morrey, J. *Inorg. Chem.* **1974**, *13*, 2510.

(16) Dreger, Z. A.; Lang, J. M.; Drickamer, H. G. *J. Phys. Chem.* **1996**, *100*, 4646.

(17) Bloomquist, D. R.; Willett, R. D. *Coord. Chem. Rev.* **1982**, *47*, 125.

(18) Fetterolf, M. L.; Offen, J. *J. Phys. Chem.* **1985**, *89*, 3320.

(19) Fetterolf, M. L.; Offen, J. *J. Phys. Chem.* **1986**, *90*, 1828.

(20) Fetterolf, M. L.; Offen, J. *Inorg. Chem.* **1987**, *26*, 1070.

(21) Yersin, H.; Gallhuber, E. *Inorg. Chem.* **1984**, *23*, 3745.

(22) Grey, J. K.; Triest, M.; Butler, I. S.; Reber, C. *J. Phys. Chem. A* **2001**, *105*, 6269.

(23) Grey, J. K.; Butler, I. S.; Reber, C. *J. Am. Chem. Soc.* **2002**, *124*, 11699.

(24) Gütlich, P.; Hauser, A.; Spiering, H. *Angew. Chem. Intl. Ed. Engl.* **1994**, *33*, 2024.

(25) Grey, J. K.; Marguerit, M.; Butler, I. S.; Reber, C. *Chem. Phys. Lett.* **2002**, *366*, 361.

(26) Turco, A.; Pecile, C. *Nature* **1961**, *191*, 66.

(27) Pearson, R. G. *J. Am. Chem. Soc.* **1963**, *85*, 3533.

(28) Pearson, R. G. *Science* **1966**, *151*, 172.

(29) (a) Bertini, I.; Sabatini, A. *Inorg. Chem.* **1966**, *5*, 1025. (b) Meek, D.W.; Nicpon, P.E.; Imhof-Meek, V. *J. Am. Chem. Soc.* **1970**, *92*, 5351. (c) Coyer, M.J.; Herber, R.H.; Chen, J.; Croft, M.; Szu, S.P. *Inorg. Chem.* **1994**, *33*, 716.

(30) Burmeister, J. L.; Basolo, F. *Inorg. Chem.* **1964**, *3*, 1587.

(31) Rohde, J.-U.; von Malottki, B.; Preetz, W. *Z. Anorg. Allg. Chem.* **2000**, *626*, 905.

(32) Pelletier, Y.; Reber, C. *Inorg. Chem.* **2000**, *39*, 4535.

(33) Basch, H.; Gray, H. B. *Inorg. Chem.* **1967**, *6*, 365.

(34) Vanquickenborne, L. G.; Ceulemans, A. *Inorg. Chem.* **1981**, *20*, 796.

(35) Harvey, P. D.; Reber, C. *Can. J. Chem.* **1999**, *77*, 16.

(36) Tuszynski, W.; Gliemann, G. *Z. Naturforsch.* **1979**, *34a*, 211.

(37) Pelletier, Y.; Reber, C. *Inorg. Chem.* **1997**, *36*, 721.

(38) The lowest energy spin-orbit state is A_{1g} (^3E_g) determined from ligand-field calculations.

(39) Preston, D. M.; Güntner, W.; Lechner, A.; Gliemann, G.; Zink, J. I. *J. Am. Chem. Soc.* **1988**, *110*, 5628.

(40) Grey, J. K.; Butler, I. S.; Reber, C. *J. Am. Chem. Soc.* **2002**, *124*, 9384.

(41) Bray, K. L. *Top. Curr. Chem.* **2001**, *213*, 1.

(42) Masson, S.; Triest, M.; Grey, J. K.; Reber, C. *Phys. Chem. Comm.* **2000**, 12.

(43) Heller, E. J. *J. Chem. Phys.* **1975**, *62*, 1544.

(44) Heller, E. J. *Acc. Chem. Res.* **1981**, *14*, 368.

(45) Zink, J. I.; Kim Shin, K.-S. In *Adv. Photochem.*; Volman, D. H., Hammond, G. S., Neckers, D. C., Eds.; John Wiley: New York, 1991; Vol. 16, p 119.

(46) Englman, R.; Jortner, J. *Mol. Phys.* **1970**, *18*, 145.

(47) Burmeister, J. L.; Al-Janabi, M. Y. *Inorg. Chem.* **1965**, *4*, 962.

(48) Burmeister, J. L.; Williams, L. E. *Inorg. Chem.* **1966**, *5*, 1113.

(49) Forster, D.; Goodgame, M. L. *Inorg. Chem.* **1965**, *4*, 1712.

(50) Davis, M. J.; Reber, C. *Inorg. Chem.* **1995**, *34*, 4585.

(51) Piermarini, G. J., Block, S., Barnett, J.D., Forman, R.A. *J. Appl. Phys.* **1975**, *46*, 2774.

(52) Solution absorption spectra of all complexes have similar spectral profiles consisting of a weak, lowest energy band with a molar absorptivity on the order of 10 M^{-1} cm^{-1} with overlapping, more intense ($\varepsilon > 100$ M^{-1} cm^{-1}) transitions with maxima ca. 2500 cm^{-1} higher in energy. At approximately 340 nm (29000 cm^{-1}), there is an intense ($\varepsilon \approx 103$ M^{-1} cm^{-1}) and sharp absorption band observed for all complexes studied.

(53) Güntner, W.; Gliemann, G.; Kunkely, H.; Reber, C.; Zink, J. I. *Inorg. Chem.* **1990**, *29*, 5238.

(54) Jørgensen, C. K.; Pergamon Press: London, 1962, p p. 109.

(55) Similar studies were performed on complex **1**. The overall pressure effect was similar to that of complex **2**.

(56) Blue-shifts in the pressure-dependent luminescence band maximum where determined by fitting a Gaussian function to the spectrum using least squares methods.

(57) Lechner, A.; Gliemann, G. *J. Am. Chem. Soc.* **1989**, *111*, 7469.

(58) Houlding, V. H.; Miskowski, V. M. *Coord. Chem. Rev.* **1991**, *111*, 145.

(59) Hidvegi, I.; Tuszynski, W.; Gliemann, G. *Chem. Phys. Lett.* **1981**, *77*, 517.

(60) Sturge, M. D. *Sol. State Phys.* **1967**, *20*, 91.

(61) The experimental frequencies (Ref. 31) of the a_{2u} and the two e_u modes, $e_u(1):e_u(2)$, for the title complexes are as follows (in cm^{-1}): 142 and 169, 287 (**1**,**2**); 140 and 165, 293 (**3**); not observed and 127,132: 221, 236 (**4**); 96 and 121,128: 242, 259 (**5**), respectively.

(62) Hollingsworth, G. J.; Shin, K.-S. K.; Zink, J. I. *Inorg. Chem.* **1990**, *29*, 2501.

(63) Ballhausen, C. J. *Theor. Chim. Acta* **1965**, *3*, 368.

Chapter 10

Conclusions, Contributions to Original Knowledge, and Ideas for Future Work.

10.1 Conclusions and contributions to original knowledge

This work has demonstrated the utility of variable temperature and pressure spectroscopic techniques on characterizing the interplay between structure and electronic properties in molecular chromophores. Second- and third-row transition metal complexes are excellent model systems for these studies due to their rich optical properties and the ability to tune these properties with only minor changes in molecular geometry. The large structural distortions experienced upon absorption or emission of a photon lead to broad optical bands, which offer a unique insight into how an external perturbation can affect both the ground and excited state properties of the molecule.

The pressure dependent Raman spectra of rhenium(V) and osmium(VI) oxo and nitrido complexes possessing metal-ligand double and triple bonds are presented in Chapter 3. This work established trends in the ability to tune the molecular geometries that can be correlated to the luminescence properties. It was found that the shift of metal-oxo frequencies depended on the nature of the ancillary ligand. Namely, complexes with ancillary ligands having significant overlap with metal d_{xz}, d_{yz} orbitals (π^*) led to stronger blue-shifts of the metal-oxo frequencies than for complexes with ligands with little or no π overlap, which shows quantitatively that these ancillary ligands 'compete' with the oxo ligands for π electron density thus removing double bond character from the metal-oxo unit. Because it is easier to compress metal-ligand single bonds than double bonds, a systematic study of various ligand systems has allowed for a detailed comparison of bonding properties between related complexes. This observation is important for interpreting the influence of the ancillary ligands on the luminescence properties of these and related complexes since the energy separation, Δ_π, depends explicitly on the overlap between the metal and ligand orbitals. Furthermore, this technique shows promise as an effective probe for uncovering the elusive d^2 spin crossover problem where a significant

pressure-induced decrease of luminescence energies in near-infrared emitters could possibly trap the molecule into a triplet ground state due to the unpairing of the two electrons.

Chapters 4—6 show that models originally developed to reproduce vibronic patterns in low temperature luminescence spectra can be quantitatively adapted to room temperature pressure-dependent spectra when there is sufficient resolved vibronic structure. This represents the first time in which it is possible to determine how important spectroscopic parameters depend on small structural changes in the molecule. Accompanying Raman measurements provide information on the geometry of the complex that reflect the influence of intermolecular forces on this intramolecular property. The essential link between both temperature- and pressure-dependent models is the normal coordinate offset parameter ΔQ, which dictates band widths and intensity distributions of resolved vibronic progressions. In the *trans*-dioxo rhenium(V) complexes studied in Chapters 4—6, room temperature luminescence spectra exhibit resolved structure in the high frequency O=Re=O stretching mode that enables a quantitative analysis of the emitting state distortions as a function of pressure. These measurements and analyses provide a new insight into how the parameters describing the ground and emitting state potential energy surfaces change with varying molecular geometry.

Chapter 4 has shown that an effective coordinate model can be used to determine pressure-dependent emitting state displacements in room-temperature luminescence spectra of the *trans*-$[ReO_2(pyridine)_4]^+$ complex. Low temperature luminescence spectra were successfully modeled using two-dimensional harmonic potential energy surfaces displaced along the totally symmetric O=Re=O and Re-N(py) stretching modes. It was demonstrated that this model could be adapted to room temperature, pressure-dependent spectra where only one vibronic progression was resolved. By calculating luminescence spectra at different pressures, it was possible to correlate the trends in empirical quantities and calculated spectroscopic parameters to changes in bonding properties between the metal and oxo/pyridine ligands. The large pressure-induced red-shift of the luminescence band could be attributed to both increased covalency (i.e., a decrease in interelectronic

repulsion energies) and reduction in the HOMO-LUMO energy caused by an increased π-contribution from the pyridine ligand.

In Chapters 5 and 6, luminescence spectra of substituted ethylenediamine *trans*-dioxo rhenium(V) complexes exhibited anharmonic band shapes that changed as a function of pressure. This anharmonicity was due to interactions between electronic states of the same symmetry, which varied according to the energy separation between interacting states and could be tuned by changing the substituent groups on the ethylenediamine ligand. These seemingly small structural changes to the ligands resulted in markedly different luminescence band shapes and energies for structurally similar complexes. Resolved vibronic structure in the high frequency O=Re=O stretching mode enabled the use of a coupled electronic states model. It provided a window through which it is possible to extract how these interactions change through pressure-dependent luminescence spectra. This work has shown for the first time that it is possible to study how interactions between states change with molecular geometry through analysis of resolved band shapes.

Luminescence spectra of *trans*-dioxo metal complexes are formally transitions between metal-centered electronic states and are expected to have vibronic progressions in the metal-ligand symmetric stretching modes only. The temperature–dependent luminescence spectra of the *trans*-$[OsO_2(NCS)_4]^{2-}$ complex reported in Chapter 7 show emitting state displacements in a symmetric ligand-centered CS stretching mode, approximately 30 cm^{-1} lower in frequency than the high frequency O=Os=O mode. This leads to a resolved high frequency interval that does not exactly match either the CS or O=Os=O frequencies, which is a result similar to the missing mode effect (MIME). Detailed analysis of low temperature luminescence spectra of three salts of this complex showed that the normal coordinate offset along the CS mode was also related to the offset along the Os—N mode. These results are very important for this class of complexes considering the current interest in their synthetic applications.

Typically, d—d luminescence transitions are very weak with little or no resolved vibronic structure, even at low temperature. Temperature- and pressure-dependent luminescence spectra of square-planar platinum(II) and palladium(II) complexes show remarkable variation over the range of these parameters reported in Chapters 8 and 9.

Low temperature luminescence spectra showed highly resolved vibronic structure including progressions in non-totally symmetric Jahn-Teller-active modes that allowed for a detailed analysis of the emitting state geometries. Pressure-dependent luminescence intensities and lifetimes showed large and unexpected increases, which could be rationalized using a model for the nonradiative rate constant, k_{NR}, that depended on the emitting state offset along a single effective vibrational mode. Using parameters determined from temperature-dependent studies, this model was adapted to the variable pressure data where the effective offset could be varied to reproduce the experimental pressure-dependent luminescence properties.

The ability to characterize the interplay between structure and electronic properties in molecular chromophores is often a difficult task. When the electronic structures have been fully characterized, the application of an external pressure has proven to be a valuable means to determine how energies of electronic states vary as a function of molecular geometry through changes in the environment of the complex. This is facilitated by resolved vibronic structure in optical spectra that provides a window through which the ground and excited state geometries can be determined. Most pressure-dependent spectra reported in the literature have no resolved structure, which makes a detailed quantitative analysis virtually impossible. Until now, the methods of analysis used in this thesis have not been possible due to limitations of both experimental and theoretical techniques.

The systematic studies on structurally related complexes presented in the main body of this thesis has also uncovered interesting trends in the response of a luminescent solid as a function of an applied pressure. In both d^2 and d^8 tetragonal systems, it was determined that the largest variations in luminescence properties always occurs with lower energy emitting complexes. The physical picture that emerges from this trend can be rationalized using simple PES diagrams for both the ground and emitting states. Depending on luminescence energies ($\sim E_{max}$) and normal coordinate offsets (ΔQ) the proximity of crossing point to the Franck-Condon can have a large influence on luminescence band shapes and emitting state relaxation dynamics. As pressure increases, the ΔQ decrease causing the minimum of the emitting state PES to shift toward the ground state equilibrium value at $Q = 0$. In systems with significant interactions between

states, such as the *trans*-dioxo rhenium(V) complexes with substituted ethylenediamine ligands in Chapter 6, an avoided crossing is produced which can change in position with applied pressure. As $\Delta Q_{Re=O}$ decreased, the avoided crossing was pushed to higher energy and at larger (positive) values along the $Q_{Re=O}$ coordinate, further away from the Franck-Condon region. This caused the higher pressure spectra to appear more harmonic in character and was most apparent in the lowest energy emitting $ReO_2(en)_2Cl$ complex. In the square-planar platinum(II) and palladium(II0 complexes, the large enhancement in luminescence intensities and lifetimes were also shown to depend on the luminescence energy. The largest enhancement occurred for the lower energy emitting palladium(II) complexes where the ground and emitting state PESs crossed relatively close to the minimum of the emitting state PES. The pressure-induced decrease of all normal coordinate offsets cause the activation energy barrier for a nonradiative transition to increase, thus leading to an exponential decrease of k_{NR}. Based on these trends established for two fundamentally different systems, it is therefore expected that lower energy (i.e., NIR) emitting molecules will show the largest change with an applied perturbation.

10.2 Ideas for future work

i) Enhancement of luminescence properties of metal complexes with applied external pressure is unexpected due to efficient nonradiative deactivation of the emitting state at room temperature. Doping square-planar thiocyanate or selenocyanate complexes into host matrices may provide additional insight into the mechanisms responsible for this effect. For example, the unit cell volume of $[Pd(SCN)_4](n\text{-}Bu_4N)_2$ is ca. 50 $Å^3$ smaller than that of $[Pt(SCN)_4](n\text{-}Bu_4N)_2$, thus a mixed crystal system of $[Pt_xPd_{1-x}(SCN)_4](n\text{-}Bu_4N)_2$ could be used as a means to apply a chemical pressure to the Pt(II) metal center and possibly achieve the same effect as with an externally applied pressure.

ii) The effect of ligand structure and electronic properties on complexes of platinum(II) and palladium(II) should also be investigated with the goal of enhancing luminescence intensity. Preliminary work was performed using the 1-

pyrroleidinecarbodithioate ligand that clamps to the metal center in a bidentate fashion through the two sulfur atoms. A similar ligand system could be employed where the five-member heterocycle ring is aromatic, which could lead to different bonding properties to the metal center and ultimately to different electronic properties of the entire complex. The pressure-dependent luminescence spectra of these bidentate complexes will allow a comparison to the previous studies involving monodentate ligands.

iii) Interactions between electronic states can have a large influence on both photophysical and photochemical properties of a molecular chromophore. In *trans*-dioxo rhenium(V) complexes, there are three A_{1g} states that can interact both through spin-orbit coupling and configuration interactions. The highest energy A_{1g} state has not been observed spectroscopically because it is masked by more intense charge transfer transitions. However, two-photon spectroscopy could be used that, in the different selection rules, should permit a study of this elusive state and determine its actual role in the photophysical properties.

iv) Gold(I) complexes often show strong interactions between metal centers that lead to the formation of oligomers and linear arrays that possess unique optical properties. Recent work from the Eisenberg group at the University of Rochester reported a tribochromic gold(I) system that became strongly emissive after gentle grinding.[1] Application of external pressure on this complex showed evidence for a similar effect, but it was not possible to study the entire band due to instrument limitations. Further measurements with UV excitation would reveal how the luminescence properties vary with an applied external pressure and Raman spectra would also provide an insight changes in the structure or geometry of the complexes.

References

1) Lee, Y-A; Eisenberg, R. *J. Am. Chem. Soc.* **2003**, *125*, 7778.

Appendix 1

Scientific articles published

10) J.K. Grey, I.S. Butler, C. Reber, *Emitting-state displacements in ligand-centered vibrational modes in the trans-*$[OsO_2(NCS)_4]^{2-}$ *complex determined from near-infrared luminescence spectroscopy.*
Submitted Feb. 8, 2004.

9) J.K. Grey, I.S. Butler, C. Reber, *Temperature- and pressure-dependent luminescence spectroscopy on the trans-*$[ReO_2(pyridine)_4]^+$ *complex: Analysis of vibronic structure, luminescence energies, and bonding characteristics.*
Can. J. Chem. (Gerhard Herzberg memorial issue) accepted Dec. 11, 2003.

8) J.K. Grey, I.S. Butler, C. Reber, *Pressure-induced enhancements of luminescence intensities and lifetimes correlated with emitting state distortions in thiocyanate and selenocyanate complexes of platinum*(II) *and palladium*(II).
Inorg. Chem., 42 (2003) 6503-6518.

7) Y. Cohen, B. Hatton, H. Miguez, N. Coombs, S. Fourner-Bidoz, J.K. Grey, R. Beaulac, C. Reber, G.A. Ozin, *Spin-on nanostructured silicon-silica film displaying room temperature nanosecond lifetime photoluminescence.*
Adv. Mater., 15 (2003) 572-576.

6) J.K. Grey, M. Marguerit, I.S. Butler, C. Reber, *Pressure-dependent Raman spectroscopy of metal-oxo multiple bonds in rhenium*(V) *and osmium*(VI) *complexes.*
Chem. Phys. Lett., 366 (2002) 361-367.

5) J.K. Grey, I.S. Butler, C. Reber, *Effect of pressure on coupled electronic ground and excited states from luminescence spectra of trans-dioxo rhenium*(V) *complexes.*
J. Am. Chem. Soc., 124 (2002) 11699-11708.

4) J.K. Grey, I.S. Butler, C. Reber, *Large pressure-induced increase in luminescence intensity for the* $[Pd(SCN)_4]^{2-}$ *complex.*
J. Am. Chem. Soc., 124 (2002) 9384-9385.

3) J.K. Grey, I.S. Butler, *Effect of high external pressures on the electronic spectra of coordination compounds.*
Coord. Chem. Rev., 219-221 (2001) 713-759.

2) J.K. Grey, M. Triest, I.S. Butler, C. Reber, *Effect of pressure on the vibronic luminescence spectrum of a trans-dioxo rhenium*(V) *complex.*
J. Phys. Chem. A, 105 (2001) 6269-6972.

1) M. Triest, S. Masson, J.K. Grey, C. Reber, *Vibronic structure in the luminescence spectra of tetragonal d^2 and d^8 complexes analyzed by wavepacket dynamics on two-dimensional potential surfaces.*
Phys. Chem. Comm. (2000) article 12, 64-70.

Conference presentations (refereed and non-refereed)

11) J.K. Grey, I.S. Butler, C. Reber, *Large variations in luminescence intensities and decay behavior of platinum*(II) *and palladium*(II) *thiocyanate and selenocyanate complexes.* 225th American Chemical Society national meeting, New Orleans, LA, March 2003.

10) J.K. Grey, I.S. Butler, C. Reber, *Physical methods for probing the electronic structures of d^2 and d^8 transition metal complexes.* 225th American Chemical Society National Meeting, New Orleans, LA, March 2003.

9) J.K. Grey, *Large variations in luminescence properties of platinum*(II) *and palladium*(II) *thiocyanate and selenocyanate complexes.* Departmental seminar, Département de Chimie, Université de Montréal, February 28, 2003.

8) J.K. Grey, I.S. Butler, C. Reber, *Large variations in luminescence properties of platinum*(II) *and palladium*(II) *thiocyanate and selenocyanate complexes.* 35th Inorganic Discussion Weekend, Université de Montréal, Montreal, Québec, October 2002.

7) J.K. Grey, I.S. Butler, C. Reber, *Temperature- and pressure-dependent vibronic luminescence in platinum*(II) *and palladium*(II) *thiocyanate and selenocyanate complexes.* 85th Canadian Society of Chemistry Conference, Vancouver, British Columbia, June 2002.

6) J.K. Grey, I.S. Butler, C. Reber, *Molecular electronic spectroscopy oftransition metal, d^2 and d^8, thiocyanate complexes: Temperature and pressure-dependent vibronic features.* 85th Canadian Society of Chemistry Conference, Vancouver, British Columbia, June 2002.

5) J.K. Grey, I.S. Butler, C. Reber, *Temperature and pressure-dependent luminescence in of platinum*(II) *and palladium*(II) *thiocyanate and selenocyante complexes.* 48th International Conference of Analytical Sciences and Spectroscopy (ICASS), Toronto, Ontario, May 2002.

4) J.K. Grey, I.S. Butler, C. Reber, *Electronic spectroscopy of d^2 and d^8 transition metal complexes: Temperature- and pressure-dependent vibronic features.* 13th annual Inter-American Photochemical Society Conference, Tempe, AZ, January 2002.

3) J.K. Grey, I.S. Butler, C. Reber, *Electronic spectroscopy of d^2 and d^8 transition metal complexes: Unusual temperature- and pressure-dependent vibronic features.* 7th Symposium Annuel de Chimie Inorganique du Québec (SACIQ), Lennoxville, Quebec, August 2001.

2) J.K. Grey, I.S. Butler, C. Reber, *Effect of high-pressures on metal-ligand single and double bonds: Luminescence spectra of trans-dioxo complexes of rhenium*(V). 84th Canadian Society of Chemistry Conference, Montreal, Quebec, May 2001.

1) J.K. Grey, I.S. Butler, C. Reber, *Effect of high-pressures on the luminescence spectra of trans-dioxo complexes of rhenium*(V). 33rd Inorganic Discussion Weekend, York University, Toronto, Ontario, October 2000.

Scholarships and awards

Student travel award, 225th ACS national meeting, Division of Inorganic Chemistry, 2003
Robert Zamboni prize (travel award), McGill University, 2003
Udho, Parsini, Diwan award (best graduate research paper), McGill University, 2002
Natural Sciences and Engineering Research Council (Canada) scholarship, 2002-2004
Fonds de Recherche sur la nature et les technologies (Québec) scholarship, 2002
Student travel award, 13th annual I-APS conference, Arizona State University, 2002
Third prize, oral presentation 33rd Inorganic Discussion Weekend, York University, 2000

Appendix 2

Input file for calculating luminescence spectra using harmonic potentials (EMISS)

Time max [sec] = 5.00000e-13
Gamma [cm-1] = 50.0
Number of Time steps = 2000

Spectrum Limits
Low [cm-1] = 8500.000000
Hi [cm-1] = 13500.000000

Number of Points = 2000

Number of normal mode = 3

mode 1 freq = 858.000 S = 4.0
mode 2 freq = 885.000 S = 2.0
mode 3 freq = 255.000 S = 3.0

Electronic origin [cm-1] = 12990.000000
Do you want overlap [y/n] = Y
Do you want absolute or complex overlap [a/c] = A

spectrum= spc
overlap= olp
info= info

Input file for calculating spectra with two coupled potentials (MIRO)

```
'Miro  (2-surface 1-dim. propagation)'
'b2g MXCN4'
1.D-12,'totaltime'
1000,'number of timesteps'
1,'steps between correlation'
1,10,'# of plots and time of plots'
-0.6,'xstart'
1.0,'xend'
1024,'ngrid'
1.,'nstart (1,2,3=on both)'
1.,1.,'transition moments for diabatic states'
t,0.2,0.0,140.,'gaussian initial wavepacket, position, momentum,vib.energy'
f,-10.25,0.2209,-5.,0,'morse initial wavepacket NOT TESTED!!'
16.0,'mass of mode'
f,'single','plotfiles'
t,'b2gpotl','potentialfiles'
f,'mvwave','wavefunction'
f,'BNGaus','initial wavepacket from file'
f,'swap parts of initial wavepacket from file'
f,'mvsave','savefile'
t,'mvcora','mvcorc','correlationfiles abs. and complex'
f,'mvdd1','mvdd2','mvdc1','mvdc2','complex corr-files for terms in sum'
f,'mvpopu','populationfiles'
140.,140.,5000.,0.0,0.2,0.0,12000.,'vib. energy coupl qm1 qm2 em1 em2'
f,'StevMA','filename for absorption spectrum'
t,'emissi','filename for emission spectrum'
16821.,'e00 in cm**-1'
600.,13000.,18000.,'# points, min, max of abs-spectrum'
1024.,12000.,18500.,'# points, min, max of emi-spectrum'
285.,'damping factor gamma in cm**-1'
f,14177.,'Smiro1','eigenvalue, eigenf.-filename'
```

Input file for calculating spectra (MAGRITTE)

'inputfile for MAGRITTE: 1D split operator on one surface'
'PROPAGATION:'
1D-12,'totaltime sec'
1000,'number of timesteps'
1,'number of steps between correlation'
-0.2,'xstart angstrom'
0.2,'xend angstrom'
1024,'number of points on grid'
'FILES:'
F,'maplo','plotfilename'
1,1,'number of plots, timestep for each plot'
T,'pot','potentialfile'
F,'mawave','wavefunctionfile'
F,'masave','savefile'
T,'fftaa4','fftcc4','correlationfiles (absolute,complex)'
F,'absorp','absorption spectrum file'
T,'emissn','emission spectrum file'
'POTENTIALS:'
16.0,'mass of mode g/mole'
T,0.15,1015.,0.0,'harmonic initial wp (shift,vib.energy,momentum)'
F,-0.18,600.,46000.,0,'Morse initial wp (shift,vib.energy,dissenergy,qu#)'
F,'efunc','file containing user-defined initial wavepacket'
F,0.3,'factor for coordinate dependent transition moment: mu=factor*x'
F,274.,'harmonic final potential, vib.energy(cm^{-1})'
T,1015.,50000.,'Morse final potential, vib.energy(cm^{-1}),dissenergy(cm^{-1})'
F,274.,10000.,11.5305,631.4,'Coon pot., zero pt.en.,A,a,Emin (all cm^{-1})'
F,'JTpot','Potential read from file (energy in cm^{-1})'
'SPECTRA:'
17600,'energy of electronic origin transition(cm^{-1})'
10000.,25000.,1024,'absorption spectrum min(cm^{-1}),max(cm^{-1}),#points'
10000.,19000.,1024,'emission_spectrum min(cm^{-1}),max(cm^{-1}),#points'
250,'damping factor(gamma,cm^{-1})'
'EIGENFUNCTION'
F,.,'efunc','eigenvalue, eigenfunction file'

Input for calculating ligand-field states (AOMX)

Program AOMX, 09-Jun-96 Version
Author Heribert Adamsky, Theoretical Chemistry, HHU Duesseldorf, FRG
MDET=252, MLIG=150, MVAR=40, MAOP=10, MOCS=10, MEEX=20

ReO2py4

2 electrons
rotation group: D4

esig(py) = 11000
epis(py) = 0
epic(py) = 500
esig(O) = 20000
epis(O) = 13500
epic(O) = 13500
B = 285
C = 1140
zeta = 2900

1 THETA = 90 PHI = 0 PSI = 90
2 THETA = 90 PHI = 90 PSI = 90
3 THETA = 90 PHI = 180 PSI = 90
4 THETA = 90 PHI = -90 PSI = 90
5 THETA = 0 PHI = 0 PSI = 0
6 THETA = 180 PHI = 0 PSI = 0

1 ESIG = esig(py) EPIS = epis(py) EPIC = epic(py)
2 ESIG = esig(py) EPIS = epis(py) EPIC = epic(py)
3 ESIG = esig(py) EPIS = epis(py) EPIC = epic(py)
4 ESIG = esig(py) EPIS = epis(py) EPIC = epic(py)
5 ESIG = esig(O) EPIS = epis(O) EPIC = epic(O)
6 ESIG = esig(O) EPIS = epis(O) EPIC = epic(O)

A = 0 B = B C = C
ZETA = zeta

Samples of output files may be obtained from the Supporting Information section of pub. 8 in Appendix 1.

Input file for diagonalizing a 3×3 matrix (THREEP)

```
'Inputfile for three coupled potentials in one dimension'
1024, 'Number of gridpoints, max=1024'
-.6,.6,'grid limits in Angstrom'
950.,'harmonic vib frequency in cm-1'
16.,'Mass of mode in g/mole'
0.09,'Offset DeltaQ in Angstrom'
5000.,1000.,'Ligand field parameters Kxy and DeltaPi in cm-1'
2500.,2500.,2500.,'Coupling constants V12, V13, V23 in cm-1'
```

Source code for diagonalization of a 3×3 matrix (THREEP)

```
parameter(kdim=1024)
    DOUBLE PRECISION A(3,3),EV1(3),EVEC(6),EVG(20),HREAL,TF,SD,TP,SG,
    *
SS,DQ,L,MIN,LOWLIMIT,UPLIMIT,FVIBH,AMASS,DELTAQ,KXY,DPI,V12,V13,V
23,
    * Q(kdim),EH1(kdim), EH2(kdim), EH3(kdim), EAD1(kdim), EAD2(kdim),
    * EAD3(kdim), DX
    INTEGER ID,LP,I,J,II,NPOINT
    CHARACTER*80 NAME,DUMMY
    CHARACTER*3 EVNAME(20),HCHAR
    ID=5
    LP=6
C
C    one-dimensional coupled potentials, three state model
C    February 18, 2001 version
C

C    Input
C
C    Arbitrary title
    read(ID,*) dummy
C
C    Number of gridpoints, max=1024 (identical to subsequent Magritte calc)
    read(ID,*) NPOINT,DUMMY
C
C    low and high limit of grid in Angstrom (identical to subsequent Magritte calc)
    read(ID,*) LOWLIMIT, UPLIMIT, DUMMY
C
C    harmonic vib frequency in cm-1 (identical to subsequent Magritte calc)
    read(ID,*) FVIBH, DUMMY
C
C    Mass of mode in g/mole (identical to subsequent Magritte calc)
    read(ID,*) AMASS, DUMMY
C
C    Offset DeltaQ in Angstrom
    read(ID,*) DELTAQ, DUMMY
C
C    Ligand field parameters in cm-1
    read(ID,*) KXY, DPI, DUMMY
C
C    Coupling constants in cm-1
    read(ID,*) V12,V13,V23, DUMMY

C    Write info on screen to check
```

```
      WRITE(LP,*)'3 coupled potentials - 1 dimensional'
      WRITE(LP,*)'creates Magritte input potentials'
      WRITE(LP,*)'make sure to match parameters'
      WRITE(LP,*)'number of points',NPOINT
      WRITE(LP,*)'grid limits in Angstrom',LOWLIMIT,UPLIMIT
      WRITE(LP,*)'harmonic vib frequency in cm-1', FVIBH
      WRITE(LP,*)'mass of mode in g/mole)', AMASS
      WRITE(LP,*)'DeltaQ in Angstrom', DELTAQ
      WRITE(LP,*)'Kxy and DeltaPi in cm-1', KXY, DPI
      WRITE(LP,*)'V12, V13, V23 in cm-1', v12,V13,V23

C     Unit conversion
C     DeltaQ and limits to dimless

      LOWLIMIT=LOWLIMIT/5.80655*SQRT(FVIBH*AMASS)
      UPLIMIT=UPLIMIT/5.80655*SQRT(FVIBH*AMASS)
      DELTAQ=DELTAQ/5.80655*SQRT(FVIBH*AMASS)
      DX= (UPLIMIT-LOWLIMIT)/(NPOINT-1)

C     Calculate crystal-field energies

      ECF1= 3*KXY
      ECF2= DPI
      ECF3= 2*DPI+4*KXY

C     Calculate arrays with potentials

      DO II=1, NPOINT

       Q(II)=LOWLIMIT+(II-1)*DX

       CALL ZERO(A)

       A(1,1)= ECF1+0.5D00*FVIBH*Q(II)**2
       A(2,1)= V12
       A(3,1)= V13
       A(2,2)= ECF2+0.5D00*FVIBH*(Q(II)**2-2*Q(II)*DELTAQ)
       A(3,2)= V23
       A(3,3)= ECF3+0.5D00*FVIBH*(Q(II)**2-4*Q(II)*DELTAQ)
       EH1(II)=A(1,1)
       EH2(II)=A(2,2)
       EH3(II)=A(3,3)

       CALL HERMQR(3,A,EV1,0,EVEC,3)
```

```
      EAD1(II)=EV1(1)
      EAD2(II)=EV1(2)
      EAD3(II)=EV1(3)
    ENDDO


C   Write files

1000  FORMAT(2D15.7)

    DO II=1,NPOINT
      Q(II)=Q(II)*5.80655/SQRT(AMASS*FVIBH)
    ENDDO

    OPEN(UNIT=2,name='EH1')
    DO II=1,NPOINT
      WRITE(2,1000) Q(II),EH1(II)
    ENDDO
    CLOSE(2)

    OPEN(UNIT=2,name='EH2')
    DO II=1,NPOINT
      WRITE(2,1000) Q(II),EH2(II)
    ENDDO
    CLOSE(2)

    OPEN(UNIT=2,name='EH3')
    DO II=1,NPOINT
      WRITE(2,1000) Q(II),EH3(II)
    ENDDO
    CLOSE(2)

    OPEN(UNIT=2,name='EAD1')
    DO II=1,NPOINT
      WRITE(2,1000) Q(II),EAD1(II)
    ENDDO
    CLOSE(2)

    OPEN(UNIT=2,name='EAD2')
    DO II=1,NPOINT
      WRITE(2,1000) Q(II),EAD2(II)
    ENDDO
    CLOSE(2)

    OPEN(UNIT=2,name='EAD3')
    DO II=1,NPOINT
```

```
      WRITE(2,1000) Q(II),EAD3(II)
    ENDDO
    CLOSE(2)

    WRITE(LP,*) 'ALL DONE...'
    END
C
    SUBROUTINE ZERO(A)
    DOUBLE PRECISION A(3,3)
    INTEGER I,J
    DO 10 I=1,3
    DO 10 J=1,3
   10 A(I,J)=0.
    END
```

This program requires the library routine HERMQR, only the heading is reproduced here.

```
    SUBROUTINE HERMQR(NN,A,EIGVAL,IVEC,EIGVEC,MAX)
    IMPLICIT DOUBLE PRECISION (A-H,O-Z)
C
C   CALCULATION OF EIGENVALUES AND EIGENVECTORS OF A
HERMITIAN MATRIX
C   REFERENCES :
C   D.J.MUELLER,'HOUSEHOLDER'S METHOD FOR COMPLEX MATRICES
AND
C   EIGENSYSTEMS OF HERMITIAN MATRICES',NUM.MATH.,VOL.8,PP72-
92,(1966)
C   P.A.BUSINGER,'EIGENVALUES AND EIGENVECTORS OF A REAL
SYMMETRIC
C   MATRIX BY THE QR METHOD',COMM.ACM,VOL.8,P218,(APRIL,1965)
C
C   A        HERMITIAN MATRIX OF ORDER NN - REAL PART AS LOWER
C            TRIANGULAR MATRIX. ABOVE DIAGONAL IMAGINARY PART
C            OF LOWER TRIANGULAR MATRIX - CHOOSE CORRECT SIGN
C   EIGVAL   VECTOR CONTAINING ORDERED EIGENVALUES OF A
(LOWEST
C            FIRST)
C   EIGVEC   VECTOR CONTAINING REAL AND IMAGINARY PARTS OF
C            EIGENVECTORS OF A FOR REQUIRED EIGENVALUE 'EIGVAL'
C   IVEC=0   NO EIGENVECTORS TO BE CALCULATED, ONLY
EIGENVALUES
C      =N    FIRST N EIGENVECTORS ARE CALCULATED - REAL VECTORS
C            IN COLUMN 1 TO N AND IMAGINARY VECTORS IN N+1 TO 2N
C   MAX      ACTUAL DIMENSION IN MAIN PROGRAM
C
```

ACS PUBLICATIONS DIVISION GUIDELINES

FOR THESES AND DISSERTATIONS

ATTENTION: STUDENTS, STUDENT ADVISORS, AND TEACHERS

Permission is automatically granted to include **your** paper(s) or portions of **your** paper(s) in your thesis; please pay special attention to the implications paragraph below. The Copyright Subcommittee of the Joint Board/Council Committees on Publications approved the following:

> Copyright permission for published and submitted material from theses and dissertations
> ACS extends blanket permission to students to include in their theses and dissertations their own articles, or portions thereof, that have been published in ACS journals or submitted to ACS journals for publication, provided that the ACS copyright credit line is noted on the appropriate page(s).
>
> Publishing implications of electronic publication of theses and dissertation material
> Students and their mentors should be aware that posting of theses and dissertation material on the Web prior to submission of material from that thesis or dissertation to an ACS journal may affect publication in that journal. Whether Web posting is considered prior publication may be evaluated on a case-by-case basis by the journal's editor. If an ACS journal editor considers Web posting to be "prior publication", the paper will not be accepted for publication in that journal. If you intend to submit your unpublished paper to ACS for publication, check with the appropriate editor prior to posting your manuscript electronically.

If your paper has **not** yet been published by ACS, we have no objection to your including the text or portions of the text in your thesis/dissertation in **print and microfilm formats**; please note, however, that electronic distribution or Web posting of the unpublished paper as part of your thesis in electronic formats might jeopardize publication of your paper by ACS. Please print the following credit line on the first page of your article: "Reproduced (or 'Reproduced in part') with permission from [JOURNAL NAME], in press (or 'submitted for publication'). Unpublished work copyright [CURRENT YEAR] American Chemical Society." Include appropriate information.

If your paper has already been published by ACS and you want to include the text or portions of the text in your thesis/dissertation in **print or microfilm formats**, please print the ACS copyright credit line on the first page of your article: "Reproduced (or 'Reproduced in part') with permission from [FULL REFERENCE CITATION.] Copyright [YEAR] American Chemical Society." Include appropriate information.

Note: If you plan to submit your thesis to UMI or to another dissertation distributor, you should not include the unpublished ACS paper in your thesis if the thesis will be disseminated electronically, until ACS has published your paper. After publication of the paper by ACS, you may release the entire thesis (**not the individual ACS article by itself**) for electronic dissemination; ACS's copyright credit line should be printed on the first page of the ACS paper.

SUMMARY: The inclusion of your ACS unpublished or published manuscript is permitted in your thesis in print and microfilm formats. If ACS has published your paper you may include the manuscript in your thesis on an intranet that is not publicly available. Your ACS article cannot be posted electronically on a publicly available medium, such as but not limited to, electronic archives, Internet, intranet, library server, etc. The only material from your paper that can be posted on a public electronic medium is the article abstract, figures, and tables and you may link to the article's DOI.

Questions? Please contact the ACS Publications Division Copyright Office at copyright@acs.org or at 202-872-4368.

August 1998, March 2003, October 2003